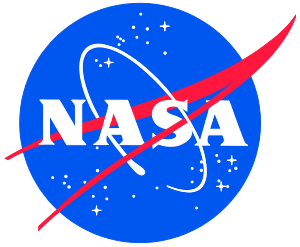


NASA/TM-2019-220424



Experimental Investigation of Hexcomb-Pattern Roughness Effects on Transition Onset and Turbulent Heating Augmentation at Mach 6

*Brian R. Hollis
Langley Research Center, Hampton, Virginia*

November 2019

NASA STI Program . . . in Profile

Since its founding, NASA has been dedicated to the advancement of aeronautics and space science. The NASA scientific and technical information (STI) program plays a key part in helping NASA maintain this important role.

The NASA STI program operates under the auspices of the Agency Chief Information Officer. It collects, organizes, provides for archiving, and disseminates NASA's STI. The NASA STI program provides access to the NTRS Registered and its public interface, the NASA Technical Reports Server, thus providing one of the largest collections of aeronautical and space science STI in the world. Results are published in both non-NASA channels and by NASA in the NASA STI Report Series, which includes the following report types:

- **TECHNICAL PUBLICATION.** Reports of completed research or a major significant phase of research that present the results of NASA Programs and include extensive data or theoretical analysis. Includes compilations of significant scientific and technical data and information deemed to be of continuing reference value. NASA counter-part of peer-reviewed formal professional papers but has less stringent limitations on manuscript length and extent of graphic presentations.
- **TECHNICAL MEMORANDUM.** Scientific and technical findings that are preliminary or of specialized interest, e.g., quick release reports, working papers, and bibliographies that contain minimal annotation. Does not contain extensive analysis.
- **CONTRACTOR REPORT.** Scientific and technical findings by NASA-sponsored contractors and grantees.

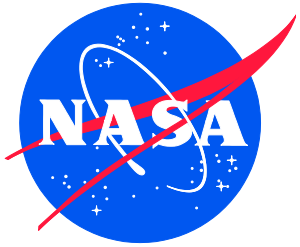
- **CONFERENCE PUBLICATION.** Collected papers from scientific and technical conferences, symposia, seminars, or other meetings sponsored or co-sponsored by NASA.
- **SPECIAL PUBLICATION.** Scientific, technical, or historical information from NASA programs, projects, and missions, often concerned with subjects having substantial public interest.
- **TECHNICAL TRANSLATION.** English-language translations of foreign scientific and technical material pertinent to NASA's mission.

Specialized services also include organizing and publishing research results, distributing specialized research announcements and feeds, providing information desk and personal search support, and enabling data exchange services.

For more information about the NASA STI program, see the following:

- Access the NASA STI program home page at <http://www.sti.nasa.gov>
- E-mail your question to help@sti.nasa.gov
- Phone the NASA STI Information Desk at 757-864-9658
- Write to:
NASA STI Information Desk
Mail Stop 148
NASA Langley Research Center
Hampton, VA 23681-2199

NASA/TM-2019-220424



Experimental Investigation of Hexcomb-Pattern Roughness Effects on Transition Onset and Turbulent Heating Augmentation at Mach 6

Brian R. Hollis
Langley Research Center, Hampton, Virginia

National Aeronautics and
Space Administration

Langley Research Center
Hampton, Virginia 23681-2199

November 2019

The use of trademarks or names of manufacturers in the report is for accurate reporting and does not constitute an official endorsement, either expressed or implied, of such products or manufacturers by the National Aeronautics and Space Administration.

Available from:

NASA Center for AeroSpace Information
7115 Standard Drive
Hanover, MD 21076-1320
443-757-5802

Table of Contents

Table of Contents.....	i
List of Tables.....	ii
Abstract.....	1
Symbols.....	2
Subscripts and Superscripts.....	2
Acronyms.....	2
Introduction.....	3
Background	3
Experimental Tools and Methods	4
Wind Tunnel Models.....	4
Model Geometries.....	4
Model Fabrication.....	4
Wind Tunnel Test Facility.....	4
Facility Description.....	4
Facility Operating Conditions.....	5
Experimental Data.....	5
Data Acquisition and Reduction	5
Data Mapping and Presentation	6
Phosphor Thermography Data Quality.....	7
Heat Transfer Data Uncertainty	7
Transition Onset Location Definition.....	7
Computational Tools and Methods.....	8
Experimental Data Analysis	9
Reynolds Number Effects on Heating and Transition	9
Roughness Pattern Effects on Heating and Transition	9
General Reynolds Number and Roughness Pattern Trends	9
Transition Onset Data.....	10
Roughness Heating Augmentation.....	10
Summary	10
References.....	10
Appendix A. Spherical-Cap Geometry Global Heating Images.....	94
Appendix B. Sphere-Cone Geometry Global Heating Images.....	119

List of Tables

Table 1. Wind tunnel model geometry parameters.....	12
Table 2. Wind tunnel model hexcomb parameters	12
Table 3. 20-Inch Mach 6 Air Tunnel Test 6991 run matrix.....	13
Table 4. Spherical-cap 1200-0025 transition locations.....	16
Table 5. Spherical-cap 1200-0050 transition locations.....	17
Table 6. Spherical-cap 1200-0100 transition locations.....	18
Table 7. Spherical-cap 3700-0015 transition locations.....	19
Table 8. Spherical-cap 3700-0025 transition locations.....	20
Table 9. Spherical-cap 3700-0050 transition locations.....	21
Table 10. Spherical-cap 3700-0100 transition locations.....	22
Table 11. Sphere-cone 1200-0025 transition locations.....	23
Table 12. Sphere-cone 1200-0050 transition locations.....	24
Table 13. Sphere-cone 1200-0100 transition locations.....	25
Table 14. Sphere-cone 3700-0015 transition locations.....	26
Table 15. Sphere-cone 3700-0025 transition locations.....	27
Table 16. Sphere-cone 3700-0050 transition locations.....	28
Table 17. Sphere-cone 3700-0100 transition locations.....	29

List of Figures

Figure 1. Discrete surface roughness types.....	30
Figure 2. Distributed surface roughness types.....	30
Figure 3. Avcoat arc jet test sample coupon.....	30
Figure 4. Spherical-cap geometry.....	31
Figure 5. Sphere-cone geometry.....	31
Figure 6. Schematic of Langley Research Center 20-Inch Mach 6 Air Tunnel.....	32
Figure 7. Langley Research Center 20-Inch Mach 6 Air Tunnel test section.....	32
Figure 8. Sample phosphor thermography 2-D image data.....	33
Figure 9. Sample 3-D mapping of phosphor thermography data.....	33
Figure 10. Streamlines for data extraction on spherical-cap geometry.....	34
Figure 11. Streamlines for data extraction on sphere-cone geometry.....	34
Figure 12. Illustration of camera field-of-view for hemisphere model in 20-Inch Mach 6 Air Tunnel.....	35
Figure 13. Tangent-slope-intercept method for determination of effect transition onset location.....	36
Figure 14. Comparison of irregular transition wedges vs. mean transition front.....	36
Figure 15. Reynolds Number effects, smooth spherical-cap model images.....	38
Figure 16. Reynolds number effects, smooth spherical-cap geometry plots.....	39
Figure 17. Reynolds Number effects, spherical-cap 3700-0015 model images.....	40
Figure 18. Reynolds Number effects, spherical-cap 3700-0015 model plots.....	41
Figure 19. Reynolds Number effects, spherical-cap 1200-0025 model images.....	42
Figure 20. Reynolds Number effects, spherical-cap 1200-0025 model plots.....	43
Figure 21. Reynolds Number effects, spherical-cap 3700-0025 model images.....	44
Figure 22. Reynolds Number effects, spherical-cap 3700-0025 model plots.....	45
Figure 23. Reynolds Number effects, spherical-cap 1200-0050 model images.....	46
Figure 24. Reynolds Number effects, spherical-cap 1200-0050 model plots.....	47
Figure 25. Reynolds Number effects, spherical-cap 3700-0050 model images.....	48
Figure 26. Reynolds Number effects, spherical-cap 3700-0050 model plots.....	49
Figure 27. Reynolds Number effects, spherical-cap 1200-0100 model images.....	50
Figure 28. Reynolds Number effects, spherical-cap 1200-0100 model plots.....	51
Figure 29. Reynolds Number effects, spherical-cap 3700-0100 model images.....	52
Figure 30. Reynolds Number effects, spherical-cap 3700-0100 model plots.....	53
Figure 31. Reynolds Number effects, smooth sphere-cone model images.....	54
Figure 32. Reynolds Number effects, smooth sphere-cone model plots.....	55
Figure 33. Reynolds Number effects, sphere-cone 3700-0015 model images.....	56
Figure 34. Reynolds Number effects, sphere-cone 3700-0015 model plots.....	57
Figure 35. Reynolds Number effects, sphere-cone 1200-0025 model images.....	58
Figure 36. Reynolds Number effects, sphere-cone 1200-0025 model plots.....	59
Figure 37. Reynolds Number effects, sphere-cone 3700-0025 model images.....	60
Figure 38. Reynolds Number effects, sphere-cone 3700-0025 model plots.....	61
Figure 39. Reynolds Number effects, sphere-cone 1200-0050 model images.....	62
Figure 40. Reynolds Number effects, sphere-cone 1200-0050 model plots.....	63
Figure 41. Reynolds Number effects, sphere-cone 3700-0050 model images.....	64
Figure 42. Reynolds Number effects, sphere-cone 3700-0050 model plots.....	65
Figure 43. Reynolds Number effects, sphere-cone 1200-0100 model images.....	66
Figure 44. Reynolds Number effects, sphere-cone 1200-0100 model plots.....	67
Figure 45. Reynolds Number effects, sphere-cone 3700-0100 model images.....	68
Figure 46. Reynolds Number effects, sphere-cone 3700-0100 model plots.....	69
Figure 47. Roughness pattern effects, spherical-cap geometry, $Re_\infty = 2.1 \times 10^6/\text{ft}$ images.....	70
Figure 48. Roughness pattern effects, spherical-cap geometry, $Re_\infty = 2.1 \times 10^6/\text{ft}$ plots.....	71

Figure 49. Roughness pattern effects, spherical-cap geometry, $Re_{\infty} = 3.0 \times 10^6/\text{ft}$ images.....	72
Figure 50. Roughness pattern effects, spherical-cap geometry, $Re_{\infty} = 3.0 \times 10^6/\text{ft}$ plots.....	73
Figure 51. Roughness pattern effects, spherical-cap geometry, $Re_{\infty} = 5.0 \times 10^6/\text{ft}$ images.....	74
Figure 52. Roughness pattern effects, spherical-cap geometry, $Re_{\infty} = 5.0 \times 10^6/\text{ft}$ plots.....	75
Figure 53. Roughness pattern effects, spherical-cap geometry, $Re_{\infty} = 6.6 \times 10^6/\text{ft}$ images.....	76
Figure 54. Roughness pattern effects, spherical-cap geometry, $Re_{\infty} = 6.6 \times 10^6/\text{ft}$ plots.....	77
Figure 55. Roughness pattern effects, spherical-cap geometry, $Re_{\infty} = 7.5 \times 10^6/\text{ft}$ images.....	78
Figure 56. Roughness pattern effects, spherical-cap geometry, $Re_{\infty} = 7.5 \times 10^6/\text{ft}$ plots.....	79
Figure 57. Roughness pattern effects, spherical-cap geometry, $Re_{\infty} = 8.3 \times 10^6/\text{ft}$ images.....	80
Figure 58. Roughness pattern effects, spherical-cap geometry, $Re_{\infty} = 8.3 \times 10^6/\text{ft}$ plots.....	81
Figure 59. Roughness pattern effects, sphere-cone geometry, $Re_{\infty} = 2.1 \times 10^6/\text{ft}$ images.....	82
Figure 60. Roughness pattern effects, sphere-cone cap geometry, $Re_{\infty} = 2.1 \times 10^6/\text{ft}$ plots.....	83
Figure 61. Roughness pattern effects, sphere-cone geometry, $Re_{\infty} = 3.0 \times 10^6/\text{ft}$ images.....	84
Figure 62. Roughness pattern effects, spherical-cap geometry, $Re_{\infty} = 3.0 \times 10^6/\text{ft}$ plots.....	85
Figure 63. Roughness pattern effects, sphere-cone geometry, $Re_{\infty} = 5.0 \times 10^6/\text{ft}$ images.....	86
Figure 64. Roughness pattern effects, spherical-cap geometry, $Re_{\infty} = 5.0 \times 10^6/\text{ft}$ plots.....	87
Figure 65. Roughness pattern effects, sphere-cone geometry, $Re_{\infty} = 6.6 \times 10^6/\text{ft}$ images.....	88
Figure 66. Roughness pattern effects, spherical-cap geometry, $Re_{\infty} = 6.6 \times 10^6/\text{ft}$ plots.....	89
Figure 67. Roughness pattern effects, sphere-cone geometry, $Re_{\infty} = 7.5 \times 10^6/\text{ft}$ images.....	90
Figure 68. Roughness pattern effects, spherical-cap geometry, $Re_{\infty} = 7.5 \times 10^6/\text{ft}$ plots.....	91
Figure 69. Roughness pattern effects, sphere-cone geometry, $Re_{\infty} = 8.3 \times 10^6/\text{ft}$ images.....	92
Figure 70. Roughness pattern effects, spherical-cap geometry, $Re_{\infty} = 8.3 \times 10^6/\text{ft}$ plots.....	93
Figure 71. Test 6991, Run 24, $Re_{\infty} = 2.1 \times 10^6/\text{ft}$, spherical-cap, smooth OML.....	95
Figure 72. Test 6991, Run 1, $Re_{\infty} = 3.0 \times 10^6/\text{ft}$, spherical-cap, smooth OML.....	95
Figure 73. Test 6991, Run 2, $Re_{\infty} = 5.0 \times 10^6/\text{ft}$, spherical-cap, smooth OML.....	96
Figure 74. Test 6991, Run 3, $Re_{\infty} = 6.6 \times 10^6/\text{ft}$, spherical-cap, smooth OML.....	96
Figure 75. Test 6991, Run 4, $Re_{\infty} = 7.5 \times 10^6/\text{ft}$, spherical-cap, smooth OML.....	97
Figure 76. Test 6991, Run 5, $Re_{\infty} = 8.3 \times 10^6/\text{ft}$, spherical-cap, smooth OML.....	97
Figure 77. Test 6991, Run 25, $Re_{\infty} = 2.1 \times 10^6/\text{ft}$, spherical-cap 1200-0025.....	98
Figure 78. Test 6991, Run 28, $Re_{\infty} = 3.0 \times 10^6/\text{ft}$, spherical-cap 1200-0025.....	98
Figure 79. Test 6991, Run 26, $Re_{\infty} = 5.0 \times 10^6/\text{ft}$, spherical-cap 1200-0025.....	99
Figure 80. Test 6991, Run 27, $Re_{\infty} = 6.6 \times 10^6/\text{ft}$, spherical-cap 1200-0025.....	99
Figure 81. Test 6991, Run 29, $Re_{\infty} = 7.5 \times 10^6/\text{ft}$, spherical-cap 1200-0025.....	100
Figure 82. Test 6991, Run 30, $Re_{\infty} = 8.3 \times 10^6/\text{ft}$, spherical-cap 1200-0025.....	100
Figure 83. Test 6991, Run 31, $Re_{\infty} = 2.1 \times 10^6/\text{ft}$, spherical-cap 1200-0050.....	101
Figure 84. Test 6991, Run 32, $Re_{\infty} = 3.0 \times 10^6/\text{ft}$, spherical-cap 1200-0050.....	101
Figure 85. Test 6991, Run 33, $Re_{\infty} = 5.0 \times 10^6/\text{ft}$, spherical-cap 1200-0050.....	102
Figure 86. Test 6991, Run 34, $Re_{\infty} = 6.6 \times 10^6/\text{ft}$, spherical-cap 1200-0050.....	102
Figure 87. Test 6991, Run 35, $Re_{\infty} = 7.5 \times 10^6/\text{ft}$, spherical-cap 1200-0050.....	103
Figure 88. Test 6991, Run 36, $Re_{\infty} = 8.3 \times 10^6/\text{ft}$, spherical-cap 1200-0050.....	103
Figure 89. Test 6991, Run 37, $Re_{\infty} = 2.1 \times 10^6/\text{ft}$, spherical-cap 1200-0100.....	104
Figure 90. Test 6991, Run 38, $Re_{\infty} = 3.0 \times 10^6/\text{ft}$, spherical-cap 1200-0100.....	104
Figure 91. Test 6991, Run 39, $Re_{\infty} = 5.0 \times 10^6/\text{ft}$, spherical-cap 1200-0100.....	105
Figure 92. Test 6991, Run 40, $Re_{\infty} = 6.6 \times 10^6/\text{ft}$, spherical-cap 1200-0100.....	105
Figure 93. Test 6991, Run 41, $Re_{\infty} = 7.5 \times 10^6/\text{ft}$, spherical-cap 1200-0100.....	106
Figure 94. Test 6991, Run 42, $Re_{\infty} = 8.3 \times 10^6/\text{ft}$, spherical-cap 1200-0100.....	106
Figure 95. Test 6991, Run 104, $Re_{\infty} = 2.1 \times 10^6/\text{ft}$, spherical-cap 3700-0015.....	107
Figure 96. Test 6991, Run 103, $Re_{\infty} = 3.0 \times 10^6/\text{ft}$, spherical-cap 3700-0015.....	107
Figure 97. Test 6991, Run 102, $Re_{\infty} = 5.0 \times 10^6/\text{ft}$, spherical-cap 3700-0015.....	108
Figure 98. Test 6991, Run 101, $Re_{\infty} = 6.6 \times 10^6/\text{ft}$, spherical-cap 3700-0015.....	108
Figure 99. Test 6991, Run 105, $Re_{\infty} = 7.5 \times 10^6/\text{ft}$, spherical-cap 3700-0015.....	109

Figure 100. Test 6991, Run 106, $Re_{\infty} = 8.3 \times 10^6/\text{ft}$, spherical-cap	3700-0015.....	109
Figure 101. Test 6991, Run 8, $Re_{\infty} = 2.1 \times 10^6/\text{ft}$, spherical-cap	3700-0025.....	110
Figure 102. Test 6991, Run 6, $Re_{\infty} = 3.0 \times 10^6/\text{ft}$, spherical-cap	3700-0025.....	110
Figure 103. Test 6991, Run 7, $Re_{\infty} = 5.0 \times 10^6/\text{ft}$, spherical-cap	3700-0025.....	111
Figure 104. Test 6991, Run 9, $Re_{\infty} = 6.6 \times 10^6/\text{ft}$, spherical-cap	3700-0025.....	111
Figure 105. Test 6991, Run 10, $Re_{\infty} = 7.5 \times 10^6/\text{ft}$, spherical-cap	3700-0025.....	112
Figure 106. Test 6991, Run 11, $Re_{\infty} = 8.3 \times 10^6/\text{ft}$, spherical-cap	3700-0025.....	112
Figure 107. Test 6991, Run 19, $Re_{\infty} = 2.1 \times 10^6/\text{ft}$, spherical-cap	3700-0050.....	113
Figure 108. Test 6991, Run 18, $Re_{\infty} = 3.0 \times 10^6/\text{ft}$, spherical-cap	3700-0050.....	113
Figure 109. Test 6991, Run 20, $Re_{\infty} = 5.0 \times 10^6/\text{ft}$, spherical-cap	3700-0050.....	114
Figure 110. Test 6991, Run 21, $Re_{\infty} = 6.6 \times 10^6/\text{ft}$, spherical-cap	3700-0050.....	114
Figure 111. Test 6991, Run 22, $Re_{\infty} = 7.5 \times 10^6/\text{ft}$, spherical-cap	3700-0050.....	115
Figure 112. Test 6991, Run 23, $Re_{\infty} = 8.3 \times 10^6/\text{ft}$, spherical-cap	3700-0050.....	115
Figure 113. Test 6991, Run 13, $Re_{\infty} = 2.1 \times 10^6/\text{ft}$, spherical-cap	3700-0100.....	116
Figure 114. Test 6991, Run 12, $Re_{\infty} = 3.0 \times 10^6/\text{ft}$, spherical-cap	3700-0100.....	116
Figure 115. Test 6991, Run 14, $Re_{\infty} = 5.0 \times 10^6/\text{ft}$, spherical-cap	3700-0100.....	117
Figure 116. Test 6991, Run 15, $Re_{\infty} = 6.6 \times 10^6/\text{ft}$, spherical-cap	3700-0100.....	117
Figure 117. Test 6991, Run 16, $Re_{\infty} = 7.5 \times 10^6/\text{ft}$, spherical-cap	3700-0100.....	118
Figure 118. Test 6991, Run 17, $Re_{\infty} = 8.3 \times 10^6/\text{ft}$, spherical-cap	3700-0100.....	118
Figure 119. Test 6991, Run 55, $Re_{\infty} = 2.1 \times 10^6/\text{ft}$, sphere-cone, smooth OML	120
Figure 120. Test 6991, Run 56, $Re_{\infty} = 3.0 \times 10^6/\text{ft}$, sphere-cone, smooth OML	120
Figure 121. Test 6991, Run 52, $Re_{\infty} = 5.0 \times 10^6/\text{ft}$, sphere-cone, smooth OML	121
Figure 122. Test 6991, Run 53, $Re_{\infty} = 6.6 \times 10^6/\text{ft}$, sphere-cone, smooth OML	121
Figure 123. Test 6991, Run 63, $Re_{\infty} = 7.5 \times 10^6/\text{ft}$, sphere-cone, smooth OML	122
Figure 124. Test 6991, Run 54, $Re_{\infty} = 8.3 \times 10^6/\text{ft}$, sphere-cone, smooth OML	122
Figure 125. Test 6991, Run 76, $Re_{\infty} = 2.1 \times 10^6/\text{ft}$, sphere-cone 1200-0025	123
Figure 126. Test 6991, Run 77, $Re_{\infty} = 3.0 \times 10^6/\text{ft}$, sphere-cone 1200-0025	123
Figure 127. Test 6991, Run 78, $Re_{\infty} = 5.0 \times 10^6/\text{ft}$, sphere-cone 1200-0025	124
Figure 128. Test 6991, Run 79, $Re_{\infty} = 6.6 \times 10^6/\text{ft}$, sphere-cone 1200-0025	124
Figure 129. Test 6991, Run 81, $Re_{\infty} = 7.5 \times 10^6/\text{ft}$, sphere-cone 1200-0025	125
Figure 130. Test 6991, Run 80, $Re_{\infty} = 8.3 \times 10^6/\text{ft}$, sphere-cone 1200-0025	125
Figure 131. Test 6991, Run 82, $Re_{\infty} = 2.1 \times 10^6/\text{ft}$, sphere-cone 1200-0050	126
Figure 132. Test 6991, Run 83, $Re_{\infty} = 3.0 \times 10^6/\text{ft}$, spherical-cap 1200-0050	126
Figure 133. Test 6991, Run 84, $Re_{\infty} = 5.0 \times 10^6/\text{ft}$, sphere-cone 1200-0050	127
Figure 134. Test 6991, Run 85, $Re_{\infty} = 6.6 \times 10^6/\text{ft}$, sphere-cone 1200-0050	127
Figure 135. Test 6991, Run 87, $Re_{\infty} = 7.5 \times 10^6/\text{ft}$, sphere-cone 1200-0050	128
Figure 136. Test 6991, Run 86, $Re_{\infty} = 8.3 \times 10^6/\text{ft}$, sphere-cone 1200-0050	128
Figure 137. Test 6991, Run 88, $Re_{\infty} = 2.1 \times 10^6/\text{ft}$, sphere-cone 1200-0100	129
Figure 138. Test 6991, Run 89, $Re_{\infty} = 3.0 \times 10^6/\text{ft}$, sphere-cone 1200-0100	129
Figure 139. Test 6991, Run 90, $Re_{\infty} = 5.0 \times 10^6/\text{ft}$, sphere-cone 1200-0100	130
Figure 140. Test 6991, Run 91, $Re_{\infty} = 6.6 \times 10^6/\text{ft}$, sphere-cone 1200-0100	130
Figure 141. Test 6991, Run 93, $Re_{\infty} = 7.5 \times 10^6/\text{ft}$, sphere-cone 1200-0100	131
Figure 142. Test 6991, Run 92, $Re_{\infty} = 8.3 \times 10^6/\text{ft}$, sphere-cone 1200-0100	131
Figure 143. Test 6991, Run 107, $Re_{\infty} = 2.1 \times 10^6/\text{ft}$, sphere-cone 3700-0015	132
Figure 144. Test 6991, Run 108, $Re_{\infty} = 3.0 \times 10^6/\text{ft}$, sphere-cone 3700-0015	132
Figure 145. Test 6991, Run 109, $Re_{\infty} = 5.0 \times 10^6/\text{ft}$, sphere-cone 3700-0015	133
Figure 146. Test 6991, Run 110, $Re_{\infty} = 6.6 \times 10^6/\text{ft}$, sphere-cone 3700-0015	133
Figure 147. Test 6991, Run 111, $Re_{\infty} = 7.5 \times 10^6/\text{ft}$, sphere-cone 3700-0015	134
Figure 148. Test 6991, Run 112, $Re_{\infty} = 8.3 \times 10^6/\text{ft}$, sphere-cone 3700-0015	134
Figure 149. Test 6991, Run 64, $Re_{\infty} = 2.1 \times 10^6/\text{ft}$, sphere-cone 3700-0025	135
Figure 150. Test 6991, Run 65, $Re_{\infty} = 3.0 \times 10^6/\text{ft}$, sphere-cone 3700-0025	135

Figure 151. Test 6991, Run 66, $Re_{\infty} = 5.0 \times 10^6/\text{ft}$, sphere-cone 3700-0025.....	136
Figure 152. Test 6991, Run 67, $Re_{\infty} = 6.6 \times 10^6/\text{ft}$, sphere-cone 3700-0025.....	136
Figure 153. Test 6991, Run 68, $Re_{\infty} = 7.5 \times 10^6/\text{ft}$, sphere-cone 3700-0025.....	137
Figure 154. Test 6991, Run 69, $Re_{\infty} = 8.3 \times 10^6/\text{ft}$, sphere-cone 3700-0025.....	137
Figure 155. Test 6991, Run 57, $Re_{\infty} = 2.1 \times 10^6/\text{ft}$, sphere-cone 3700-0050.....	138
Figure 156. Test 6991, Run 58, $Re_{\infty} = 3.0 \times 10^6/\text{ft}$, sphere-cone 3700-0050.....	138
Figure 157. Test 6991, Run 59, $Re_{\infty} = 5.0 \times 10^6/\text{ft}$, sphere-cone 3700-0050.....	139
Figure 158. Test 6991, Run 60, $Re_{\infty} = 6.6 \times 10^6/\text{ft}$, sphere-cone 3700-0050.....	139
Figure 159. Test 6991, Run 62, $Re_{\infty} = 7.5 \times 10^6/\text{ft}$, sphere-cone 3700-0050.....	140
Figure 160. Test 6991, Run 61, $Re_{\infty} = 8.3 \times 10^6/\text{ft}$, sphere-cone 3700-0050.....	140
Figure 161. Test 6991, Run 70, $Re_{\infty} = 2.1 \times 10^6/\text{ft}$, sphere-cone 3700-0100.....	141
Figure 162. Test 6991, Run 71, $Re_{\infty} = 3.0 \times 10^6/\text{ft}$, sphere-cone 3700-0100.....	141
Figure 163. Test 6991, Run 72, $Re_{\infty} = 5.0 \times 10^6/\text{ft}$, sphere-cone 3700-0100.....	142
Figure 164. Test 6991, Run 73, $Re_{\infty} = 6.6 \times 10^6/\text{ft}$, sphere-cone 3700-0100.....	142
Figure 165. Test 6991, Run 75, $Re_{\infty} = 7.5 \times 10^6/\text{ft}$, sphere-cone 3700-0100.....	143
Figure 166. Test 6991, Run 74, $Re_{\infty} = 8.3 \times 10^6/\text{ft}$, sphere-cone 3700-0100.....	143

Abstract

An experimental investigation of hexcomb-patterned surface roughness effects on boundary-layer transition and turbulent heating has been performed. Two representative entry vehicle geometries, a spherical-cap aeroshell and a sphere-cone aeroshell, were considered. Multiple cast ceramic models of each geometry were fabricated with varying roughness pattern densities and depths that simulated an ablated hexcomb-structure thermal protection system. Wind tunnel testing was performed at Mach 6 over a range of Reynolds numbers sufficient to produce laminar, transitional, and turbulent flow. Aeroheating and boundary-layer transition onset data were obtained using global phosphor thermography. The experimental heating data are presented herein, as are comparisons to laminar and turbulent smooth-wall heat transfer distributions from computational flow field simulations.

Symbols

d	hexcomb depth
H_0	tunnel total (reservoir) enthalpy
H_{AW}	adiabatic wall enthalpy
H_W	wall enthalpy
H_{300K}	wall enthalpy at 300 K
h	measured heat-transfer film coefficient
h	hexcomb depth
h_{FR}	Fay-Riddell theory heat-transfer film coefficient
M_e	boundary-layer edge Mach number
M_∞	free stream Mach number
q	heat transfer rate
r_{stag}	approximate radius of edge Mach cutoff region
R	model radius
R_N	model nose radius
R_C	model corner radius
Re_θ	boundary-layer momentum thickness Reynolds number
Re_∞	free stream unit Reynolds number
s/R	normalized surface running length from edge Mach cutoff
s_0/R	normalized surface running length from stagnation point
$T_{w,AVG}$	average wall temperature
T_∞	free stream temperature
U_∞	free stream velocity
x, y, z	Cartesian coordinates
β	model spherical nose included angle
ϕ	streamline angular coordinate identifier
ρ_∞	free stream density
θ	boundary-layer momentum thickness

Subscripts and Superscripts

∞	wind tunnel free stream condition
0	wind tunnel stagnation or reservoir condition
e	boundary layer edge condition
w	model wall condition

Acronyms

CFD	Computational Fluid Dynamics
IHEAT	Imaging for Hypersonic Experimental Aerothermodynamic Testing
LAL	Langley Aerothermodynamic Laboratories
LARC	Langley Research Center
LAURA	Langley Aerothermodynamic Upwind Relaxation Algorithm
OML	Outer Mold Line
SLA	Stereo-Lithographic Apparatus
TPS	Thermal Protection System

Introduction

This report details an experimental dataset of hexcomb pattern surface roughness effects on boundary-layer transition and heating augmentation. The data were obtained through hypersonic wind tunnel testing of a set of representative entry vehicle geometries with roughness patterns that simulated those produced by the ablation of a hexcomb-structure thermal protection system (TPS). This report serves as a reference document that can be used as the basis for future detailed analysis of the heat-transfer distributions and boundary-layer transition onset locations measured in the test program.

Background

“Roughness” is a generic term in aerospace literature that encompasses many types of surface features that deviate from that of a smooth outer mold line (OML). Roughness can be divided into two general types, discrete and distributed. Discrete roughness (Figure 1) includes surface features such as: a) protruding compression pads or recessed cavities at mechanical attachment points; b) steps or gaps between heat shield tiles resulting from differential ablation of the tiles and the filler material between them; and c) physical damage to a TPS. Distributed roughness (Figure 2) includes features such as: a) regular patterns resulting from ablation of hexcomb-structure TPS; b) irregular deflections of a flexible TPS under aerodynamic loading; c) random “sand-grain” features resulting from ablation of a monolithic TPS; or d) the texture of overlapping fibers on a woven TPS.

Data on the effects of surface roughness are valuable because the roughness of an entry vehicle’s TPS can promote earlier boundary-layer transition and produce higher turbulent heating (and shear) levels than would be expected based on an idealized, smooth-wall analysis. However, due to the complexities of roughness effects, a vehicle’s TPS is typically designed using analytical, computational, and/or experimental techniques that are based on the assumption of a smooth surface. The effects of roughness on the aerothermodynamic environment can then be included through approximate engineering correlations and methods.

The purpose of this test program was to obtain data on the effects of distributed hexcomb pattern type roughness. Examples of ablating TPS that produce such patterns include the Avcoat material used on the Apollo capsules and the Orion EFT-1 flight test vehicle and the SLA-561V material used on the Mars Viking, Mars Exploration Rover, and Mars Pathfinder entry vehicles. These growth of hexcomb ablation patterns can be seen by comparing the pretest (Figure 3a) and post-test (Figure 3b) photographs of an Avcoat sample coupon subjected to an arc jet flow for material response testing.

The data obtained in this test program are intended for use in the development and/or validation of engineering correlations for the effects of hexcomb pattern roughness on boundary-layer transition and turbulent heat transfer. These data can also serve as the basis for development and/or validation of higher-fidelity, numerical flow-field simulation models for roughness effects.

Experimental Tools and Methods

Wind Tunnel Models

Model Geometries

Roughness effects data were obtained on two representative entry vehicle geometries: a spherical-cap geometry (Figure 4) and a sphere-cone geometry (Figure 5). The spherical-cap geometry is similar to that of the Mercury – Gemini – Apollo – Orion family of entry vehicles employed in NASA’s crewed space program. The sphere-cone geometry is similar to that of the Mars Viking – Mars Pathfinder – Mars Exploration Rover – Mars Phoenix – Mars Science Laboratory – Mars 2020 family of entry vehicle used in NASA’s robotic Mars exploration program. Geometry parameters for both configurations are listed in Table 1. Multiple models of each configuration were fabricated with a range of hexcomb roughness patterns, as detailed below.

Model Fabrication

The fabrication process for a ceramic model is documented in (Ref. 1). The first step in fabrication of a model is the production of a rapid-prototype, resin pattern of the geometry in a stereo-lithographic apparatus (SLA) machine. The pattern is then hand-worked to a smooth surface finish to remove any SLA manufacturing artifacts (note this this step was skipped for the pattern-roughness models in order to avoid damaging the hexcombs). A multiple-piece injection mold, from which the resin model can easily be removed, is then built around the resin pattern. The resin pattern is then removed and wax is injected into the mold to form a wax pattern. Next, a new two-piece shell mold is built around the wax pattern, and then the wax is burned out of the shell mold. A silica ceramic model is then slip-cast in the shell mold. Then, the ceramic model is removed from the shell mold, dried, and sintered. The finished ceramic model is then back-filled with a hydraulically setting magnesia ceramic for strength and support and mounted on a stainless-steel cylindrical sting. Finally, the model is coated with a mixture of phosphors that luminesce under ultraviolet lighting.

The parametric range of hexcomb densities and depths is detailed in Table 2. There were two limitations on the range of parameters that were considered. The first was the minimum resolution of the SLA machine, which is on the order of 0.001 in.; thus, the minimum hexcomb depth considered was 0.0015 inches. The second limitation was the memory of the computer used to generate the CAD files for the SLA machine, which allowed a maximum of 3700 hexcombs per model. A total of 7 patterns were generated for each geometry with hexcomb depths of 0.0015 in. to 0.0100 in. and either 1200 or 3700 hexcombs. The nomenclature for identifying the model and hexcomb pattern was *Geometry - number of hexcombs - hexcomb depth*; e.g. *Spherical-cap 3700-0100*, which identifies the spherical-cap geometry model with 3700 hexcombs of 0.0100 in. depth.

Wind Tunnel Test Facility

Facility Description

Wind tunnel testing was performed at the Langley Aerothermodynamics Laboratory (LAL) in the 20-Inch Mach 6 Air Tunnel. This wind tunnel is described in brief below and more detailed information on the LAL facilities can be found in Refs 2-3.

The NASA LaRC 20-Inch Mach 6 Air Tunnel (Figure 6 - Figure 7) is a blow-down facility in which heated, dried, and filtered air is used as the test gas. The tunnel has a two-dimensional contoured nozzle that opens into a 20.5 in. × 20.0 in. test section. The tunnel is equipped with a bottom-mounted injection

system with a -5-deg to +55-deg pitch range and ± 5 -deg yaw range that can transfer a model from a sheltered model box to the tunnel centerline in less than 0.5 sec. Run times of up to 15 minutes are possible in this facility, although for the current aeroheating study, run times of only a few seconds were required. The nominal reservoir conditions of this facility produce perfect-gas free stream flows with Mach numbers between 5.8 and 6.1 and unit Reynolds numbers of $0.5 \times 10^6/\text{ft}$ to $8.3 \times 10^6/\text{ft}$. With its wide Reynolds number operating range capable of producing laminar, transitional, or turbulent flow on most geometries, this tunnel is primarily used for heat-transfer and boundary-layer transition studies.

Facility Operating Conditions

Data were obtained in the 20-Inch Mach 6 Air Tunnel Test 6991 for six unit Reynolds numbers from $Re_\infty = 3.0 \times 10^6/\text{ft}$ to $8.3 \times 10^6/\text{ft}$. These conditions are listed in Table 3. Entries in this table are sorted first by model geometry and hexcomb pattern, and then by free stream unit Reynolds number. All spherical-cap data were obtained at $\alpha = 28$ deg. and all sphere-cone data were obtained at $\alpha = 16$ deg. The values were selected for continuity with smooth-OML data obtained in prior testing of the Orion entry vehicle and the MSL entry vehicle (e.g. Ref. 4).

Free stream velocity (U_∞), density (ρ_∞), temperature (T_∞), unit Reynolds number (Re_∞), and Mach number (M_∞) are provided in Table 3. Additionally, an average model surface temperature (T_w), enthalpy difference (ΔH_{tot}), and reference heat transfer film-coefficient value (h_{FR}) are provided. The temperature is the average over the model surface when the thermographic phosphor image was obtained and is provided because boundary-layer transition is known to be sensitive to wall temperature. The enthalpy term is defined as the difference $H_0 - H_{300\text{K}}$ between the free stream total enthalpy and the wall enthalpy at cold wall (300 K) conditions. The film coefficient is the value from the Fay-Riddell theory (Ref. 5) for a hemispherical radius at cold wall conditions, where the radius is the nose radius of the model geometry.

Experimental Data

Data Acquisition and Reduction

Aeroheating data were obtained using the two-color, relative-intensity, global phosphor thermography method (Ref. 6) and reduced using the IHEAT (Imaging for Hypersonic Experimental Aerothermodynamic Testing) code (Ref. 7). In this method, a model is illuminated by ultraviolet light sources that induce temperature-dependent fluorescence of the phosphor coating. Fluorescent intensity images of a model are taken in the tunnel before and during a run using a three-color, charge-coupled device camera and the images are processed to determine heat-transfer distributions. The intensity data are then converted to temperature using pretest calibrations of the data acquisition system.

Heat-transfer film coefficients are determined by assuming a step function in the film coefficient from the prerun temperature to the run temperature, which corresponds to a parabolic temperature-time history. The heating data are typically reported in terms of the ratio h/h_{FR} where the heat-transfer film coefficient, h , is defined in terms of enthalpy as:

$$h = q/\Delta H_{\text{tot}} = q/(H_{\text{AW}} - H_w) = q/(H_0 - H_w) \quad (1)$$

In the calculation of the heat-transfer film coefficient, it is assumed that, for a blunt-body, the adiabatic wall enthalpy H_{AW} is equal to the free stream total enthalpy of the tunnel, H_0 . This heat transfer coefficient definition provides a theoretically near-constant value over the course of a run since the decrease in time of the heat transfer rate in the numerator as the model surface becomes hotter is balanced by the decrease of

the enthalpy-difference term in the denominator.

Data Mapping and Presentation

The two-dimensional (2-D) image data output from IHEAT (Figure 8) for each run were transformed to account for optical perspective effects and mapped to a three-dimensional (3-D) CAD surface of the wind tunnel model (Figure 9). To accomplish this mapping, perspective, translational, and rotational transformations were first performed on the 3-D CAD surface until its 2-D projection matched that of the 2-D image data. The image data were then assigned transformed (x, y, z) coordinates based on interpolation between the image and surface geometry. Finally, the transformation was inverted to obtain an orthographic, 3-D heating distribution map of the experimental data.

The mapped data from all runs are collected in the Appendices and presented therein as large, high-resolution images. These images are ordered by model geometry, hexcomb pattern, and Reynolds numbers. Smaller images will be shown in the body of the report along with streamline-based heating distributions.

An additional data manipulation was performed to extract the streamline-based heating distributions from the mapped wind tunnel data set. These streamline-based data sets are used in boundary-layer transition analyses and for comparisons of Reynolds number and hexcomb pattern effects. For each run, streamlines were defined based on the boundary-layer edge velocity vectors from the computed flow fields (to be discussed in the next section). Thirty-six streamline termini were established at locations spaced in 10-deg increments around the circumference of the geometry and the streamlines were then traced backward from each terminus toward the flow field stagnation point. Each streamline is identified by the angular location, ϕ , of its terminus. The resulting streamlines are shown in Figure 10 for the spherical-cap geometry and in Figure 11 for the sphere-cone geometry. The geometric definition (x, y, z) of each streamline were then interpolated onto the 3-D mapped image and data were extracted along each streamline in terms of h/h_{FR} vs. s/R , where s/R is the normalized streamline distance from the stagnation point. Additionally, the predicted flow field quantities (boundary-layer height, momentum-thickness Reynolds number, etc.) were also extracted along these streamlines and combined with the wind tunnel data set to enable transition onset analyses.

One additional complication needs to be noted with respect to extraction of data along streamlines. The extraction algorithm tended to fail near the stagnation point where the velocity vectors approach zero; essentially the physical location became indeterminate, resulting in unreliable path-lengths through the stagnation region. This problem was resolved by stopping the reverse tracing of the streamlines from the outer edge of the model toward that stagnation point at the location where the edge Mach number, M_e , dropped below 0.025. The “true” streamline length value, s_0 was determined from an estimate of the physical length from the M_e cutoff to the stagnation region as a function of the streamline terminus angular location ϕ and the approximate radius of the stagnation region, r_{stag} :

$$s_0 = s + \Delta s \quad (2)$$

$$\Delta s = \cos(2\phi) \times r_{stag}/3 + r_{stag}, \text{ where } r_{stag} \cong 0.003 \text{ m} \quad (3)$$

In the body of this report, plotted data will be shown in terms of s/R , as that is the quantity in which the data were extracted along streamlines. However, the estimated actual distance, s_0/R , will be provided in data tabulations and conversions between the two quantities may be made using Eqs. 2-3.

Phosphor Thermography Data Quality

An important factor that influences the quality of phosphor thermography data quality is the local surface inclination at a given point on the model with respect to both the camera and the UV lights. Phosphor thermography provides the best result when the surface to be imaged is normal to the camera, which reduces perspective distortion and image smearing, and when the surface is well illuminated, which induces the best temperature response of the phosphor coating. Because of the three-dimensional nature of a wind tunnel model, the entire surface of a model cannot be optimally imaged, or in some cases cannot even be viewed. For blunt bodies such as those in this test, the windward centerline region of the model – the ‘bottom’ of the model with respect to the view orientation - is the area where the data quality is most affected. This situation is illustrated for a simple hemispherical model in Figure 12. Because of this limitation, windward centerline region data are only regarded as qualitative, not quantitative. Although image data from this region will be shown, quantitative plotted data and transition location data will not be provided for the streamlines originating from the 160-deg through 200-deg termini.

Heat Transfer Data Uncertainty

The experimental uncertainty for convective heat transfer measurements on a *smooth, blunt body geometry* model in the 20-Inch Mach 6 Air Tunnel is quantified as a function of net uncertainties resulting from: the data acquisition method ($\pm 10\%$); flow quality and test-condition repeatability ($\pm 5\%$); and the accuracy of the 3D mapping process ($\pm 10\%$), which results in an overall root-sum-squared value of $\pm 15\%$. Experience with this technique indicates that these values are usually conservative and as will be shown later, the predicted and measured heating distributions were in close agreement (generally less than $\pm 5\%$) for laminar, smooth-wall cases. It is assumed that the hexcomb patterns introduced additional uncertainties for two reasons. First, the hexcomb cell walls were extremely thin, and the one-dimensional heat conduction assumption does not apply to them. Second, the hexcombs produced very detailed heating patterns, which in some cases, were smaller than the resolution of the camera system; thus, a measurement in such areas is, in effect, a spatial average rather than a point measurement. Quantification of such errors on a macro-scale is not possible because of the localized and position/pattern dependency of hexcomb features, but is probably on the order of $\pm 10\text{--}20\%$. Taken together with the smooth-wall uncertainty, the uncertainty in hexcomb heating is estimated to be in the $\pm 18\text{--}25\%$ range.

Transition Onset Location Definition

From a flow physics standpoint, transition onset is defined as the point where smooth, laminar flow in the boundary layer begins to break down. This location can, in theory, be determined through flow field imaging and/or diagnostic techniques (e.g., high-frequency pressure measurements, laser velocimetry) to determine when fluctuations in a quantity of interest, e.g., mean velocity, exceeded a specified criterion. However, in this study, the only measurements are of the surface temperature and (through data reduction) the surface heating. For such measurements, the differences in temperature or heating levels between laminar flow and transitional flow can be too subtle at some conditions to permit precise definition of the onset location. This measurement is more difficult when the local roughness height is small, in which case, the change from laminar to transitional/turbulent flow is gradual, but easier when the local roughness height is large and the transition length is very short.

In lieu of a precise measurement of the transition location, transition onset is defined herein through a common approach in which an “effective” or “apparent” point is determined through the “tangent-slope-intercept” method. As shown in Figure 13, using sample data for a hemisphere from Ref. 8, the effective transition onset location is identified as the point where a line drawn tangent to the slope of the heat-transfer

distribution curve through the transition region intercepts the nominal, laminar level. While this method does not identify the location at which fluctuations in the boundary-layer flow begin, it is consistent with common practice for determining the roughness-induced transition location via surface-based measurement techniques. This method also permits a more consistent means of identifying a relevant transition parameter since identification of the small rise in heating levels at the actual transition onset location would be highly susceptible to error through surface measurement techniques alone. If the data herein are compared to other datasets, then it will be necessary to ensure that the same definition of transition onset is applied to ensure consistency.

While this effective transition onset location is easy to define in principle, in practice, there can still be considerable uncertainty in determining the effects of roughness on transition location because of the difficulty in precisely defining the relevant roughness height. Consider again the distributed roughness hemisphere example, where now the heating data are shown in image form (Figure 14) rather than a plotted distribution. In the ideal case, where the surface roughness was invariant over the entire model surface, the transition onset location would be at a constant streamline length around the circumference of the model since the flow field is axisymmetric. However, as shown in Figure 14, there are clearly circumferential variations in the transition onset location. These variations are due to the fact that the local roughness height at any given location can vary from the nominal value for many reasons, including: the fidelity of the model fabrication process; the uniformity in application of the phosphor coating; and damage to the coating due to handling of the model or particle impacts during testing.

For an axisymmetric flow such as that over the example hemisphere, it is possible to reduce the uncertainty in the transition onset location by averaging multiple onset locations around the body to determine a mean value. This approach was followed in Ref. 8. However, for the three-dimensional flow fields produced by the sphere-cone and spherical-cap geometries considered herein, that is not possible. Thus, any correlations drawn from this dataset can be expected to have greater scatter than those that were derived from Ref. 8.

Computational Tools and Methods

Flow field solutions were generated using the LAURA (Langley Aerothermodynamic Upwind Relaxation Algorithm) code. LAURA (Refs. 9-10) is a three-dimensional, structured-grid, finite-volume solver that includes perfect-gas and nonequilibrium chemistry options, a variety of turbulence models, and ablation and radiative transport capabilities. LAURA solutions were used for comparisons of predicted heating levels with the measured data and to define the streamlines along which to extract the mapped experimental data, as described above.

Solutions were computed on multiblock grids of each geometry with a smooth (no hexcombs) outer mold line. Grid adaption was performed to align the grid outer boundary with the bow shock and to cluster cells near the surface to produce wall cell Reynolds numbers on the order of 1 to 10. Free stream conditions were set to the nominal wind tunnel conditions for each run as given in Table 3. For these wind tunnel conditions, the perfect-gas air option was used. Both laminar and turbulent solutions were generated. Turbulent cases were computed using the Cebeci-Smith algebraic model with fully-turbulent flow over the entire geometry.

For the wall temperature boundary condition, a change in the normal practice for wind tunnel simulations of setting this value to a “cold-wall” ambient temperature (because of the usually small variation in heat-transfer coefficient with temperature) was employed. Literature on roughness effects indicates a dependence of transition onset location on the ratio of boundary-layer edge temperature to wall

temperature T_e/T_w . To approximately account for this effect (which was expected to be small for these test conditions), the computations were performed using a uniform “hot-wall” wall temperature set to the average of the measured surface temperature on the model. These values varied between 327 K to 411 K, depending on roughness height and test condition.

Experimental Data Analysis

Reynolds Number Effects on Heating and Transition

The effects of Reynolds number on the heating levels and boundary-layer transition onset locations are illustrated for each hexcomb roughness pattern in Figure 15 - Figure 30 for the spherical-cap geometry and in Figure 31 - Figure 46 for the sphere-cone geometry. Two figures are provided for each case: in the first figure, global heating images are shown for each Reynolds number, ordered left-to-right, top-to-bottom in terms of increasing Reynolds number; in the second figure, line plots of h/h_{FR} vs. s/R are shown, ordered left-to-right, top-to-bottom in terms of streamline angular coordinate. For brevity, all of the streamlines are not shown in these figures. Instead, streamlines are shown at 30-deg increments from 0-deg to 150-deg. As noted earlier, the data for streamlines between 160-deg and 200-deg is considered to be qualitative, not quantitative. Data for streamlines from 210-deg to 360-deg are nominally symmetric with the data from 0-deg to 150-deg, although in practice, model surface irregularities can cause asymmetric behavior. Such local asymmetries can be observed in the images that accompany the line plots.

In these line-plots, the CFD predictions for smooth-wall, laminar and turbulent heating levels are also shown. Because the heat-transfer film coefficient ratio, h/h_{FR} , remains nearly constant with Reynolds number, only the lowest Reynolds number laminar prediction is shown for each case. However, since this invariance does not hold for turbulent flow, turbulent predictions are shown for each Reynolds number. As noted previously, turbulent cases were treated as fully-turbulent flow over the entire geometry. These turbulent cases are shown as limiting bounds, since the actual transition occurred at different locations for each test condition / model geometry.

Roughness Pattern Effects on Heating and Transition

The same data are shown in the next group of figures, but they are reordered to show the effects of the roughness pattern (number of hexcombs, hexcomb depth) on transition and heating at each Reynolds number. The spherical-cap data are shown in Figure 47 - Figure 58 and the sphere-cone data are shown in Figure 59 - Figure 70. Two figures are provided for each case: in the first figure, global heating images are shown for each Reynolds number, ordered left-to-right, top-to-bottom in terms of increasing number of hexcombs and hexcomb depth; in the second figure, line plots of h/h_{FR} vs. s/R are shown, ordered left-to-right, top-to-bottom in terms of streamline angular coordinate. As with the Reynold number effects figure set, both laminar and turbulent CFD heating predictions are shown in figure.

General Reynolds Number and Roughness Pattern Trends

In these line-plots for Reynolds number and roughness pattern effects, the laminar CFD predictions shown allow for baseline assessment of the computational accuracy through comparisons with the low-Reynolds number, small roughness height cases for which transition did not occur. In general, good agreement between data and predictions was observed for all laminar cases. However, the turbulent predictions are shown only for illustrative purposes since the fully-turbulent, smooth-wall computations do not account for roughness effects on transition location or heating augmentation.

Reynolds-number and roughness-pattern effects on transition and heating follow expected trends. As Reynolds number is increased, the transition onset location moves upstream toward the stagnation point of the model. The transition onset location also moves upstream as roughness height is increased and the measured rough-wall turbulent heating levels grow increasingly greater than the predicted smooth-wall turbulent heating levels.

Transition Onset Data

Tabulations of the transition onset location for each streamline as determined using the tangent-slope-intercept definition are given in Table 4 - Table 10 for the spherical-cap geometry and in Table 11 - Table 17 for the sphere-cone geometry. As noted earlier, these values are given in terms of the estimated actual streamline distance, s_0/R , not the length from the $M_e = 0.025$ cutoff. Tabular entries are only provided for those streamlines on which transition was noted. For streamlines which are not listed, either the flow remained laminar over the model or the roughness height was sufficiently large to produce turbulent flow at the stagnation point. For reference, the boundary-layer momentum thickness, Re_0 , value at transition is also listed. This quantity, along with the roughness height, is a first-order factor in the correlation of roughness transition data. As the intent of this activity is to document and release the data for future analyses, development of transition correlations based on these data is not within the scope of this report.

Roughness Heating Augmentation

In this report, analysis of the heating augmentation due to the roughness patterns is limited to the expected observation that heating levels increase with roughness height. This limitation is due to the complexities of the problem and the goal of releasing this data set as a basis for further analysis. For any given roughness-pattern / Reynolds-number / body-point-location, the heating augmentation with respect to smooth-wall laminar or turbulent predictions can be determined through reference to the data and figures presented herein. However, the development of engineering correlations or numerical models for simulation of these data depend on not just modeling the effects of roughness on heating, but also modeling the effects of roughness on transition onset; that is, it is not possible to accurately predict heating levels without being able to first predict the transition onset location. Such activities are deferred to future in-depth analyses.

Summary

The effects of distributed surface roughness on boundary-layer transition and turbulent heating have been investigated through hypersonic wind tunnel testing of two representative entry vehicle geometry models with roughness patterns simulating those of a heat shield with an ablated TPS. Heating and transition onset data were obtained at Mach 6 over a range of roughness heights and free stream Reynolds numbers sufficient to produce laminar, transitional and turbulent flow. Boundary-layer transition onset locations have been tabulated and heating distributions have been provided as both line plots and image data.

References

1. Buck, G. M., "Rapid Model Fabrication and Testing for Aerospace Vehicles," AIAA Paper 2000-0826, 38th AIAA Aerospace Sciences Meeting and Exhibit, Reno, NV, January 10-13, 2000.
2. Berger, K., Rufer, S., Hollingsworth, K. and Wright, S., "NASA Langley Aerothermodynamic Laboratory: Hypersonic Testing Capabilities," AIAA Paper 2015-1337, 53rd AIAA Aerospace Sciences Meeting, Kissimmee, FL, January 5-9, 2015.

3. Hollis, B. R., Berger, K. T., Berry, S. A., Brauckmann, G. J., et al, "Entry, Descent, and Landing Aerothermodynamics: NASA Langley Experimental Capabilities and Contributions," AIAA Paper 2014-1154, AIAA 52nd Aerospace Science Meeting, National Harbor, MD, January 13-17, 2014.
4. Hollis, B. R., "Blunt-Body Entry Vehicle Aerothermodynamics: Transition and Turbulent Heating," *Journal of Spacecraft and Rockets*, Vol. 49, No. 3, May-June 2012, pp. 435-449.
5. Fay, J. A., and Riddell, F. R., "Theory of Stagnation Point Heat Transfer in Dissociated Air," *Journal of Aeronautical Sciences*, Vol. 25, No. 2., February 1958, pp. 73-85.
6. Buck, G. M., "Surface Temperature/Heat Transfer Measurement Using a Quantitative Phosphor Thermography System," AIAA Paper 91-0064, 29th Aerospace Sciences Meeting, Reno, NV, January 7-10, 1991.
7. Merski, N. R., "Global Aeroheating Wind-Tunnel Measurements Using Improved Two-Color Phosphor Thermography Methods," *Journal of Spacecraft and Rockets*, Vol. 36, No. 2, March-April 1999, pp. 160-170.
8. Hollis, B. R., "Experimental Investigation of Roughness Effects on Transition Onset and Turbulent Heating Augmentation at Mach 6 and Mach 10," NASA TM-2017-219613, May 2017.
9. Gnoffo, P. A., "An Upwind-Biased, Point-Implicit Algorithm for Viscous, Compressible Perfect-Gas Flows," NASA TP-2953, February 1990.
10. Mazaheri, A., Gnoffo, P. A., Johnston, C. O., and Kleb, B., "LAURA User's Manual: 5.5-65135," NASA TM-2013-217800, February 2013.

Table 1. Wind tunnel model geometry parameters.

Model geometry	Model radius, <i>R</i>		Nose radius, <i>R_n</i>		Shoulder radius, <i>R_s</i>		Nose included angle, β		<i>R_n/R</i>	<i>R_s/R</i>
	in.	m	in.	m	in.	m	deg.			
Spherical-cap	3.000	0.0762	7.200	0.1829	0.3000	0.00762	23.04	2.4	0.100	
Sphere-cone	3.000	0.0762	1.500	0.0371	0.1500	0.00381	20.00	0.5	0.050	

Table 2. Wind tunnel model hexcomb parameters

Hexcomb Pattern	Number of hexcombs	Hexcomb depth, <i>h</i>		Hexcomb width, <i>d</i>		<i>d/h</i>
		in.	m	in.	m	
Smooth	N/A	N/A	N/A	N/A	N/A	N/A
1200-0025	1200	0.0025	6.350E-05	0.1300	3.302E-03	52.0
1200-0025	1200	0.0050	1.270E-04	0.1300	3.302E-03	26.0
1200-0050	1200	0.0100	2.540E-04	0.1300	3.302E-03	13.0
3700-0015	3700	0.0015	3.810E-05	0.0650	1.651E-03	43.3
3700-0025	3700	0.0025	6.350E-05	0.0650	1.651E-03	26.0
3700-0050	3700	0.0050	1.270E-04	0.0650	1.651E-03	13.0
3700-0100	3700	0.0100	2.540E-04	0.0650	1.651E-03	6.5

Table 3. 20-Inch Mach 6 Air Tunnel Test 6991 run matrix.

Run	Config- uration	Hexcomb pattern	α_{∞} (kg/m ³)	Re_{∞} (1/ft)	M_{∞}	T_{∞} (K)	ρ_{∞} (kg/m ³)	U_{∞} (m/s)	ΔH (MJ/kg)	h_{FR} (kg/m ² -s)	$T_{w,avg}$ (K)
24	Spherical-cap	Smooth	28	2.10E+06	5.96	61.9	3.253E-02	939.5	2.030E+05	1.144E-01	327
1	Spherical-cap	Smooth	28	3.03E+06	5.99	62.5	4.708E-02	948.7	2.120E+05	1.396E-01	333
2	Spherical-cap	Smooth	28	5.04E+06	6.02	63.2	7.843E-02	957.5	2.213E+05	1.822E-01	348
3	Spherical-cap	Smooth	28	6.63E+06	6.04	62.6	1.023E-01	954.6	2.170E+05	2.074E-01	357
4	Spherical-cap	Smooth	28	7.46E+06	6.04	62.5	1.154E-01	953.6	2.167E+05	2.196E-01	361
5	Spherical-cap	Smooth	28	8.34E+06	6.03	58.6	1.249E-01	918.1	1.791E+05	2.199E-01	349
104	Spherical-cap	3700-0015	28	2.10E+06	5.96	61.9	3.253E-02	939.5	2.030E+05	2.507E-01	330
103	Spherical-cap	3700-0015	28	3.03E+06	5.99	62.5	4.708E-02	948.7	2.120E+05	3.056E-01	337
102	Spherical-cap	3700-0015	28	5.04E+06	6.02	63.2	7.843E-02	957.5	2.213E+05	3.993E-01	361
101	Spherical-cap	3700-0015	28	6.63E+06	6.04	62.6	1.023E-01	954.6	2.170E+05	4.552E-01	379
105	Spherical-cap	3700-0015	28	7.46E+06	6.04	62.5	1.154E-01	953.6	2.167E+05	4.806E-01	388
106	Spherical-cap	3700-0015	28	8.34E+06	6.03	58.6	1.249E-01	918.1	1.791E+05	4.818E-01	377
25	Spherical-cap	1200-0025	28	2.10E+06	5.96	61.9	3.253E-02	939.5	2.030E+05	1.144E-01	330
28	Spherical-cap	1200-0025	28	3.03E+06	5.99	62.5	4.708E-02	948.7	2.120E+05	1.396E-01	345
26	Spherical-cap	1200-0025	28	5.04E+06	6.02	63.2	7.843E-02	957.5	2.213E+05	1.822E-01	374
27	Spherical-cap	1200-0025	28	6.63E+06	6.04	62.6	1.023E-01	954.6	2.170E+05	2.074E-01	393
29	Spherical-cap	1200-0025	28	7.46E+06	6.04	62.5	1.154E-01	953.6	2.167E+05	2.196E-01	400
30	Spherical-cap	1200-0025	28	8.34E+06	6.03	58.6	1.249E-01	918.1	1.791E+05	2.199E-01	384
8	Spherical-cap	3700-0025	28	2.10E+06	5.96	61.9	3.253E-02	939.5	2.030E+05	1.144E-01	327
6	Spherical-cap	3700-0025	28	3.03E+06	5.99	62.5	4.708E-02	948.7	2.120E+05	1.396E-01	345
7	Spherical-cap	3700-0025	28	5.04E+06	6.02	63.2	7.843E-02	957.5	2.213E+05	1.822E-01	382
9	Spherical-cap	3700-0025	28	6.63E+06	6.04	62.6	1.023E-01	954.6	2.170E+05	2.074E-01	398
10	Spherical-cap	3700-0025	28	7.46E+06	6.04	62.5	1.154E-01	953.6	2.167E+05	2.196E-01	404
11	Spherical-cap	3700-0025	28	8.34E+06	6.03	58.6	1.249E-01	918.1	1.791E+05	2.199E-01	387
31	Spherical-cap	1200-0050	28	2.10E+06	5.96	61.9	3.253E-02	939.5	2.030E+05	1.144E-01	332
32	Spherical-cap	1200-0050	28	3.03E+06	5.99	62.5	4.708E-02	948.7	2.120E+05	1.396E-01	354
33	Spherical-cap	1200-0050	28	5.04E+06	6.02	63.2	7.843E-02	957.5	2.213E+05	1.822E-01	384
34	Spherical-cap	1200-0050	28	6.63E+06	6.04	62.6	1.023E-01	954.6	2.170E+05	2.074E-01	399
35	Spherical-cap	1200-0050	28	7.46E+06	6.04	62.5	1.154E-01	953.6	2.167E+05	2.196E-01	403
36	Spherical-cap	1200-0050	28	8.34E+06	6.03	58.6	1.249E-01	918.1	1.791E+05	2.199E-01	388
19	Spherical-cap	3700-0050	28	2.10E+06	5.96	61.9	3.253E-02	939.5	2.030E+05	1.144E-01	335
18	Spherical-cap	3700-0050	28	3.03E+06	5.99	62.5	4.708E-02	948.7	2.120E+05	1.396E-01	358
20	Spherical-cap	3700-0050	28	5.04E+06	6.02	63.2	7.843E-02	957.5	2.213E+05	1.822E-01	391
21	Spherical-cap	3700-0050	28	6.63E+06	6.04	62.6	1.023E-01	954.6	2.170E+05	2.074E-01	404
22	Spherical-cap	3700-0050	28	7.46E+06	6.04	62.5	1.154E-01	953.6	2.167E+05	2.196E-01	409
23	Spherical-cap	3700-0050	28	8.34E+06	6.03	58.6	1.249E-01	918.1	1.791E+05	2.199E-01	393
37	Spherical-cap	1200-0100	28	2.10E+06	5.96	61.9	3.253E-02	939.5	2.030E+05	1.144E-01	350
38	Spherical-cap	1200-0100	28	3.03E+06	5.99	62.5	4.708E-02	948.7	2.120E+05	1.396E-01	371
39	Spherical-cap	1200-0100	28	5.04E+06	6.02	63.2	7.843E-02	957.5	2.213E+05	1.822E-01	397
40	Spherical-cap	1200-0100	28	6.63E+06	6.04	62.6	1.023E-01	954.6	2.170E+05	2.074E-01	402
41	Spherical-cap	1200-0100	28	7.46E+06	6.04	62.5	1.154E-01	953.6	2.167E+05	2.196E-01	408
42	Spherical-cap	1200-0100	28	8.34E+06	6.03	58.6	1.249E-01	918.1	1.791E+05	2.199E-01	392

Table 3 continued.

Run	Config- uration	Hexcomb pattern	α_∞ (kg/m ³)	Re_∞ (1/ft)	M_∞	T_∞ (K)	ρ_∞ (kg/m ³)	U_∞ (m/s)	ΔH (MJ/kg)	h_{FR} (kg/m ² -s)	$T_{w,avg}$ (K)
13	Spherical-cap	3700-0100	28	2.10E+06	5.96	61.9	3.253E-02	939.5	2.030E+05	1.144E-01	350
12	Spherical-cap	3700-0100	28	3.03E+06	5.99	62.5	4.708E-02	948.7	2.120E+05	1.396E-01	369
14	Spherical-cap	3700-0100	28	5.04E+06	6.02	63.2	7.843E-02	957.5	2.213E+05	1.822E-01	398
15	Spherical-cap	3700-0100	28	6.63E+06	6.04	62.6	1.023E-01	954.6	2.170E+05	2.074E-01	406
16	Spherical-cap	3700-0100	28	7.46E+06	6.04	62.5	1.154E-01	953.6	2.167E+05	2.196E-01	411
17	Spherical-cap	3700-0100	28	8.34E+06	6.03	58.6	1.249E-01	918.1	1.791E+05	2.199E-01	394
55	Sphere-cone	Smooth	16	2.10E+06	5.96	61.9	3.253E-02	939.5	2.030E+05	2.507E-01	333
56	Sphere-cone	Smooth	16	3.03E+06	5.99	62.5	4.708E-02	948.7	2.120E+05	3.056E-01	339
52	Sphere-cone	Smooth	16	5.04E+06	6.02	63.2	7.843E-02	957.5	2.213E+05	3.987E-01	351
53	Sphere-cone	Smooth	16	6.63E+06	6.04	62.6	1.023E-01	954.6	2.170E+05	4.552E-01	360
63	Sphere-cone	Smooth	16	7.46E+06	6.04	62.5	1.154E-01	953.6	2.167E+05	4.806E-01	328
54	Sphere-cone	Smooth	16	8.34E+06	6.03	58.6	1.249E-01	918.1	1.791E+05	4.818E-01	350
107	Sphere-cone	3700-0015	16	2.10E+06	5.96	61.9	3.253E-02	939.5	2.030E+05	2.507E-01	345
108	Sphere-cone	3700-0015	16	3.03E+06	5.99	62.5	4.708E-02	948.7	2.120E+05	3.056E-01	345
109	Sphere-cone	3700-0015	16	5.04E+06	6.02	63.2	7.843E-02	957.5	2.213E+05	3.987E-01	369
110	Sphere-cone	3700-0015	16	6.63E+06	6.04	62.6	1.023E-01	954.6	2.170E+05	4.552E-01	382
111	Sphere-cone	3700-0015	16	7.46E+06	6.04	62.5	1.154E-01	953.6	2.167E+05	4.818E-01	388
112	Sphere-cone	3700-0015	16	8.34E+06	6.03	58.6	1.249E-01	918.1	1.791E+05	4.806E-01	375
76	Sphere-cone	1200-0025	16	2.10E+06	5.96	61.9	3.253E-02	939.5	2.030E+05	2.507E-01	333
77	Sphere-cone	1200-0025	16	3.03E+06	5.99	62.5	4.708E-02	948.7	2.120E+05	3.056E-01	354
78	Sphere-cone	1200-0025	16	5.04E+06	6.02	63.2	7.843E-02	957.5	2.213E+05	3.987E-01	384
79	Sphere-cone	1200-0025	16	6.63E+06	6.04	62.6	1.023E-01	954.6	2.170E+05	4.552E-01	398
81	Sphere-cone	1200-0025	16	7.46E+06	6.04	62.5	1.154E-01	953.6	2.167E+05	4.806E-01	399
80	Sphere-cone	1200-0025	16	8.34E+06	6.03	58.6	1.249E-01	918.1	1.791E+05	4.818E-01	382
64	Sphere-cone	3700-0025	16	2.10E+06	5.96	61.9	3.253E-02	939.5	2.030E+05	2.507E-01	347
65	Sphere-cone	3700-0025	16	3.03E+06	5.99	62.5	4.708E-02	948.7	2.120E+05	3.056E-01	378
66	Sphere-cone	3700-0025	16	5.04E+06	6.02	63.2	7.843E-02	957.5	2.213E+05	3.987E-01	393
67	Sphere-cone	3700-0025	16	6.63E+06	6.04	62.6	1.023E-01	954.6	2.170E+05	4.552E-01	393
68	Sphere-cone	3700-0025	16	7.46E+06	6.04	62.5	1.154E-01	953.6	2.167E+05	4.806E-01	400
69	Sphere-cone	3700-0025	16	8.34E+06	6.03	58.6	1.249E-01	918.1	1.791E+05	4.818E-01	381
82	Sphere-cone	1200-0050	16	2.10E+06	5.96	61.9	3.253E-02	939.5	2.030E+05	2.507E-01	337
83	Sphere-cone	1200-0050	16	3.03E+06	5.99	62.5	4.708E-02	948.7	2.120E+05	3.056E-01	357
84	Sphere-cone	1200-0050	16	5.04E+06	6.02	63.2	7.843E-02	957.5	2.213E+05	3.987E-01	384
85	Sphere-cone	1200-0050	16	6.63E+06	6.04	62.6	1.023E-01	954.6	2.170E+05	4.552E-01	398
87	Sphere-cone	1200-0050	16	7.46E+06	6.04	62.5	1.154E-01	953.6	2.167E+05	4.806E-01	404
86	Sphere-cone	1200-0050	16	8.34E+06	6.03	58.6	1.249E-01	918.1	1.791E+05	4.818E-01	389
57	Sphere-cone	3700-0050	16	2.10E+06	5.96	61.9	3.253E-02	939.5	2.030E+05	2.507E-01	339
58	Sphere-cone	3700-0050	16	3.03E+06	5.99	62.5	4.708E-02	948.7	2.120E+05	3.056E-01	361
59	Sphere-cone	3700-0050	16	5.04E+06	6.02	63.2	7.843E-02	957.5	2.213E+05	3.987E-01	390
60	Sphere-cone	3700-0050	16	6.63E+06	6.04	62.6	1.023E-01	954.6	2.170E+05	4.552E-01	401
62	Sphere-cone	3700-0050	16	7.46E+06	6.04	62.5	1.154E-01	953.6	2.167E+05	4.806E-01	403
61	Sphere-cone	3700-0050	16	8.34E+06	6.03	58.6	1.249E-01	918.1	1.791E+05	4.818E-01	390

Table 3 continued.

Run	Config- uration	Hexcomb pattern	α_∞ (kg/m ³)	Re_∞ (1/ft)	M_∞	T_∞ (K)	ρ_∞ (kg/m ³)	U_∞ (m/s)	ΔH (MJ/kg)	h_{FR} (kg/m ² -s)	$T_{w,avg}$ (K)
88	Sphere-cone	1200-0100	16	2.10E+06	5.96	61.9	3.253E-02	939.5	2.030E+05	2.507E-01	356
89	Sphere-cone	1200-0100	16	3.03E+06	5.99	62.5	4.708E-02	948.7	2.120E+05	3.056E-01	369
90	Sphere-cone	1200-0100	16	5.04E+06	6.02	63.2	7.843E-02	957.5	2.213E+05	3.987E-01	392
91	Sphere-cone	1200-0100	16	6.63E+06	6.04	62.6	1.023E-01	954.6	2.170E+05	4.552E-01	403
93	Sphere-cone	1200-0100	16	7.46E+06	6.04	62.5	1.154E-01	953.6	2.167E+05	4.806E-01	406
92	Sphere-cone	1200-0100	16	8.34E+06	6.03	58.6	1.249E-01	918.1	1.791E+05	4.818E-01	391
70	Sphere-cone	3700-0100	16	2.10E+06	5.96	61.9	3.253E-02	939.5	2.030E+05	2.507E-01	350
71	Sphere-cone	3700-0100	16	3.03E+06	5.99	62.5	4.708E-02	948.7	2.120E+05	3.056E-01	366
72	Sphere-cone	3700-0100	16	5.04E+06	6.02	63.2	7.843E-02	957.5	2.213E+05	3.987E-01	391
73	Sphere-cone	3700-0100	16	6.63E+06	6.04	62.6	1.023E-01	954.6	2.170E+05	4.552E-01	403
75	Sphere-cone	3700-0100	16	7.46E+06	6.04	62.5	1.154E-01	953.6	2.167E+05	4.806E-01	403
74	Sphere-cone	3700-0100	16	8.34E+06	6.03	58.6	1.249E-01	918.1	1.791E+05	4.818E-01	387

Table 4. Spherical-cap 1200-0025 transition locations.

Model	Run	Ray	s_0/R	Re_θ	Model	Run	Ray	s_0/R	Re_θ	Model	Run	Ray	s_0/R	Re_θ
1200-0025	28	0	0.788	108.9	1200-0025	27	220	0.441	73.1	1200-0025	30	270	0.331	71.0
1200-0025	28	10	0.984	133.1	1200-0025	27	230	0.446	76.2	1200-0025	30	280	0.337	74.2
1200-0025	28	20	0.962	130.0	1200-0025	27	240	0.373	65.2	1200-0025	30	290	0.287	63.9
1200-0025	28	30	1.009	134.3	1200-0025	27	250	0.366	66.2	1200-0025	30	300	0.294	67.7
1200-0025	28	40	1.004	132.7	1200-0025	27	260	0.429	79.7	1200-0025	30	310	0.266	60.2
1200-0025	28	50	0.987	129.9	1200-0025	27	270	0.404	77.6	1200-0025	30	320	0.218	50.0
1200-0025	28	60	0.812	109.3	1200-0025	27	280	0.390	76.7	1200-0025	30	330	0.195	43.9
1200-0025	28	70	0.901	117.8	1200-0025	27	290	0.339	68.8	1200-0025	30	340	0.217	49.6
1200-0025	28	80	0.920	117.1	1200-0025	27	300	0.351	72.8	1200-0025	30	350	0.244	56.2
1200-0025	28	90	0.735	95.2	1200-0025	27	310	0.320	66.0					
1200-0025	28	100	0.948	112.6	1200-0025	27	320	0.317	66.3					
1200-0025	28	270	1.089	126.6	1200-0025	27	330	0.282	59.6					
1200-0025	28	280	1.105	133.0	1200-0025	27	340	0.278	60.0					
1200-0025	28	290	0.951	122.4	1200-0025	27	350	0.257	54.9					
1200-0025	28	300	0.937	123.1	1200-0025	29	0	0.212	49.9					
1200-0025	28	310	1.049	136.3	1200-0025	29	10	0.243	56.8					
1200-0025	28	320	0.995	131.2	1200-0025	29	20	0.229	51.7					
1200-0025	28	330	0.980	130.8	1200-0025	29	30	0.199	44.4					
1200-0025	28	340	1.058	139.4	1200-0025	29	40	0.236	52.0					
1200-0025	28	350	0.984	132.4	1200-0025	29	50	0.247	53.7					
1200-0025	26	0	0.327	63.2	1200-0025	29	60	0.293	63.4					
1200-0025	26	10	0.250	49.0	1200-0025	29	70	0.265	56.8					
1200-0025	26	20	0.306	57.7	1200-0025	29	80	0.273	58.3					
1200-0025	26	30	0.265	50.1	1200-0025	29	90	0.278	58.6					
1200-0025	26	40	0.397	72.8	1200-0025	29	100	0.282	58.6					
1200-0025	26	50	0.355	65.3	1200-0025	29	110	0.283	56.9					
1200-0025	26	60	0.462	82.3	1200-0025	29	120	0.310	60.0					
1200-0025	26	70	0.435	77.9	1200-0025	29	130	0.404	73.4					
1200-0025	26	80	0.464	81.5	1200-0025	29	140	0.393	69.7					
1200-0025	26	90	0.481	82.7	1200-0025	29	150	0.334	59.2					
1200-0025	26	100	0.440	74.3	1200-0025	29	210	0.382	65.6					
1200-0025	26	110	0.495	80.4	1200-0025	29	220	0.446	77.6					
1200-0025	26	120	0.545	84.2	1200-0025	29	230	0.428	76.9					
1200-0025	26	130	0.529	79.0	1200-0025	29	240	0.385	72.6					
1200-0025	26	140	0.516	75.5	1200-0025	29	250	0.357	69.7					
1200-0025	26	150	0.457	65.3	1200-0025	29	260	0.393	79.4					
1200-0025	26	220	0.483	71.6	1200-0025	29	270	0.393	81.1					
1200-0025	26	230	0.529	79.1	1200-0025	29	280	0.373	78.7					
1200-0025	26	240	0.585	89.9	1200-0025	29	290	0.300	64.6					
1200-0025	26	250	0.583	93.8	1200-0025	29	300	0.329	71.7					
1200-0025	26	260	0.624	100.6	1200-0025	29	310	0.300	64.8					
1200-0025	26	270	0.549	92.0	1200-0025	29	320	0.250	54.4					
1200-0025	26	280	0.590	100.8	1200-0025	29	330	0.223	50.7					
1200-0025	26	290	0.502	88.2	1200-0025	29	340	0.249	55.8					
1200-0025	26	300	0.488	87.7	1200-0025	29	350	0.242	54.3					
1200-0025	26	310	0.383	70.6	1200-0025	30	0	0.220	51.3					
1200-0025	26	320	0.410	75.1	1200-0025	30	10	0.207	47.8					
1200-0025	26	330	0.373	70.3	1200-0025	30	20	0.194	45.7					
1200-0025	26	340	0.325	61.7	1200-0025	30	30	0.172	37.5					
1200-0025	26	350	0.292	54.9	1200-0025	30	40	0.193	42.9					
1200-0025	27	0	0.287	61.1	1200-0025	30	50	0.215	50.1					
1200-0025	27	10	0.266	56.7	1200-0025	30	60	0.236	54.2					
1200-0025	27	20	0.253	53.2	1200-0025	30	70	0.238	54.1					
1200-0025	27	30	0.235	48.2	1200-0025	30	80	0.227	50.1					
1200-0025	27	40	0.277	57.7	1200-0025	30	90	0.228	48.9					
1200-0025	27	50	0.282	59.8	1200-0025	30	100	0.222	46.5					
1200-0025	27	60	0.346	72.7	1200-0025	30	110	0.252	51.3					
1200-0025	27	70	0.328	67.8	1200-0025	30	120	0.286	57.1					
1200-0025	27	80	0.346	68.5	1200-0025	30	130	0.295	56.5					
1200-0025	27	90	0.388	74.6	1200-0025	30	140	0.377	69.5					
1200-0025	27	100	0.382	71.7	1200-0025	30	150	0.309	56.4					
1200-0025	27	110	0.378	69.9	1200-0025	30	210	0.342	62.1					
1200-0025	27	120	0.378	68.1	1200-0025	30	220	0.393	71.0					
1200-0025	27	130	0.466	80.1	1200-0025	30	230	0.370	69.5					
1200-0025	27	140	0.461	77.0	1200-0025	30	240	0.344	66.2					
1200-0025	27	150	0.372	61.9	1200-0025	30	250	0.331	67.3					
1200-0025	27	210	0.388	62.5	1200-0025	30	260	0.337	69.5					

Table 5. Spherical-cap 1200-0050 transition locations.

Model	Run	Ray	s_0/R	Re_θ	Model	Run	Ray	s_0/R	Re_θ	Model	Run	Ray	s_0/R	Re_θ
1200-0050	31	0	0.742	87.6	1200-0050	33	150	0.364	53.1	1200-0050	35	250	0.264	52.2
1200-0050	31	10	0.783	91.1	1200-0050	33	210	0.407	59.5	1200-0050	35	260	0.269	54.5
1200-0050	31	20	0.722	85.7	1200-0050	33	220	0.395	58.6	1200-0050	35	270	0.289	60.1
1200-0050	31	30	0.903	102.5	1200-0050	33	230	0.385	59.7	1200-0050	35	280	0.262	56.8
1200-0050	31	40	0.844	96.1	1200-0050	33	240	0.407	64.7	1200-0050	35	290	0.240	52.3
1200-0050	31	50	0.686	79.9	1200-0050	33	250	0.359	58.7	1200-0050	35	300	0.227	49.9
1200-0050	31	60	0.797	90.5	1200-0050	33	260	0.317	53.2	1200-0050	35	310	0.232	49.8
1200-0050	31	70	0.666	76.6	1200-0050	33	270	0.347	60.2	1200-0050	35	320	0.236	50.2
1200-0050	31	80	0.820	89.3	1200-0050	33	280	0.344	60.5	1200-0050	35	330	0.224	49.4
1200-0050	31	90	0.821	88.1	1200-0050	33	290	0.363	65.8	1200-0050	35	340	0.218	48.1
1200-0050	31	100	0.732	78.2	1200-0050	33	300	0.291	54.0	1200-0050	35	350	0.244	54.3
1200-0050	31	110	0.609	65.0	1200-0050	33	310	0.262	48.5	1200-0050	36	0	0.152	35.6
1200-0050	31	120	0.775	75.4	1200-0050	33	320	0.286	53.5	1200-0050	36	10	0.131	28.2
1200-0050	31	270	0.852	90.2	1200-0050	33	330	0.306	56.6	1200-0050	36	20	0.182	40.9
1200-0050	31	280	0.724	80.5	1200-0050	33	340	0.278	53.1	1200-0050	36	30	0.190	42.3
1200-0050	31	290	0.889	97.3	1200-0050	33	350	0.266	51.4	1200-0050	36	40	0.193	42.5
1200-0050	31	300	0.846	95.2	1200-0050	34	0	0.161	33.7	1200-0050	36	50	0.214	47.6
1200-0050	31	310	1.080	117.4	1200-0050	34	10	0.165	33.1	1200-0050	36	60	0.217	48.6
1200-0050	31	320	1.028	112.9	1200-0050	34	20	0.217	45.2	1200-0050	36	70	0.233	52.2
1200-0050	31	330	0.857	97.9	1200-0050	34	30	0.267	55.3	1200-0050	36	80	0.233	50.3
1200-0050	31	340	0.780	91.4	1200-0050	34	40	0.219	44.5	1200-0050	36	90	0.224	47.9
1200-0050	31	350	0.755	89.4	1200-0050	34	50	0.259	53.8	1200-0050	36	100	0.219	45.9
1200-0050	32	0	0.443	65.3	1200-0050	34	60	0.277	57.4	1200-0050	36	110	0.245	49.1
1200-0050	32	10	0.554	80.5	1200-0050	34	70	0.261	53.3	1200-0050	36	120	0.254	49.2
1200-0050	32	20	0.499	73.0	1200-0050	34	80	0.266	54.3	1200-0050	36	130	0.257	47.9
1200-0050	32	30	0.436	63.1	1200-0050	34	90	0.248	48.3	1200-0050	36	140	0.287	51.7
1200-0050	32	40	0.415	60.6	1200-0050	34	100	0.262	50.6	1200-0050	36	150	0.248	43.7
1200-0050	32	50	0.482	69.2	1200-0050	34	110	0.266	49.1	1200-0050	36	210	0.233	42.4
1200-0050	32	60	0.498	71.0	1200-0050	34	120	0.274	48.5	1200-0050	36	220	0.236	42.9
1200-0050	32	70	0.483	67.3	1200-0050	34	130	0.298	51.8	1200-0050	36	230	0.267	51.7
1200-0050	32	80	0.444	61.9	1200-0050	34	140	0.292	49.7	1200-0050	36	240	0.290	56.7
1200-0050	32	90	0.513	68.3	1200-0050	34	150	0.288	47.9	1200-0050	36	250	0.264	53.3
1200-0050	32	100	0.497	64.8	1200-0050	34	210	0.298	48.5	1200-0050	36	260	0.264	55.1
1200-0050	32	110	0.470	60.5	1200-0050	34	220	0.317	54.1	1200-0050	36	270	0.255	54.9
1200-0050	32	120	0.461	57.1	1200-0050	34	230	0.303	52.0	1200-0050	36	280	0.248	55.4
1200-0050	32	130	0.515	61.4	1200-0050	34	240	0.310	56.3	1200-0050	36	290	0.225	50.0
1200-0050	32	140	0.497	57.7	1200-0050	34	250	0.284	53.4	1200-0050	36	300	0.208	45.4
1200-0050	32	150	0.406	47.6	1200-0050	34	260	0.284	55.1	1200-0050	36	310	0.204	45.1
1200-0050	32	220	0.526	60.8	1200-0050	34	270	0.294	57.4	1200-0050	36	320	0.231	51.3
1200-0050	32	230	0.608	70.9	1200-0050	34	280	0.277	55.8	1200-0050	36	330	0.220	49.0
1200-0050	32	240	0.612	73.3	1200-0050	34	290	0.259	53.1	1200-0050	36	340	0.212	49.2
1200-0050	32	250	0.518	66.0	1200-0050	34	300	0.236	48.1	1200-0050	36	350	0.214	48.2
1200-0050	32	260	0.549	72.0	1200-0050	34	310	0.241	49.3					
1200-0050	32	270	0.572	75.6	1200-0050	34	320	0.258	52.9					
1200-0050	32	280	0.477	66.4	1200-0050	34	330	0.242	51.0					
1200-0050	32	290	0.373	53.9	1200-0050	34	340	0.244	51.7					
1200-0050	32	300	0.348	51.1	1200-0050	34	350	0.257	54.5					
1200-0050	32	310	0.323	47.8	1200-0050	35	0	0.152	35.0					
1200-0050	32	320	0.360	52.8	1200-0050	35	10	0.157	35.0					
1200-0050	32	330	0.405	59.5	1200-0050	35	20	0.213	48.1					
1200-0050	32	340	0.441	65.6	1200-0050	35	30	0.211	46.1					
1200-0050	32	350	0.456	67.5	1200-0050	35	40	0.197	41.8					
1200-0050	33	0	0.326	62.2	1200-0050	35	50	0.237	51.3					
1200-0050	33	10	0.245	46.2	1200-0050	35	60	0.240	52.3					
1200-0050	33	20	0.324	62.3	1200-0050	35	70	0.233	51.0					
1200-0050	33	30	0.347	64.2	1200-0050	35	80	0.252	54.3					
1200-0050	33	40	0.283	53.0	1200-0050	35	90	0.234	49.7					
1200-0050	33	50	0.354	65.9	1200-0050	35	100	0.233	48.8					
1200-0050	33	60	0.329	60.2	1200-0050	35	110	0.266	52.3					
1200-0050	33	70	0.358	63.9	1200-0050	35	120	0.249	47.1					
1200-0050	33	80	0.353	61.5	1200-0050	35	130	0.267	50.6					
1200-0050	33	90	0.392	66.7	1200-0050	35	140	0.297	54.4					
1200-0050	33	100	0.317	53.0	1200-0050	35	150	0.278	48.7					
1200-0050	33	110	0.333	55.2	1200-0050	35	210	0.263	46.0					
1200-0050	33	120	0.347	54.2	1200-0050	35	220	0.302	54.6					
1200-0050	33	130	0.372	56.9	1200-0050	35	230	0.293	55.0					
1200-0050	33	140	0.369	54.3	1200-0050	35	240	0.295	55.7					

Table 6. Spherical-cap 1200-0100 transition locations.

Model	Run	Ray	s_0/R	Re_θ	Model	Run	Ray	s_0/R	Re_θ
1200-0100	37	0	0.323	40.3	1200-0100	39	50	0.228	41.1
1200-0100	37	10	0.399	49.2	1200-0100	39	60	0.199	36.6
1200-0100	37	20	0.372	46.6	1200-0100	39	70	0.210	38.3
1200-0100	37	30	0.353	43.3	1200-0100	39	80	0.184	32.4
1200-0100	37	40	0.402	48.9	1200-0100	39	90	0.193	34.2
1200-0100	37	50	0.397	48.7	1200-0100	39	100	0.190	32.9
1200-0100	37	60	0.395	47.8	1200-0100	39	110	0.189	31.8
1200-0100	37	70	0.396	47.2	1200-0100	39	120	0.182	28.0
1200-0100	37	80	0.292	34.9	1200-0100	39	130	0.209	31.2
1200-0100	37	90	0.265	31.1	1200-0100	39	140	0.213	30.9
1200-0100	37	100	0.267	30.2	1200-0100	39	150	0.203	30.0
1200-0100	37	110	0.255	28.0	1200-0100	39	210	0.277	39.9
1200-0100	37	120	0.415	42.8	1200-0100	39	220	0.266	39.2
1200-0100	37	130	0.365	37.7	1200-0100	39	230	0.252	38.4
1200-0100	37	140	0.411	40.5	1200-0100	39	240	0.289	46.1
1200-0100	37	150	0.353	34.0	1200-0100	39	250	0.254	41.6
1200-0100	37	210	0.405	39.6	1200-0100	39	260	0.261	44.4
1200-0100	37	220	0.452	44.3	1200-0100	39	270	0.247	42.3
1200-0100	37	230	0.392	40.2	1200-0100	39	280	0.250	45.0
1200-0100	37	240	0.448	47.0	1200-0100	39	290	0.264	47.1
1200-0100	37	250	0.520	55.0	1200-0100	39	300	0.232	41.5
1200-0100	37	260	0.372	42.0	1200-0100	39	310	0.246	44.3
1200-0100	37	270	0.450	50.4	1200-0100	39	320	0.231	41.4
1200-0100	37	280	0.419	49.2	1200-0100	39	330	0.281	52.1
1200-0100	37	290	0.314	37.3	1200-0100	39	340	0.273	50.6
1200-0100	37	300	0.333	40.7	1200-0100	39	350	0.212	38.3
1200-0100	37	310	0.352	43.4					
1200-0100	37	320	0.407	49.1					
1200-0100	37	330	0.397	48.0					
1200-0100	37	340	0.432	52.7					
1200-0100	37	350	0.337	41.5					
1200-0100	38	0	0.293	44.4					
1200-0100	38	10	0.284	41.7					
1200-0100	38	20	0.279	41.3					
1200-0100	38	30	0.324	47.3					
1200-0100	38	40	0.322	46.6					
1200-0100	38	50	0.333	48.2					
1200-0100	38	60	0.310	44.3					
1200-0100	38	70	0.295	41.9					
1200-0100	38	80	0.278	38.9					
1200-0100	38	90	0.241	33.4					
1200-0100	38	100	0.267	35.7					
1200-0100	38	110	0.235	31.2					
1200-0100	38	120	0.239	30.8					
1200-0100	38	130	0.244	30.4					
1200-0100	38	140	0.272	32.6					
1200-0100	38	150	0.242	27.5					
1200-0100	38	210	0.384	43.6					
1200-0100	38	220	0.407	47.9					
1200-0100	38	230	0.378	44.9					
1200-0100	38	240	0.405	50.6					
1200-0100	38	250	0.404	51.4					
1200-0100	38	260	0.337	44.6					
1200-0100	38	270	0.373	50.9					
1200-0100	38	280	0.394	53.9					
1200-0100	38	290	0.307	44.2					
1200-0100	38	300	0.307	43.7					
1200-0100	38	310	0.334	48.2					
1200-0100	38	320	0.344	49.5					
1200-0100	38	330	0.379	55.7					
1200-0100	38	340	0.366	53.6					
1200-0100	38	350	0.288	42.5					
1200-0100	39	0	0.240	46.3					
1200-0100	39	10	0.229	41.7					
1200-0100	39	20	0.204	37.0					
1200-0100	39	30	0.220	40.5					
1200-0100	39	40	0.197	34.4					

Table 7. Spherical-cap 3700-0015 transition locations.

Model	Run	Ray	s_0/R	Re_θ	Model	Run	Ray	s_0/R	Re_θ
3700-0015	102	0	0.827	143.8	3700-0015	105	100	0.473	93.4
3700-0015	102	10	1.155	189.9	3700-0015	105	110	0.487	94.8
3700-0015	102	20	1.178	197.9	3700-0015	105	120	0.486	89.9
3700-0015	102	30	1.217	195.3	3700-0015	105	130	0.456	81.7
3700-0015	102	40	1.099	180.5	3700-0015	105	140	0.418	73.2
3700-0015	102	50	1.041	172.8	3700-0015	105	150	0.381	66.0
3700-0015	102	60	0.948	157.7	3700-0015	105	210	0.419	71.2
3700-0015	102	70	0.860	145.2	3700-0015	105	220	0.490	86.4
3700-0015	102	80	0.861	141.2	3700-0015	105	230	0.522	93.9
3700-0015	102	90	0.858	136.9	3700-0015	105	240	0.501	93.8
3700-0015	102	100	0.892	136.4	3700-0015	105	250	0.436	83.3
3700-0015	102	110	0.695	108.5	3700-0015	105	260	0.488	97.2
3700-0015	102	120	0.663	101.5	3700-0015	105	270	0.499	101.7
3700-0015	102	130	0.569	86.2	3700-0015	105	280	0.438	90.7
3700-0015	102	240	0.762	111.7	3700-0015	105	290	0.466	98.2
3700-0015	102	250	0.828	124.6	3700-0015	105	300	0.432	94.2
3700-0015	102	260	0.779	123.5	3700-0015	105	310	0.373	84.0
3700-0015	102	270	0.862	136.9	3700-0015	105	320	0.349	78.6
3700-0015	102	280	0.833	137.6	3700-0015	105	330	0.296	66.9
3700-0015	102	290	0.953	156.0	3700-0015	105	340	0.572	124.4
3700-0015	102	300	1.000	164.7	3700-0015	105	350	0.509	112.5
3700-0015	102	310	1.006	168.0	3700-0015	106	0	0.660	146.2
3700-0015	102	320	1.181	190.9	3700-0015	106	10	0.431	101.6
3700-0015	102	330	1.240	198.4	3700-0015	106	20	0.402	92.6
3700-0015	102	340	1.141	192.3	3700-0015	106	30	0.517	118.0
3700-0015	102	350	1.161	191.1	3700-0015	106	40	0.327	75.9
3700-0015	101	0	0.716	143.9	3700-0015	106	50	0.298	71.1
3700-0015	101	10	0.686	139.9	3700-0015	106	60	0.294	68.3
3700-0015	101	20	0.757	153.9	3700-0015	106	70	0.400	88.2
3700-0015	101	30	0.669	135.0	3700-0015	106	80	0.396	85.2
3700-0015	101	40	0.748	147.9	3700-0015	106	90	0.413	86.8
3700-0015	101	50	0.495	102.0	3700-0015	106	100	0.443	91.1
3700-0015	101	60	0.657	130.3	3700-0015	106	110	0.471	93.5
3700-0015	101	70	0.688	133.3	3700-0015	106	120	0.401	78.3
3700-0015	101	80	0.615	119.4	3700-0015	106	130	0.388	74.0
3700-0015	101	90	0.560	107.5	3700-0015	106	140	0.381	70.2
3700-0015	101	100	0.532	99.9	3700-0015	106	150	0.300	53.3
3700-0015	101	110	0.560	102.5	3700-0015	106	210	0.413	73.4
3700-0015	101	120	0.548	97.2	3700-0015	106	220	0.456	83.6
3700-0015	101	130	0.492	85.3	3700-0015	106	230	0.515	95.4
3700-0015	101	140	0.464	78.1	3700-0015	106	240	0.487	92.3
3700-0015	101	150	0.425	69.7	3700-0015	106	250	0.441	88.4
3700-0015	101	210	0.454	73.8	3700-0015	106	260	0.464	95.3
3700-0015	101	220	0.594	94.9	3700-0015	106	270	0.469	97.6
3700-0015	101	230	0.583	97.5	3700-0015	106	280	0.408	88.1
3700-0015	101	240	0.639	109.4	3700-0015	106	290	0.397	87.3
3700-0015	101	250	0.543	98.9	3700-0015	106	300	0.417	92.8
3700-0015	101	260	0.582	107.5	3700-0015	106	310	0.368	81.8
3700-0015	101	270	0.561	107.6	3700-0015	106	320	0.298	68.2
3700-0015	101	280	0.551	106.6	3700-0015	106	330	0.230	53.1
3700-0015	101	290	0.566	112.0	3700-0015	106	340	0.446	102.6
3700-0015	101	300	0.491	99.9	3700-0015	106	350	0.431	99.0
3700-0015	101	310	0.545	111.6					
3700-0015	101	320	0.726	144.8					
3700-0015	101	330	0.837	162.6					
3700-0015	101	340	0.847	167.9					
3700-0015	101	350	0.818	161.1					
3700-0015	105	0	0.683	147.0					
3700-0015	105	10	0.547	122.3					
3700-0015	105	20	0.563	124.2					
3700-0015	105	30	0.609	132.9					
3700-0015	105	40	0.526	115.3					
3700-0015	105	50	0.376	84.5					
3700-0015	105	60	0.411	90.4					
3700-0015	105	70	0.501	105.9					
3700-0015	105	80	0.510	105.3					
3700-0015	105	90	0.483	98.9					

Table 8. Spherical-cap 3700-0025 transition locations.

Model	Run	Ray	s_0/R	Re_θ	Model	Run	Ray	s_0/R	Re_θ	Model	Run	Ray	s_0/R	Re_θ
3700-0025	6	0	1.089	144.1	3700-0025	9	130	0.336	57.4	3700-0025	11	230	0.290	55.4
3700-0025	6	10	1.069	142.2	3700-0025	9	140	0.375	61.8	3700-0025	11	240	0.309	60.5
3700-0025	6	20	1.099	144.3	3700-0025	9	150	0.327	54.3	3700-0025	11	250	0.313	61.9
3700-0025	6	30	1.036	136.9	3700-0025	9	210	0.335	54.7	3700-0025	11	260	0.265	54.5
3700-0025	6	40	1.053	136.6	3700-0025	9	220	0.348	57.3	3700-0025	11	270	0.252	53.3
3700-0025	6	50	0.948	125.0	3700-0025	9	230	0.341	59.0	3700-0025	11	280	0.223	48.3
3700-0025	6	60	1.006	129.3	3700-0025	9	240	0.330	57.5	3700-0025	11	290	0.226	51.4
3700-0025	6	70	0.944	121.9	3700-0025	9	250	0.339	60.9	3700-0025	11	300	0.185	42.8
3700-0025	6	80	0.967	121.4	3700-0025	9	260	0.307	58.1	3700-0025	11	310	0.169	38.0
3700-0025	6	90	0.920	114.2	3700-0025	9	270	0.287	56.1	3700-0025	11	320	0.182	41.9
3700-0025	6	100	0.939	111.2	3700-0025	9	280	0.275	54.5	3700-0025	11	330	0.193	43.6
3700-0025	6	110	0.874	101.5	3700-0025	9	290	0.281	56.9	3700-0025	11	340	0.164	34.3
3700-0025	6	120	0.789	89.8	3700-0025	9	300	0.235	48.1	3700-0025	11	350	0.184	42.4
3700-0025	6	260	0.829	102.7	3700-0025	9	310	0.215	45.1					
3700-0025	6	270	0.893	111.6	3700-0025	9	320	0.241	50.7					
3700-0025	6	280	0.935	117.9	3700-0025	9	330	0.245	51.2					
3700-0025	6	290	0.918	118.3	3700-0025	9	340	0.205	42.2					
3700-0025	6	300	0.804	107.8	3700-0025	9	350	0.197	41.4					
3700-0025	6	310	0.876	117.2	3700-0025	10	0	0.190	42.4					
3700-0025	6	320	0.916	122.5	3700-0025	10	10	0.160	35.2					
3700-0025	6	330	1.053	139.1	3700-0025	10	20	0.205	44.5					
3700-0025	6	340	1.162	150.9	3700-0025	10	30	0.212	46.2					
3700-0025	6	350	1.157	150.3	3700-0025	10	40	0.214	47.3					
3700-0025	7	0	0.347	65.7	3700-0025	10	50	0.196	43.8					
3700-0025	7	10	0.320	60.5	3700-0025	10	60	0.249	55.1					
3700-0025	7	20	0.295	55.7	3700-0025	10	70	0.270	56.7					
3700-0025	7	30	0.279	52.6	3700-0025	10	80	0.267	56.1					
3700-0025	7	40	0.371	67.9	3700-0025	10	90	0.319	63.8					
3700-0025	7	50	0.412	74.2	3700-0025	10	100	0.291	57.3					
3700-0025	7	60	0.396	71.3	3700-0025	10	110	0.285	55.9					
3700-0025	7	70	0.417	74.6	3700-0025	10	120	0.294	55.0					
3700-0025	7	80	0.429	75.0	3700-0025	10	130	0.305	54.7					
3700-0025	7	90	0.486	82.1	3700-0025	10	140	0.338	59.3					
3700-0025	7	100	0.473	77.8	3700-0025	10	150	0.307	52.0					
3700-0025	7	110	0.481	77.0	3700-0025	10	210	0.310	53.1					
3700-0025	7	120	0.433	68.4	3700-0025	10	220	0.321	57.0					
3700-0025	7	130	0.458	69.1	3700-0025	10	230	0.322	59.0					
3700-0025	7	140	0.446	65.0	3700-0025	10	240	0.330	63.0					
3700-0025	7	150	0.401	59.2	3700-0025	10	250	0.318	60.8					
3700-0025	7	210	0.439	63.7	3700-0025	10	260	0.292	57.6					
3700-0025	7	220	0.462	68.3	3700-0025	10	270	0.267	54.6					
3700-0025	7	230	0.480	71.5	3700-0025	10	280	0.247	52.3					
3700-0025	7	240	0.390	61.2	3700-0025	10	290	0.230	50.8					
3700-0025	7	250	0.357	58.8	3700-0025	10	300	0.218	49.3					
3700-0025	7	260	0.377	63.8	3700-0025	10	310	0.179	40.7					
3700-0025	7	270	0.423	72.7	3700-0025	10	320	0.205	45.3					
3700-0025	7	280	0.391	68.2	3700-0025	10	330	0.215	46.8					
3700-0025	7	290	0.390	69.1	3700-0025	10	340	0.186	40.1					
3700-0025	7	300	0.342	61.8	3700-0025	10	350	0.172	38.8					
3700-0025	7	310	0.345	62.0	3700-0025	11	0	0.182	41.0					
3700-0025	7	320	0.320	59.1	3700-0025	11	10	0.184	42.3					
3700-0025	7	330	0.303	56.9	3700-0025	11	20	0.204	45.7					
3700-0025	7	340	0.272	50.6	3700-0025	11	30	0.199	43.8					
3700-0025	7	350	0.298	55.3	3700-0025	11	40	0.183	42.3					
3700-0025	9	0	0.194	40.0	3700-0025	11	50	0.170	38.4					
3700-0025	9	10	0.189	39.6	3700-0025	11	60	0.231	51.2					
3700-0025	9	20	0.227	45.5	3700-0025	11	70	0.237	52.1					
3700-0025	9	30	0.246	51.3	3700-0025	11	80	0.229	48.5					
3700-0025	9	40	0.228	47.2	3700-0025	11	90	0.259	54.8					
3700-0025	9	50	0.260	55.0	3700-0025	11	100	0.286	58.7					
3700-0025	9	60	0.288	60.0	3700-0025	11	110	0.275	53.5					
3700-0025	9	70	0.295	60.3	3700-0025	11	120	0.269	51.8					
3700-0025	9	80	0.298	58.4	3700-0025	11	130	0.270	51.1					
3700-0025	9	90	0.343	65.4	3700-0025	11	140	0.300	54.3					
3700-0025	9	100	0.336	62.7	3700-0025	11	150	0.261	46.8					
3700-0025	9	110	0.320	57.4	3700-0025	11	210	0.258	47.2					
3700-0025	9	120	0.324	56.1	3700-0025	11	220	0.305	56.0					

Table 9. Spherical-cap 3700-0050 transition locations.

Model	Run	Ray	s_0/R	Re_θ	Model	Run	Ray	s_0/R	Re_θ	Model	Run	Ray	s_0/R	Re_θ
3700-0050	19	0	0.866	100.4	3700-0050	20	250	0.229	37.0	3700-0050	22	300	0.169	38.3
3700-0050	19	10	0.878	101.3	3700-0050	20	260	0.233	40.0	3700-0050	22	310	0.160	35.4
3700-0050	19	20	0.891	102.4	3700-0050	20	270	0.268	46.9	3700-0050	22	320	0.111	23.9
3700-0050	19	30	0.899	102.1	3700-0050	20	280	0.381	67.2	3700-0050	22	330	0.152	31.2
3700-0050	19	40	0.938	104.6	3700-0050	20	290	0.241	43.3	3700-0050	22	340	0.141	29.5
3700-0050	19	50	0.852	95.4	3700-0050	20	300	0.269	48.2	3700-0050	22	350	0.135	28.3
3700-0050	19	60	0.878	96.7	3700-0050	20	310	0.273	48.6	3700-0050	23	0	0.156	35.2
3700-0050	19	70	0.984	104.9	3700-0050	20	320	0.225	40.5	3700-0050	23	10	0.135	28.5
3700-0050	19	80	0.963	100.9	3700-0050	20	330	0.245	45.4	3700-0050	23	20	0.183	40.6
3700-0050	19	260	0.868	88.7	3700-0050	20	340	0.176	31.6	3700-0050	23	30	0.184	40.1
3700-0050	19	270	0.977	100.1	3700-0050	20	350	0.196	35.4	3700-0050	23	40	0.165	36.5
3700-0050	19	280	0.669	75.5	3700-0050	21	0	0.168	36.2	3700-0050	23	50	0.182	41.5
3700-0050	19	290	0.929	100.6	3700-0050	21	10	0.151	31.6	3700-0050	23	60	0.195	44.9
3700-0050	19	300	0.798	88.9	3700-0050	21	20	0.200	41.6	3700-0050	23	70	0.175	39.1
3700-0050	19	310	0.916	101.4	3700-0050	21	30	0.200	40.1	3700-0050	23	80	0.181	38.8
3700-0050	19	320	0.984	108.5	3700-0050	21	40	0.188	38.2	3700-0050	23	90	0.195	41.9
3700-0050	19	330	0.973	109.3	3700-0050	21	50	0.225	46.4	3700-0050	23	100	0.201	40.5
3700-0050	19	340	0.926	105.1	3700-0050	21	60	0.214	43.4	3700-0050	23	110	0.204	40.1
3700-0050	19	350	0.860	100.4	3700-0050	21	70	0.217	44.4	3700-0050	23	120	0.188	37.6
3700-0050	18	0	0.324	48.3	3700-0050	21	80	0.225	45.7	3700-0050	23	130	0.196	37.7
3700-0050	18	10	0.349	52.4	3700-0050	21	90	0.246	47.6	3700-0050	23	140	0.243	43.9
3700-0050	18	20	0.380	56.3	3700-0050	21	100	0.239	46.1	3700-0050	23	150	0.243	42.2
3700-0050	18	30	0.380	55.3	3700-0050	21	110	0.228	41.8	3700-0050	23	210	0.193	33.5
3700-0050	18	40	0.339	50.1	3700-0050	21	120	0.227	40.1	3700-0050	23	220	0.243	44.5
3700-0050	18	50	0.361	52.3	3700-0050	21	130	0.244	43.3	3700-0050	23	230	0.199	38.0
3700-0050	18	60	0.385	56.3	3700-0050	21	140	0.288	47.6	3700-0050	23	240	0.179	34.1
3700-0050	18	70	0.332	48.2	3700-0050	21	150	0.274	44.3	3700-0050	23	250	0.161	33.7
3700-0050	18	80	0.417	58.4	3700-0050	21	210	0.244	39.0	3700-0050	23	260	0.151	30.9
3700-0050	18	90	0.560	74.8	3700-0050	21	220	0.263	43.2	3700-0050	23	270	0.165	36.2
3700-0050	18	100	0.470	61.7	3700-0050	21	230	0.228	39.3	3700-0050	23	280	0.149	32.8
3700-0050	18	110	0.477	60.4	3700-0050	21	240	0.219	39.8	3700-0050	23	290	0.170	37.8
3700-0050	18	120	0.446	55.2	3700-0050	21	250	0.200	36.3	3700-0050	23	300	0.167	39.0
3700-0050	18	130	0.496	59.5	3700-0050	21	260	0.198	37.3	3700-0050	23	310	0.147	32.5
3700-0050	18	220	0.438	51.5	3700-0050	21	270	0.205	39.1	3700-0050	23	320	0.125	26.5
3700-0050	18	230	0.514	61.0	3700-0050	21	280	0.184	36.6	3700-0050	23	330	0.130	26.6
3700-0050	18	240	0.454	56.8	3700-0050	21	290	0.193	39.1	3700-0050	23	340	0.148	32.9
3700-0050	18	250	0.389	49.5	3700-0050	21	300	0.198	41.0	3700-0050	23	350	0.134	28.3
3700-0050	18	260	0.480	63.2	3700-0050	21	310	0.185	36.9					
3700-0050	18	270	0.509	67.7	3700-0050	21	320	0.162	30.8					
3700-0050	18	280	0.396	54.8	3700-0050	21	330	0.162	31.9					
3700-0050	18	290	0.385	54.3	3700-0050	21	340	0.163	33.5					
3700-0050	18	300	0.378	54.4	3700-0050	21	350	0.170	33.3					
3700-0050	18	310	0.332	48.8	3700-0050	22	0	0.151	31.9					
3700-0050	18	320	0.388	56.3	3700-0050	22	10	0.140	31.1					
3700-0050	18	330	0.495	71.1	3700-0050	22	20	0.203	44.5					
3700-0050	18	340	0.468	68.0	3700-0050	22	30	0.189	40.9					
3700-0050	18	350	0.366	54.5	3700-0050	22	40	0.182	40.6					
3700-0050	20	0	0.195	37.7	3700-0050	22	50	0.182	40.7					
3700-0050	20	10	0.222	41.8	3700-0050	22	60	0.202	44.4					
3700-0050	20	20	0.233	42.9	3700-0050	22	70	0.204	45.1					
3700-0050	20	30	0.252	45.5	3700-0050	22	80	0.211	44.8					
3700-0050	20	40	0.250	44.6	3700-0050	22	90	0.222	46.6					
3700-0050	20	50	0.262	47.7	3700-0050	22	100	0.225	45.2					
3700-0050	20	60	0.280	50.7	3700-0050	22	110	0.228	44.6					
3700-0050	20	70	0.250	44.8	3700-0050	22	120	0.203	38.2					
3700-0050	20	80	0.278	49.4	3700-0050	22	130	0.210	38.3					
3700-0050	20	90	0.294	50.8	3700-0050	22	140	0.263	46.3					
3700-0050	20	100	0.293	49.0	3700-0050	22	150	0.248	42.7					
3700-0050	20	110	0.297	48.2	3700-0050	22	210	0.224	37.9					
3700-0050	20	120	0.317	50.0	3700-0050	22	220	0.222	40.3					
3700-0050	20	130	0.325	49.5	3700-0050	22	230	0.218	41.3					
3700-0050	20	140	0.344	51.4	3700-0050	22	240	0.194	37.6					
3700-0050	20	150	0.345	50.7	3700-0050	22	250	0.175	34.3					
3700-0050	20	210	0.274	39.0	3700-0050	22	260	0.165	34.4					
3700-0050	20	220	0.324	48.8	3700-0050	22	270	0.195	41.2					
3700-0050	20	230	0.268	42.1	3700-0050	22	280	0.165	35.4					
3700-0050	20	240	0.244	39.2	3700-0050	22	290	0.177	39.0					

Table 10. Spherical-cap 3700-0100 transition locations.

Model	Run	Ray	s_0/R	Re_θ
3700-0100	13	0	0.328	40.9
3700-0100	13	10	0.323	39.8
3700-0100	13	20	0.269	32.9
3700-0100	13	30	0.249	29.9
3700-0100	13	40	0.219	26.4
3700-0100	13	50	0.317	37.9
3700-0100	13	60	0.284	34.7
3700-0100	13	70	0.338	40.1
3700-0100	13	80	0.293	35.0
3700-0100	13	90	0.444	50.2
3700-0100	13	100	0.437	48.6
3700-0100	13	110	0.362	38.8
3700-0100	13	120	0.461	47.5
3700-0100	13	130	0.346	35.4
3700-0100	13	140	0.387	37.9
3700-0100	13	150	0.392	37.4
3700-0100	13	210	0.319	31.2
3700-0100	13	220	0.353	35.4
3700-0100	13	230	0.464	47.1
3700-0100	13	240	0.455	47.5
3700-0100	13	250	0.549	57.6
3700-0100	13	260	0.413	45.8
3700-0100	13	270	0.413	47.1
3700-0100	13	280	0.465	53.8
3700-0100	13	290	0.388	46.3
3700-0100	13	300	0.290	35.0
3700-0100	13	310	0.327	40.1
3700-0100	13	320	0.244	29.3
3700-0100	13	330	0.309	37.2
3700-0100	13	340	0.231	28.3
3700-0100	13	350	0.266	33.3
3700-0100	12	0	0.251	37.4
3700-0100	12	10	0.230	33.7
3700-0100	12	20	0.209	29.6
3700-0100	12	30	0.189	27.7
3700-0100	12	40	0.157	23.2
3700-0100	12	50	0.181	26.6
3700-0100	12	60	0.189	27.1
3700-0100	12	70	0.208	29.7
3700-0100	12	80	0.226	32.1
3700-0100	12	90	0.191	27.1
3700-0100	12	100	0.282	38.4
3700-0100	12	110	0.276	35.7
3700-0100	12	120	0.261	33.7
3700-0100	12	130	0.239	30.1
3700-0100	12	140	0.272	33.0
3700-0100	12	150	0.279	32.5
3700-0100	12	210	0.279	32.2
3700-0100	12	220	0.283	33.2
3700-0100	12	230	0.378	44.9
3700-0100	12	240	0.294	36.7
3700-0100	12	250	0.304	39.6
3700-0100	12	260	0.282	38.3
3700-0100	12	270	0.295	40.2
3700-0100	12	280	0.287	40.2
3700-0100	12	290	0.298	42.5
3700-0100	12	300	0.241	35.3
3700-0100	12	310	0.293	43.5
3700-0100	12	320	0.214	31.7
3700-0100	12	330	0.227	33.3
3700-0100	12	340	0.198	28.7
3700-0100	12	350	0.191	27.0

Table 11. Sphere-cone 1200-0025 transition locations.

Model	Run	Ray	s_0/R	Re_θ	Model	Run	Ray	s_0/R	Re_θ	Model	Run	Ray	s_0/R	Re_θ
1200-0025	76	0	0.687	113.5	1200-0025	79	90	0.311	69.0	1200-0025	80	140	0.260	51.1
1200-0025	76	10	0.558	77.4	1200-0025	79	100	0.302	66.2	1200-0025	80	150	0.249	46.8
1200-0025	76	20	0.592	87.5	1200-0025	79	110	0.298	62.0	1200-0025	80	210	0.272	52.7
1200-0025	76	340	0.960	132.2	1200-0025	79	120	0.297	59.6	1200-0025	80	220	0.291	58.0
1200-0025	76	350	0.566	77.5	1200-0025	79	130	0.286	55.1	1200-0025	80	230	0.267	56.1
1200-0025	77	0	0.557	88.3	1200-0025	79	140	0.290	52.2	1200-0025	80	240	0.281	61.3
1200-0025	77	10	0.518	78.8	1200-0025	79	150	0.312	51.3	1200-0025	80	250	0.291	66.7
1200-0025	77	20	0.563	97.4	1200-0025	79	210	0.278	46.9	1200-0025	80	260	0.304	72.7
1200-0025	77	30	0.515	84.8	1200-0025	79	220	0.322	57.4	1200-0025	80	270	0.303	75.4
1200-0025	77	40	0.437	71.6	1200-0025	79	230	0.338	62.7	1200-0025	80	280	0.262	68.4
1200-0025	77	50	0.693	109.5	1200-0025	79	240	0.292	57.5	1200-0025	80	290	0.256	65.9
1200-0025	77	60	0.695	108.0	1200-0025	79	250	0.308	63.6	1200-0025	80	300	0.280	70.3
1200-0025	77	70	0.805	115.4	1200-0025	79	260	0.346	74.6	1200-0025	80	310	0.267	63.9
1200-0025	77	80	0.842	112.7	1200-0025	79	270	0.376	83.1	1200-0025	80	320	0.280	64.0
1200-0025	77	90	0.920	111.7	1200-0025	79	280	0.371	83.8	1200-0025	80	330	0.327	71.0
1200-0025	77	240	0.696	83.8	1200-0025	79	290	0.313	73.5	1200-0025	80	340	0.331	64.7
1200-0025	77	250	0.647	83.1	1200-0025	79	300	0.298	70.3	1200-0025	80	350	0.362	70.2
1200-0025	77	260	0.791	99.6	1200-0025	79	310	0.288	63.5					
1200-0025	77	270	0.794	104.6	1200-0025	79	320	0.299	63.9					
1200-0025	77	280	0.792	108.9	1200-0025	79	330	0.333	66.4					
1200-0025	77	290	0.754	109.8	1200-0025	79	340	0.342	61.5					
1200-0025	77	300	0.716	109.1	1200-0025	79	350	0.389	71.3					
1200-0025	77	310	0.678	108.2	1200-0025	81	0	0.374	69.8					
1200-0025	77	320	0.624	102.9	1200-0025	81	10	0.420	86.1					
1200-0025	77	330	0.616	102.1	1200-0025	81	20	0.381	78.3					
1200-0025	77	340	0.608	106.8	1200-0025	81	30	0.373	83.2					
1200-0025	77	350	0.521	79.2	1200-0025	81	40	0.346	79.1					
1200-0025	78	0	0.495	88.8	1200-0025	81	50	0.325	78.6					
1200-0025	78	10	0.474	85.9	1200-0025	81	60	0.260	65.3					
1200-0025	78	20	0.440	81.0	1200-0025	81	70	0.236	59.7					
1200-0025	78	30	0.451	89.1	1200-0025	81	80	0.245	61.4					
1200-0025	78	40	0.384	74.8	1200-0025	81	90	0.284	68.2					
1200-0025	78	50	0.390	79.8	1200-0025	81	100	0.239	56.3					
1200-0025	78	60	0.338	70.9	1200-0025	81	110	0.283	62.2					
1200-0025	78	70	0.298	62.8	1200-0025	81	120	0.272	57.7					
1200-0025	78	80	0.305	62.5	1200-0025	81	130	0.261	52.7					
1200-0025	78	90	0.384	75.4	1200-0025	81	140	0.274	51.2					
1200-0025	78	100	0.402	74.4	1200-0025	81	150	0.278	50.8					
1200-0025	78	110	0.375	66.4	1200-0025	81	210	0.264	46.9					
1200-0025	78	120	0.392	67.1	1200-0025	81	220	0.295	56.3					
1200-0025	78	130	0.332	55.4	1200-0025	81	230	0.320	64.7					
1200-0025	78	140	0.384	61.1	1200-0025	81	240	0.301	64.0					
1200-0025	78	150	0.390	58.5	1200-0025	81	250	0.280	61.1					
1200-0025	78	210	0.377	57.0	1200-0025	81	260	0.342	77.2					
1200-0025	78	220	0.369	58.4	1200-0025	81	270	0.360	84.6					
1200-0025	78	230	0.486	77.1	1200-0025	81	280	0.325	78.4					
1200-0025	78	240	0.470	77.6	1200-0025	81	290	0.291	71.6					
1200-0025	78	250	0.435	75.3	1200-0025	81	300	0.273	68.4					
1200-0025	78	260	0.463	83.2	1200-0025	81	310	0.264	63.3					
1200-0025	78	270	0.440	83.9	1200-0025	81	320	0.266	57.3					
1200-0025	78	280	0.411	82.6	1200-0025	81	330	0.334	69.0					
1200-0025	78	290	0.447	90.9	1200-0025	81	340	0.311	55.5					
1200-0025	78	300	0.386	81.0	1200-0025	81	350	0.365	66.0					
1200-0025	78	310	0.386	79.6	1200-0025	80	0	0.395	77.9					
1200-0025	78	320	0.388	76.5	1200-0025	80	10	0.389	77.9					
1200-0025	78	330	0.386	71.8	1200-0025	80	20	0.382	78.7					
1200-0025	78	340	0.385	66.1	1200-0025	80	30	0.360	80.7					
1200-0025	78	350	0.409	69.5	1200-0025	80	40	0.333	80.1					
1200-0025	79	0	0.426	79.6	1200-0025	80	50	0.284	71.6					
1200-0025	79	10	0.382	69.1	1200-0025	80	60	0.249	62.1					
1200-0025	79	20	0.413	82.0	1200-0025	80	70	0.222	58.3					
1200-0025	79	30	0.389	82.6	1200-0025	80	80	0.236	60.4					
1200-0025	79	40	0.327	71.5	1200-0025	80	90	0.243	62.1					
1200-0025	79	50	0.319	71.3	1200-0025	80	100	0.232	55.5					
1200-0025	79	60	0.257	58.9	1200-0025	80	110	0.239	54.7					
1200-0025	79	70	0.239	56.3	1200-0025	80	120	0.248	55.6					
1200-0025	79	80	0.248	58.0	1200-0025	80	130	0.264	55.9					

Table 12. Sphere-cone 1200-0050 transition locations.

Model	Run	Ray	s_0/R	Re_θ	Model	Run	Ray	s_0/R	Re_θ	Model	Run	Ray	s_0/R	Re_θ
1200-0050	82	0	0.553	70.0	1200-0050	84	140	0.249	40.8	1200-0050	87	240	0.259	54.8
1200-0050	82	10	0.568	77.2	1200-0050	84	150	0.296	44.5	1200-0050	87	250	0.254	56.0
1200-0050	82	20	0.456	55.5	1200-0050	84	210	0.269	39.5	1200-0050	87	260	0.253	58.0
1200-0050	82	30	0.506	68.5	1200-0050	84	220	0.331	52.4	1200-0050	87	270	0.218	51.8
1200-0050	82	40	0.523	73.1	1200-0050	84	230	0.295	50.2	1200-0050	87	280	0.244	60.9
1200-0050	82	50	0.634	86.4	1200-0050	84	240	0.313	54.8	1200-0050	87	290	0.199	48.9
1200-0050	82	60	0.624	82.7	1200-0050	84	250	0.339	62.2	1200-0050	87	300	0.195	47.9
1200-0050	82	70	0.608	78.8	1200-0050	84	260	0.356	66.8	1200-0050	87	310	0.213	49.7
1200-0050	82	80	0.615	77.0	1200-0050	84	270	0.362	71.6	1200-0050	87	320	0.173	34.8
1200-0050	82	90	0.606	73.4	1200-0050	84	280	0.307	62.9	1200-0050	87	330	0.209	38.2
1200-0050	82	100	0.713	78.8	1200-0050	84	290	0.277	57.3	1200-0050	87	340	0.342	64.4
1200-0050	82	110	0.712	74.9	1200-0050	84	300	0.289	60.5	1200-0050	87	350	0.339	59.2
1200-0050	82	120	0.581	61.7	1200-0050	84	310	0.295	58.9	1200-0050	86	0	0.304	50.5
1200-0050	82	270	0.781	86.8	1200-0050	84	320	0.277	51.2	1200-0050	86	10	0.290	48.0
1200-0050	82	280	0.722	86.0	1200-0050	84	330	0.319	55.4	1200-0050	86	20	0.320	59.6
1200-0050	82	290	0.798	96.4	1200-0050	84	340	0.398	67.9	1200-0050	86	30	0.223	41.5
1200-0050	82	300	0.687	88.6	1200-0050	84	350	0.395	63.6	1200-0050	86	40	0.228	47.1
1200-0050	82	310	0.598	81.6	1200-0050	85	0	0.373	63.5	1200-0050	86	50	0.247	58.5
1200-0050	82	320	0.424	58.0	1200-0050	85	10	0.343	57.7	1200-0050	86	60	0.205	51.8
1200-0050	82	330	0.511	69.4	1200-0050	85	20	0.326	56.7	1200-0050	86	70	0.194	50.7
1200-0050	82	340	0.646	94.8	1200-0050	85	30	0.252	45.5	1200-0050	86	80	0.194	50.7
1200-0050	82	350	0.554	72.8	1200-0050	85	40	0.231	46.6	1200-0050	86	90	0.191	48.9
1200-0050	83	0	0.514	72.7	1200-0050	85	50	0.250	56.2	1200-0050	86	100	0.198	47.0
1200-0050	83	10	0.478	67.4	1200-0050	85	60	0.242	56.3	1200-0050	86	110	0.187	43.5
1200-0050	83	20	0.449	64.3	1200-0050	85	70	0.216	50.9	1200-0050	86	120	0.164	36.5
1200-0050	83	30	0.444	68.6	1200-0050	85	80	0.201	47.2	1200-0050	86	130	0.165	34.8
1200-0050	83	40	0.431	69.4	1200-0050	85	90	0.213	48.7	1200-0050	86	140	0.200	39.5
1200-0050	83	50	0.452	74.6	1200-0050	85	100	0.210	46.5	1200-0050	86	150	0.214	39.8
1200-0050	83	60	0.462	76.2	1200-0050	85	110	0.218	46.5	1200-0050	86	210	0.242	45.0
1200-0050	83	70	0.424	68.3	1200-0050	85	120	0.253	51.6	1200-0050	86	220	0.277	54.6
1200-0050	83	80	0.492	76.4	1200-0050	85	130	0.246	46.9	1200-0050	86	230	0.258	54.5
1200-0050	83	90	0.492	74.0	1200-0050	85	140	0.218	39.4	1200-0050	86	240	0.235	51.0
1200-0050	83	100	0.433	63.1	1200-0050	85	150	0.236	39.4	1200-0050	86	250	0.242	55.1
1200-0050	83	110	0.446	62.9	1200-0050	85	210	0.240	40.2	1200-0050	86	260	0.252	59.7
1200-0050	83	120	0.396	53.5	1200-0050	85	220	0.297	53.1	1200-0050	86	270	0.204	51.2
1200-0050	83	130	0.376	48.4	1200-0050	85	230	0.323	61.6	1200-0050	86	280	0.210	54.9
1200-0050	83	140	0.428	52.1	1200-0050	85	240	0.304	61.0	1200-0050	86	290	0.191	49.3
1200-0050	83	150	0.482	55.6	1200-0050	85	250	0.293	61.9	1200-0050	86	300	0.173	42.8
1200-0050	83	210	0.469	53.7	1200-0050	85	260	0.295	63.3	1200-0050	86	310	0.173	39.7
1200-0050	83	220	0.507	60.2	1200-0050	85	270	0.294	65.7	1200-0050	86	320	0.175	35.1
1200-0050	83	230	0.496	62.9	1200-0050	85	280	0.250	58.0	1200-0050	86	330	0.215	38.8
1200-0050	83	240	0.546	69.8	1200-0050	85	290	0.232	53.8	1200-0050	86	340	0.331	62.5
1200-0050	83	250	0.585	77.3	1200-0050	85	300	0.223	52.0	1200-0050	86	350	0.331	58.9
1200-0050	83	260	0.547	76.3	1200-0050	85	310	0.208	45.9					
1200-0050	83	270	0.493	74.1	1200-0050	85	320	0.198	38.9					
1200-0050	83	280	0.526	79.6	1200-0050	85	330	0.219	38.4					
1200-0050	83	290	0.552	86.5	1200-0050	85	340	0.359	65.4					
1200-0050	83	300	0.504	81.4	1200-0050	85	350	0.357	60.9					
1200-0050	83	310	0.445	73.6	1200-0050	87	0	0.323	53.2					
1200-0050	83	320	0.352	54.6	1200-0050	87	10	0.338	58.8					
1200-0050	83	330	0.415	62.8	1200-0050	87	20	0.301	52.6					
1200-0050	83	340	0.526	86.0	1200-0050	87	30	0.246	45.8					
1200-0050	83	350	0.544	82.9	1200-0050	87	40	0.237	49.5					
1200-0050	84	0	0.417	66.6	1200-0050	87	50	0.250	59.2					
1200-0050	84	10	0.399	64.0	1200-0050	87	60	0.216	52.3					
1200-0050	84	20	0.351	56.5	1200-0050	87	70	0.196	48.9					
1200-0050	84	30	0.331	57.4	1200-0050	87	80	0.196	49.4					
1200-0050	84	40	0.289	54.4	1200-0050	87	90	0.235	55.9					
1200-0050	84	50	0.285	58.7	1200-0050	87	100	0.233	53.5					
1200-0050	84	60	0.278	58.4	1200-0050	87	110	0.215	47.6					
1200-0050	84	70	0.269	57.1	1200-0050	87	120	0.172	37.2					
1200-0050	84	80	0.213	45.8	1200-0050	87	130	0.199	40.6					
1200-0050	84	90	0.243	50.3	1200-0050	87	140	0.212	41.5					
1200-0050	84	100	0.237	46.7	1200-0050	87	150	0.214	38.7					
1200-0050	84	110	0.236	43.7	1200-0050	87	210	0.251	44.8					
1200-0050	84	120	0.284	49.8	1200-0050	87	220	0.292	55.7					
1200-0050	84	130	0.320	54.0	1200-0050	87	230	0.287	58.7					

Table 13. Sphere-cone 1200-0100 transition locations.

Model	Run	Ray	s_0/R	Re_θ
1200-0100	88	0	0.354	34.7
1200-0100	88	10	0.340	33.2
1200-0100	88	20	0.249	23.8
1200-0100	88	30	0.251	26.9
1200-0100	88	40	0.281	34.7
1200-0100	88	50	0.245	31.9
1200-0100	88	60	0.200	27.2
1200-0100	88	70	0.170	23.3
1200-0100	88	80	0.143	19.9
1200-0100	88	90	0.164	22.1
1200-0100	88	100	0.158	20.6
1200-0100	88	120	0.141	17.2
1200-0100	88	130	0.138	16.1
1200-0100	88	140	0.201	21.1
1200-0100	88	150	0.256	25.0
1200-0100	88	220	0.241	25.3
1200-0100	88	230	0.243	27.4
1200-0100	88	240	0.205	25.0
1200-0100	88	250	0.204	26.1
1200-0100	88	260	0.223	29.5
1200-0100	88	270	0.212	28.5
1200-0100	88	280	0.210	28.7
1200-0100	88	290	0.168	23.2
1200-0100	88	300	0.253	34.2
1200-0100	88	310	0.258	33.2
1200-0100	88	320	0.307	38.8
1200-0100	88	330	0.260	28.3
1200-0100	88	340	0.266	25.6
1200-0100	88	350	0.270	23.9
1200-0100	89	0	0.318	34.7
1200-0100	89	10	0.285	30.2
1200-0100	89	20	0.145	15.3
1200-0100	89	30	0.200	23.7
1200-0100	89	40	0.183	24.4
1200-0100	89	50	0.150	22.1
1200-0100	89	60	0.131	21.0
1200-0100	89	70	0.103	17.4
1200-0100	89	80	0.067	11.1
1200-0100	89	90	0.075	13.0
1200-0100	89	100	0.095	15.8
1200-0100	89	140	0.167	21.8
1200-0100	89	150	0.225	25.9
1200-0100	89	220	0.169	21.8
1200-0100	89	230	0.192	25.6
1200-0100	89	240	0.132	18.9
1200-0100	89	250	0.137	20.5
1200-0100	89	260	0.158	24.2
1200-0100	89	270	0.168	26.5
1200-0100	89	280	0.179	29.8
1200-0100	89	290	0.138	23.1
1200-0100	89	300	0.178	27.7
1200-0100	89	310	0.171	25.1
1200-0100	89	320	0.193	26.1
1200-0100	89	330	0.209	25.6
1200-0100	89	340	0.201	21.9
1200-0100	89	350	0.208	21.5

Table 14. Sphere-cone 3700-0015 transition locations.

Model	Run	Ray	s_0/R	Re_θ	Model	Run	Ray	s_0/R	Re_θ
3700-0015	109	0	0.750	194.0	3700-0015	111	70	0.539	129.1
3700-0015	109	10	0.703	179.3	3700-0015	111	80	0.473	111.8
3700-0015	109	20	0.794	186.5	3700-0015	111	90	0.446	103.4
3700-0015	109	30	0.879	186.9	3700-0015	111	100	0.458	100.7
3700-0015	109	40	0.807	171.7	3700-0015	111	110	0.441	93.8
3700-0015	109	50	0.689	147.3	3700-0015	111	120	0.433	86.9
3700-0015	109	60	0.677	143.0	3700-0015	111	130	0.398	77.9
3700-0015	109	70	0.747	146.4	3700-0015	111	140	0.406	75.7
3700-0015	109	80	0.650	128.8	3700-0015	111	150	0.364	64.1
3700-0015	109	90	0.586	114.8	3700-0015	111	210	0.420	73.3
3700-0015	109	100	0.547	102.8	3700-0015	111	220	0.515	92.0
3700-0015	109	110	0.529	96.2	3700-0015	111	230	0.447	87.3
3700-0015	109	120	0.594	102.1	3700-0015	111	240	0.411	85.5
3700-0015	109	130	0.591	97.7	3700-0015	111	250	0.381	83.1
3700-0015	109	210	0.602	91.6	3700-0015	111	260	0.450	99.9
3700-0015	109	220	0.600	95.0	3700-0015	111	270	0.449	103.4
3700-0015	109	230	0.499	85.8	3700-0015	111	280	0.425	102.4
3700-0015	109	240	0.600	102.8	3700-0015	111	290	0.471	114.5
3700-0015	109	250	0.624	109.7	3700-0015	111	300	0.512	126.0
3700-0015	109	260	0.632	116.2	3700-0015	111	310	0.508	126.4
3700-0015	109	270	0.721	133.6	3700-0015	111	320	0.554	140.4
3700-0015	109	280	0.818	150.1	3700-0015	111	330	0.655	164.3
3700-0015	109	290	0.752	146.5	3700-0015	111	340	0.576	149.5
3700-0015	109	300	0.665	141.7	3700-0015	111	350	0.618	176.4
3700-0015	109	310	0.664	143.6	3700-0015	112	0	0.566	140.6
3700-0015	109	320	0.729	158.9	3700-0015	112	10	0.511	118.7
3700-0015	109	330	0.767	167.3	3700-0015	112	20	0.571	154.4
3700-0015	109	340	0.838	191.4	3700-0015	112	30	0.598	155.7
3700-0015	109	350	0.742	186.7	3700-0015	112	40	0.507	131.8
3700-0015	110	0	0.598	153.1	3700-0015	112	50	0.465	120.3
3700-0015	110	10	0.540	122.3	3700-0015	112	60	0.414	107.3
3700-0015	110	20	0.629	161.5	3700-0015	112	70	0.499	121.3
3700-0015	110	30	0.680	164.5	3700-0015	112	80	0.443	110.3
3700-0015	110	40	0.608	147.0	3700-0015	112	90	0.447	108.3
3700-0015	110	50	0.535	124.0	3700-0015	112	100	0.390	90.9
3700-0015	110	60	0.457	109.8	3700-0015	112	110	0.410	91.4
3700-0015	110	70	0.555	124.5	3700-0015	112	120	0.405	84.6
3700-0015	110	80	0.514	113.8	3700-0015	112	130	0.327	67.9
3700-0015	110	90	0.516	110.7	3700-0015	112	140	0.343	66.7
3700-0015	110	100	0.477	99.9	3700-0015	112	150	0.340	63.5
3700-0015	110	110	0.489	96.7	3700-0015	112	210	0.363	67.5
3700-0015	110	120	0.461	87.8	3700-0015	112	220	0.471	90.6
3700-0015	110	130	0.447	81.0	3700-0015	112	230	0.440	88.1
3700-0015	110	140	0.516	87.4	3700-0015	112	240	0.395	83.8
3700-0015	110	150	0.374	64.3	3700-0015	112	250	0.370	82.6
3700-0015	110	210	0.445	74.2	3700-0015	112	260	0.444	103.1
3700-0015	110	220	0.513	87.5	3700-0015	112	270	0.417	101.7
3700-0015	110	230	0.493	88.6	3700-0015	112	280	0.418	103.1
3700-0015	110	240	0.435	83.9	3700-0015	112	290	0.469	116.6
3700-0015	110	250	0.397	81.5	3700-0015	112	300	0.473	121.3
3700-0015	110	260	0.499	104.2	3700-0015	112	310	0.482	124.6
3700-0015	110	270	0.472	102.8	3700-0015	112	320	0.562	147.3
3700-0015	110	280	0.454	101.4	3700-0015	112	330	0.611	159.4
3700-0015	110	290	0.504	115.6	3700-0015	112	340	0.581	157.9
3700-0015	110	300	0.502	118.9	3700-0015	112	350	0.611	182.5
3700-0015	110	310	0.533	124.1					
3700-0015	110	320	0.617	147.7					
3700-0015	110	330	0.674	162.2					
3700-0015	110	340	0.591	149.0					
3700-0015	110	350	0.639	176.8					
3700-0015	111	0	0.582	142.0					
3700-0015	111	10	0.511	113.9					
3700-0015	111	20	0.571	148.1					
3700-0015	111	30	0.625	157.7					
3700-0015	111	40	0.550	138.9					
3700-0015	111	50	0.482	119.9					
3700-0015	111	60	0.428	108.5					

Table 15. Sphere-cone 3700-0025 transition locations.

Model	Run	Ray	s_0/R	Re_θ	Model	Run	Ray	s_0/R	Re_θ	Model	Run	Ray	s_0/R	Re_θ
3700-0025	65	0	0.628	115.2	3700-0025	67	130	0.321	61.4	3700-0025	69	230	0.360	73.6
3700-0025	65	10	0.636	119.4	3700-0025	67	140	0.337	59.3	3700-0025	69	240	0.296	64.3
3700-0025	65	20	0.652	113.4	3700-0025	67	150	0.328	54.6	3700-0025	69	250	0.266	61.4
3700-0025	65	30	0.615	100.4	3700-0025	67	210	0.331	57.3	3700-0025	69	260	0.255	60.5
3700-0025	65	40	0.559	91.1	3700-0025	67	220	0.344	60.5	3700-0025	69	270	0.217	54.2
3700-0025	65	50	0.587	92.2	3700-0025	67	230	0.343	64.2	3700-0025	69	280	0.250	64.6
3700-0025	65	60	0.661	100.4	3700-0025	67	240	0.305	61.3	3700-0025	69	290	0.258	66.1
3700-0025	65	70	0.638	94.7	3700-0025	67	250	0.309	63.8	3700-0025	69	300	0.236	60.2
3700-0025	65	80	0.810	107.2	3700-0025	67	260	0.307	67.2	3700-0025	69	310	0.297	74.6
3700-0025	65	90	0.775	100.1	3700-0025	67	270	0.250	56.7	3700-0025	69	320	0.301	69.6
3700-0025	65	100	0.817	98.5	3700-0025	67	280	0.251	58.3	3700-0025	69	330	0.326	69.7
3700-0025	65	240	0.750	85.3	3700-0025	67	290	0.270	63.5	3700-0025	69	340	0.367	74.3
3700-0025	65	250	0.759	90.3	3700-0025	67	300	0.257	61.1	3700-0025	69	350	0.245	39.2
3700-0025	65	260	0.752	94.7	3700-0025	67	310	0.338	76.8					
3700-0025	65	270	0.659	89.8	3700-0025	67	320	0.308	66.5					
3700-0025	65	280	0.745	102.6	3700-0025	67	330	0.348	72.2					
3700-0025	65	290	0.777	110.0	3700-0025	67	340	0.377	72.4					
3700-0025	65	300	0.613	94.7	3700-0025	67	350	0.251	37.6					
3700-0025	65	310	0.737	113.1	3700-0025	68	0	0.271	43.4					
3700-0025	65	320	0.698	111.2	3700-0025	68	10	0.233	36.9					
3700-0025	65	330	0.731	118.5	3700-0025	68	20	0.268	47.3					
3700-0025	65	340	0.688	119.6	3700-0025	68	30	0.217	41.3					
3700-0025	65	350	0.615	114.3	3700-0025	68	40	0.211	46.3					
3700-0025	66	0	0.533	98.4	3700-0025	68	50	0.208	47.4					
3700-0025	66	10	0.439	74.9	3700-0025	68	60	0.170	41.9					
3700-0025	66	20	0.444	80.6	3700-0025	68	70	0.197	49.1					
3700-0025	66	30	0.358	65.4	3700-0025	68	80	0.185	46.4					
3700-0025	66	40	0.315	60.9	3700-0025	68	90	0.213	51.7					
3700-0025	66	50	0.356	71.3	3700-0025	68	100	0.267	62.1					
3700-0025	66	60	0.284	59.4	3700-0025	68	110	0.266	60.6					
3700-0025	66	70	0.363	74.4	3700-0025	68	120	0.266	56.1					
3700-0025	66	80	0.275	57.1	3700-0025	68	130	0.266	54.5					
3700-0025	66	90	0.305	60.2	3700-0025	68	140	0.251	48.8					
3700-0025	66	100	0.426	77.7	3700-0025	68	150	0.257	46.8					
3700-0025	66	110	0.444	77.6	3700-0025	68	210	0.293	52.8					
3700-0025	66	120	0.465	76.4	3700-0025	68	220	0.303	57.2					
3700-0025	66	130	0.465	74.1	3700-0025	68	230	0.326	65.3					
3700-0025	66	140	0.453	68.7	3700-0025	68	240	0.288	60.6					
3700-0025	66	150	0.400	59.2	3700-0025	68	250	0.291	65.5					
3700-0025	66	210	0.408	60.8	3700-0025	68	260	0.269	62.2					
3700-0025	66	220	0.442	68.6	3700-0025	68	270	0.233	55.7					
3700-0025	66	230	0.471	74.7	3700-0025	68	280	0.232	57.4					
3700-0025	66	240	0.429	71.9	3700-0025	68	290	0.237	59.5					
3700-0025	66	250	0.434	75.0	3700-0025	68	300	0.252	62.0					
3700-0025	66	260	0.368	68.8	3700-0025	68	310	0.298	69.9					
3700-0025	66	270	0.352	67.7	3700-0025	68	320	0.302	67.8					
3700-0025	66	280	0.359	72.0	3700-0025	68	330	0.340	72.9					
3700-0025	66	290	0.366	74.6	3700-0025	68	340	0.365	73.0					
3700-0025	66	300	0.436	89.9	3700-0025	68	350	0.262	42.4					
3700-0025	66	310	0.444	90.3	3700-0025	69	0	0.260	39.9					
3700-0025	66	320	0.454	89.9	3700-0025	69	10	0.251	40.1					
3700-0025	66	330	0.450	86.0	3700-0025	69	20	0.265	46.1					
3700-0025	66	340	0.458	83.0	3700-0025	69	30	0.214	39.2					
3700-0025	66	350	0.517	96.1	3700-0025	69	40	0.201	41.7					
3700-0025	67	0	0.240	34.6	3700-0025	69	50	0.214	50.0					
3700-0025	67	10	0.256	38.7	3700-0025	69	60	0.164	40.5					
3700-0025	67	20	0.262	43.3	3700-0025	69	70	0.192	51.2					
3700-0025	67	30	0.222	40.6	3700-0025	69	80	0.197	52.2					
3700-0025	67	40	0.222	45.9	3700-0025	69	90	0.204	51.6					
3700-0025	67	50	0.283	63.2	3700-0025	69	100	0.229	55.6					
3700-0025	67	60	0.186	42.9	3700-0025	69	110	0.241	55.2					
3700-0025	67	70	0.214	50.4	3700-0025	69	120	0.266	57.4					
3700-0025	67	80	0.203	47.4	3700-0025	69	130	0.257	54.0					
3700-0025	67	90	0.217	49.2	3700-0025	69	140	0.234	46.0					
3700-0025	67	100	0.306	67.2	3700-0025	69	150	0.250	46.8					
3700-0025	67	110	0.321	66.8	3700-0025	69	210	0.278	51.9					
3700-0025	67	120	0.323	64.7	3700-0025	69	220	0.295	58.0					

Table 16. Sphere-cone 3700-0050 transition locations.

Model	Run	Ray	s_0/R	Re_θ	Model	Run	Ray	s_0/R	Re_θ	Model	Run	Ray	s_0/R	Re_θ
3700-0050	57	0	0.501	60.3	3700-0050	59	100	0.210	41.0	3700-0050	62	150	0.202	37.9
3700-0050	57	10	0.514	65.5	3700-0050	59	110	0.224	42.5	3700-0050	62	210	0.242	44.4
3700-0050	57	20	0.498	68.0	3700-0050	59	120	0.228	41.5	3700-0050	62	220	0.211	42.3
3700-0050	57	30	0.592	83.2	3700-0050	59	130	0.251	42.1	3700-0050	62	230	0.194	39.2
3700-0050	57	40	0.595	82.9	3700-0050	59	140	0.272	42.9	3700-0050	62	240	0.174	37.3
3700-0050	57	50	0.548	74.2	3700-0050	59	150	0.294	44.3	3700-0050	62	250	0.159	36.4
3700-0050	57	60	0.575	77.2	3700-0050	59	210	0.304	46.7	3700-0050	62	260	0.168	40.4
3700-0050	57	70	0.587	76.5	3700-0050	59	220	0.311	51.2	3700-0050	62	270	0.156	39.0
3700-0050	57	80	0.574	71.7	3700-0050	59	230	0.275	46.8	3700-0050	62	280	0.146	36.2
3700-0050	57	90	0.664	77.2	3700-0050	59	240	0.263	46.2	3700-0050	62	290	0.143	34.9
3700-0050	57	100	0.592	68.6	3700-0050	59	250	0.236	43.6	3700-0050	62	300	0.143	35.2
3700-0050	57	110	0.613	67.5	3700-0050	59	260	0.228	44.3	3700-0050	62	310	0.163	36.0
3700-0050	57	120	0.507	55.0	3700-0050	59	270	0.207	43.0	3700-0050	62	320	0.174	34.4
3700-0050	57	130	0.447	47.9	3700-0050	59	280	0.197	41.4	3700-0050	62	330	0.166	29.6
3700-0050	57	240	0.654	67.2	3700-0050	59	290	0.197	41.3	3700-0050	62	340	0.173	29.0
3700-0050	57	250	0.672	71.3	3700-0050	59	300	0.199	40.0	3700-0050	62	350	0.174	28.0
3700-0050	57	260	0.709	78.0	3700-0050	59	310	0.209	40.6	3700-0050	61	0	0.153	22.4
3700-0050	57	270	0.740	83.7	3700-0050	59	320	0.223	39.2	3700-0050	61	10	0.155	23.0
3700-0050	57	280	0.749	88.0	3700-0050	59	330	0.228	36.2	3700-0050	61	20	0.159	25.1
3700-0050	57	290	0.786	94.9	3700-0050	59	340	0.245	35.4	3700-0050	61	30	0.127	21.6
3700-0050	57	300	0.659	85.2	3700-0050	59	350	0.266	35.5	3700-0050	61	40	0.169	33.0
3700-0050	57	310	0.446	61.2	3700-0050	60	0	0.233	33.1	3700-0050	61	50	0.136	30.1
3700-0050	57	320	0.450	60.5	3700-0050	60	10	0.253	36.7	3700-0050	61	60	0.137	35.9
3700-0050	57	330	0.535	72.2	3700-0050	60	20	0.187	29.0	3700-0050	61	70	0.132	34.6
3700-0050	57	340	0.464	57.5	3700-0050	60	30	0.180	30.9	3700-0050	61	80	0.124	32.5
3700-0050	57	350	0.528	67.3	3700-0050	60	40	0.181	34.7	3700-0050	61	90	0.109	28.5
3700-0050	58	0	0.461	62.1	3700-0050	60	50	0.158	34.3	3700-0050	61	100	0.148	36.8
3700-0050	58	10	0.451	62.2	3700-0050	60	60	0.116	26.8	3700-0050	61	110	0.146	34.7
3700-0050	58	20	0.408	56.2	3700-0050	60	70	0.138	32.7	3700-0050	61	120	0.161	36.3
3700-0050	58	30	0.436	67.0	3700-0050	60	80	0.140	32.8	3700-0050	61	130	0.184	39.3
3700-0050	58	40	0.388	61.5	3700-0050	60	90	0.147	33.7	3700-0050	61	140	0.193	38.6
3700-0050	58	50	0.319	52.3	3700-0050	60	100	0.175	38.7	3700-0050	61	150	0.208	38.5
3700-0050	58	60	0.293	49.3	3700-0050	60	110	0.178	38.1	3700-0050	61	210	0.246	47.5
3700-0050	58	70	0.322	53.2	3700-0050	60	120	0.182	38.2	3700-0050	61	220	0.214	44.0
3700-0050	58	80	0.329	52.8	3700-0050	60	130	0.188	36.7	3700-0050	61	230	0.184	39.6
3700-0050	58	90	0.384	59.2	3700-0050	60	140	0.220	40.3	3700-0050	61	240	0.184	41.2
3700-0050	58	100	0.376	56.1	3700-0050	60	150	0.242	40.2	3700-0050	61	250	0.141	33.6
3700-0050	58	110	0.376	53.0	3700-0050	60	210	0.281	46.8	3700-0050	61	260	0.154	37.7
3700-0050	58	120	0.397	53.3	3700-0050	60	220	0.260	46.3	3700-0050	61	270	0.138	35.7
3700-0050	58	130	0.429	54.8	3700-0050	60	230	0.238	46.2	3700-0050	61	280	0.151	40.1
3700-0050	58	140	0.395	48.9	3700-0050	60	240	0.197	39.7	3700-0050	61	290	0.117	28.8
3700-0050	58	150	0.466	53.1	3700-0050	60	250	0.159	34.2	3700-0050	61	300	0.129	31.1
3700-0050	58	210	0.494	58.1	3700-0050	60	260	0.177	39.0	3700-0050	61	310	0.128	28.4
3700-0050	58	220	0.547	64.7	3700-0050	60	270	0.170	39.3	3700-0050	61	320	0.154	29.6
3700-0050	58	230	0.476	59.6	3700-0050	60	280	0.166	39.5	3700-0050	61	330	0.144	24.1
3700-0050	58	240	0.474	62.3	3700-0050	60	290	0.182	42.7	3700-0050	61	340	0.179	29.0
3700-0050	58	250	0.511	69.7	3700-0050	60	300	0.153	33.4	3700-0050	61	350	0.164	24.8
3700-0050	58	260	0.403	59.2	3700-0050	60	310	0.169	37.0					
3700-0050	58	270	0.298	47.3	3700-0050	60	320	0.191	37.7					
3700-0050	58	280	0.279	45.7	3700-0050	60	330	0.189	32.2					
3700-0050	58	290	0.419	67.1	3700-0050	60	340	0.198	30.7					
3700-0050	58	300	0.284	45.7	3700-0050	60	350	0.230	33.7					
3700-0050	58	310	0.311	48.6	3700-0050	62	0	0.183	28.7					
3700-0050	58	320	0.336	52.1	3700-0050	62	10	0.166	26.8					
3700-0050	58	330	0.327	45.5	3700-0050	62	20	0.156	26.2					
3700-0050	58	340	0.368	48.0	3700-0050	62	30	0.147	26.6					
3700-0050	58	350	0.394	50.3	3700-0050	62	40	0.154	32.1					
3700-0050	59	0	0.325	46.6	3700-0050	62	50	0.150	32.9					
3700-0050	59	10	0.291	39.7	3700-0050	62	60	0.115	28.0					
3700-0050	59	20	0.328	50.9	3700-0050	62	70	0.110	27.7					
3700-0050	59	30	0.287	48.0	3700-0050	62	80	0.132	32.7					
3700-0050	59	40	0.271	50.0	3700-0050	62	90	0.139	34.5					
3700-0050	59	50	0.190	36.9	3700-0050	62	100	0.152	36.7					
3700-0050	59	60	0.174	35.5	3700-0050	62	110	0.164	37.9					
3700-0050	59	70	0.165	35.7	3700-0050	62	120	0.145	31.7					
3700-0050	59	80	0.171	36.1	3700-0050	62	130	0.181	38.5					
3700-0050	59	90	0.198	40.0	3700-0050	62	140	0.180	34.7					

Table 17. Sphere-cone 3700-0100 transition locations.

Model	Run	Ray	s_0/R	Re_θ
3700-0010	70	0	0.413	44.2
3700-0010	70	10	0.440	49.7
3700-0010	70	20	0.420	49.3
3700-0010	70	30	0.402	50.5
3700-0010	70	40	0.394	53.4
3700-0010	70	50	0.324	44.1
3700-0010	70	60	0.416	57.2
3700-0010	70	70	0.351	48.6
3700-0010	70	80	0.384	51.9
3700-0010	70	90	0.222	30.4
3700-0010	70	100	0.274	35.1
3700-0010	70	110	0.365	44.6
3700-0010	70	120	0.349	40.2
3700-0010	70	130	0.326	36.6
3700-0010	70	140	0.328	34.9
3700-0010	70	150	0.285	28.7
3700-0010	70	220	0.441	45.6
3700-0010	70	230	0.356	39.7
3700-0010	70	240	0.388	44.8
3700-0010	70	250	0.305	36.9
3700-0010	70	260	0.435	53.0
3700-0010	70	270	0.403	52.4
3700-0010	70	280	0.354	47.7
3700-0010	70	290	0.325	45.4
3700-0010	70	300	0.368	51.5
3700-0010	70	310	0.377	51.0
3700-0010	70	320	0.304	38.2
3700-0010	70	330	0.307	35.9
3700-0010	70	340	0.372	41.5
3700-0010	70	350	0.323	31.6
3700-0010	71	0	0.360	42.9
3700-0010	71	10	0.366	45.1
3700-0010	71	20	0.379	49.6
3700-0010	71	30	0.300	40.8
3700-0010	71	40	0.221	31.0
3700-0010	71	50	0.248	39.5
3700-0010	71	60	0.193	30.3
3700-0010	71	70	0.208	34.8
3700-0010	71	80	0.226	37.8
3700-0010	71	100	0.180	28.9
3700-0010	71	110	0.258	38.0
3700-0010	71	120	0.200	28.8
3700-0010	71	130	0.204	27.6
3700-0010	71	140	0.198	25.0
3700-0010	71	150	0.234	27.0
3700-0010	71	220	0.306	37.7
3700-0010	71	230	0.304	40.0
3700-0010	71	240	0.250	36.1
3700-0010	71	250	0.231	34.3
3700-0010	71	260	0.233	35.5
3700-0010	71	280	0.283	45.7
3700-0010	71	290	0.248	39.9
3700-0010	71	300	0.310	50.1
3700-0010	71	310	0.265	40.4
3700-0010	71	320	0.254	36.6
3700-0010	71	330	0.257	33.7
3700-0010	71	340	0.270	30.9
3700-0010	71	350	0.267	28.3

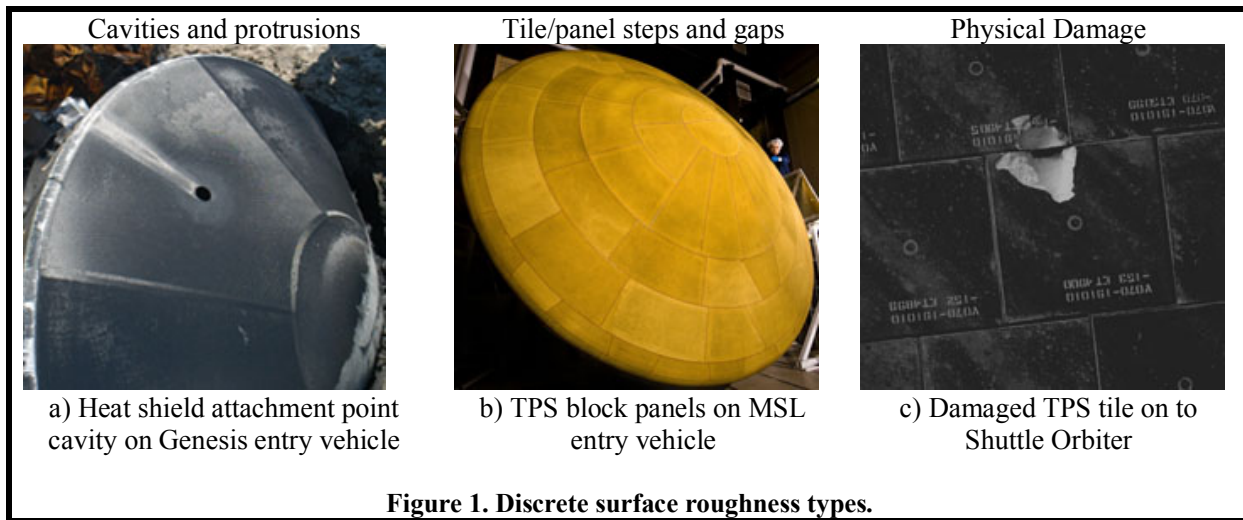


Figure 1. Discrete surface roughness types.

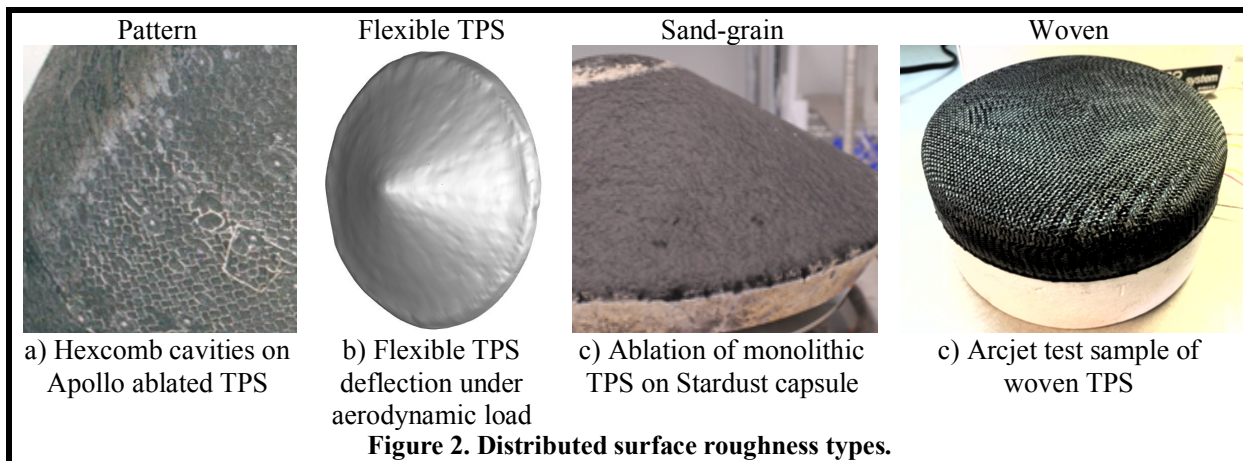


Figure 2. Distributed surface roughness types.

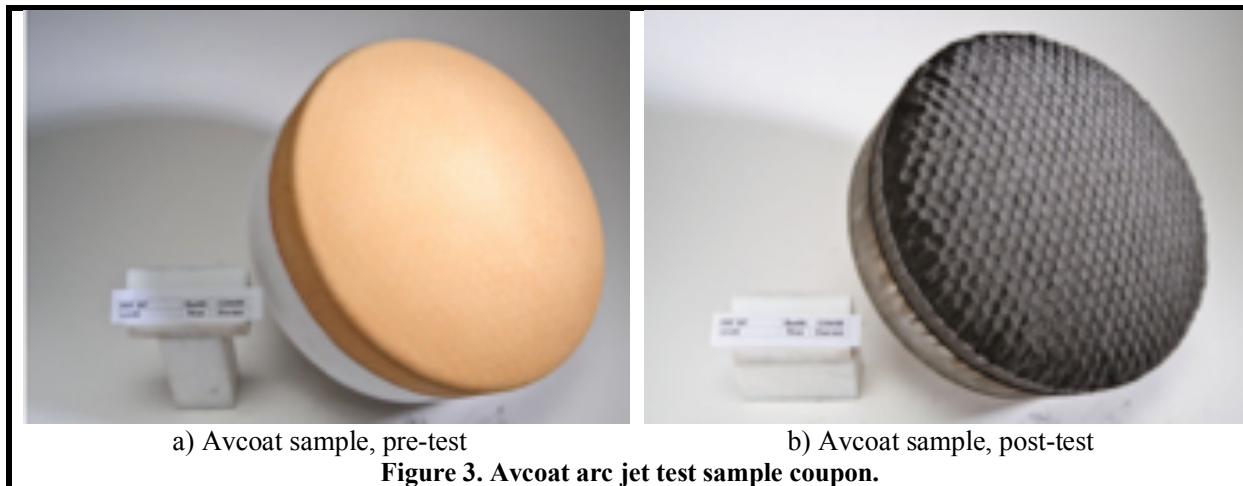


Figure 3. Avcoat arc jet test sample coupon.

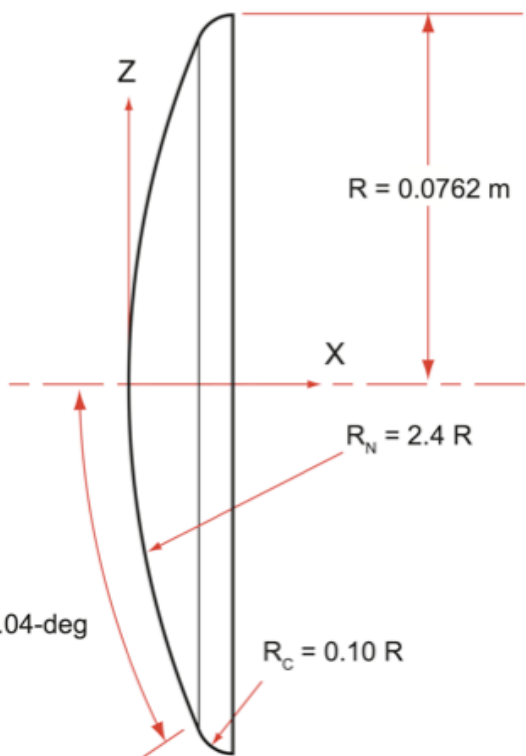


Figure 4. Spherical-cap geometry.

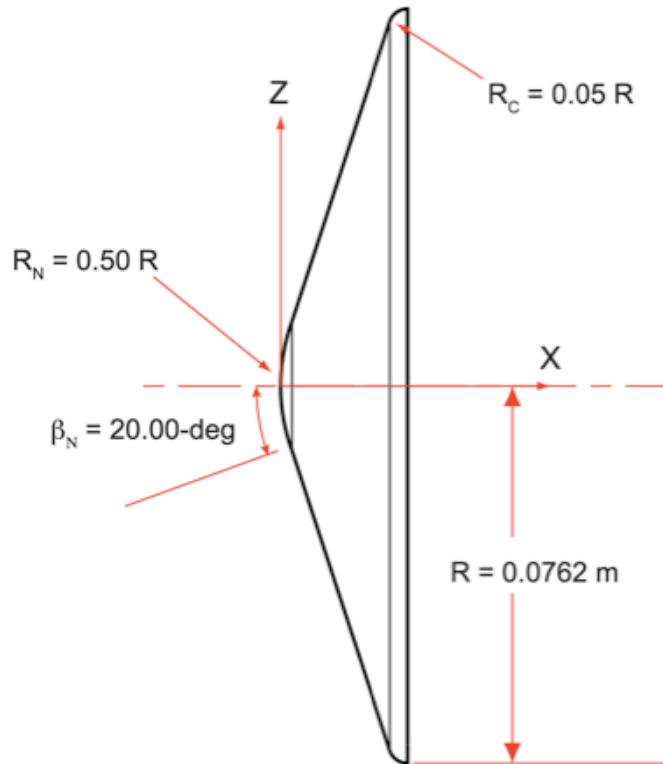


Figure 5. Sphere-cone geometry.

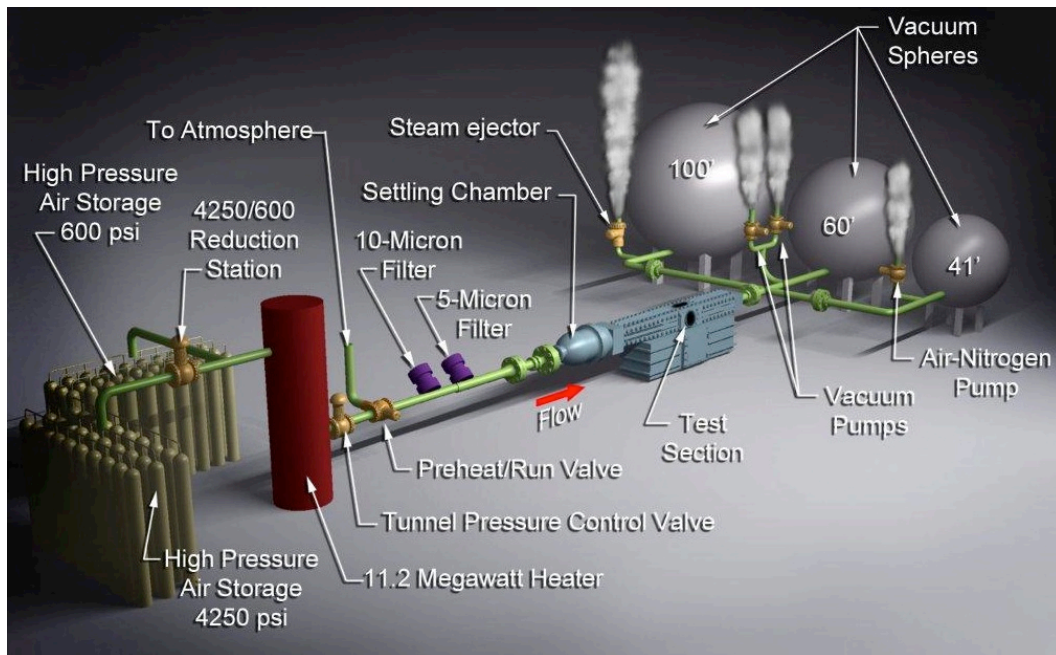


Figure 6. Schematic of Langley Research Center 20-Inch Mach 6 Air Tunnel.



Figure 7. Langley Research Center 20-Inch Mach 6 Air Tunnel test section.

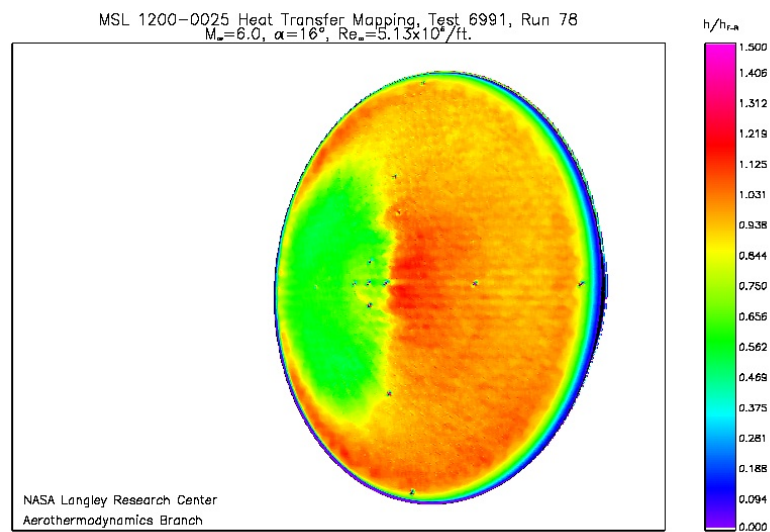


Figure 8. Sample phosphor thermography 2-D image data.

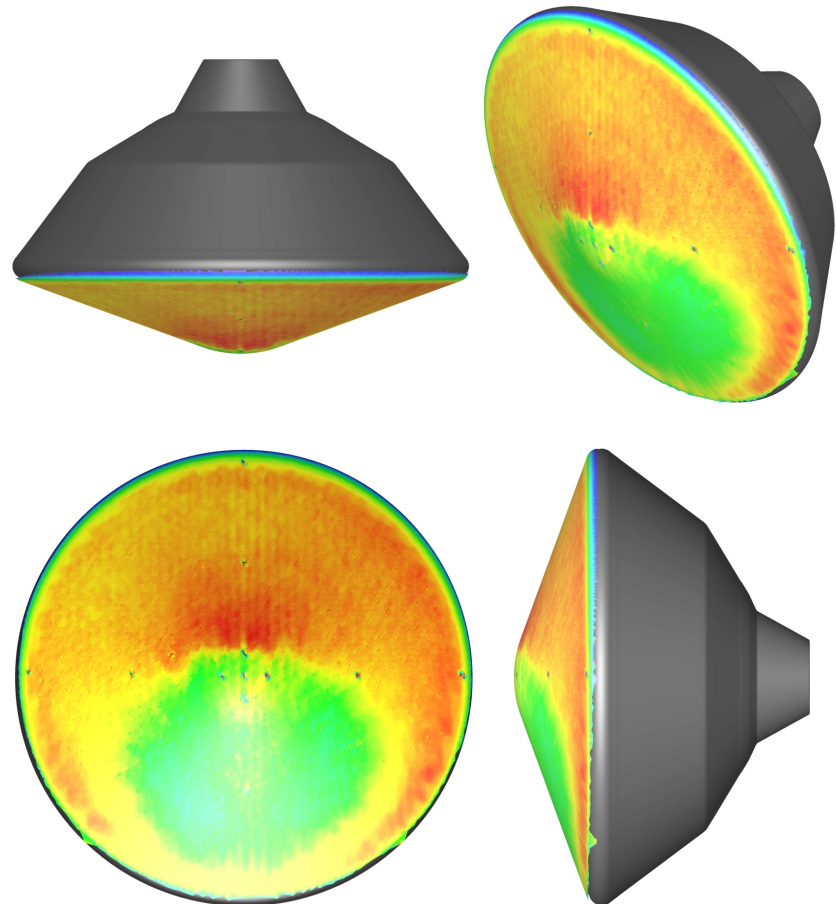


Figure 9. Sample 3-D mapping of phosphor thermography data.

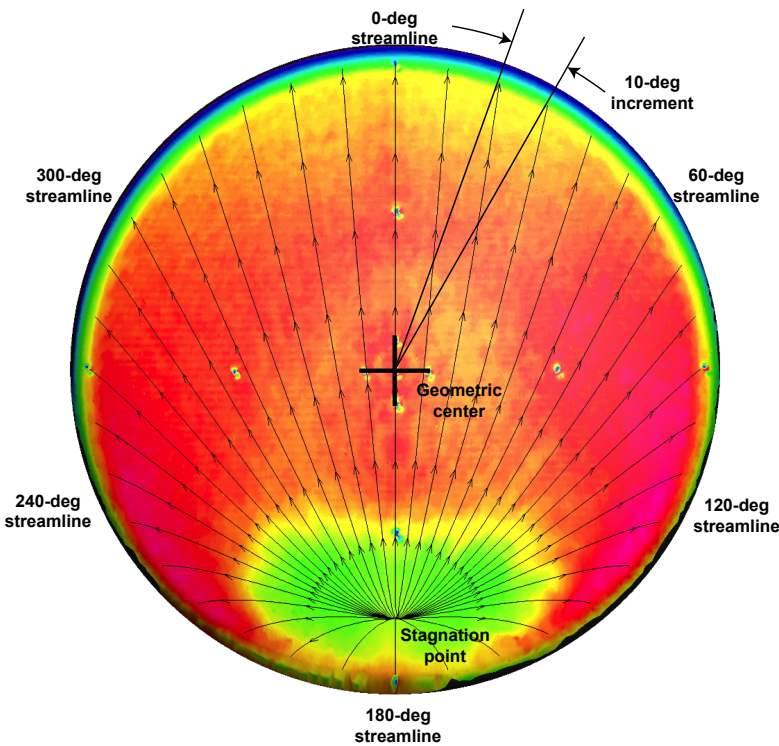


Figure 10. Streamlines for data extraction on spherical-cap geometry.

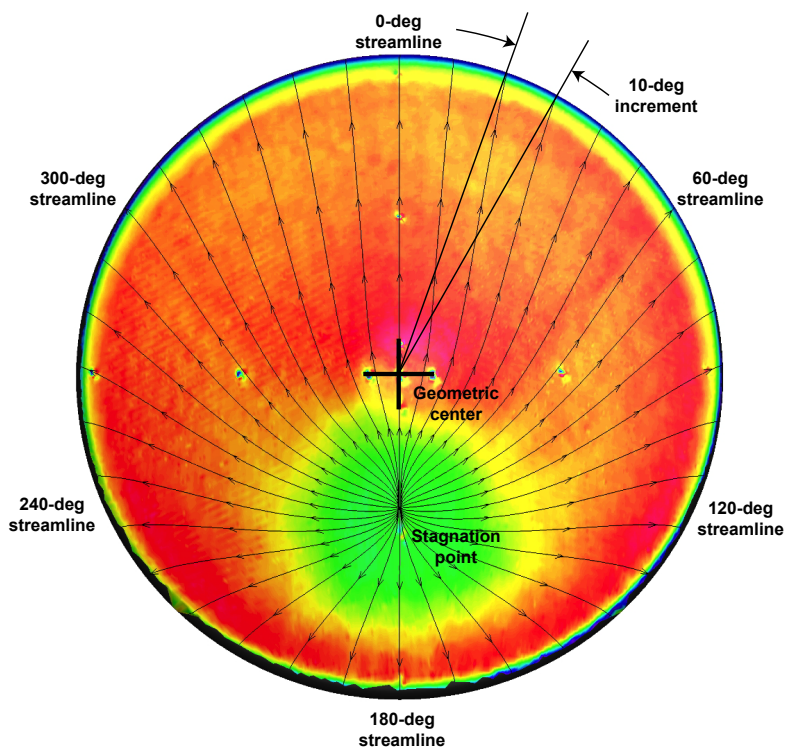


Figure 11. Streamlines for data extraction on sphere-cone geometry.

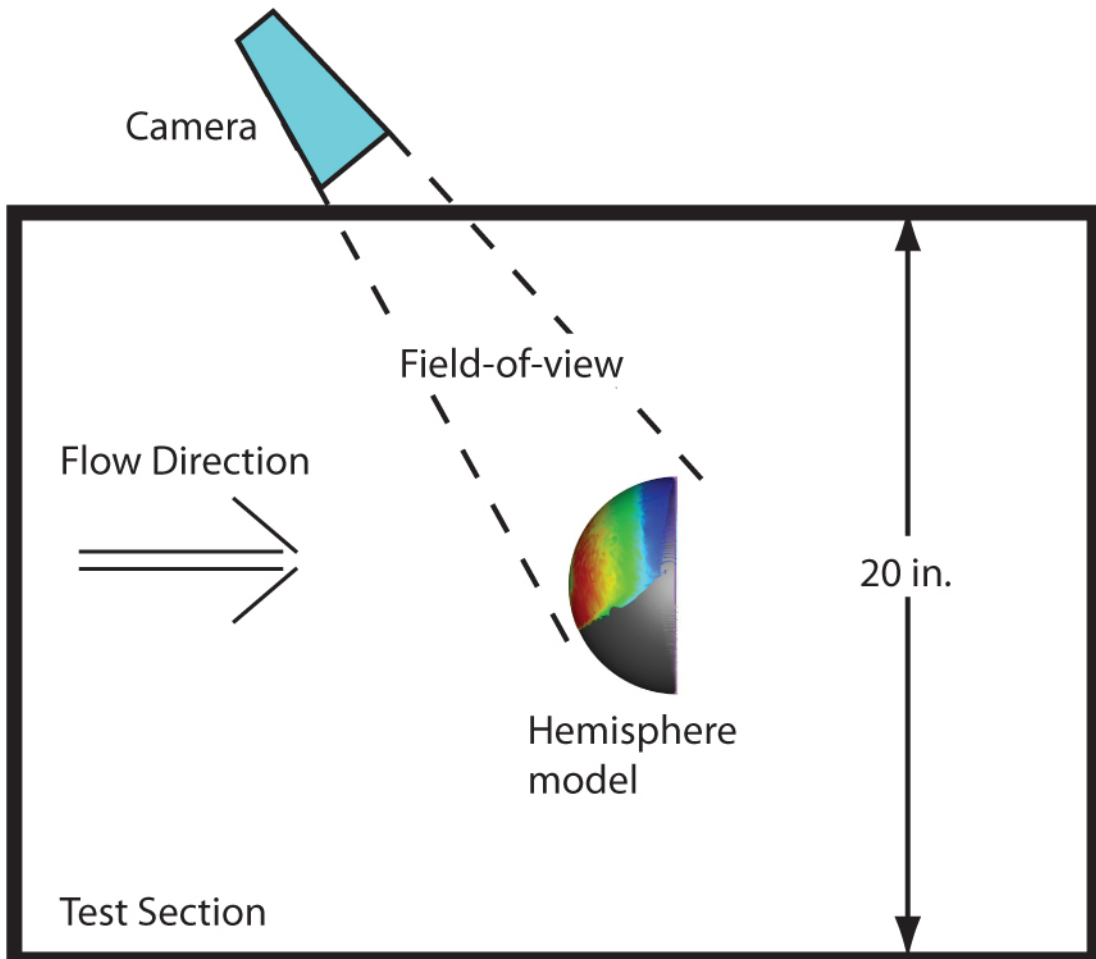


Figure 12. Illustration of camera field-of-view for hemisphere model in 20-Inch Mach 6 Air Tunnel.

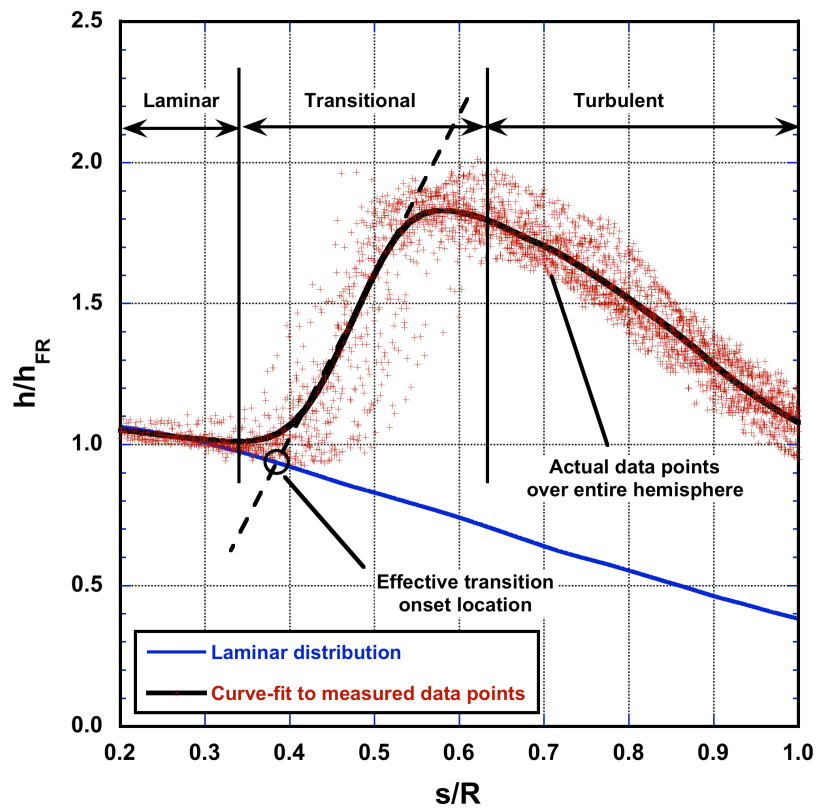


Figure 13. Tangent-slope-intercept method for determination of effect transition onset location.

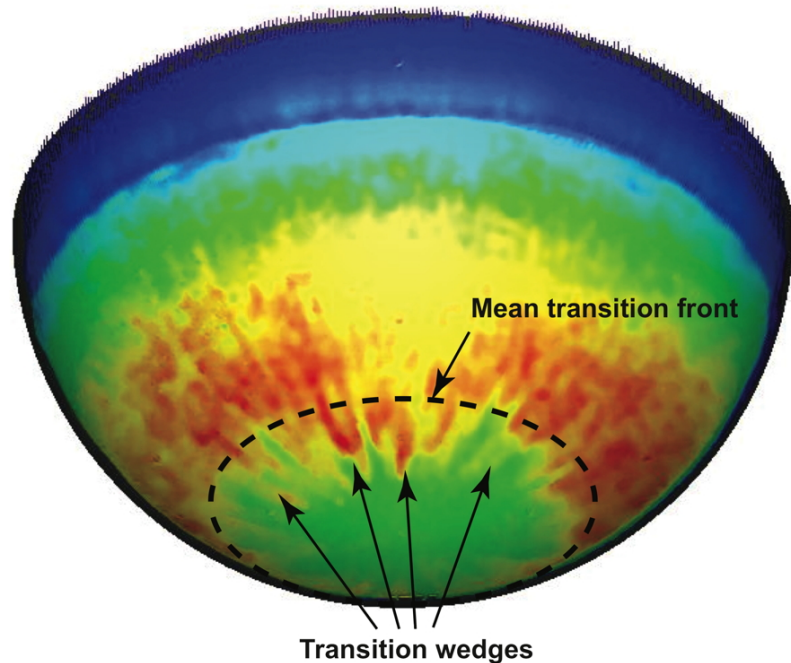


Figure 14. Comparison of irregular transition wedges vs. mean transition front.

This page intentionally left blank

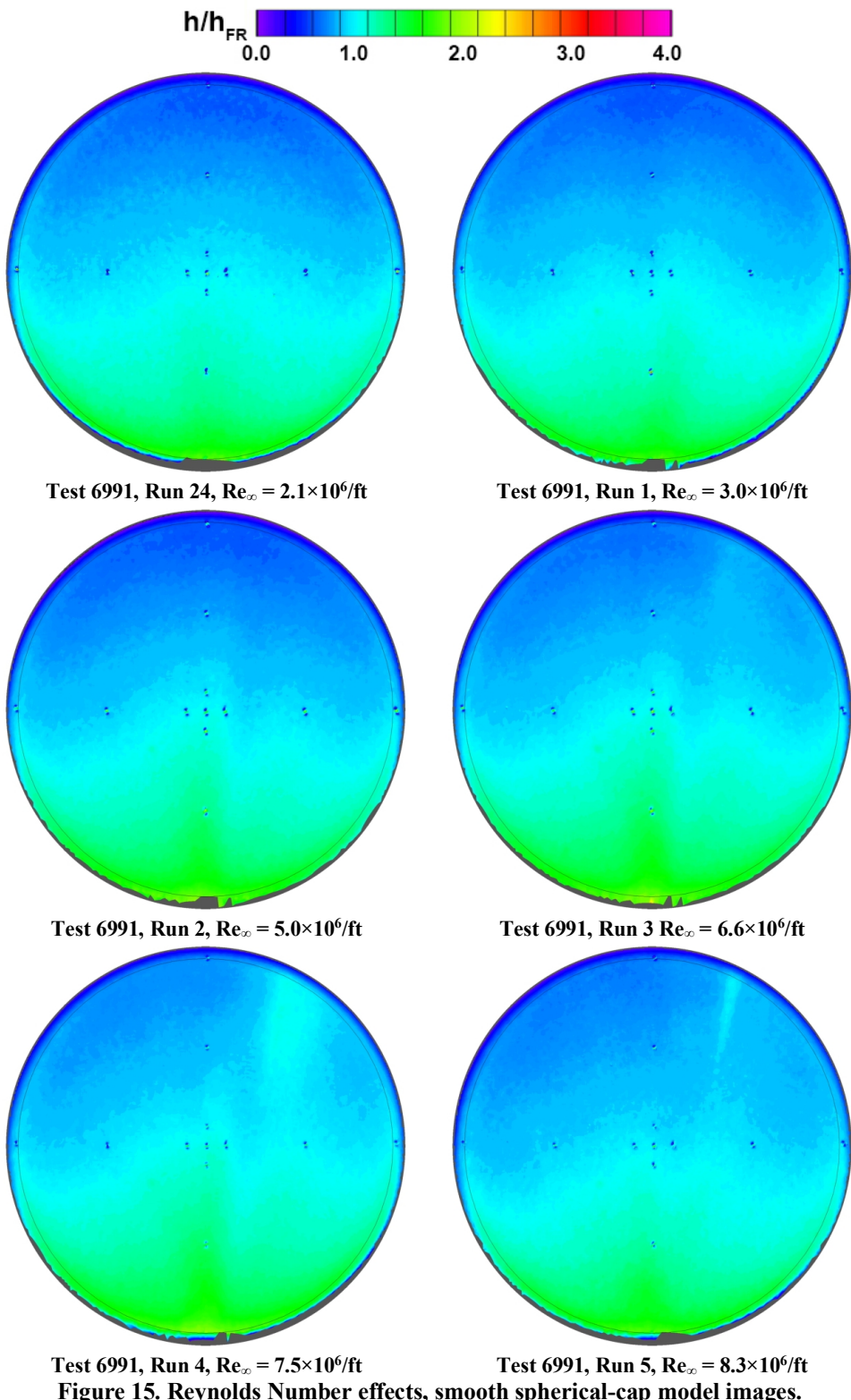


Figure 15. Reynolds Number effects, smooth spherical-cap model images.

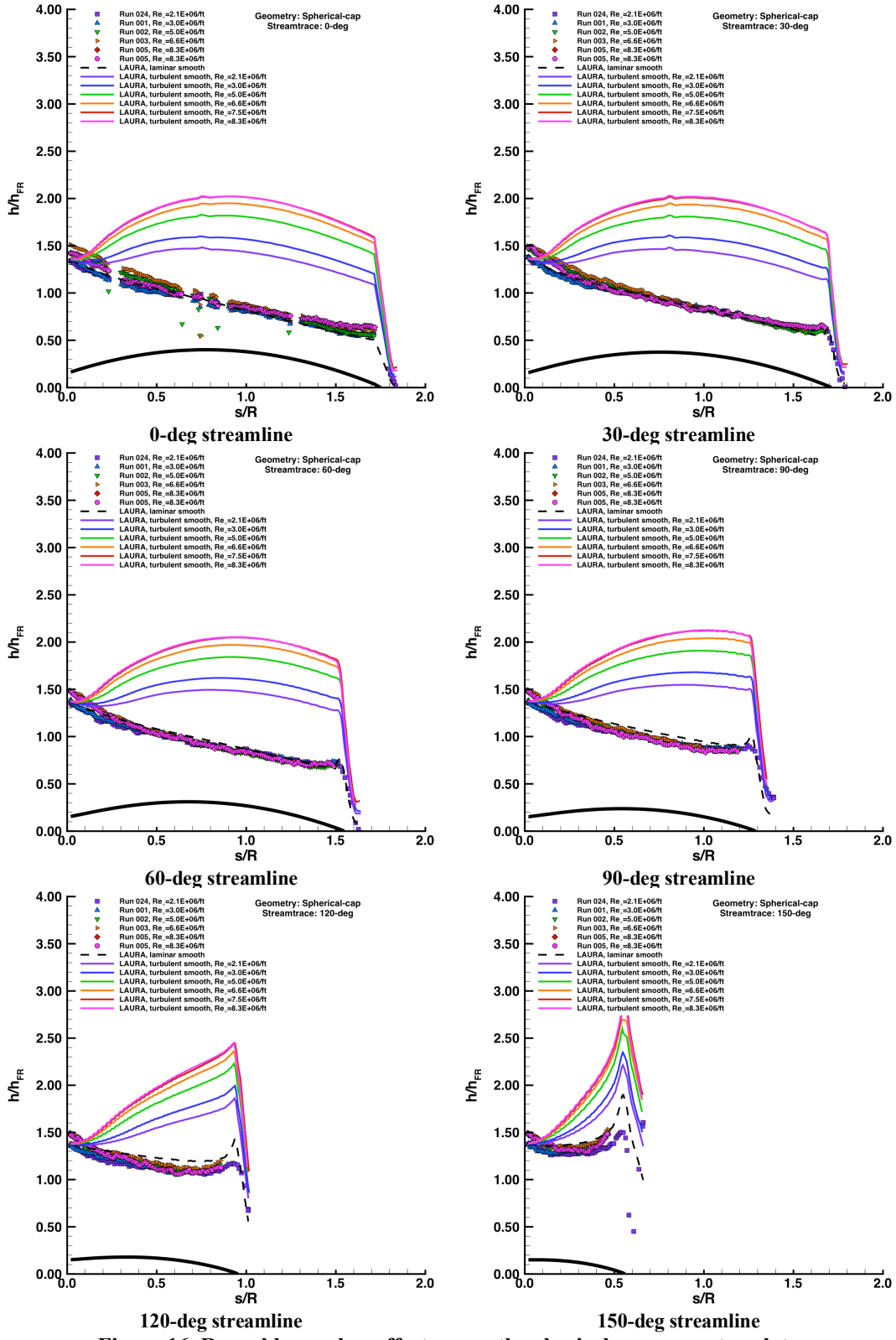


Figure 16. Reynolds number effects, smooth spherical-cap geometry plots.

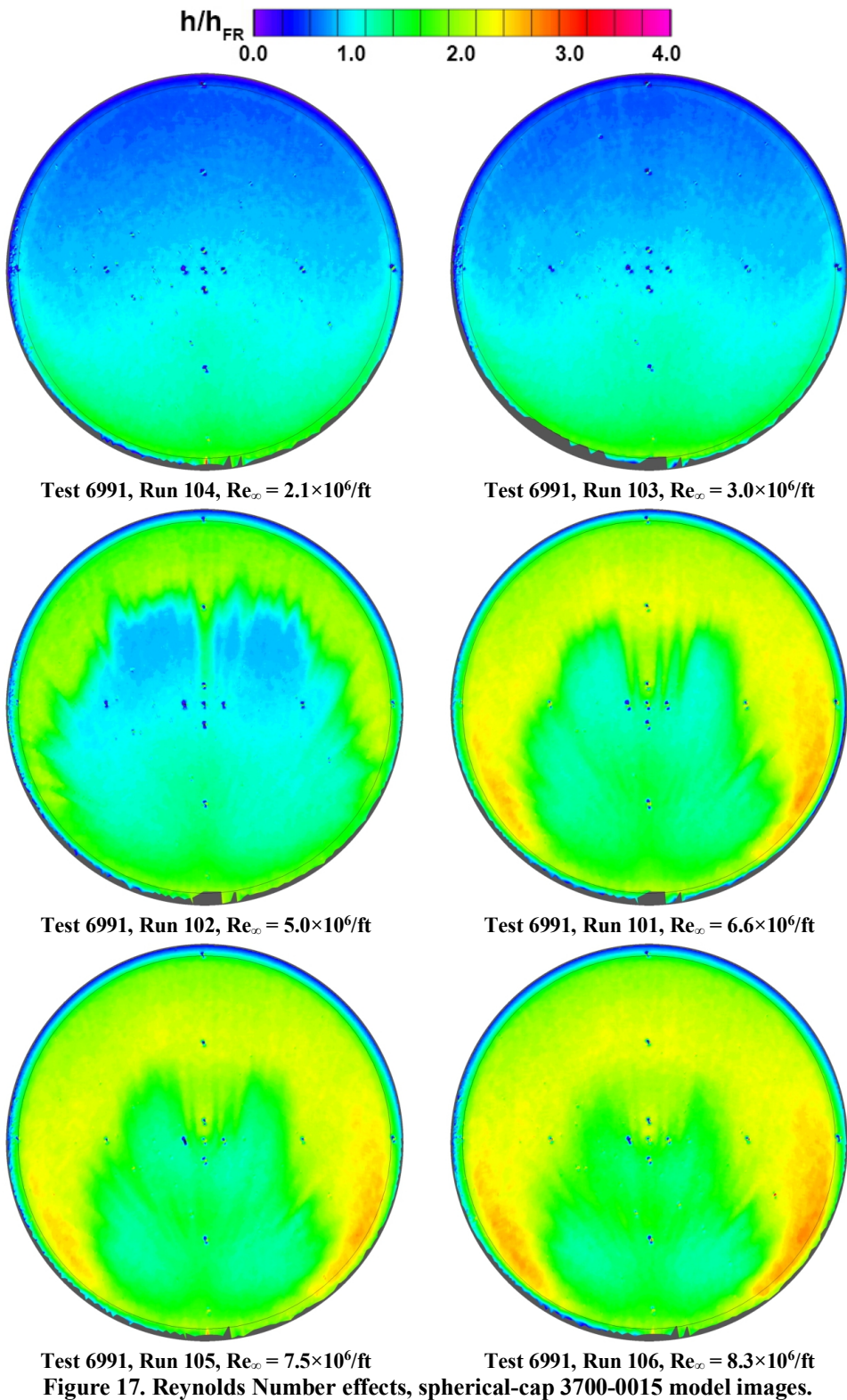


Figure 17. Reynolds Number effects, spherical-cap 3700-0015 model images.

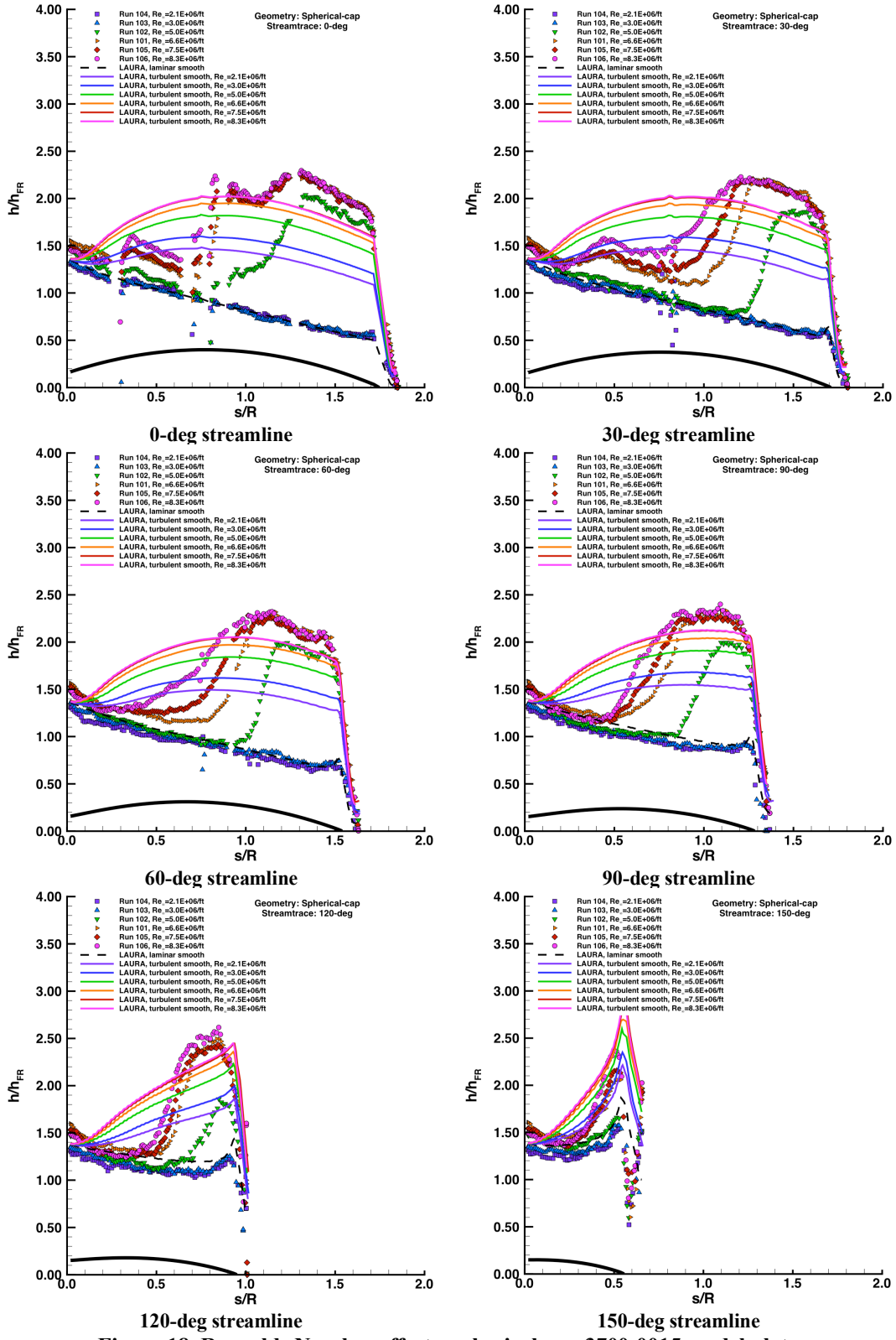


Figure 18. Reynolds Number effects, spherical-cap 3700-0015 model plots.

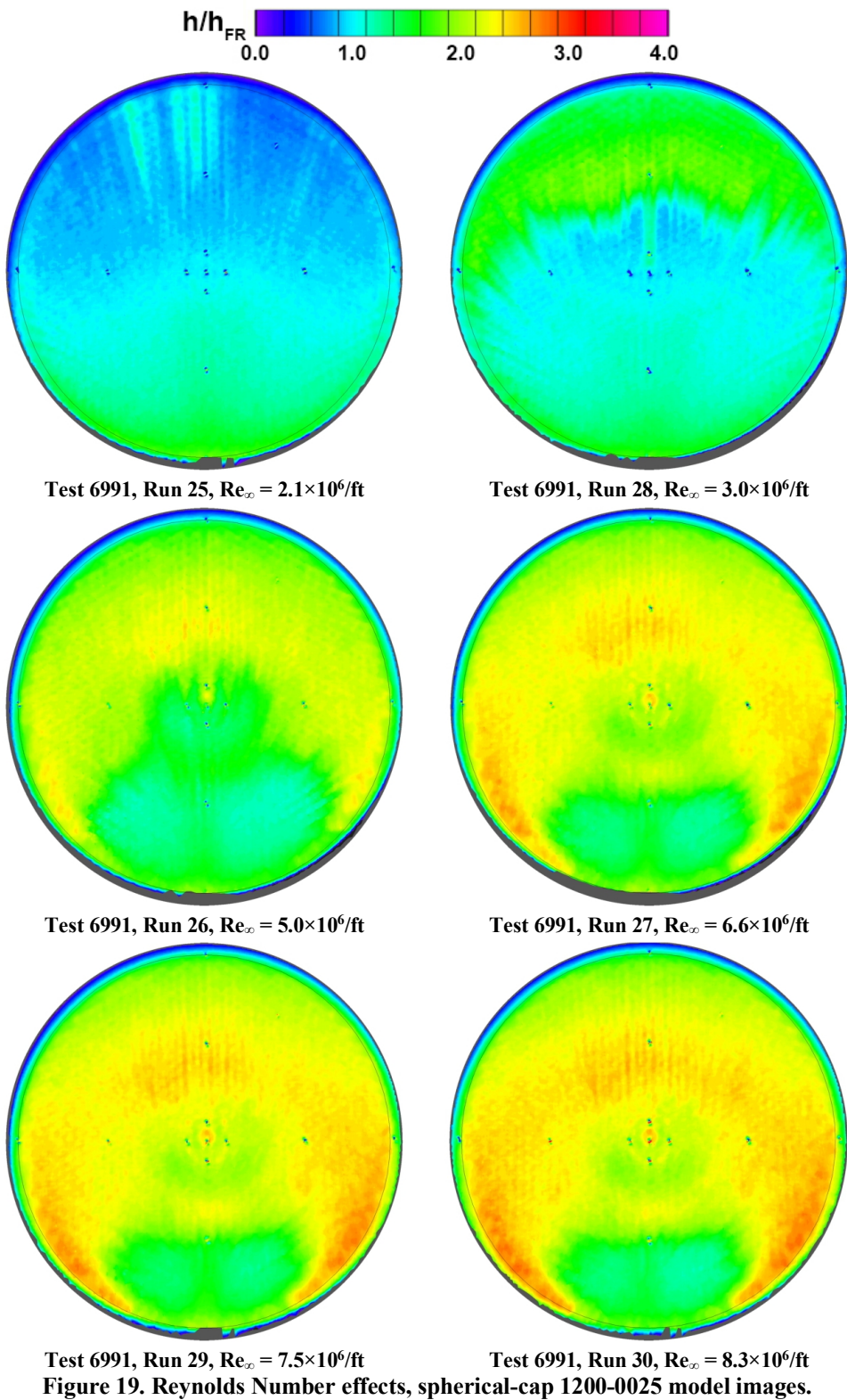


Figure 19. Reynolds Number effects, spherical-cap 1200-0025 model images.

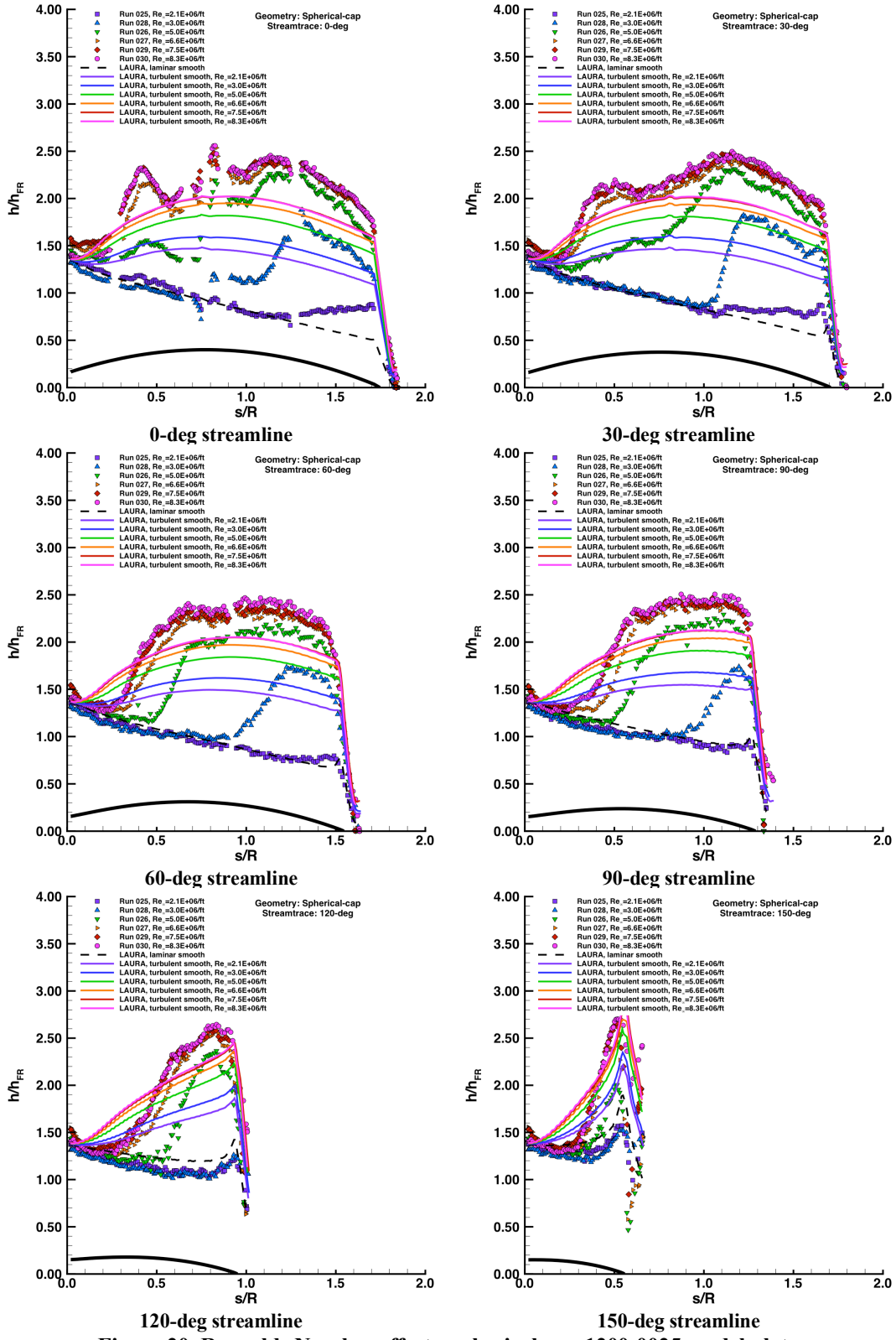


Figure 20. Reynolds Number effects, spherical-cap 1200-0025 model plots.

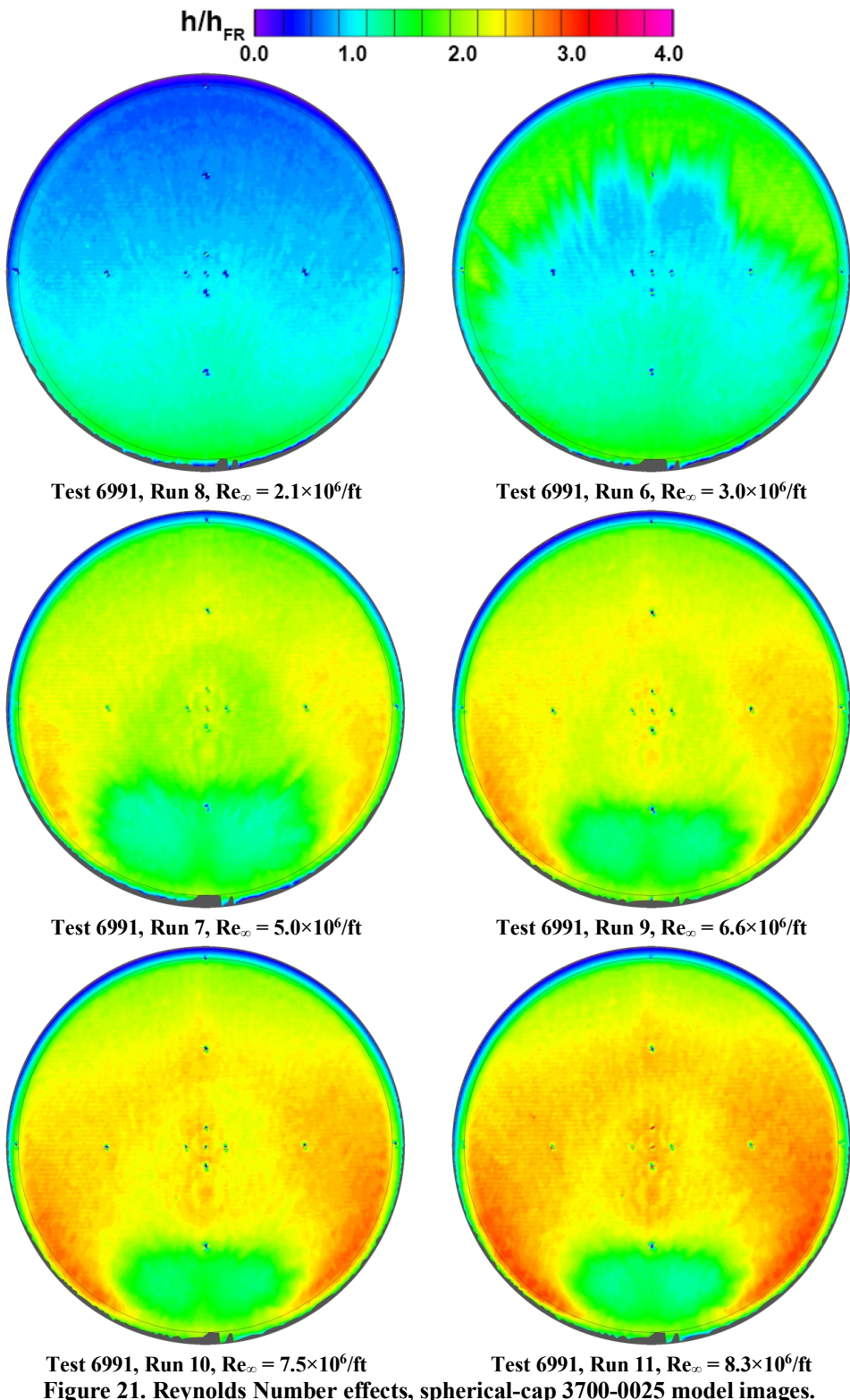


Figure 21. Reynolds Number effects, spherical-cap 3700-0025 model images.

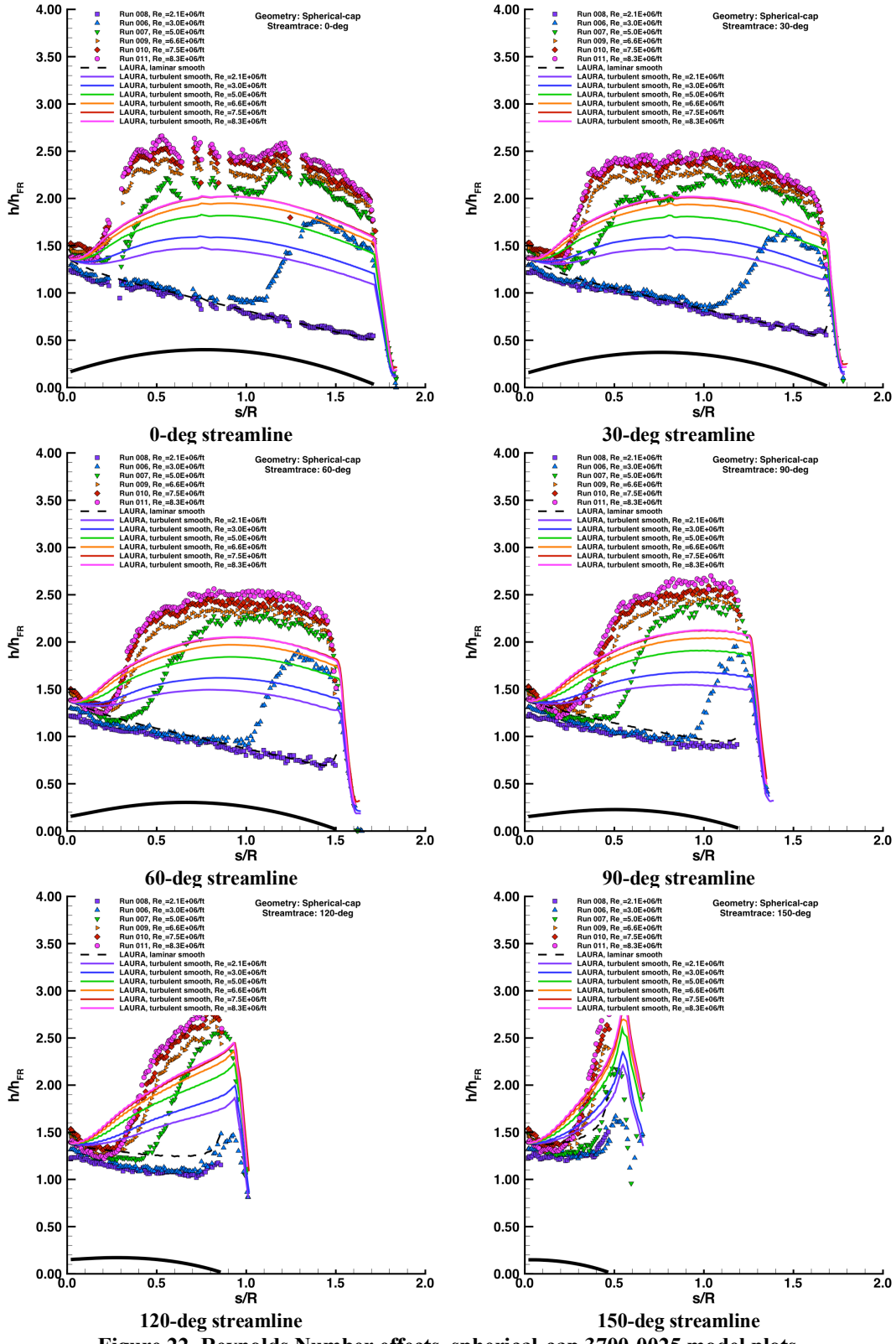


Figure 22. Reynolds Number effects, spherical-cap 3700-0025 model plots.

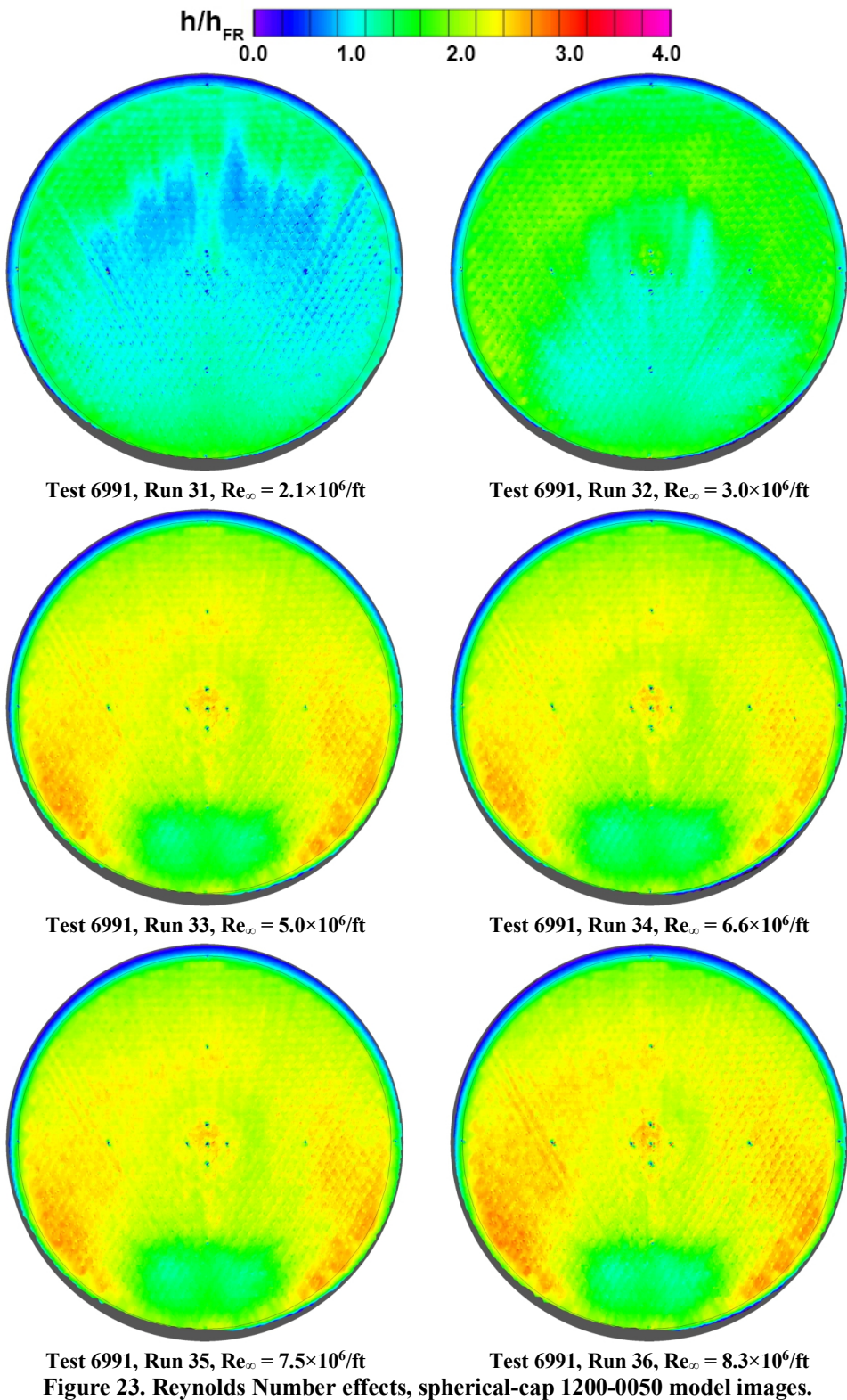


Figure 23. Reynolds Number effects, spherical-cap 1200-0050 model images.

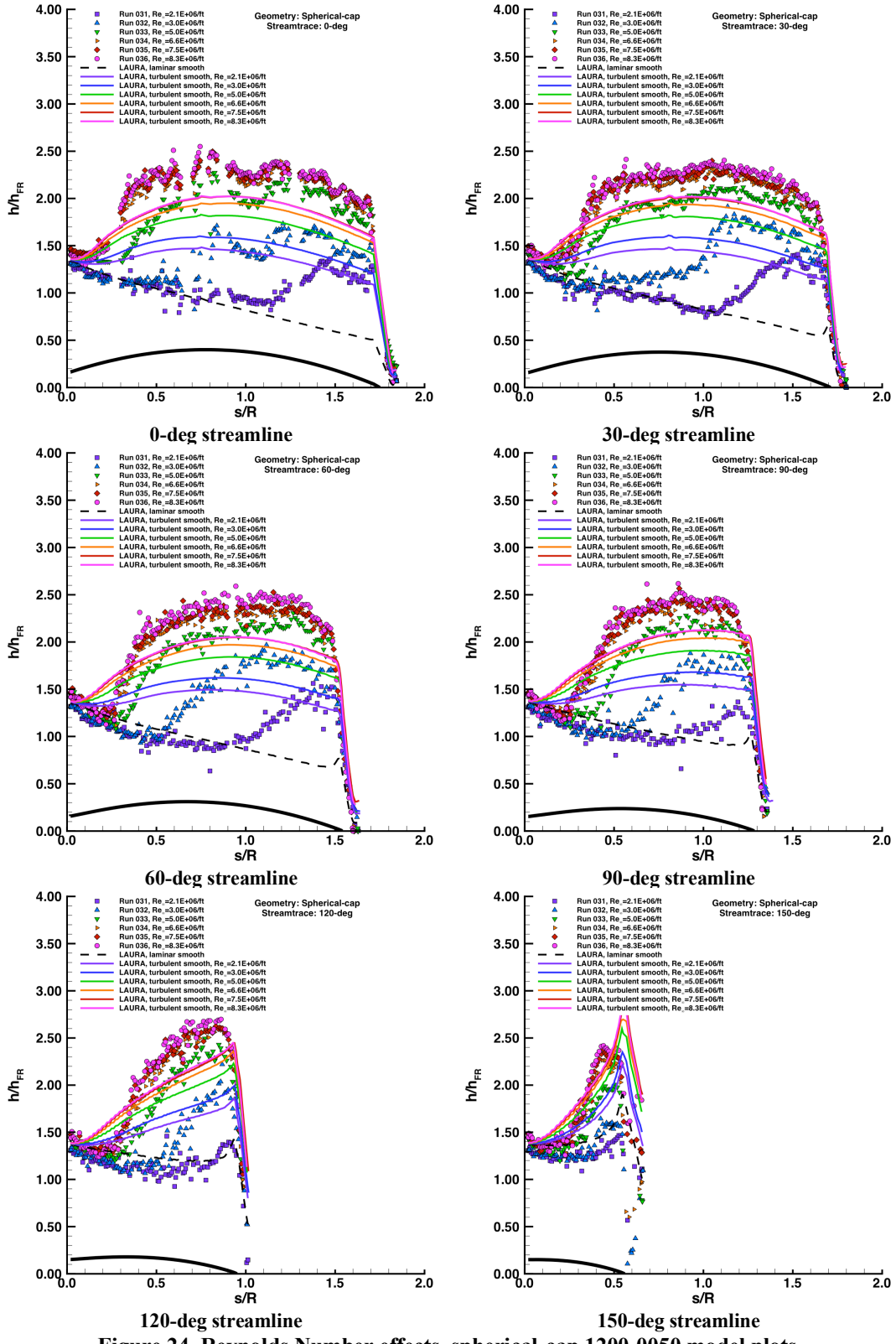


Figure 24. Reynolds Number effects, spherical-cap 1200-0050 model plots.

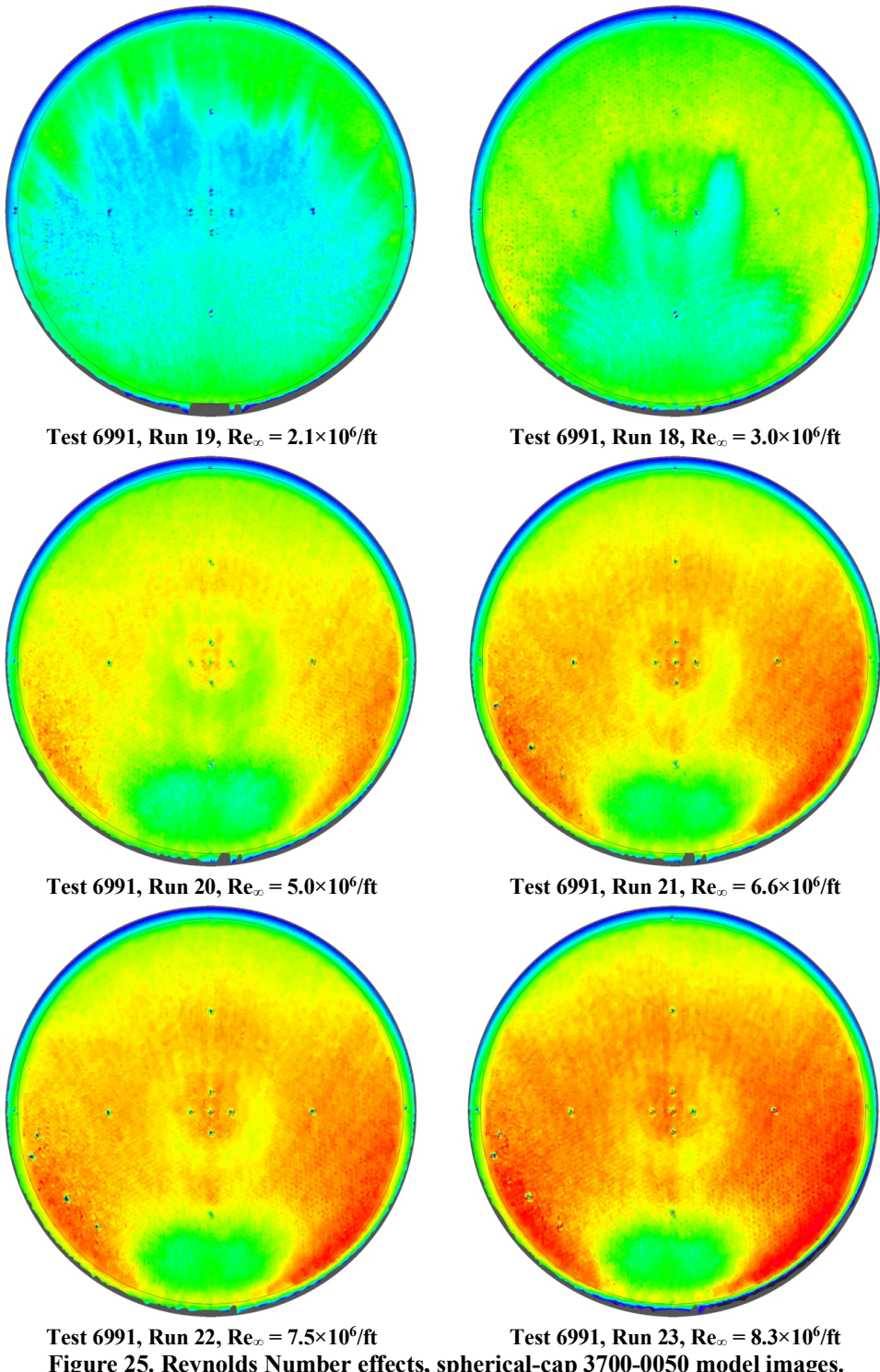
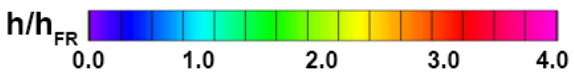


Figure 25. Reynolds Number effects, spherical-cap 3700-0050 model images.

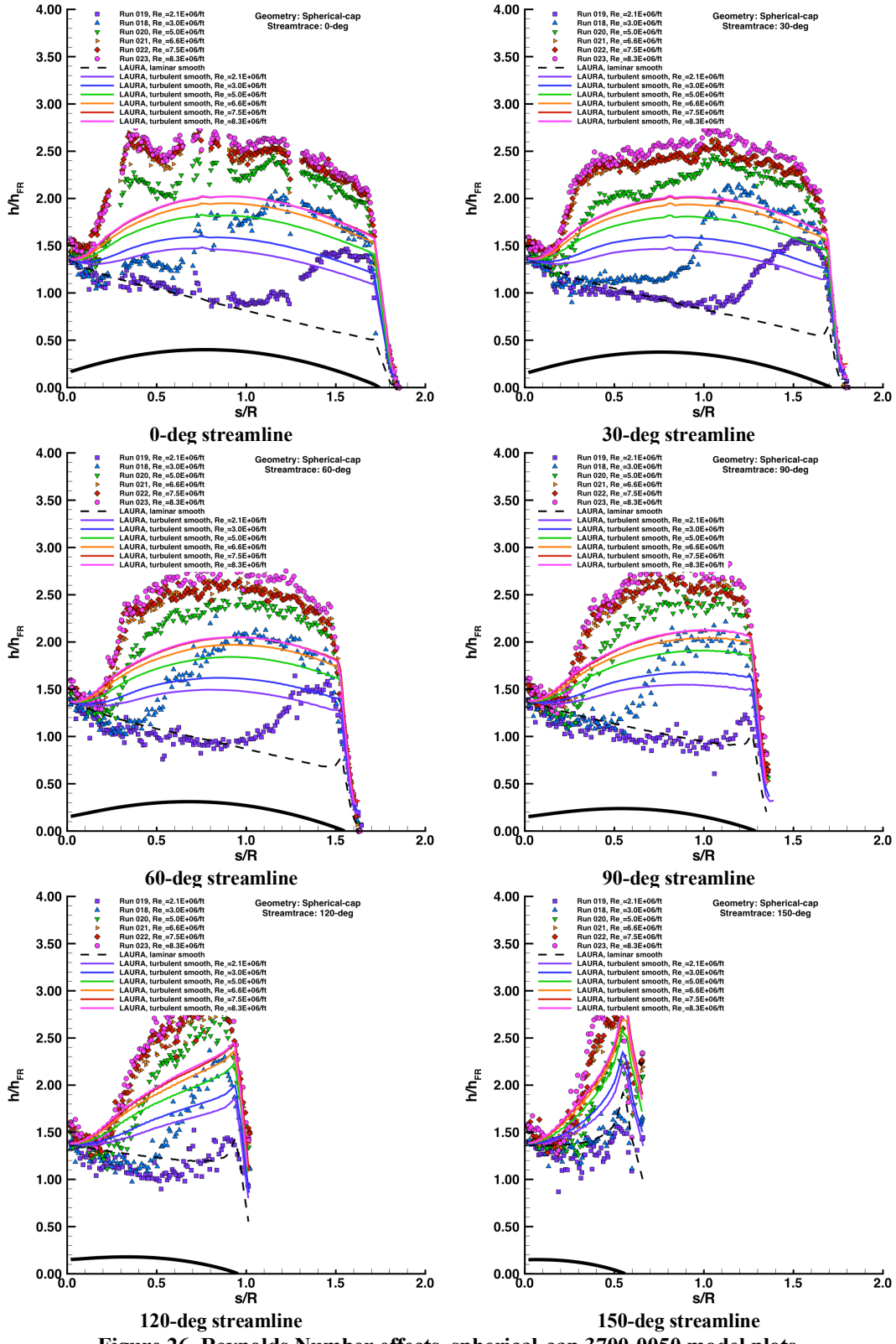


Figure 26. Reynolds Number effects, spherical-cap 3700-0050 model plots.

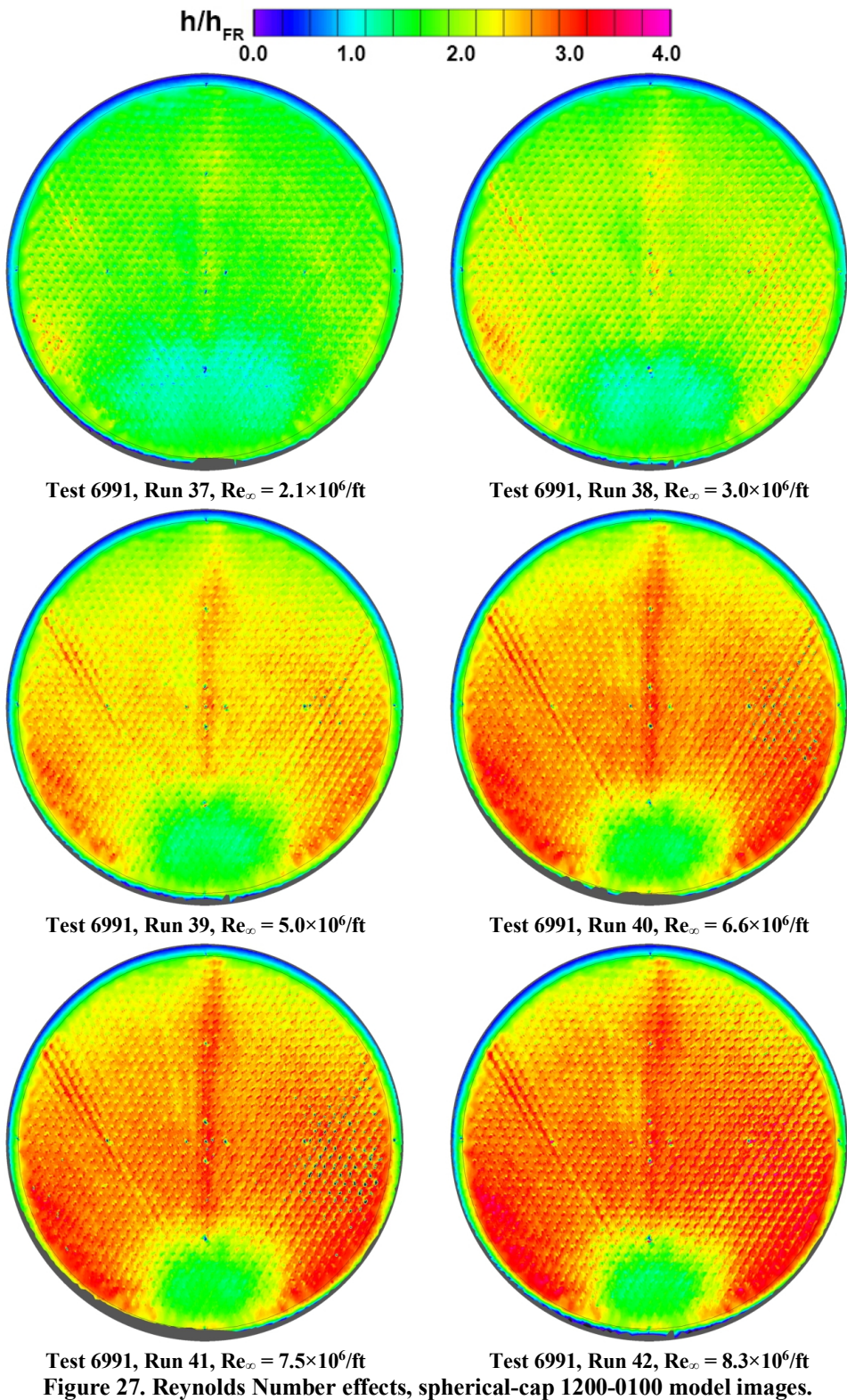


Figure 27. Reynolds Number effects, spherical-cap 1200-0100 model images.

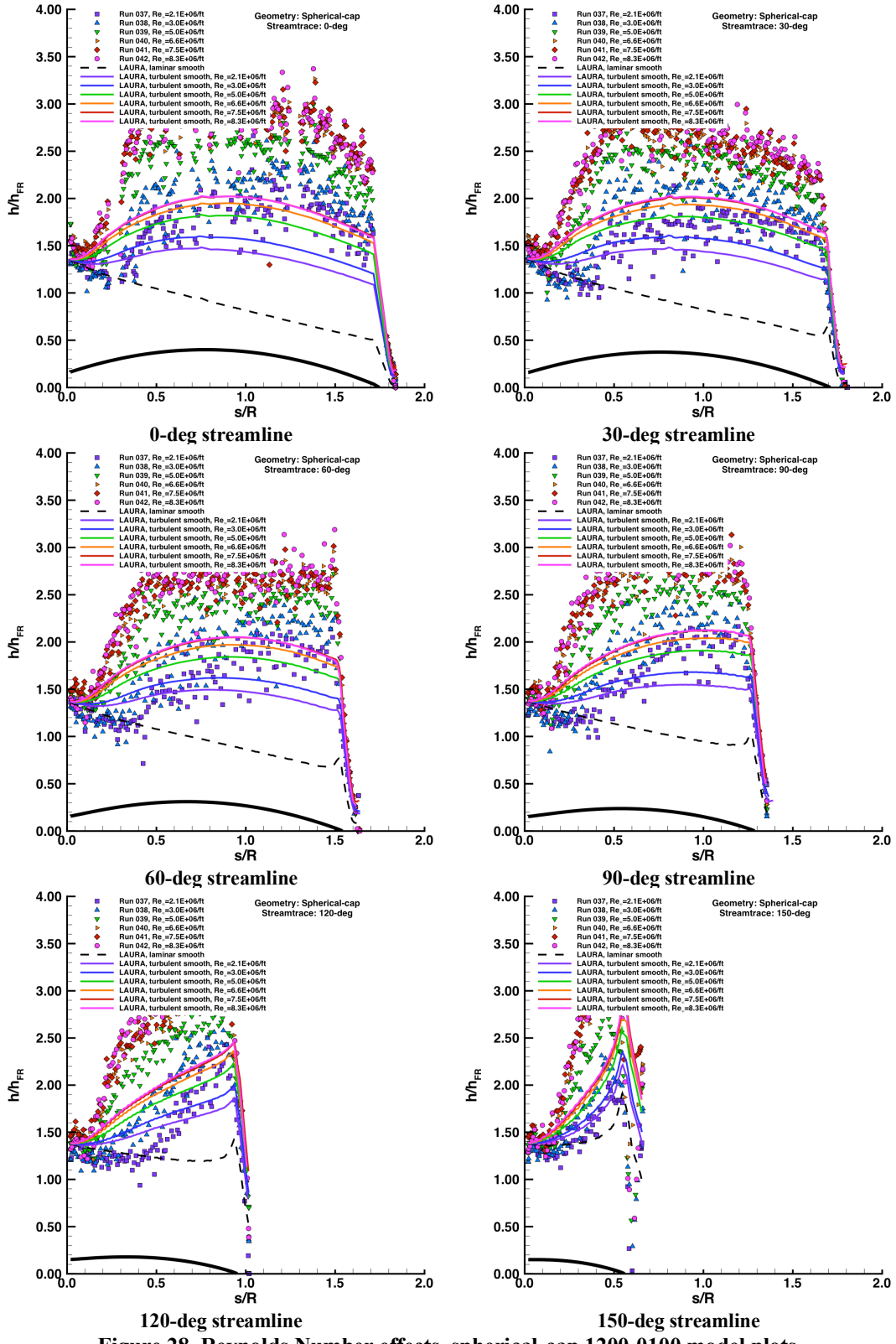


Figure 28. Reynolds Number effects, spherical-cap 1200-0100 model plots.

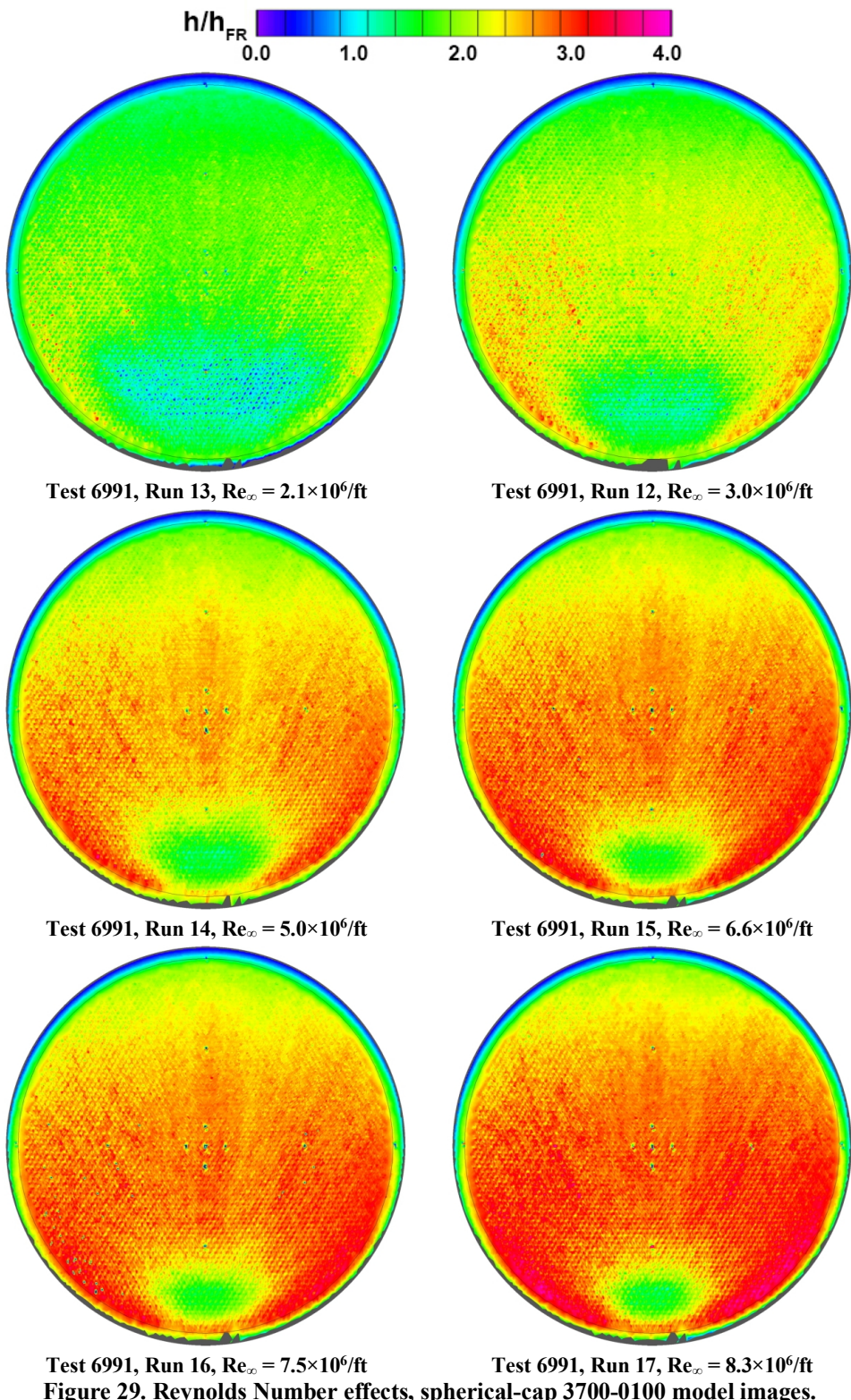


Figure 29. Reynolds Number effects, spherical-cap 3700-0100 model images.

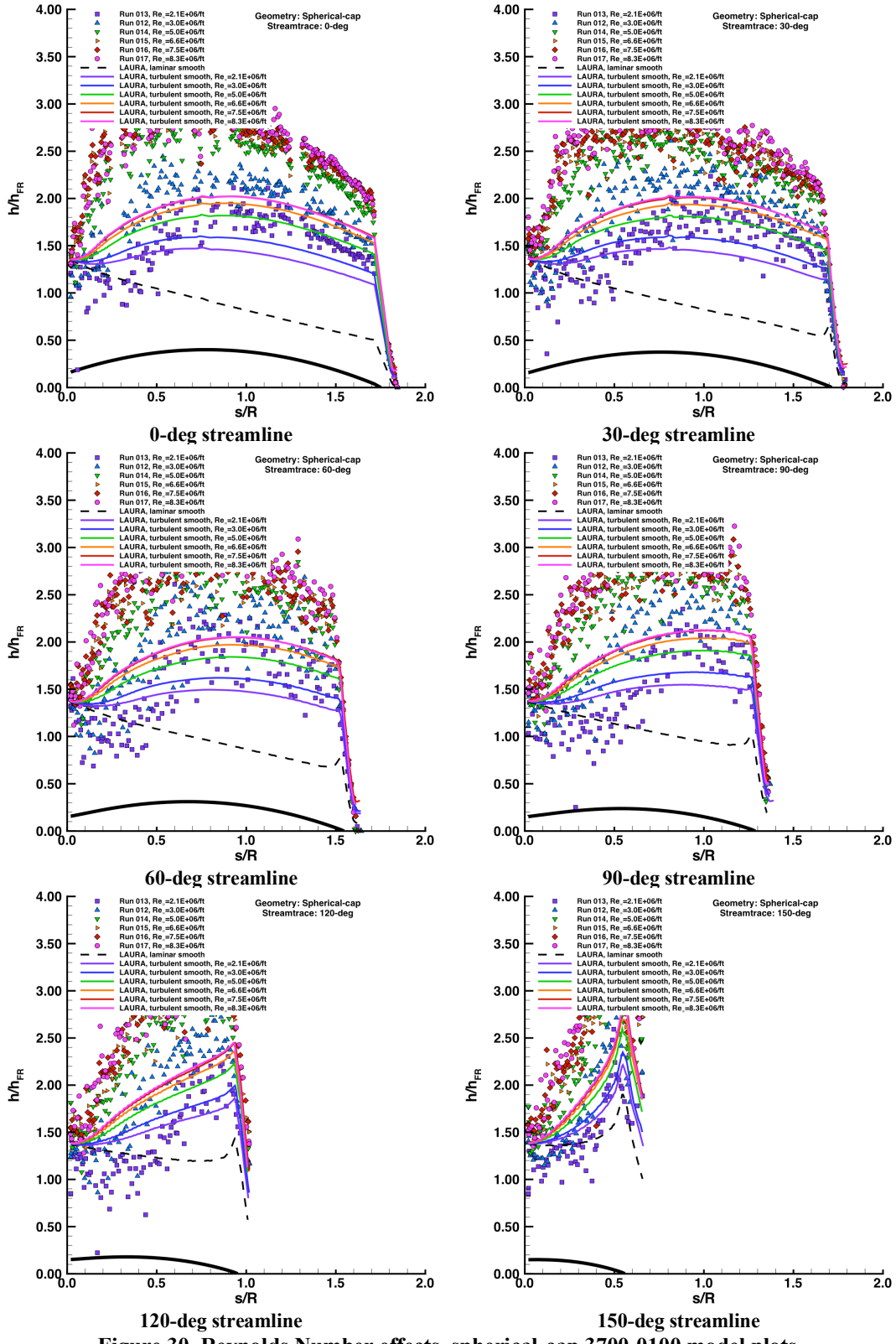


Figure 30. Reynolds Number effects, spherical-cap 3700-0100 model plots.

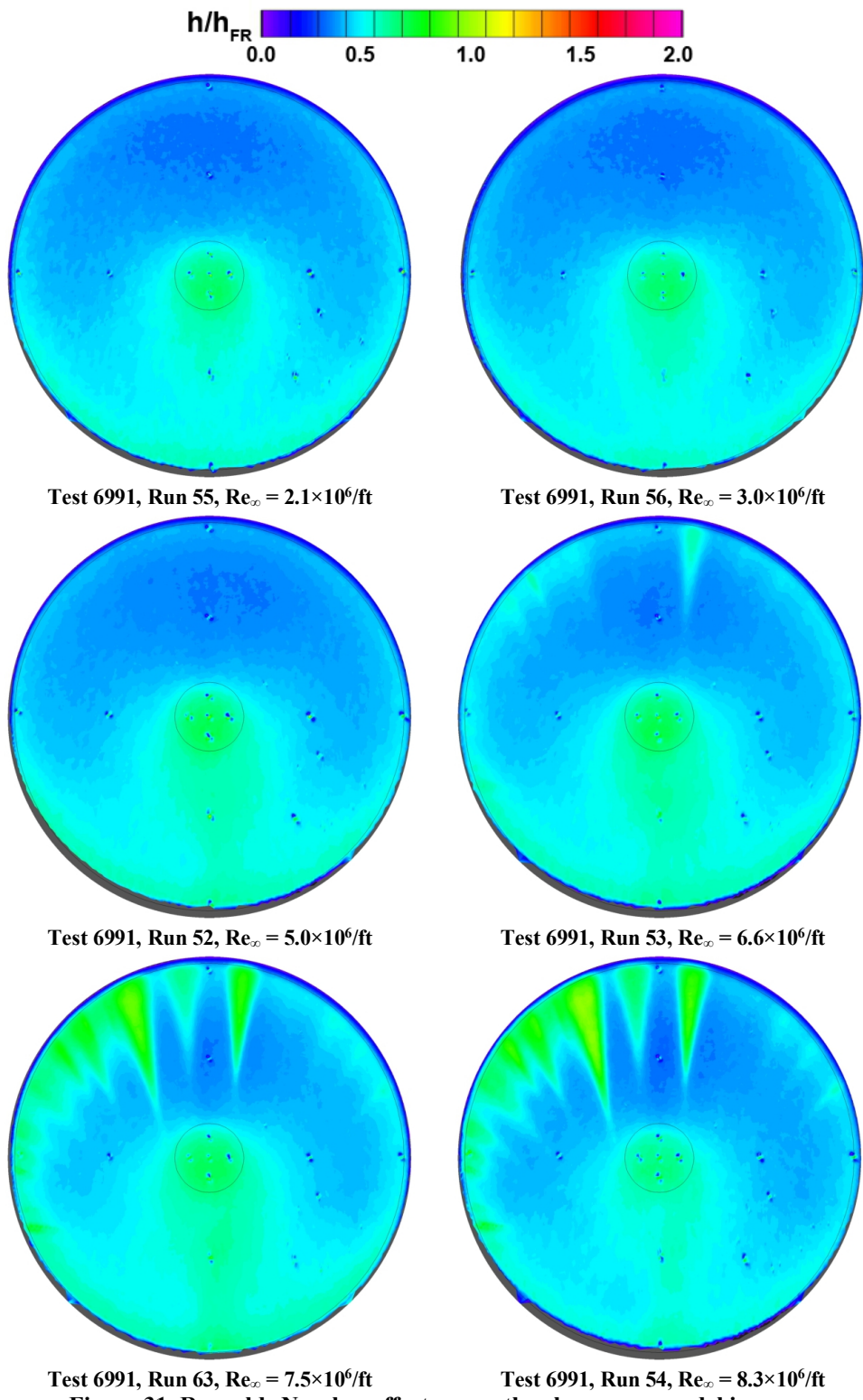


Figure 31. Reynolds Number effects, smooth sphere-cone model images.

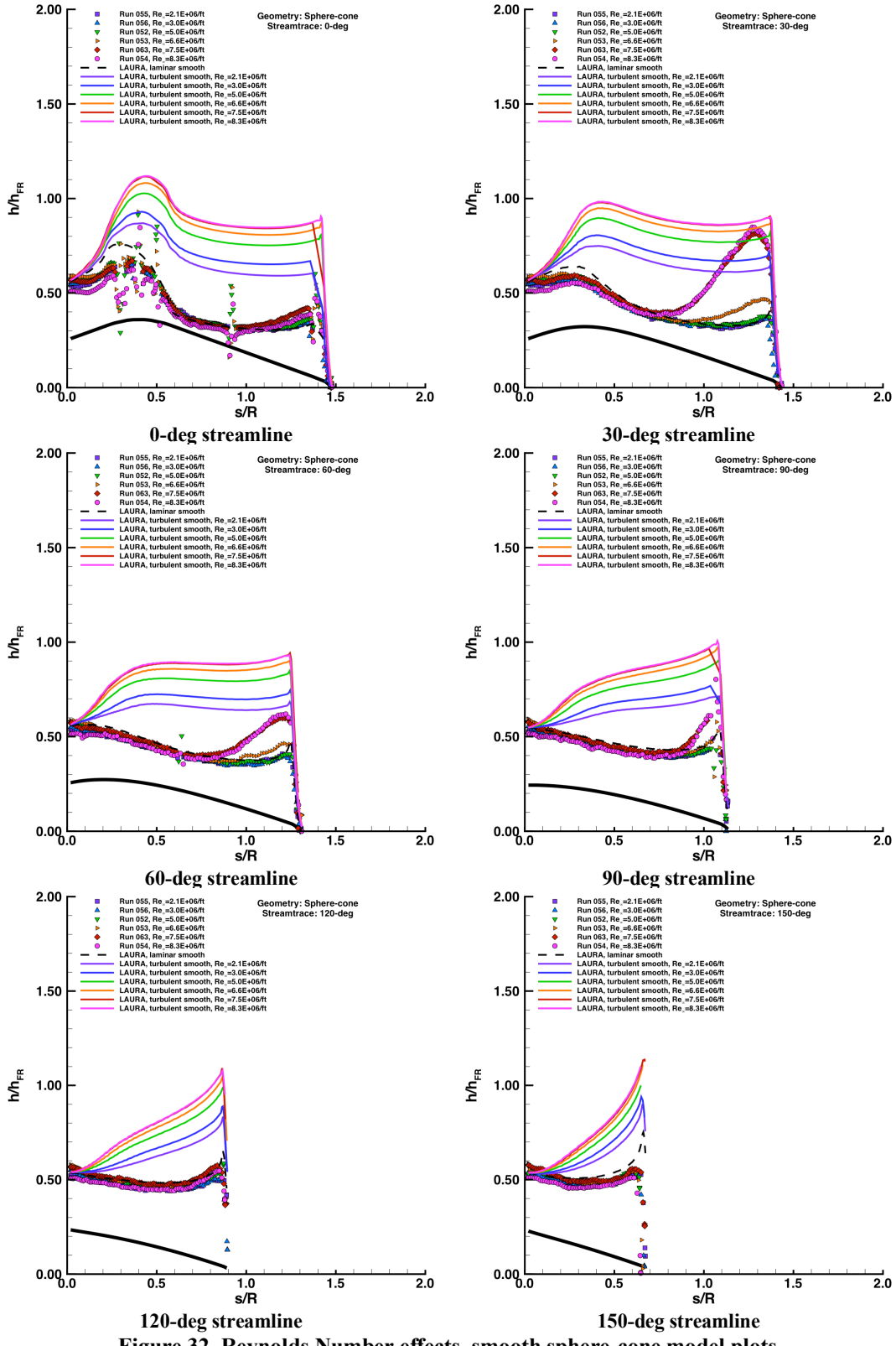


Figure 32. Reynolds Number effects, smooth sphere-cone model plots.

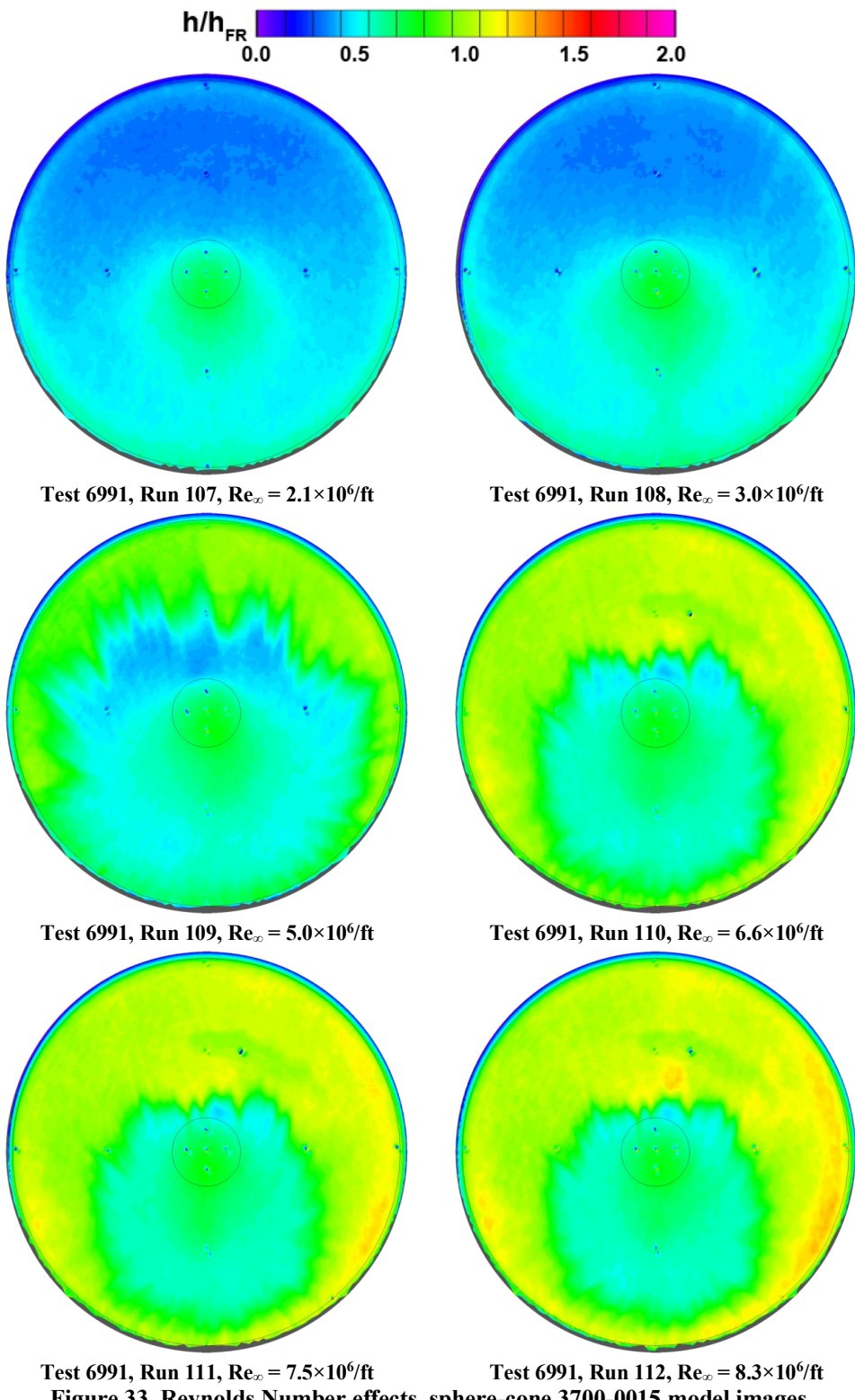


Figure 33. Reynolds Number effects, sphere-cone 3700-0015 model images.

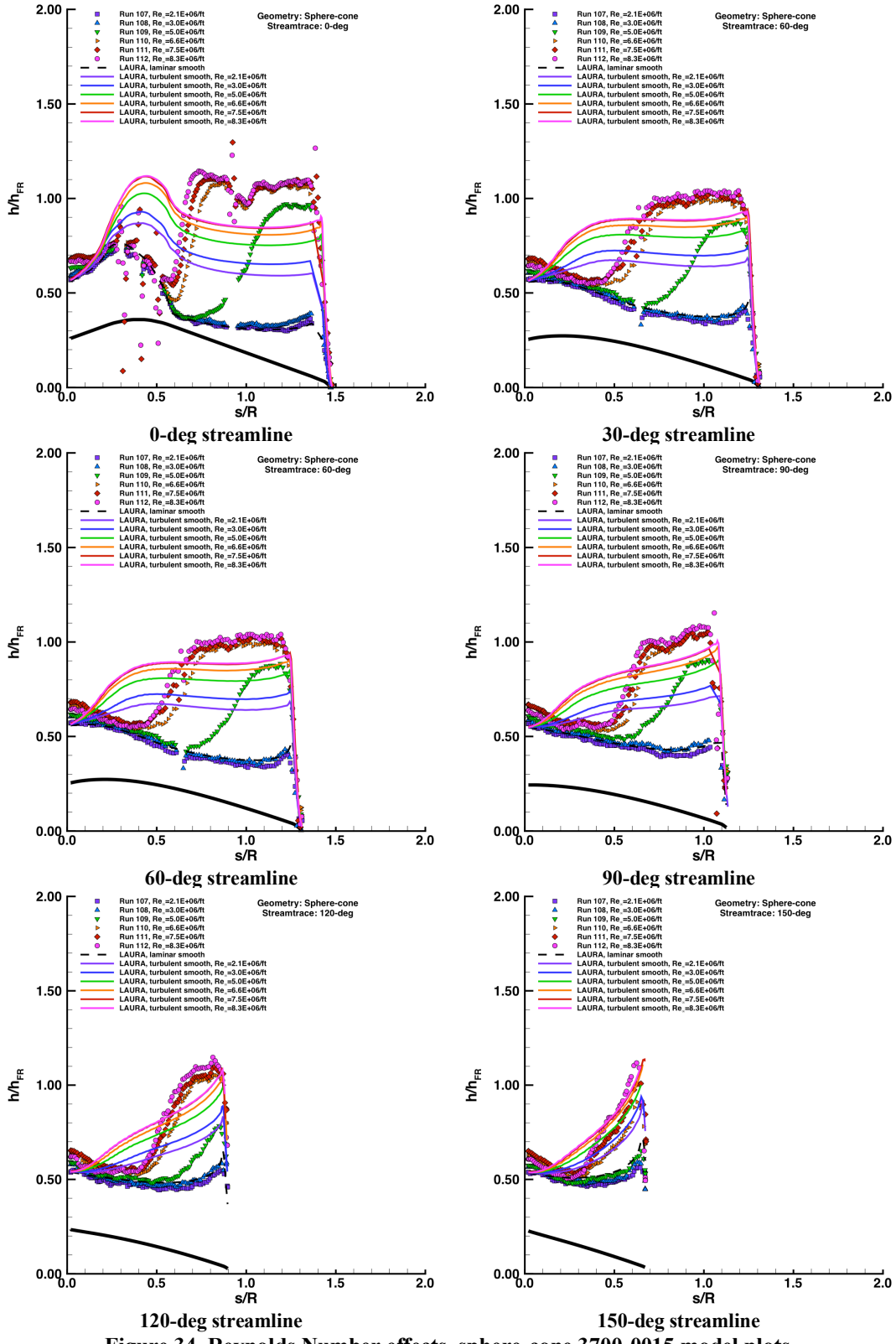


Figure 34. Reynolds Number effects, sphere-cone 3700-0015 model plots.

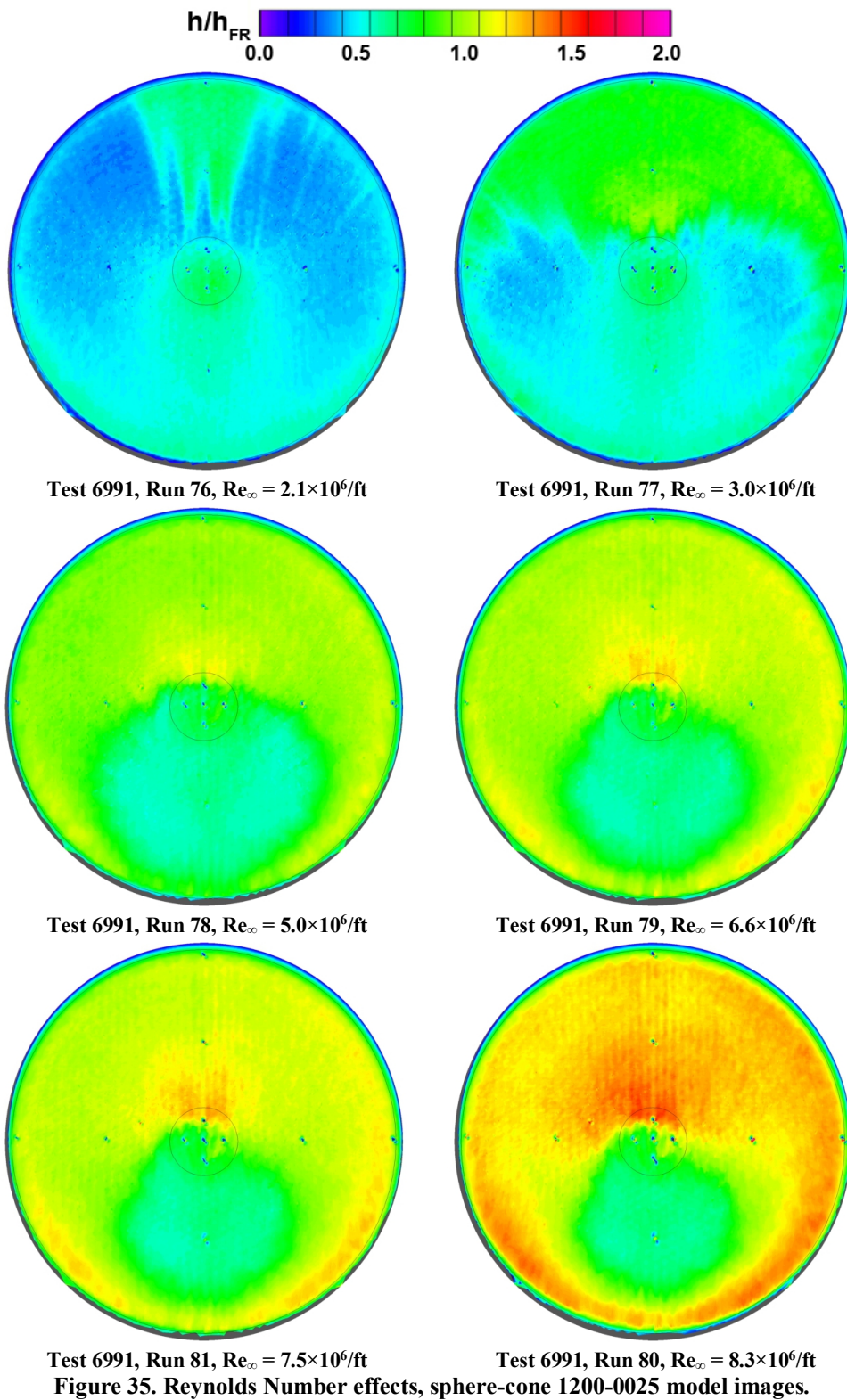


Figure 35. Reynolds Number effects, sphere-cone 1200-0025 model images.

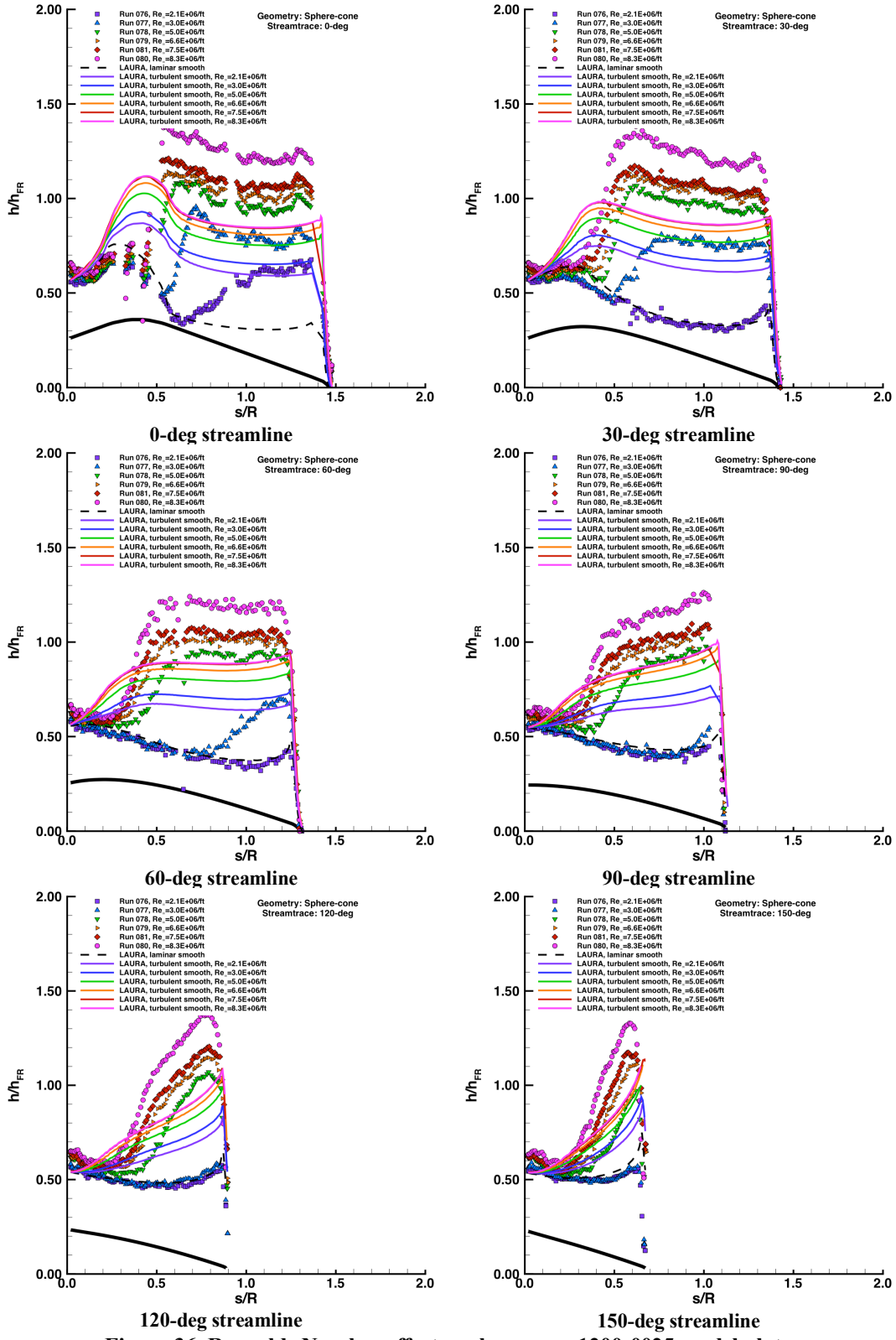


Figure 36. Reynolds Number effects, sphere-cone 1200-0025 model plots.

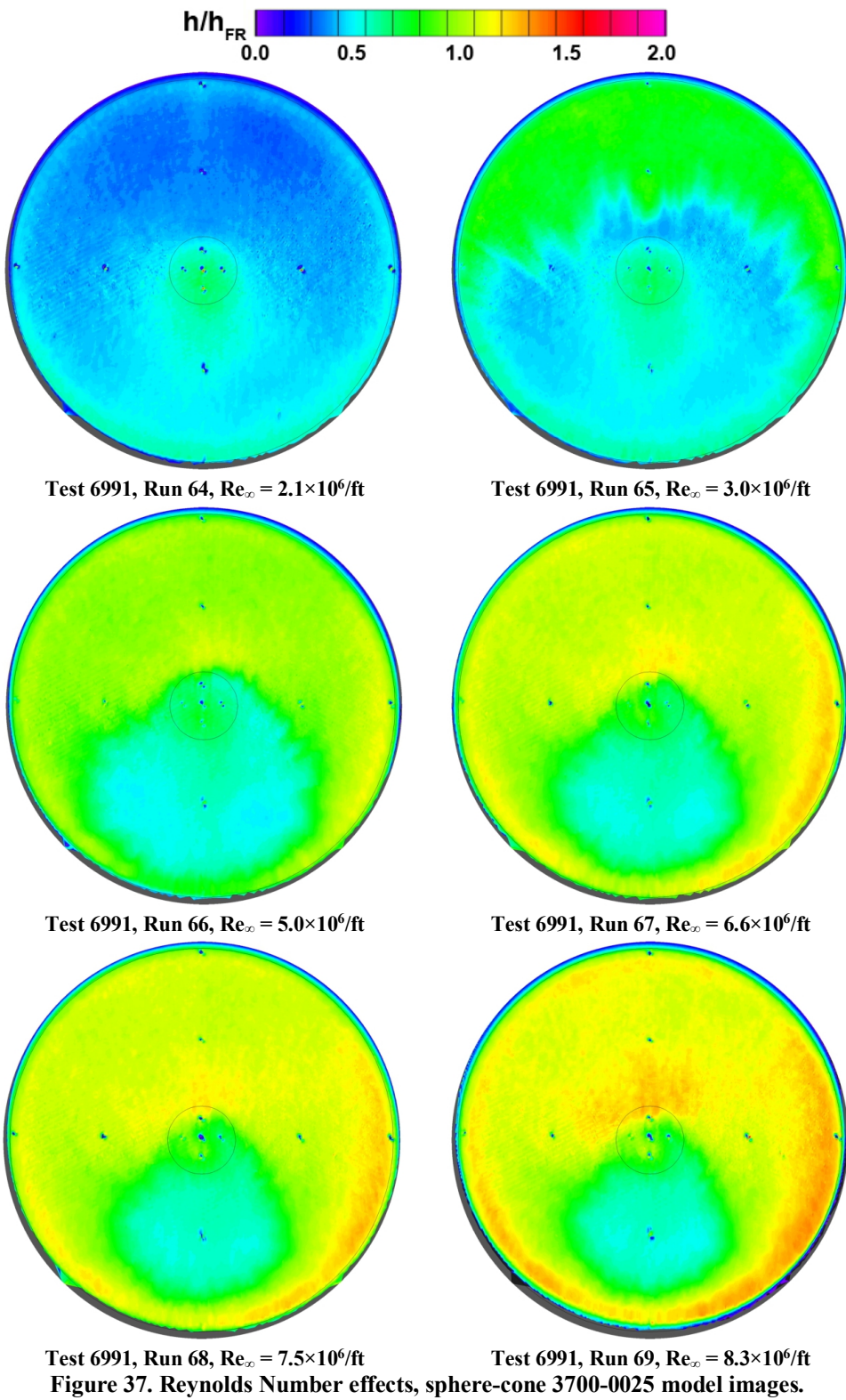


Figure 37. Reynolds Number effects, sphere-cone 3700-0025 model images.

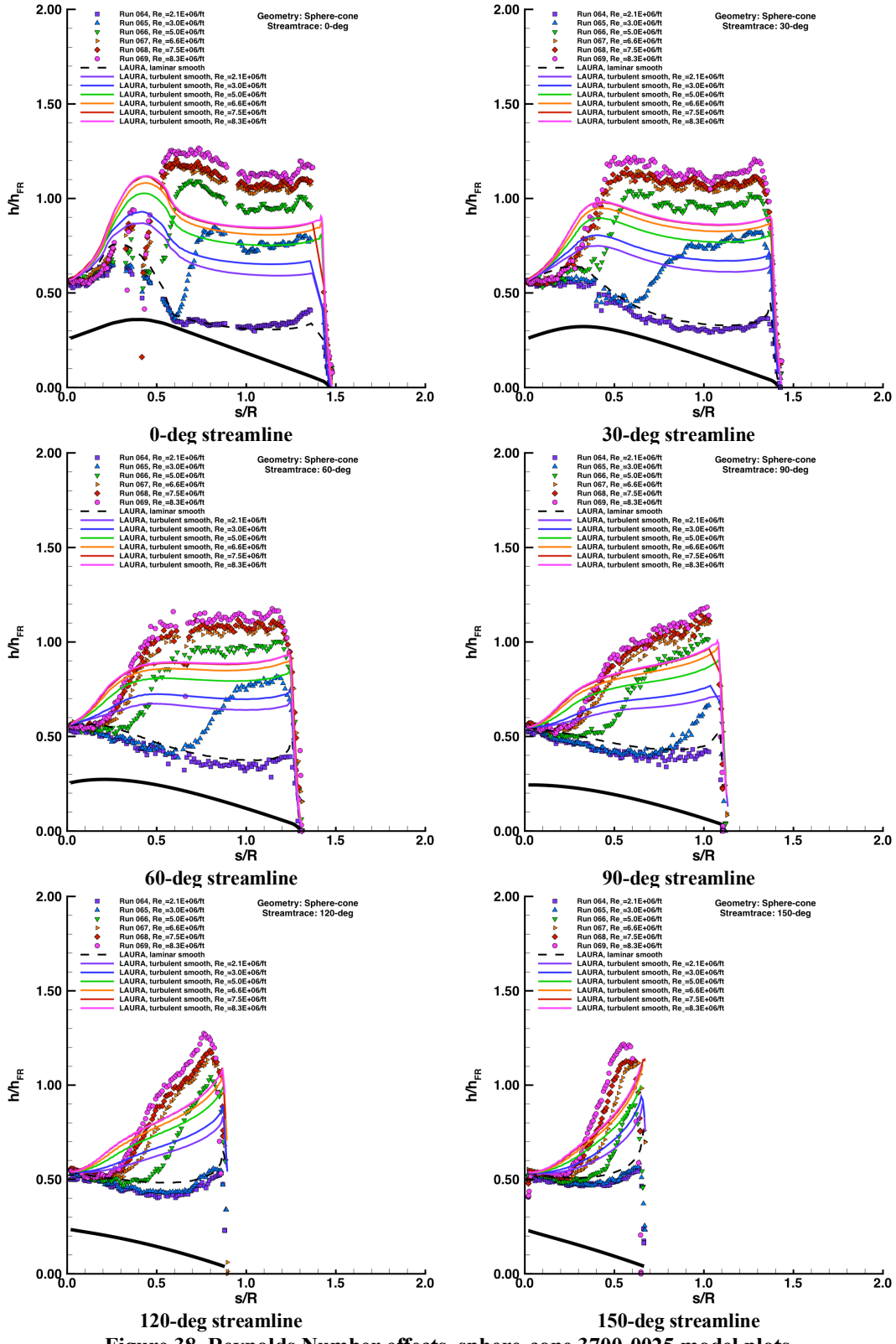


Figure 38. Reynolds Number effects, sphere-cone 3700-0025 model plots.

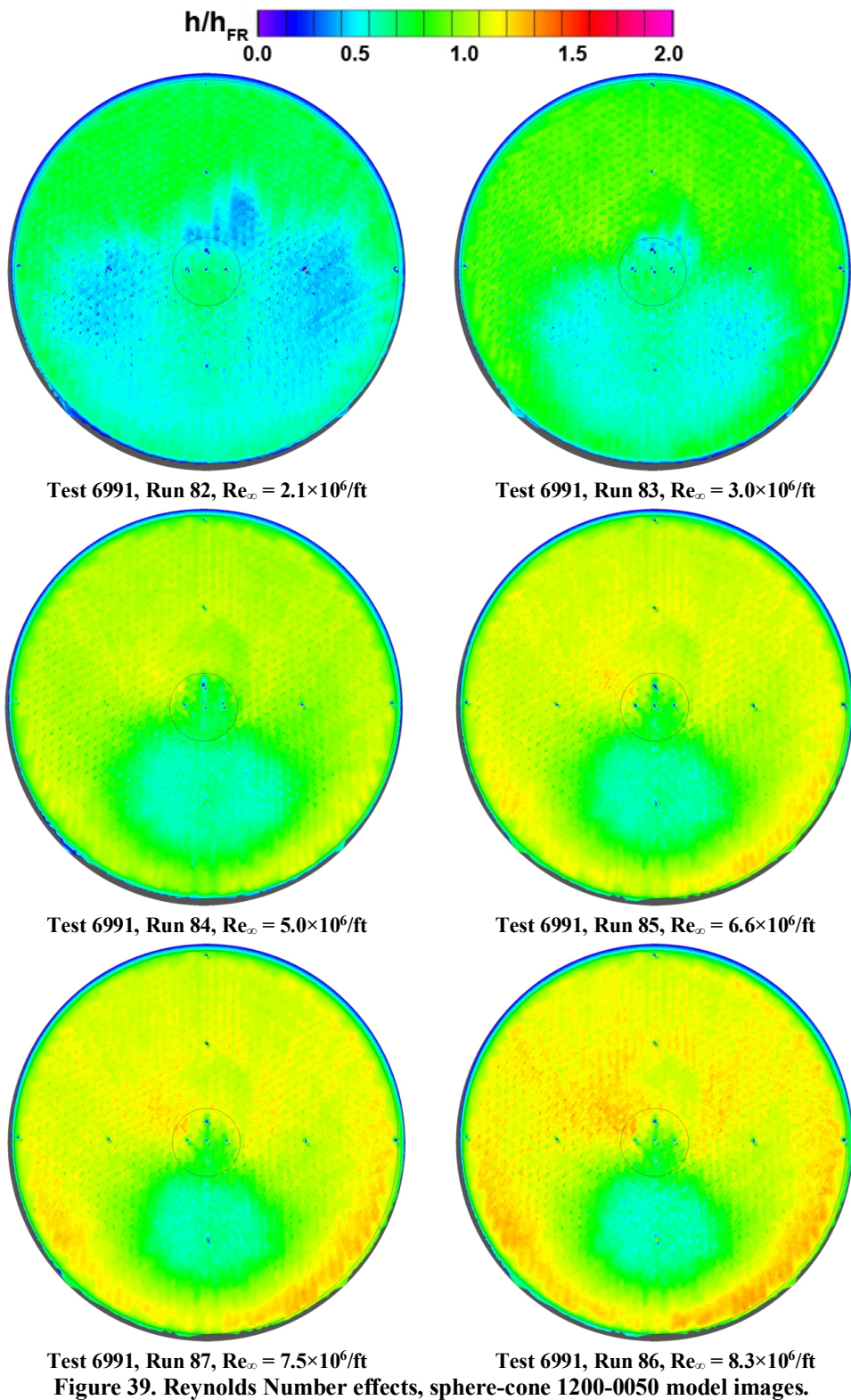


Figure 39. Reynolds Number effects, sphere-cone 1200-0050 model images.

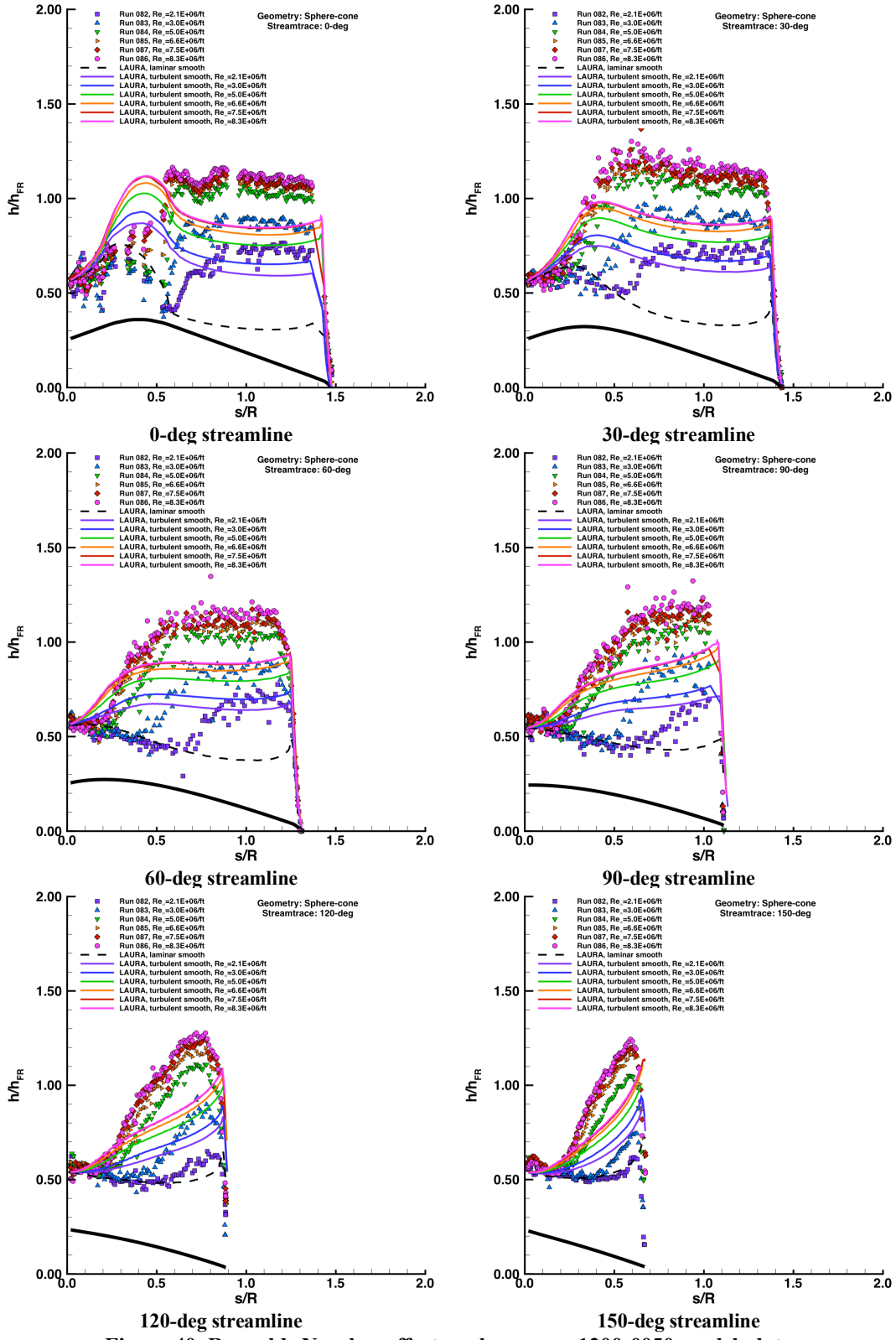


Figure 40. Reynolds Number effects, sphere-cone 1200-0050 model plots.

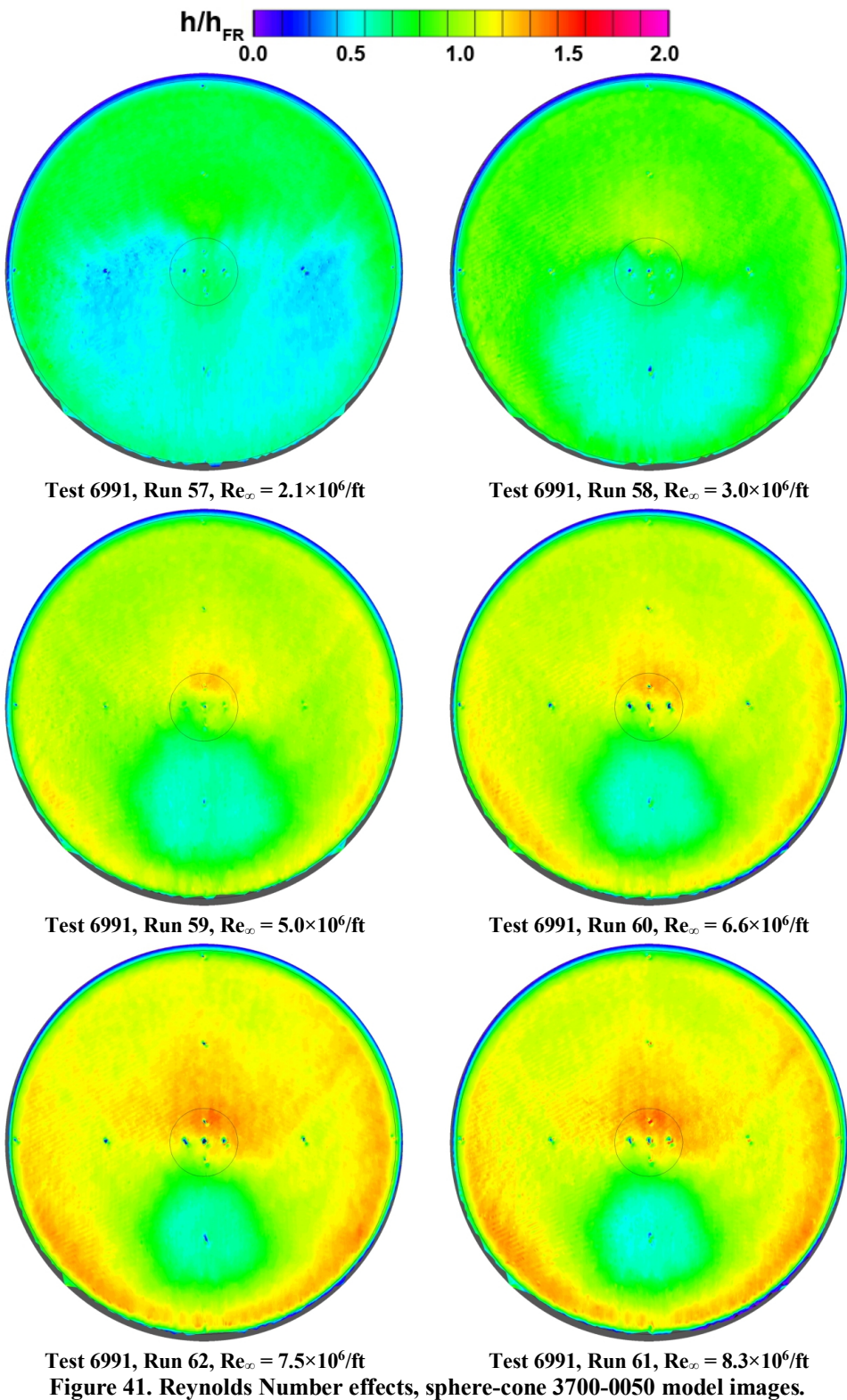


Figure 41. Reynolds Number effects, sphere-cone 3700-0050 model images.

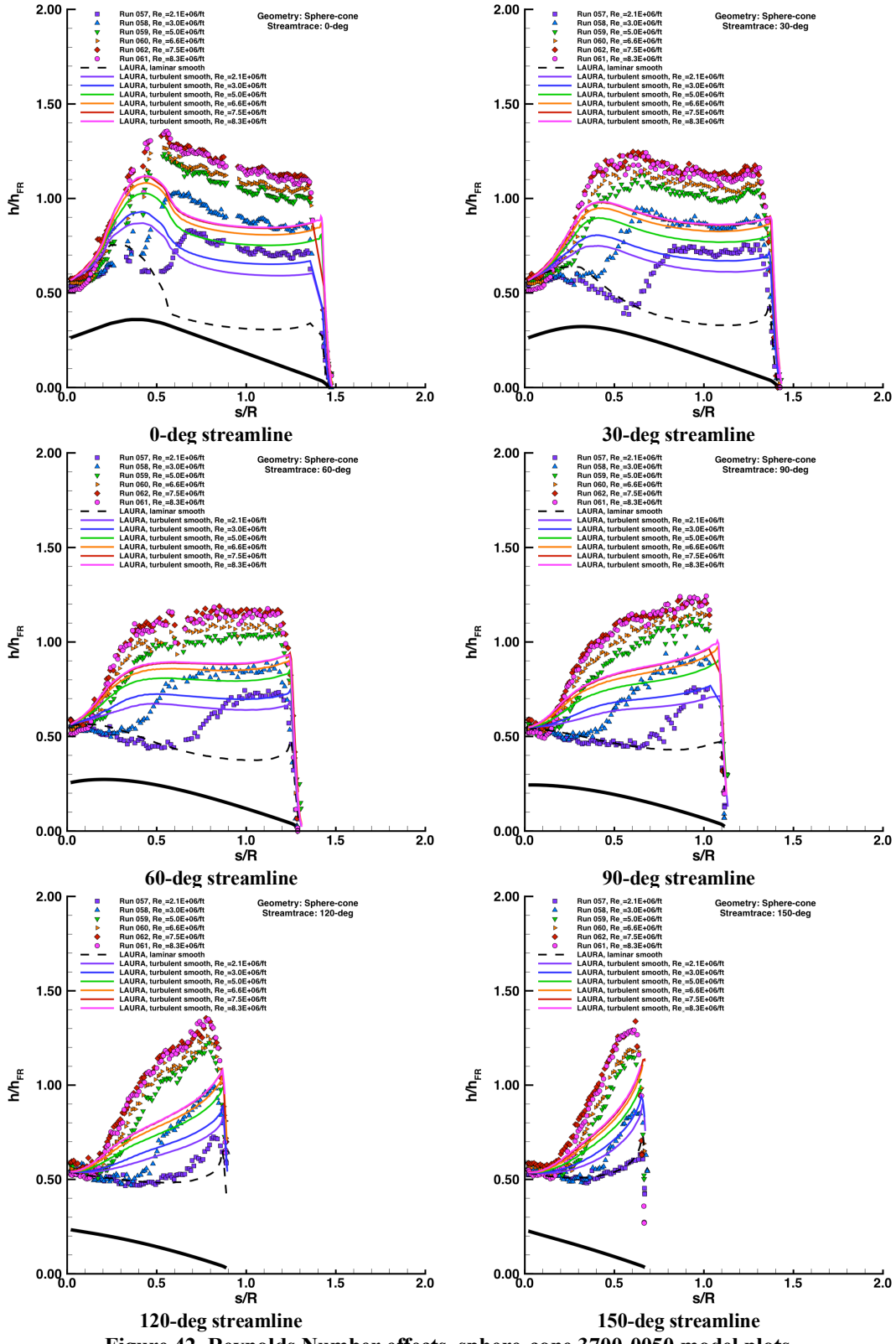


Figure 42. Reynolds Number effects, sphere-cone 3700-0050 model plots.

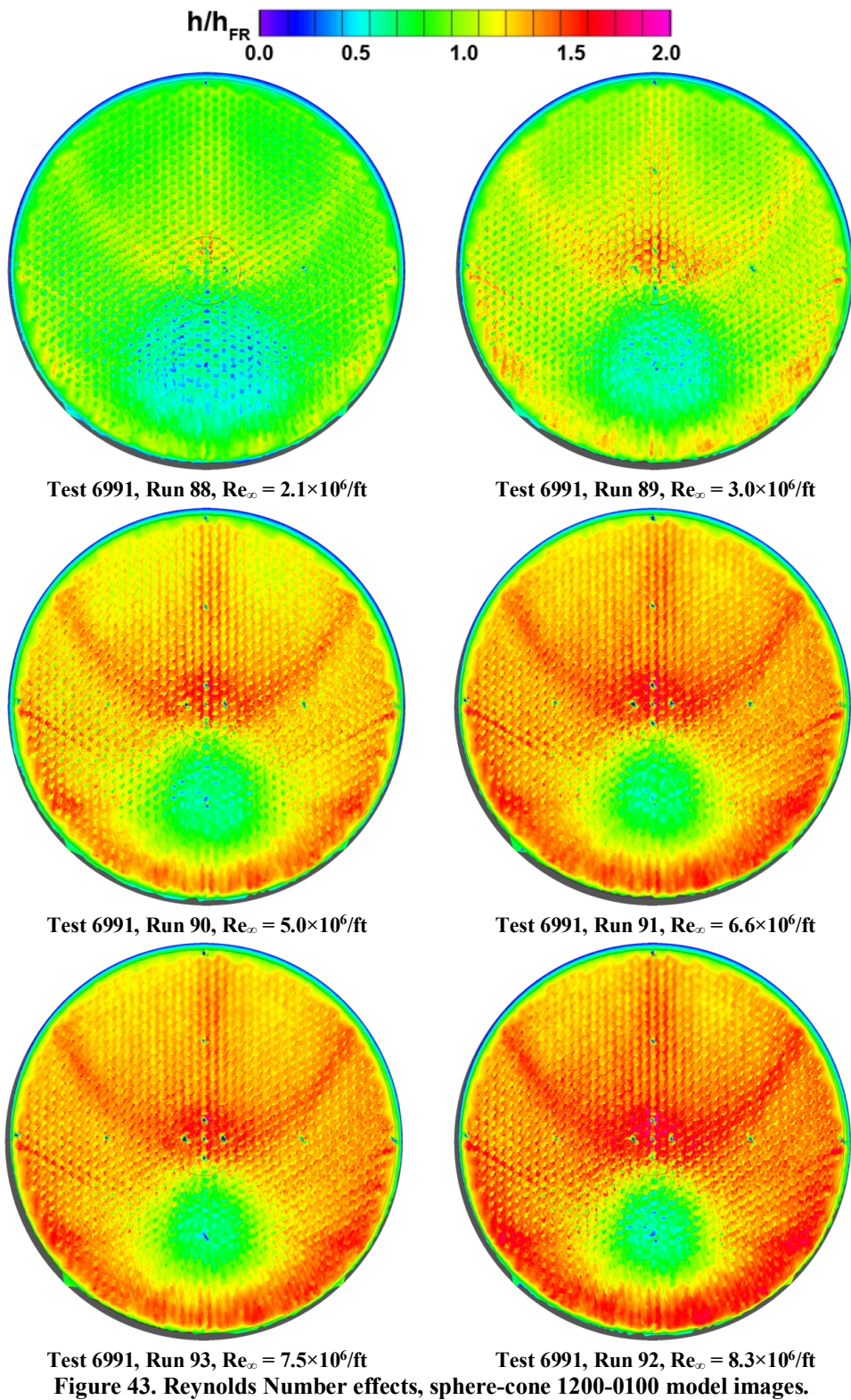


Figure 43. Reynolds Number effects, sphere-cone 1200-0100 model images.

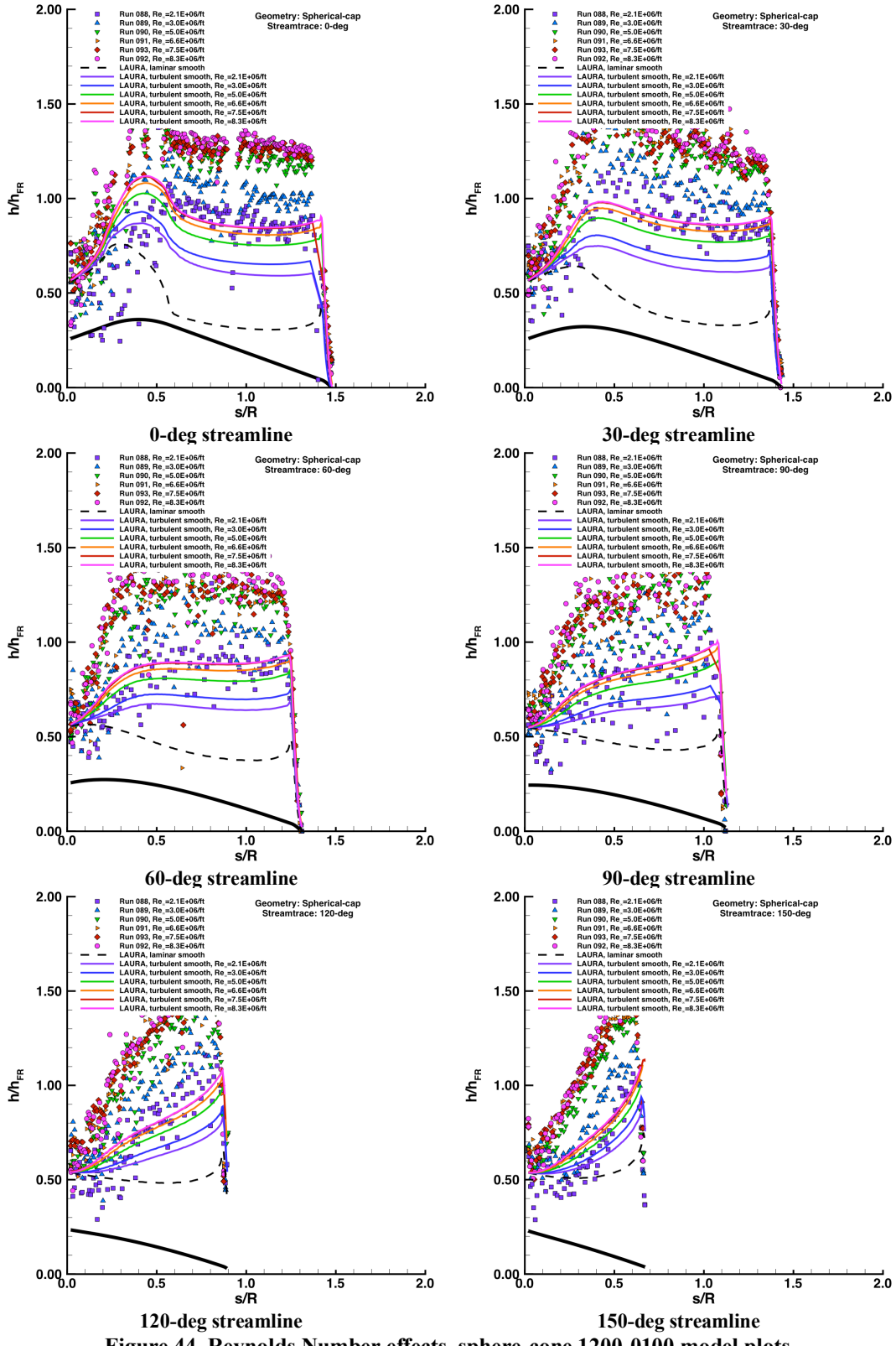


Figure 44. Reynolds Number effects, sphere-cone 1200-0100 model plots.

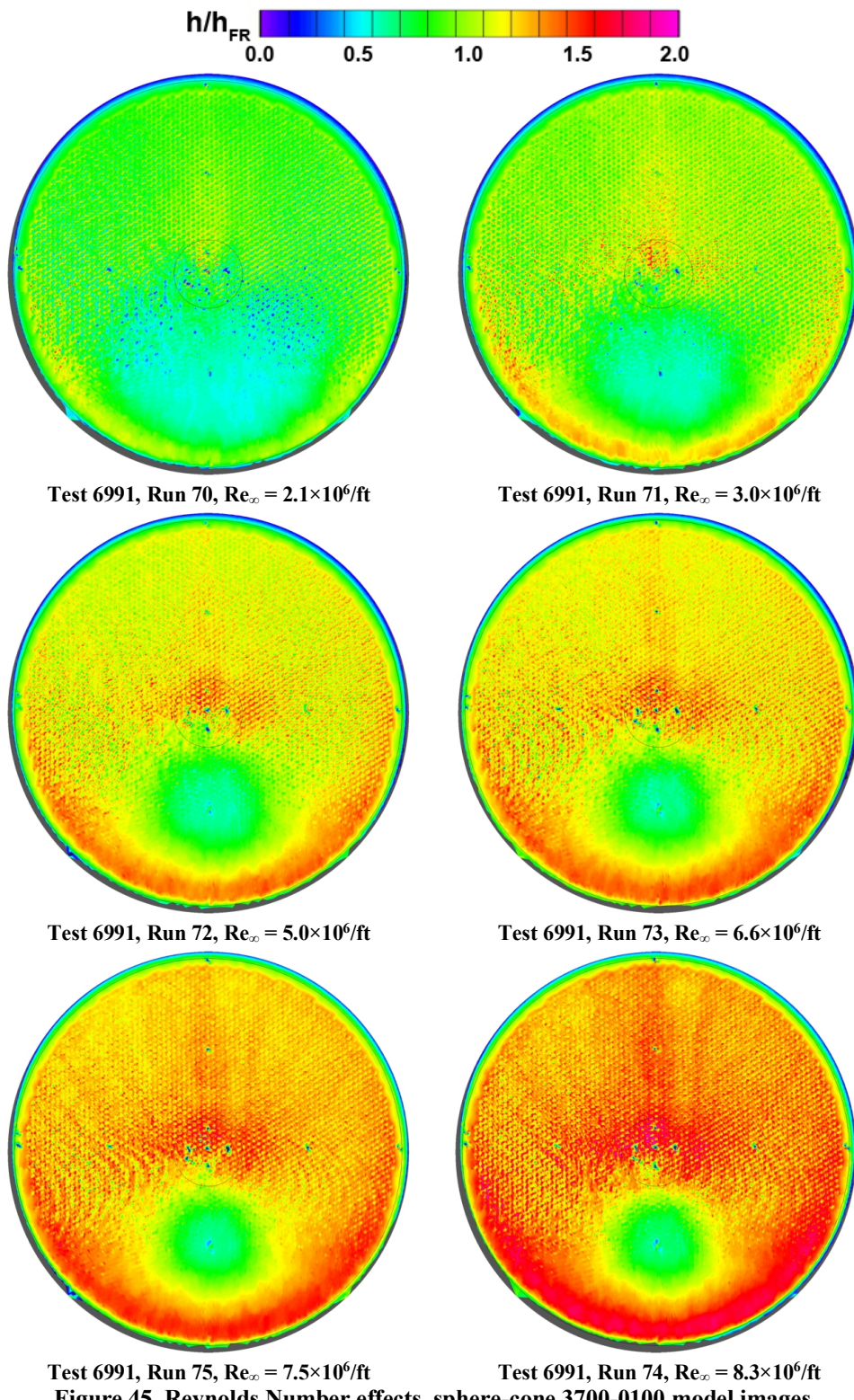


Figure 45. Reynolds Number effects, sphere-cone 3700-0100 model images.

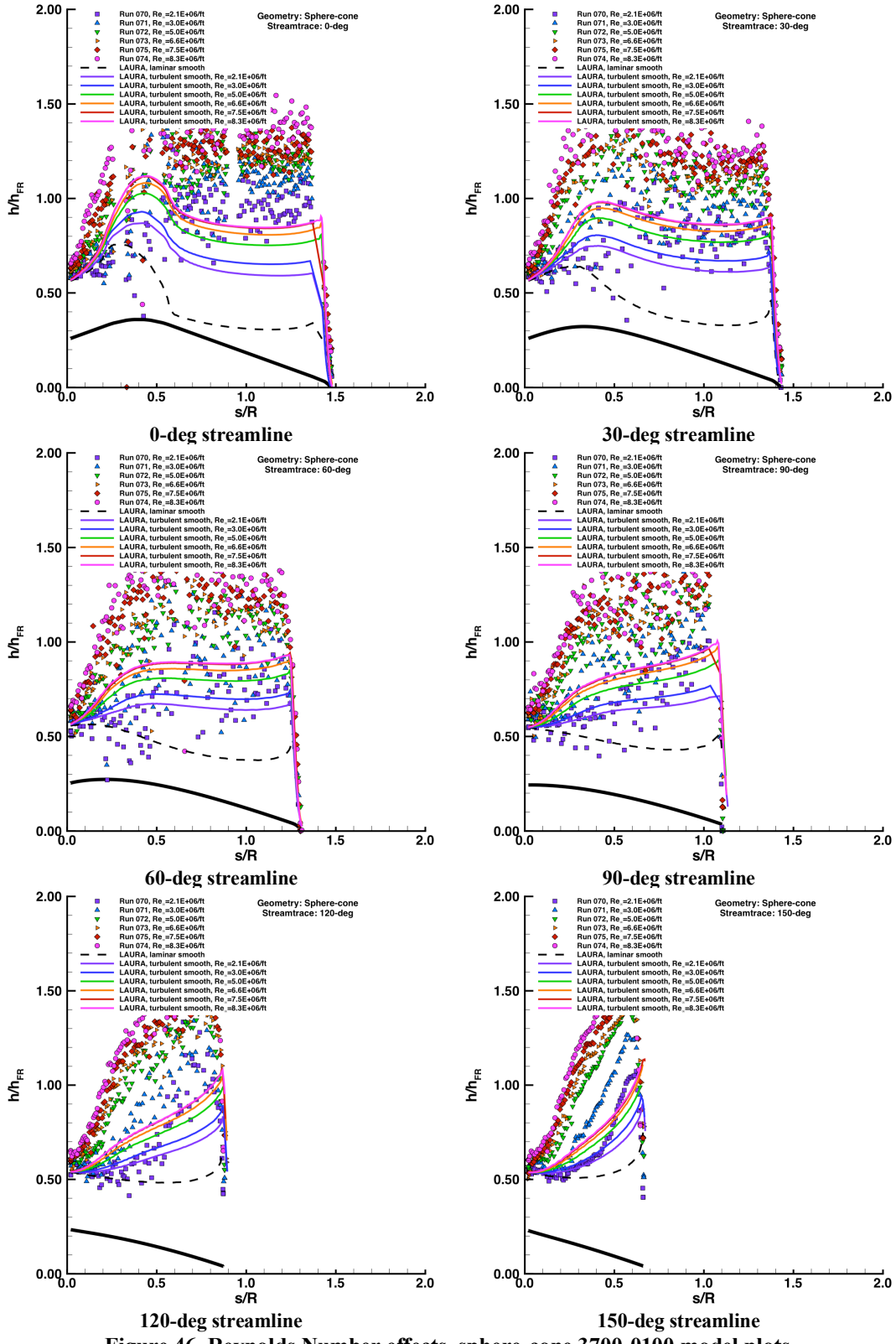


Figure 46. Reynolds Number effects, sphere-cone 3700-0100 model plots.

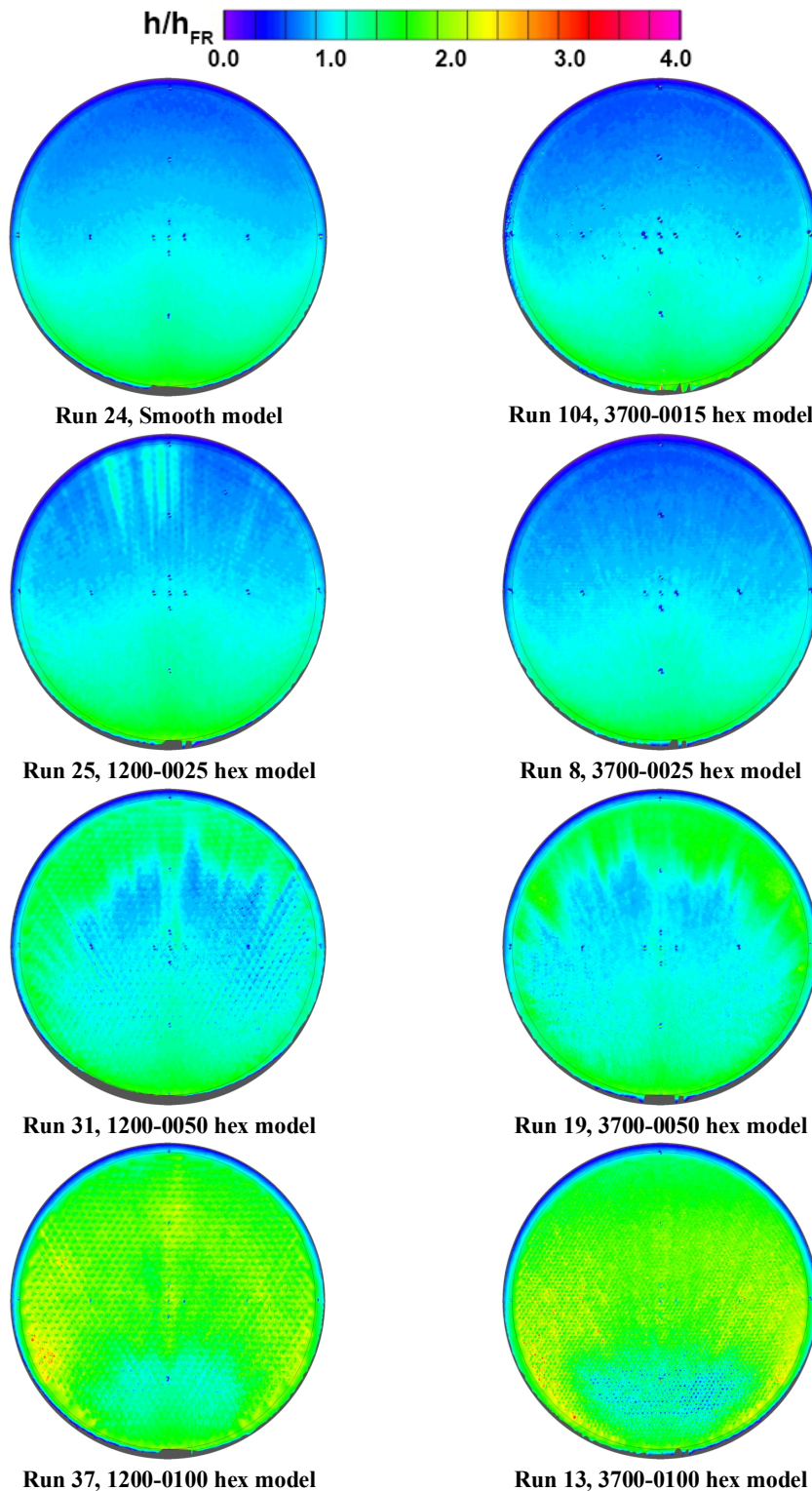


Figure 47. Roughness pattern effects, spherical-cap geometry, $Re_\infty = 2.1 \times 10^6/\text{ft}$ images.

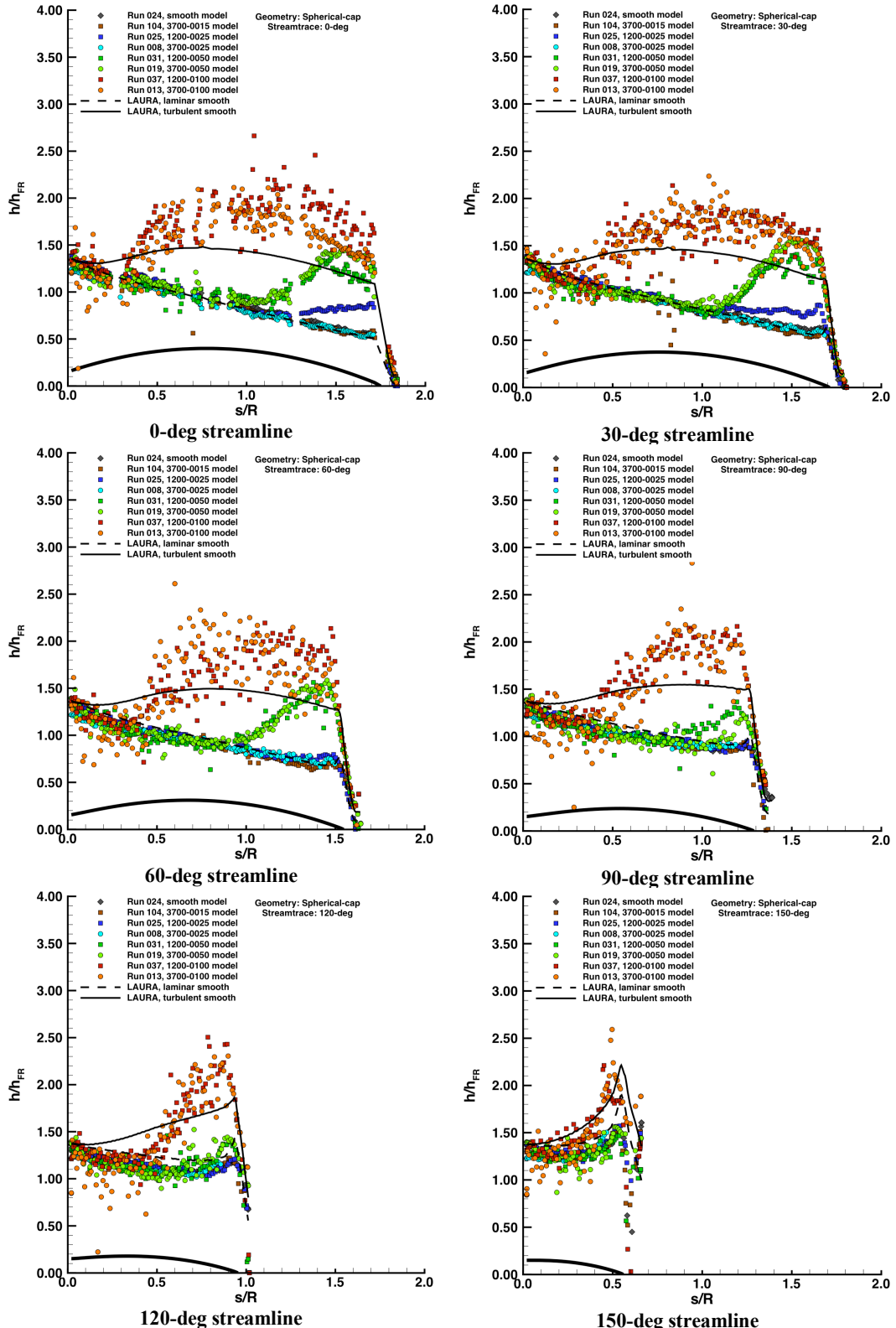


Figure 48. Roughness pattern effects, spherical-cap geometry, $Re_\infty = 2.1 \times 10^6/\text{ft}$ plots.

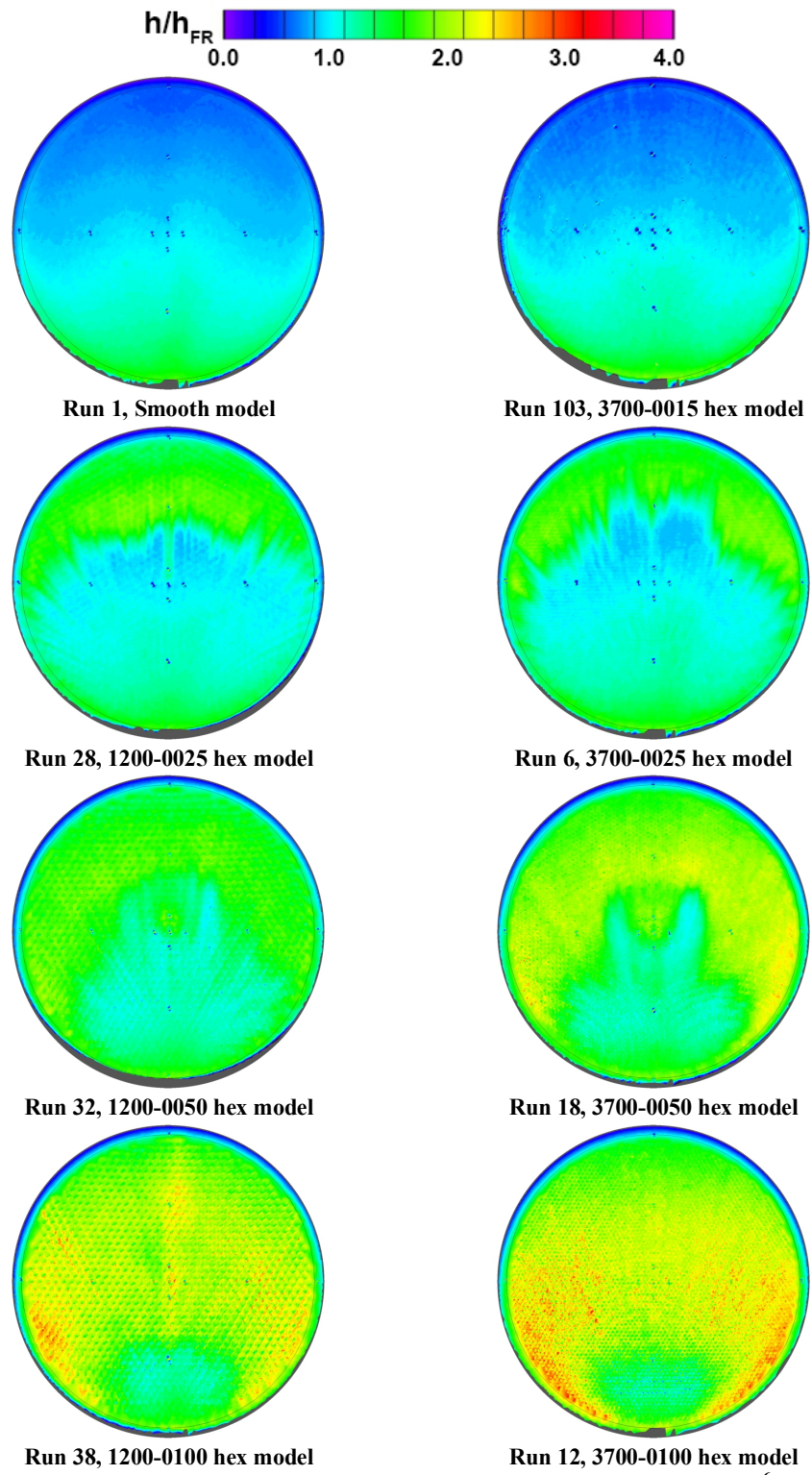


Figure 49. Roughness pattern effects, spherical-cap geometry, $Re_\infty = 3.0 \times 10^6/\text{ft}$ images.

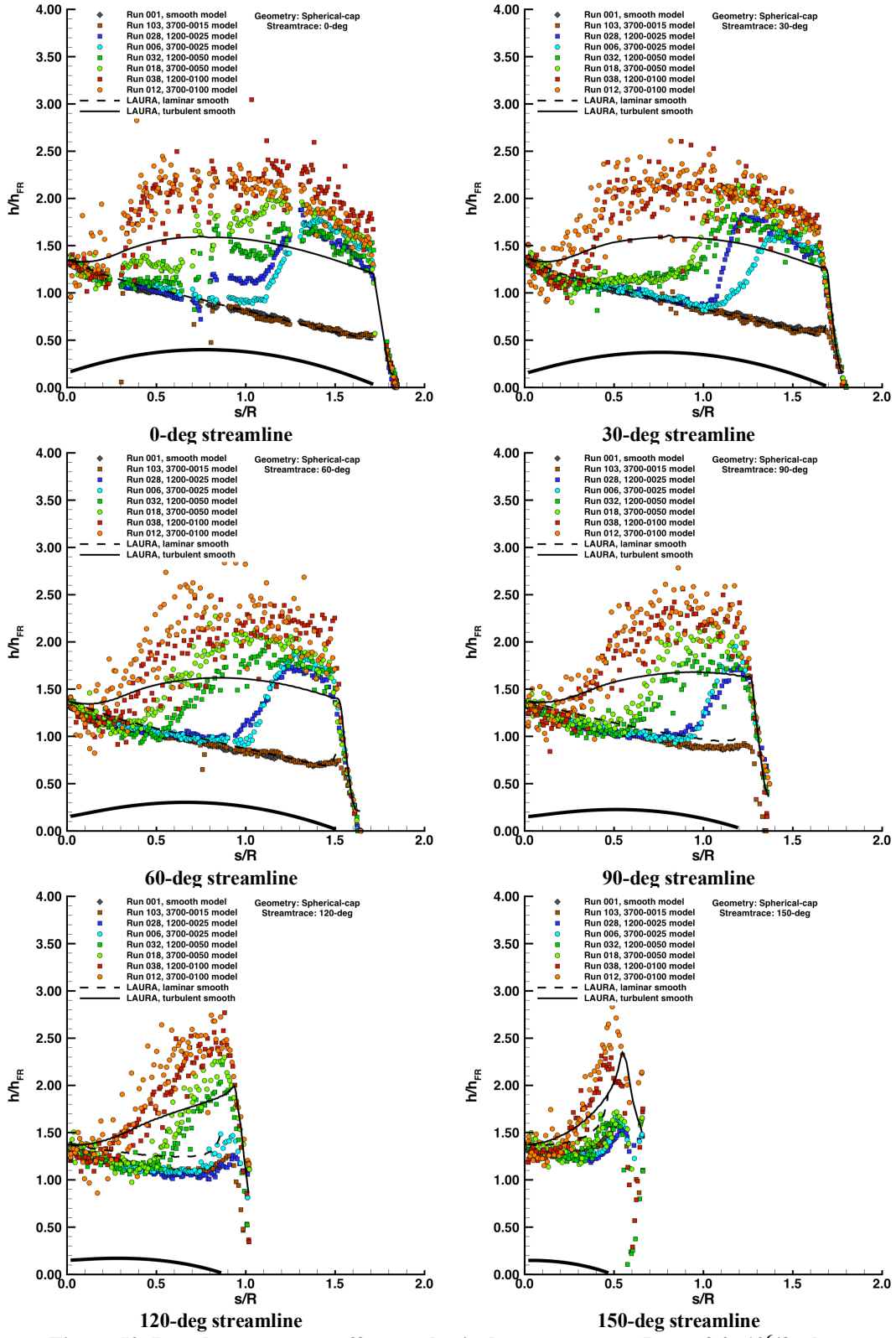


Figure 50. Roughness pattern effects, spherical-cap geometry, $Re_\infty = 3.0 \times 10^6/\text{ft}$ plots.

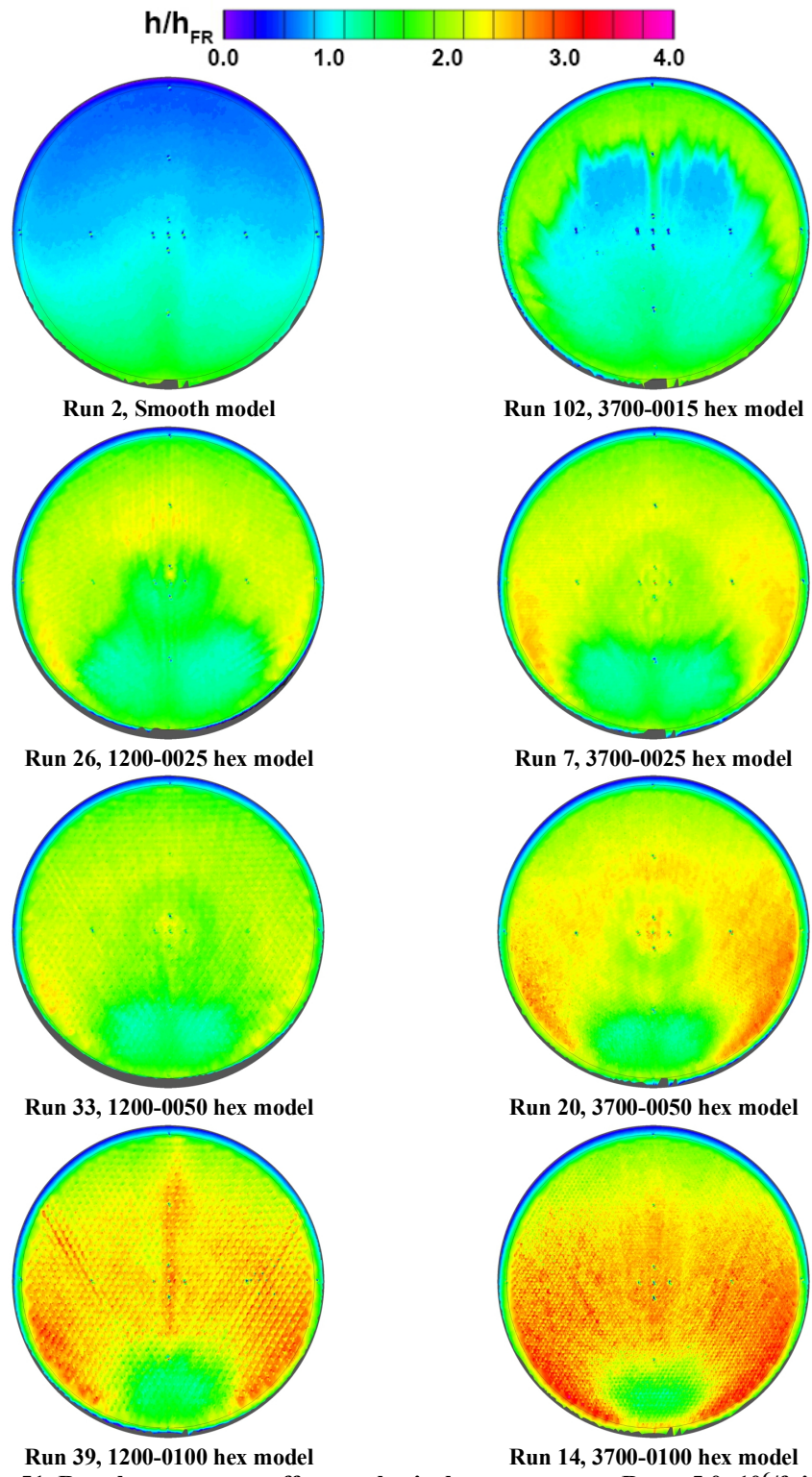


Figure 51. Roughness pattern effects, spherical-cap geometry, $Re_\infty = 5.0 \times 10^6/\text{ft}$ images.

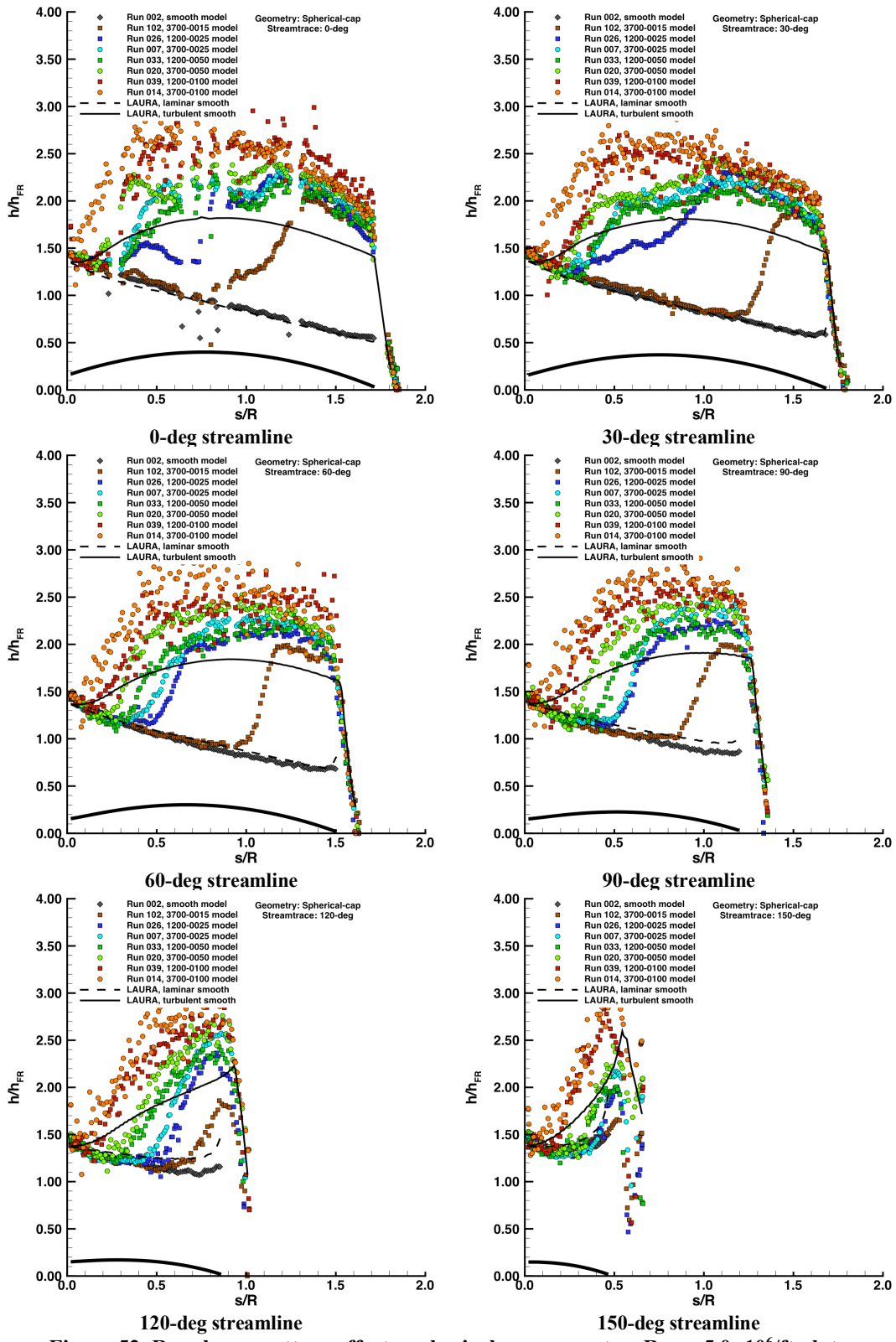


Figure 52. Roughness pattern effects, spherical-cap geometry, $Re_\infty = 5.0 \times 10^6/\text{ft}$ plots.

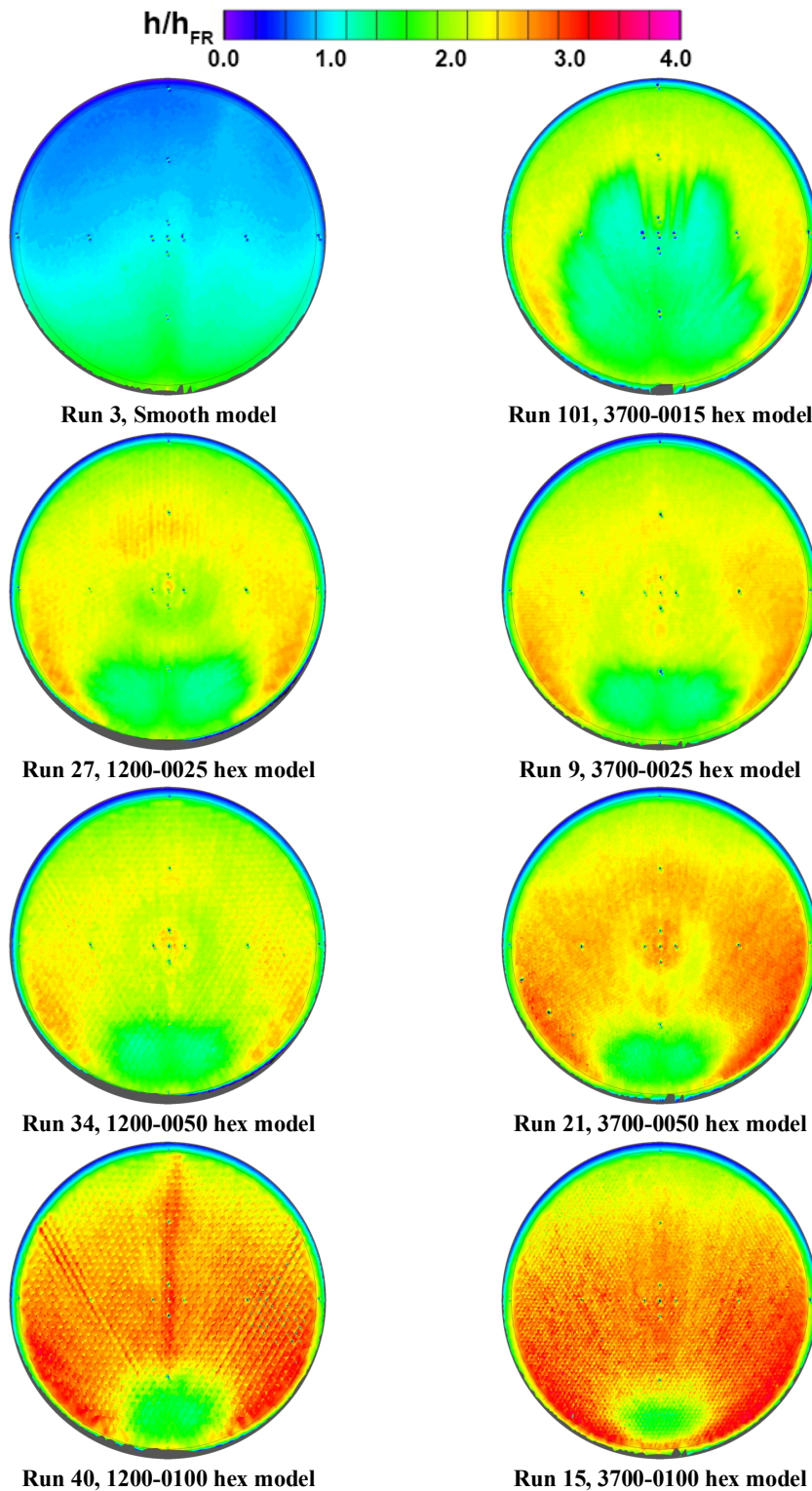


Figure 53. Roughness pattern effects, spherical-cap geometry, $Re_\infty = 6.6 \times 10^6/\text{ft}$ images.

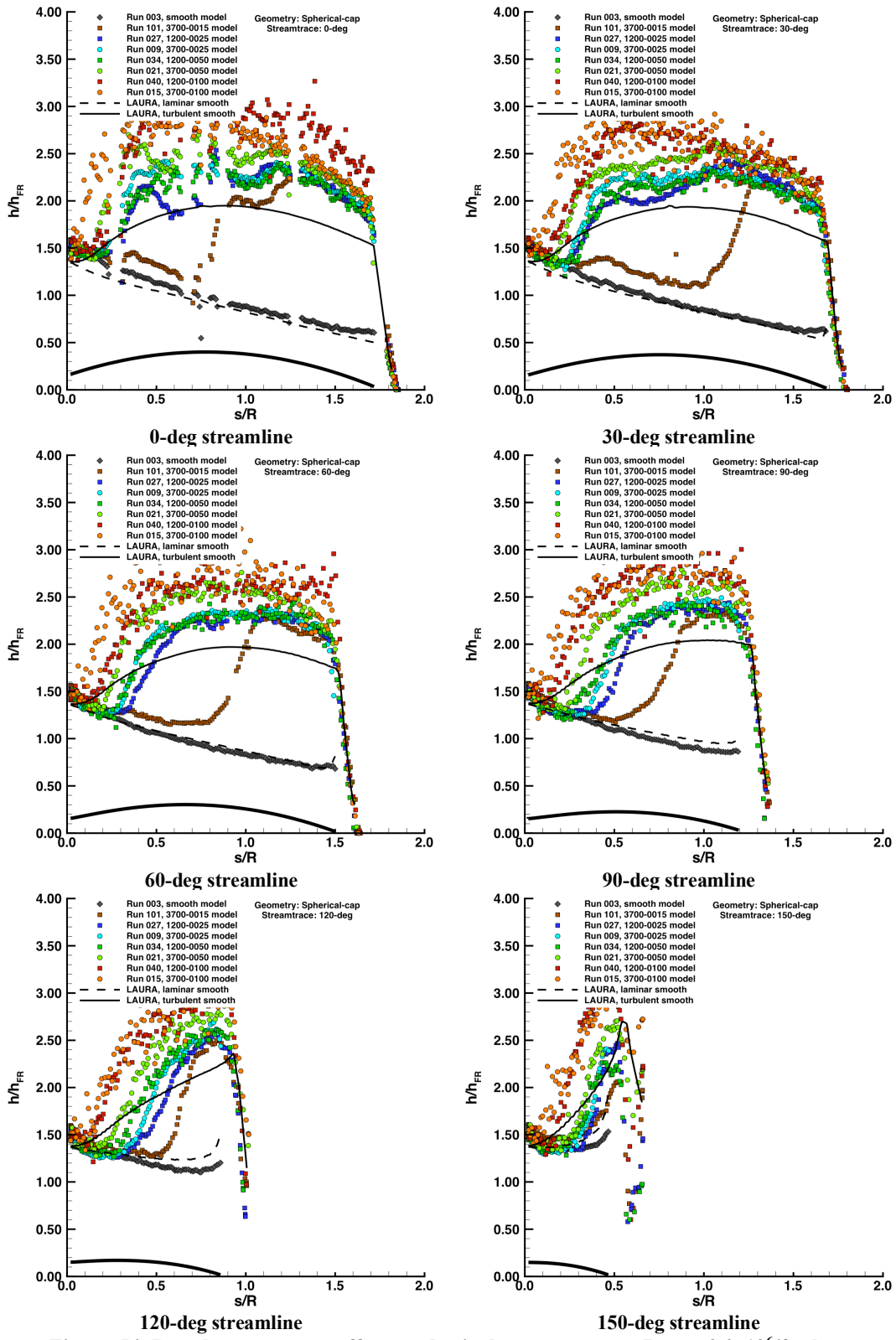


Figure 54. Roughness pattern effects, spherical-cap geometry, $Re_\infty = 6.6 \times 10^6/\text{ft}$ plots.

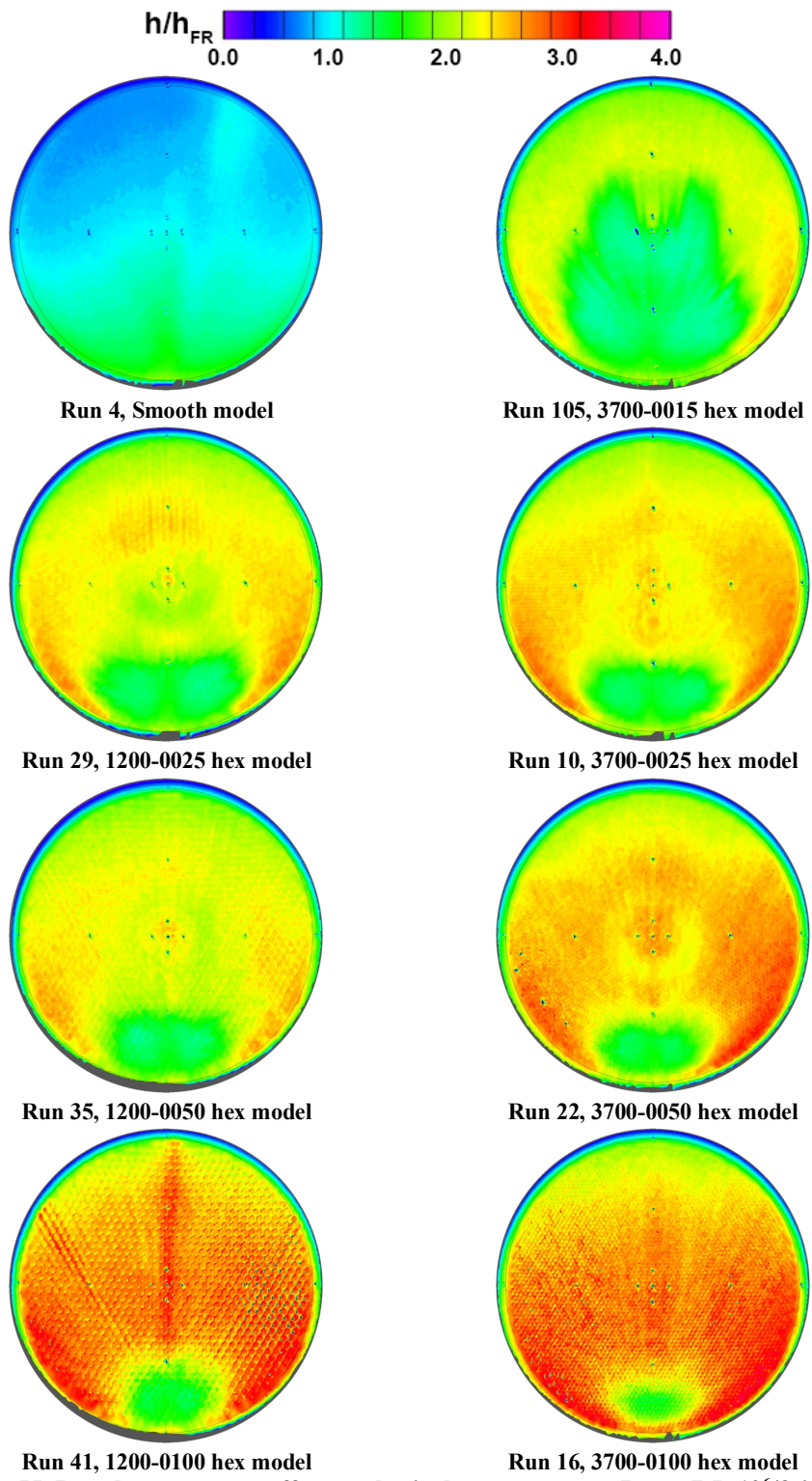


Figure 55. Roughness pattern effects, spherical-cap geometry, $Re_\infty = 7.5 \times 10^6/\text{ft}$ images.

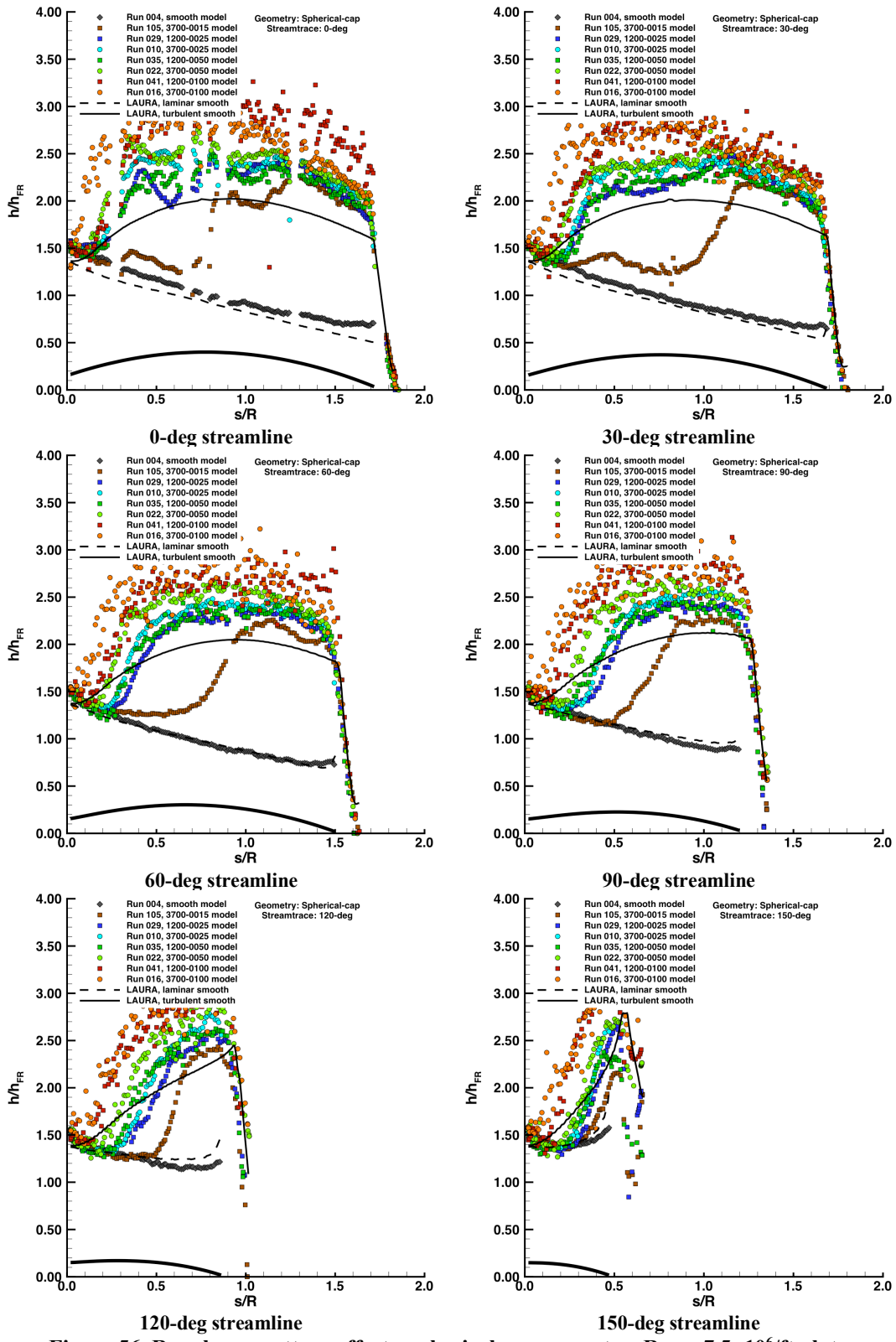


Figure 56. Roughness pattern effects, spherical-cap geometry, $Re_\infty = 7.5 \times 10^6/\text{ft}$ plots.

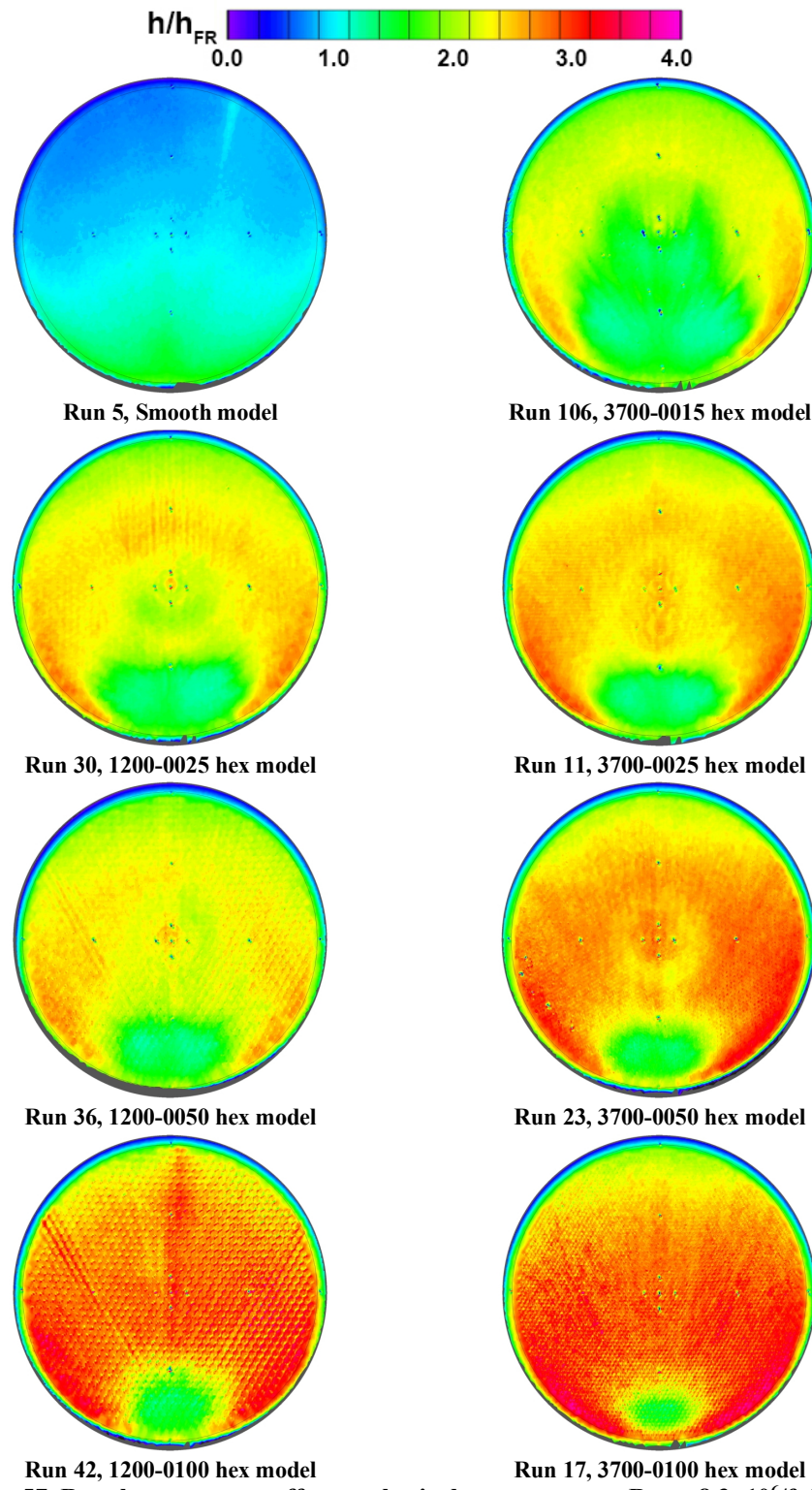


Figure 57. Roughness pattern effects, spherical-cap geometry, $Re_\infty = 8.3 \times 10^6/\text{ft}$ images.

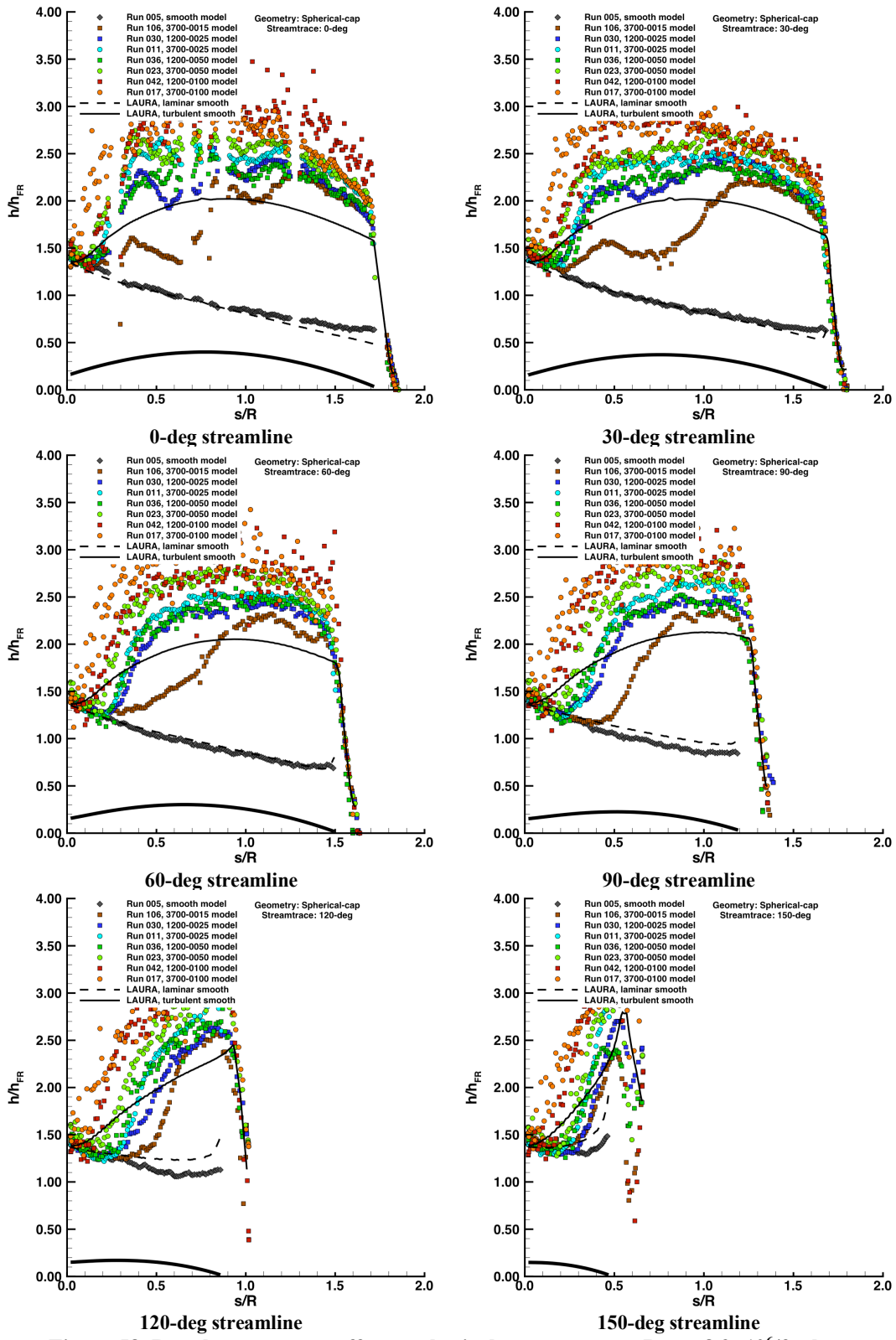


Figure 58. Roughness pattern effects, spherical-cap geometry, $Re_\infty = 8.3 \times 10^6/\text{ft}$ plots.

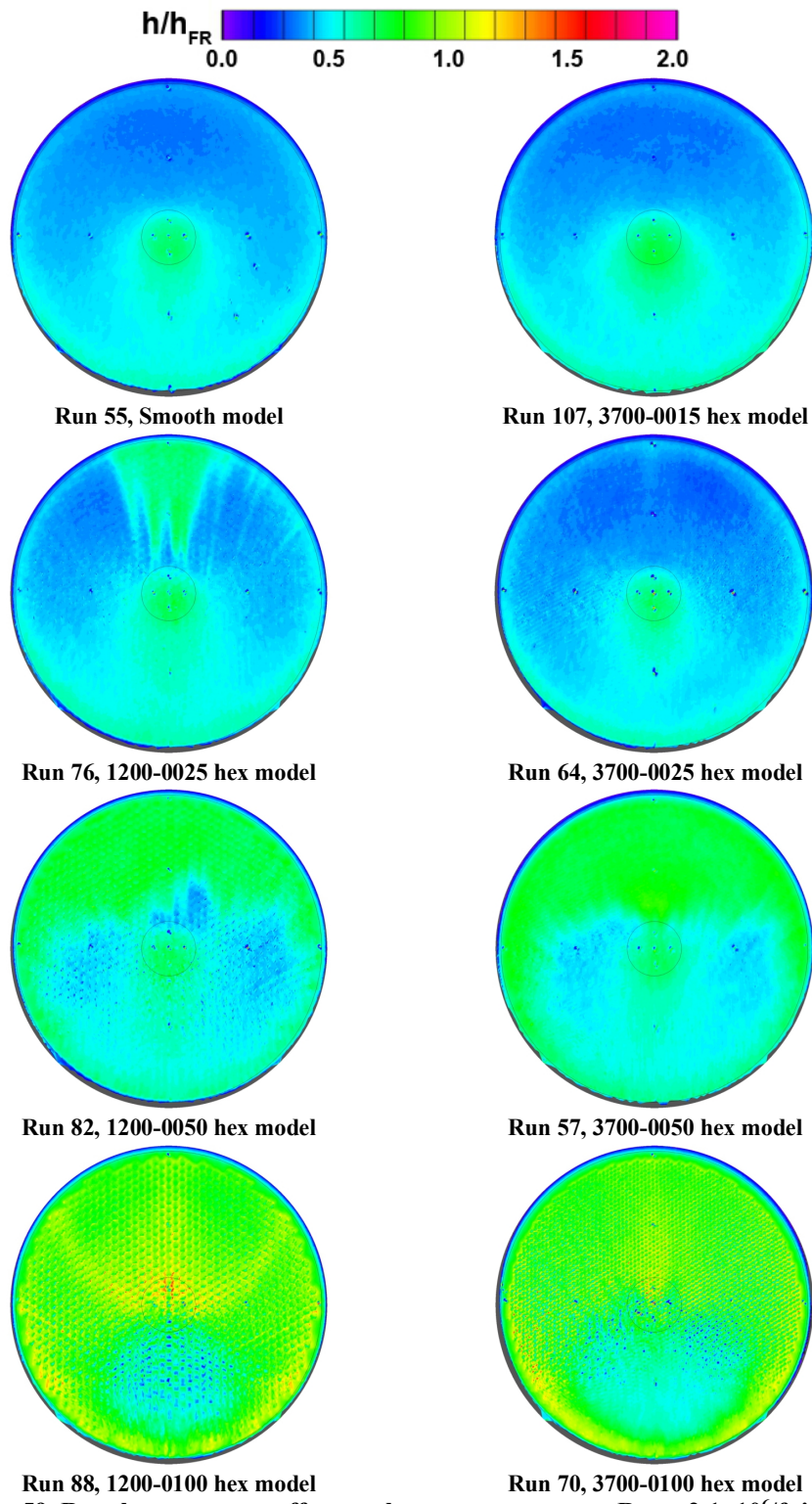


Figure 59. Roughness pattern effects, sphere-cone geometry, $Re_\infty = 2.1 \times 10^6/\text{ft}$ images.

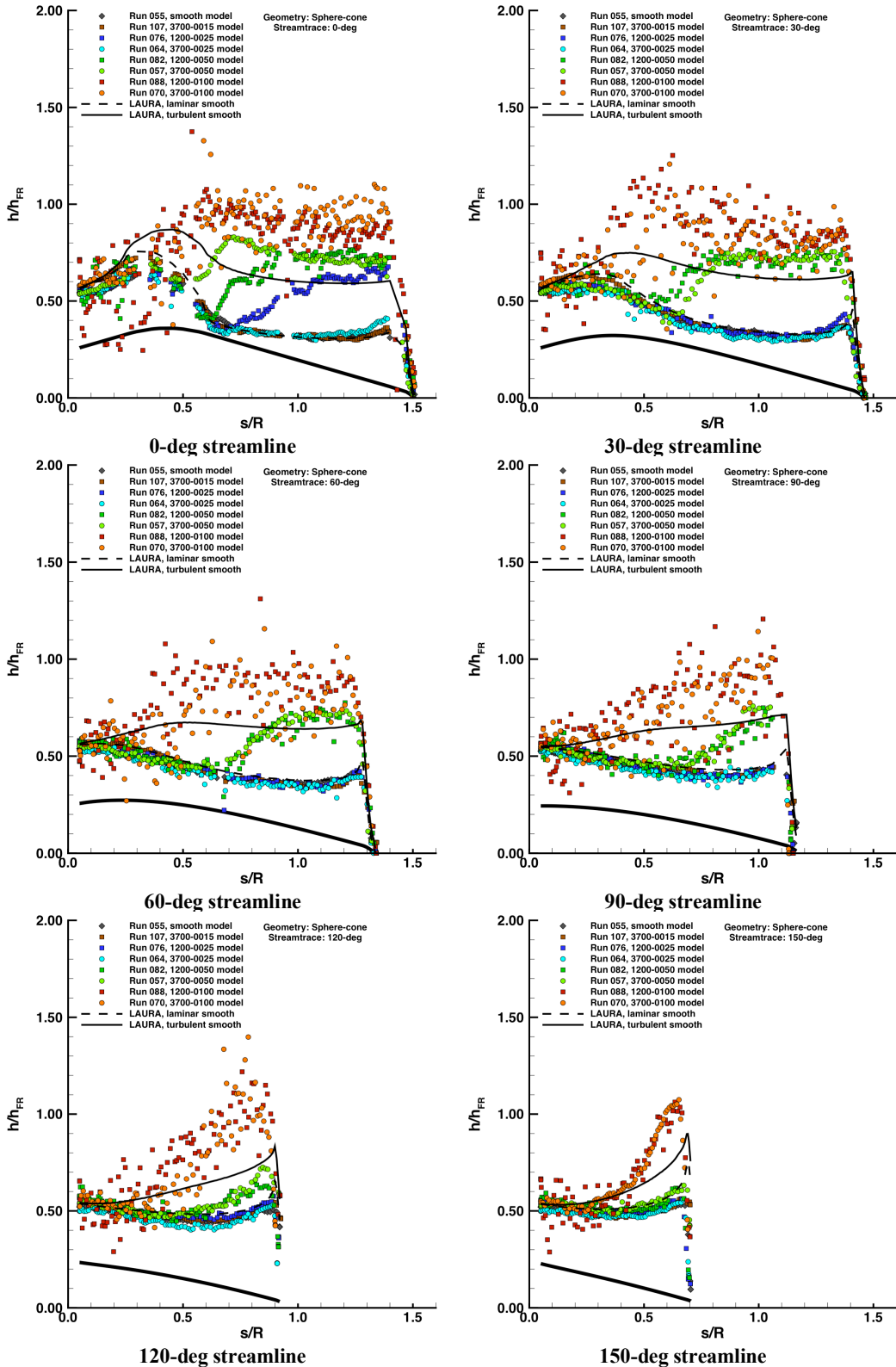


Figure 60. Roughness pattern effects, sphere-cone cap geometry, $Re_\infty = 2.1 \times 10^6/\text{ft}$ plots.

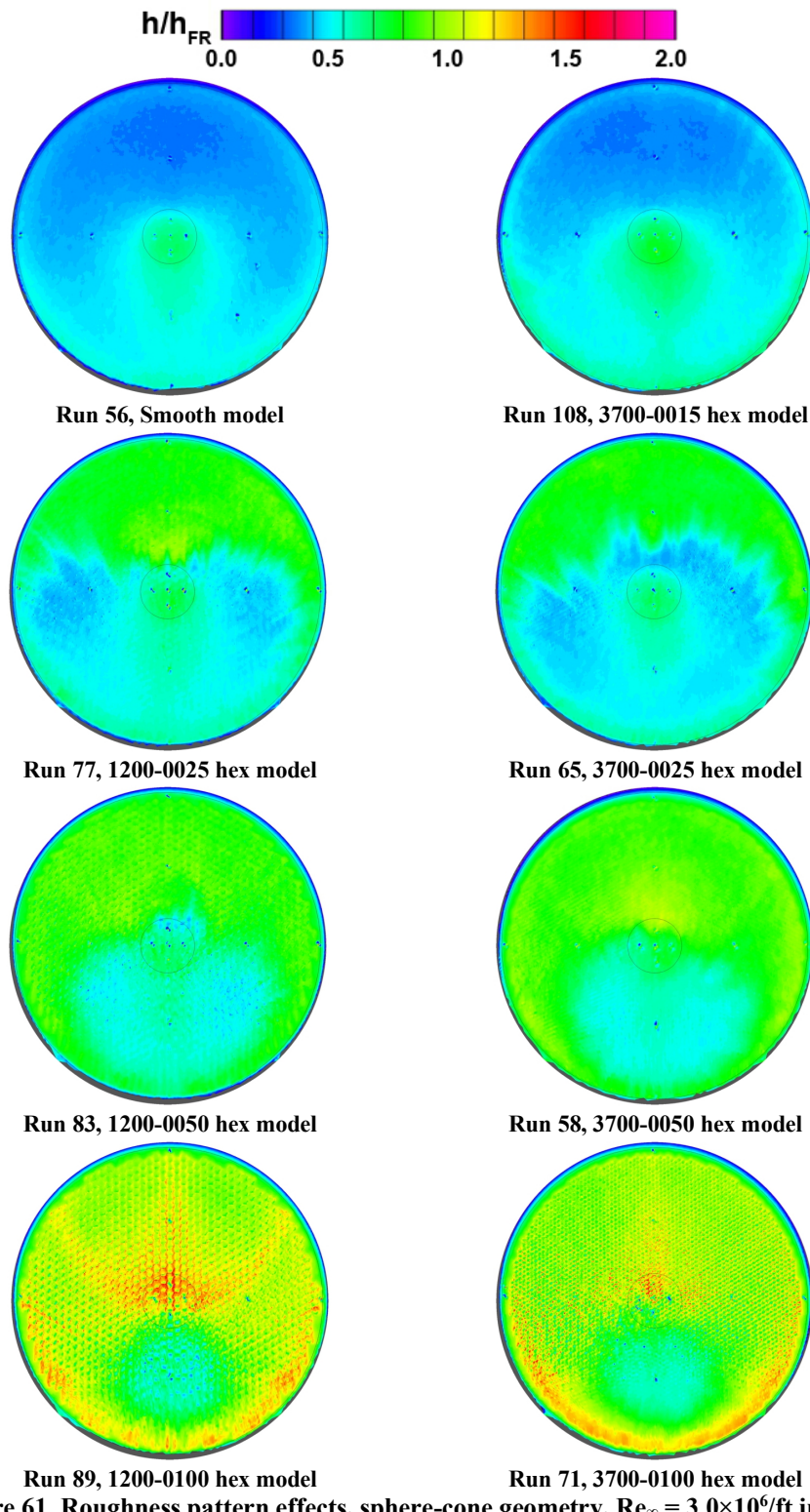


Figure 61. Roughness pattern effects, sphere-cone geometry, $Re_\infty = 3.0 \times 10^6/\text{ft}$ images.

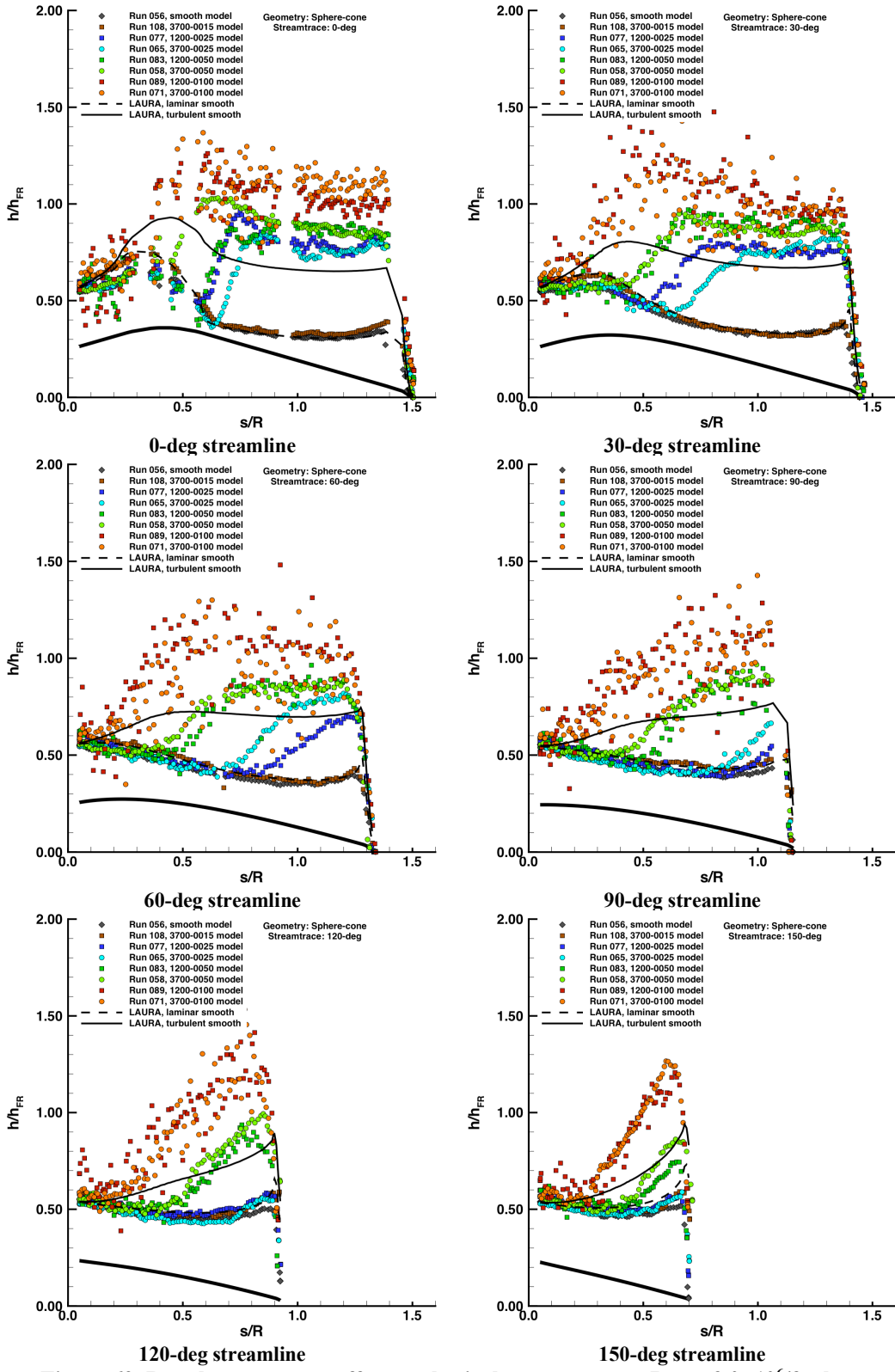


Figure 62. Roughness pattern effects, spherical-cap geometry, $Re_{\infty} = 3.0 \times 10^6$ /ft plots.

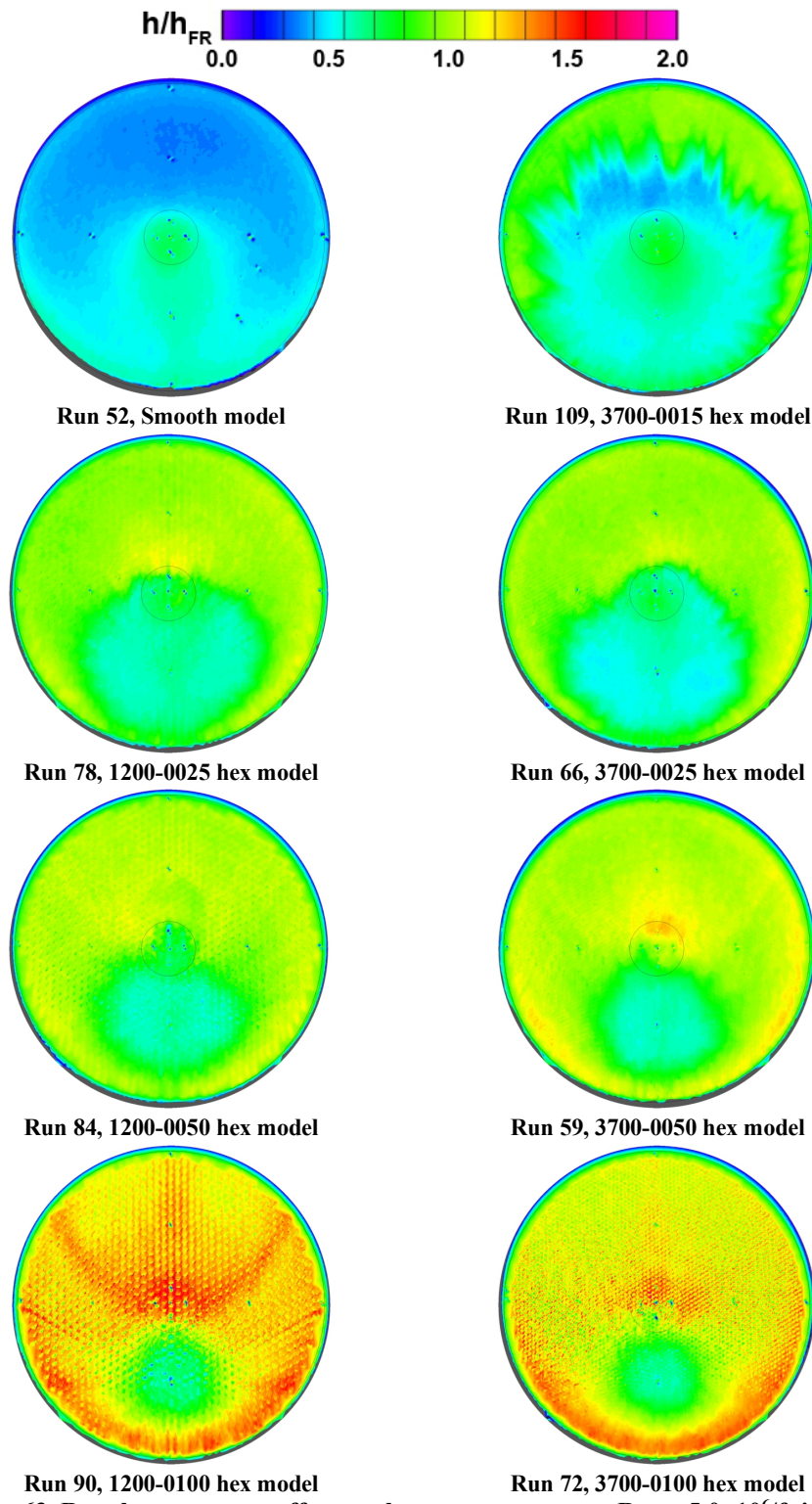


Figure 63. Roughness pattern effects, sphere-cone geometry, $Re_\infty = 5.0 \times 10^6/\text{ft}$ images.

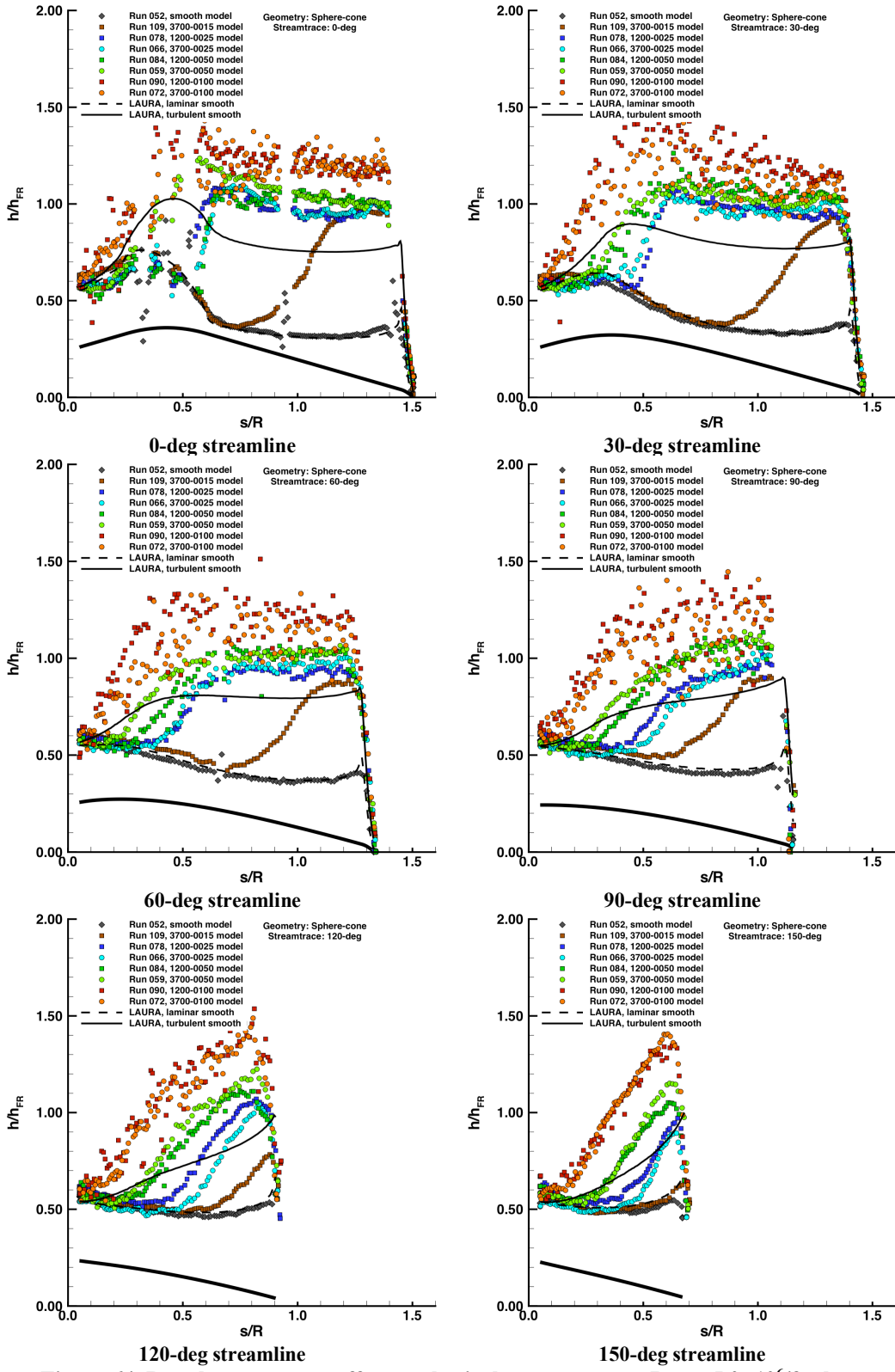


Figure 64. Roughness pattern effects, spherical-cap geometry, $Re_\infty = 5.0 \times 10^6/\text{ft}$ plots.

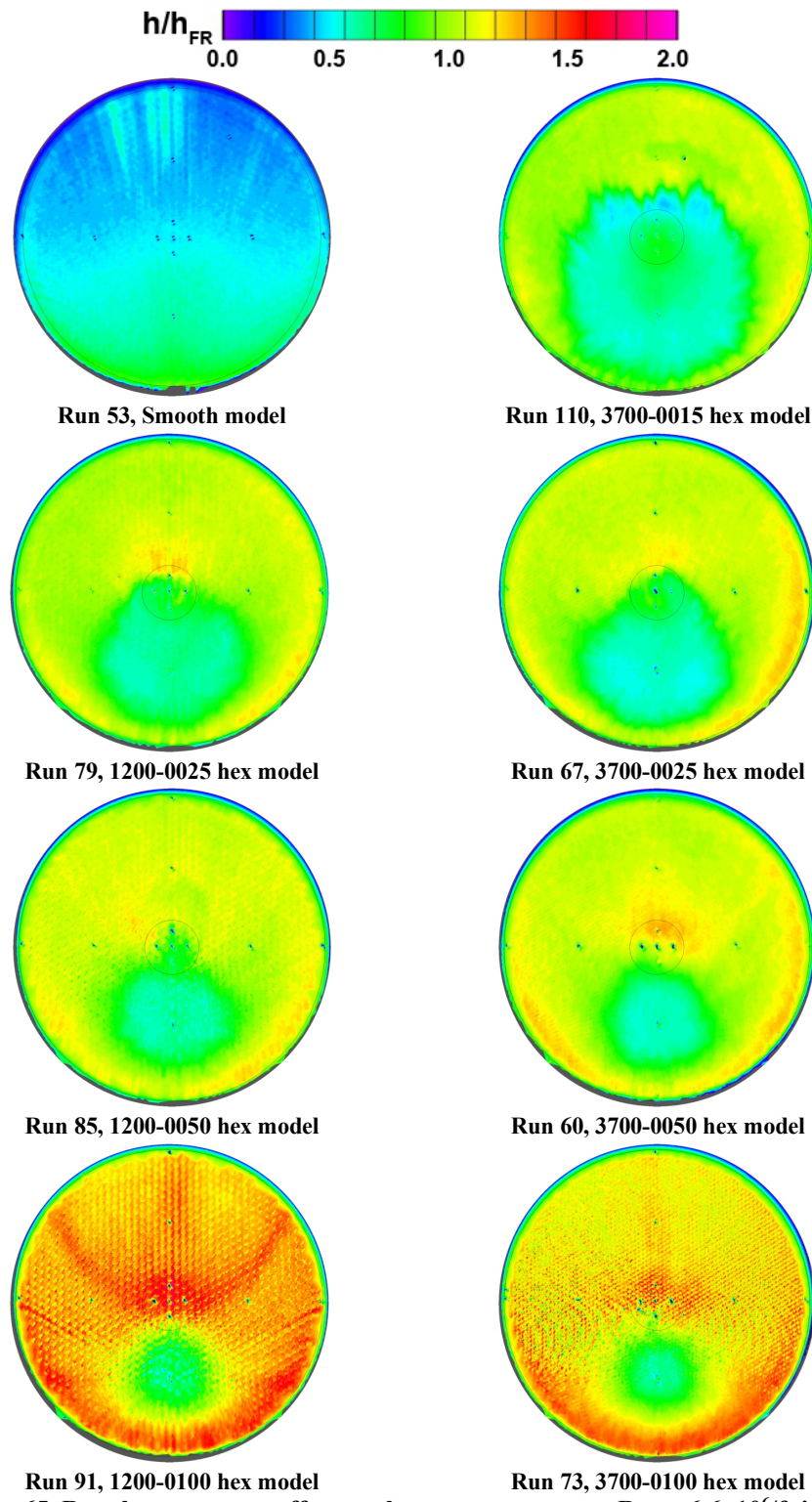


Figure 65. Roughness pattern effects, sphere-cone geometry, $Re_\infty = 6.6 \times 10^6/\text{ft}$ images.

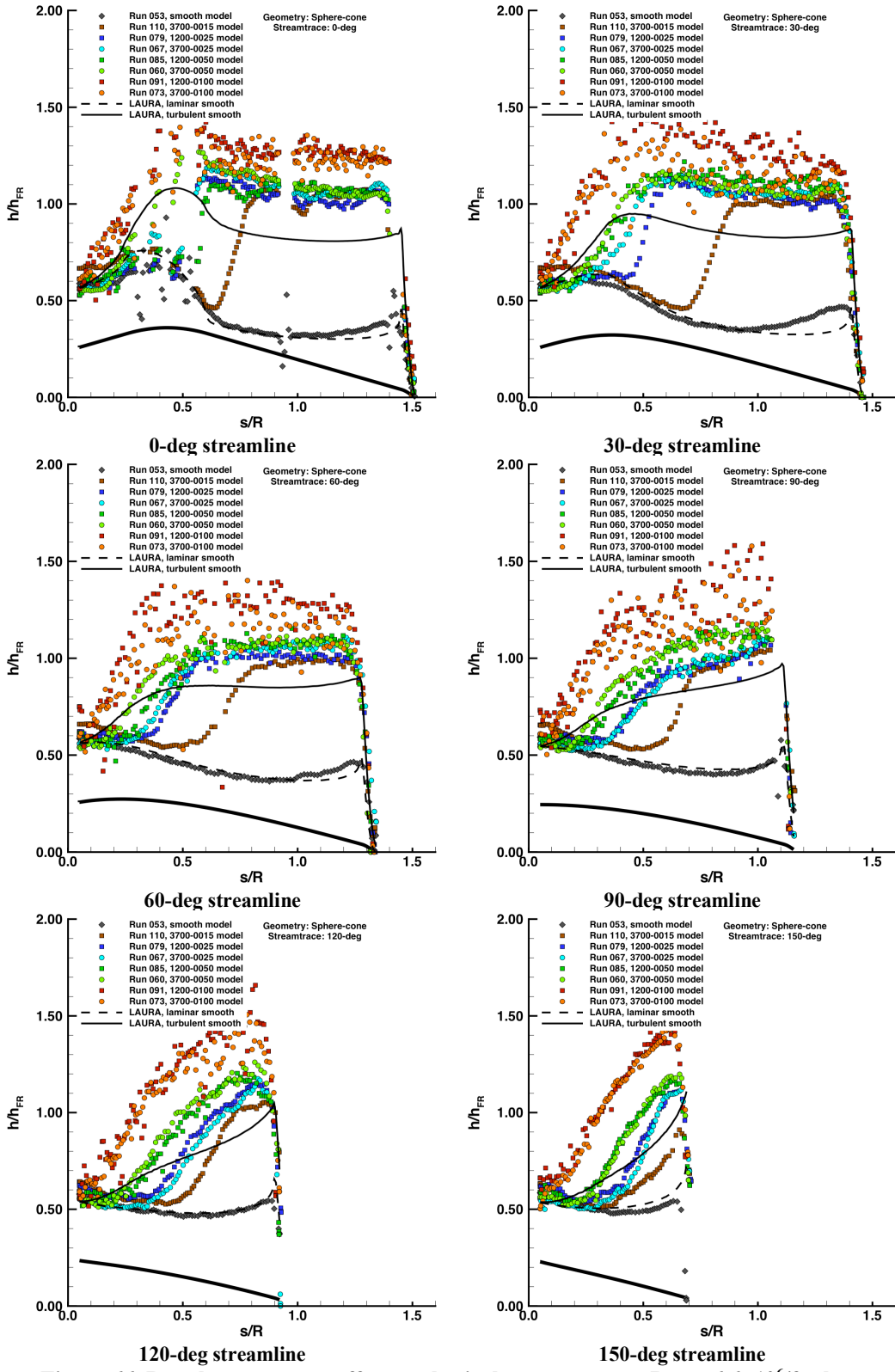


Figure 66. Roughness pattern effects, spherical-cap geometry, $Re_{\infty} = 6.6 \times 10^6/\text{ft}$ plots.

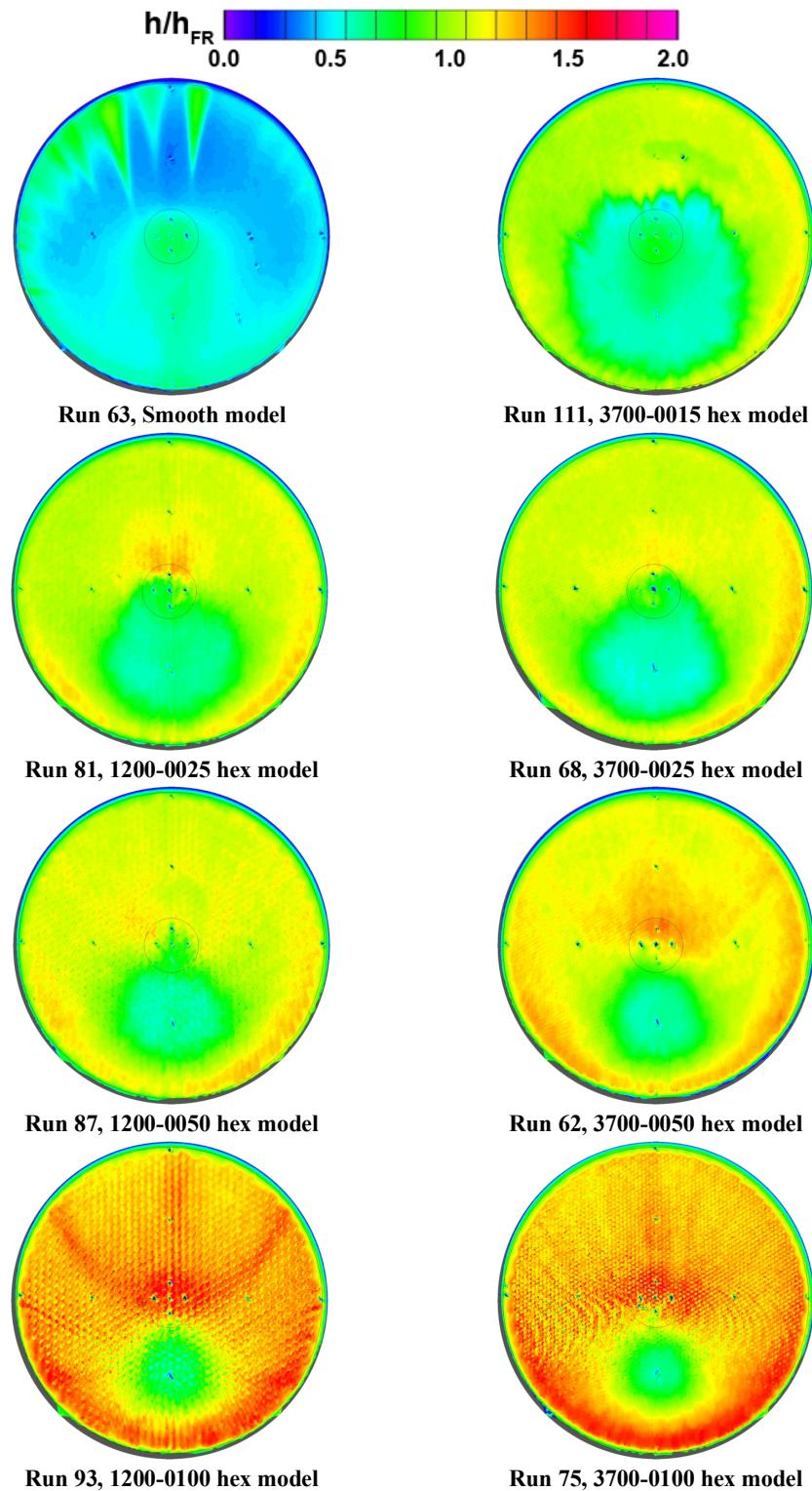


Figure 67. Roughness pattern effects, sphere-cone geometry, $Re_\infty = 7.5 \times 10^6/\text{ft}$ images.

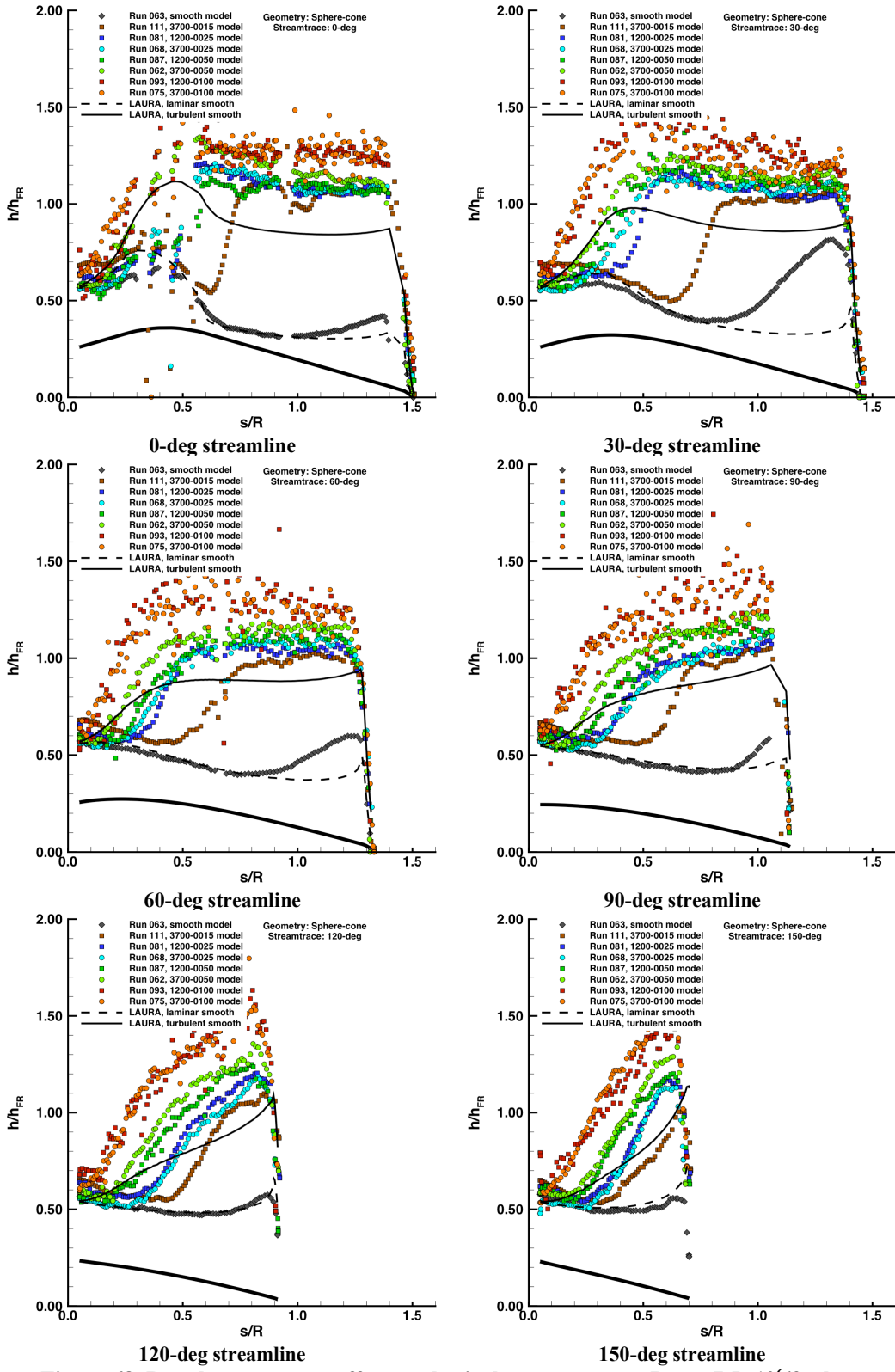


Figure 68. Roughness pattern effects, spherical-cap geometry, $Re_\infty = 7.5 \times 10^6/\text{ft}$ plots.

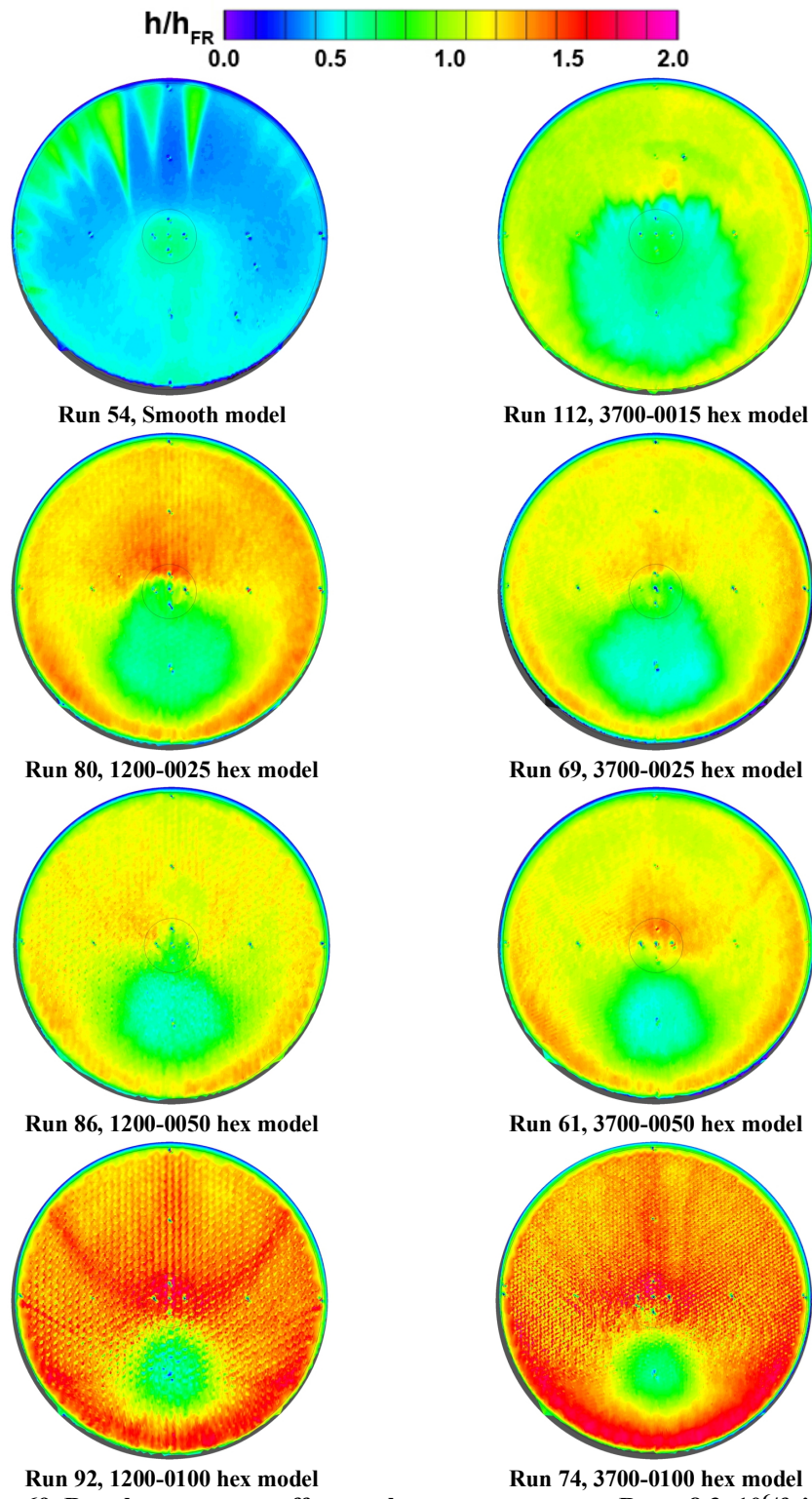


Figure 69. Roughness pattern effects, sphere-cone geometry, $Re_\infty = 8.3 \times 10^6/\text{ft}$ images.

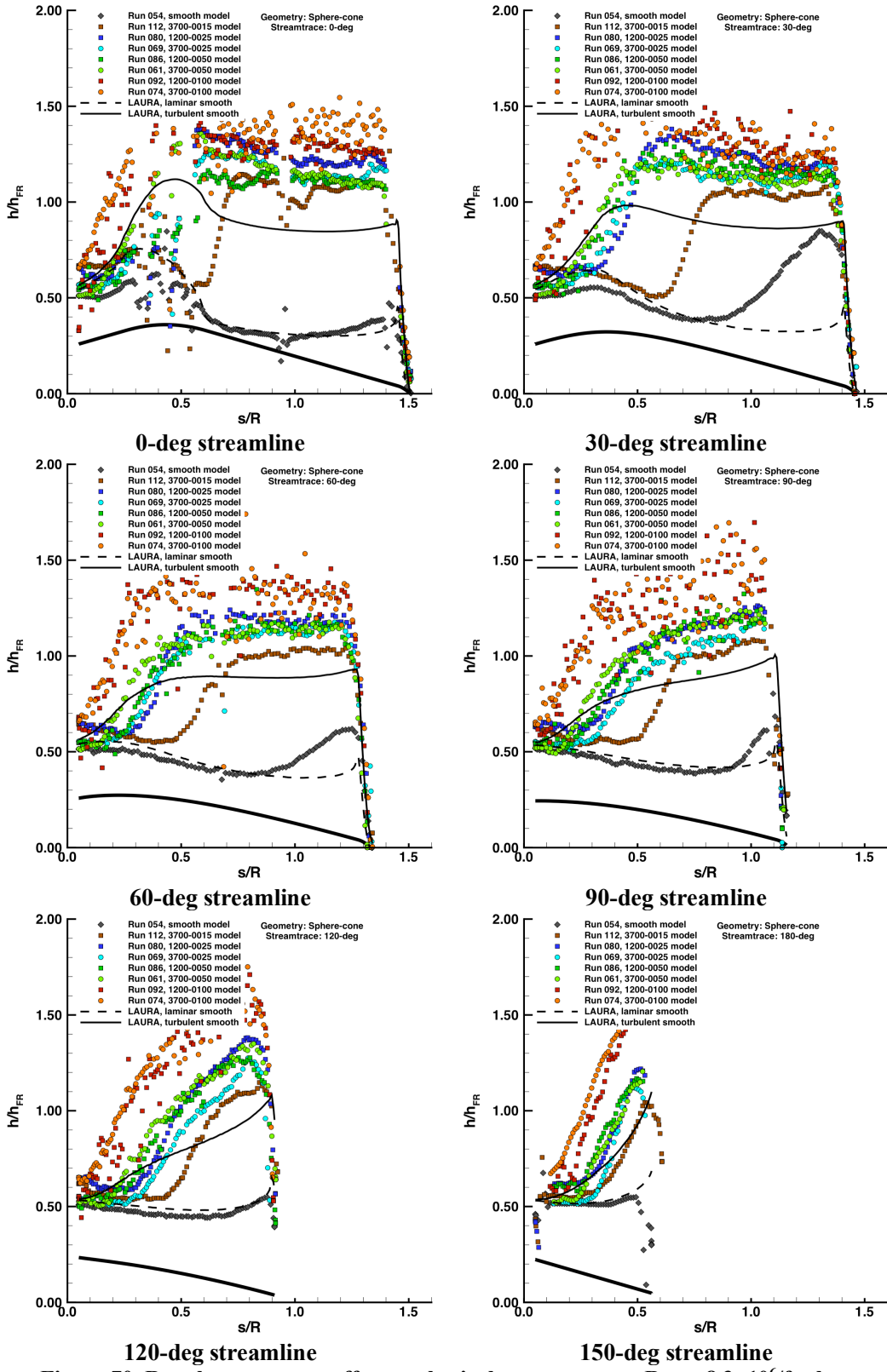


Figure 70. Roughness pattern effects, spherical-cap geometry, $Re_{\infty} = 8.3 \times 10^6/\text{ft}$ plots.

Appendix A. Spherical-Cap Geometry Global Heating Images

Global heating images for the spherical-cap geometry from Test 6991 in the LAL 20-Inch Mach 6 Air Tunnel are presented in this Appendix in Figure 71 - Figure 118.

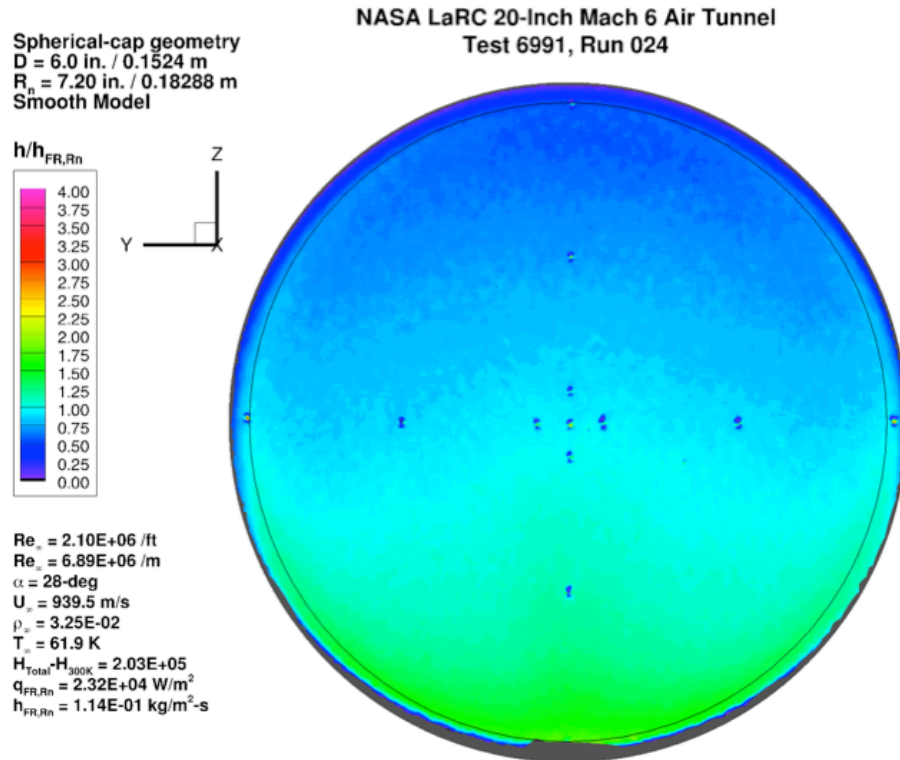


Figure 71. Test 6991, Run 24, $Re_\infty = 2.1 \times 10^6 / \text{ft}$, spherical-cap, smooth OML.

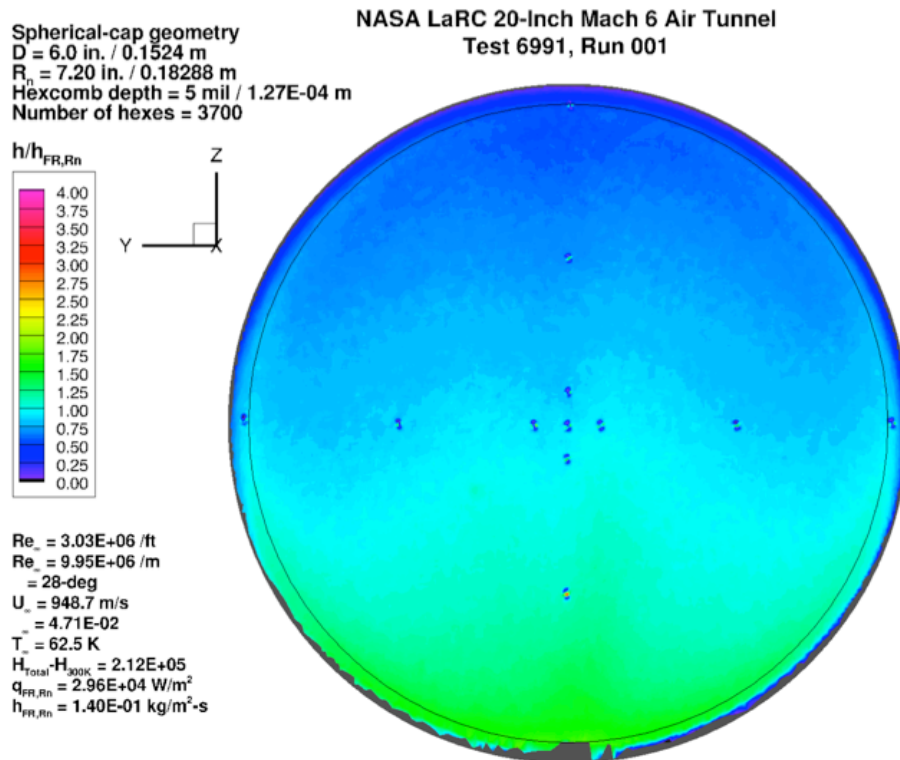


Figure 72. Test 6991, Run 1, $Re_\infty = 3.0 \times 10^6 / \text{ft}$, spherical-cap, smooth OML.

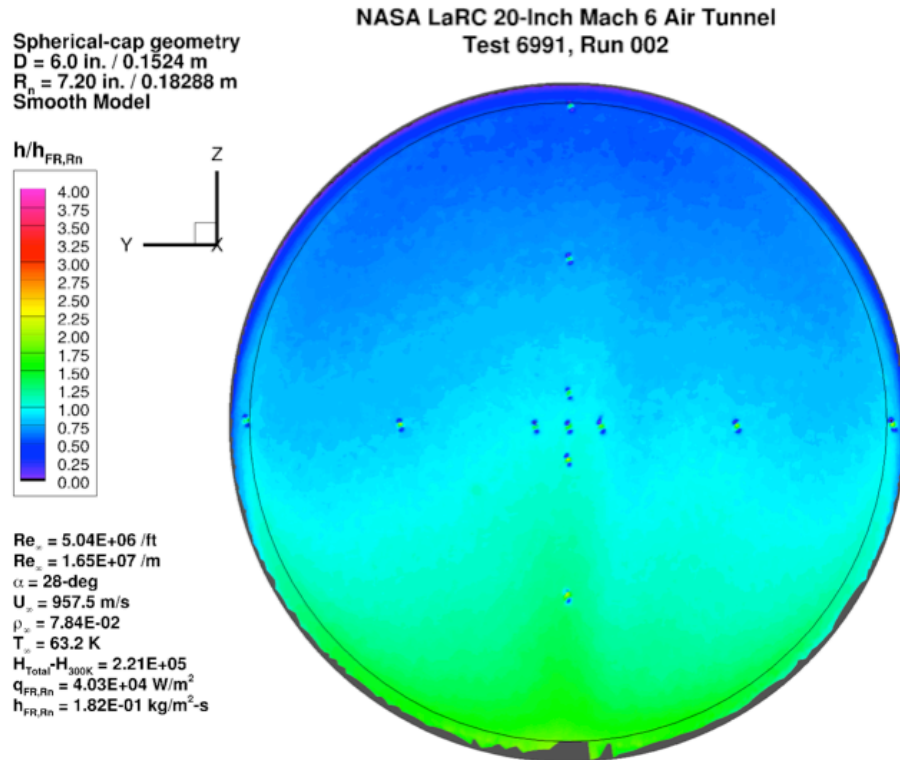


Figure 73. Test 6991, Run 2, $Re_\infty = 5.0 \times 10^6/\text{ft}$, spherical-cap, smooth OML.

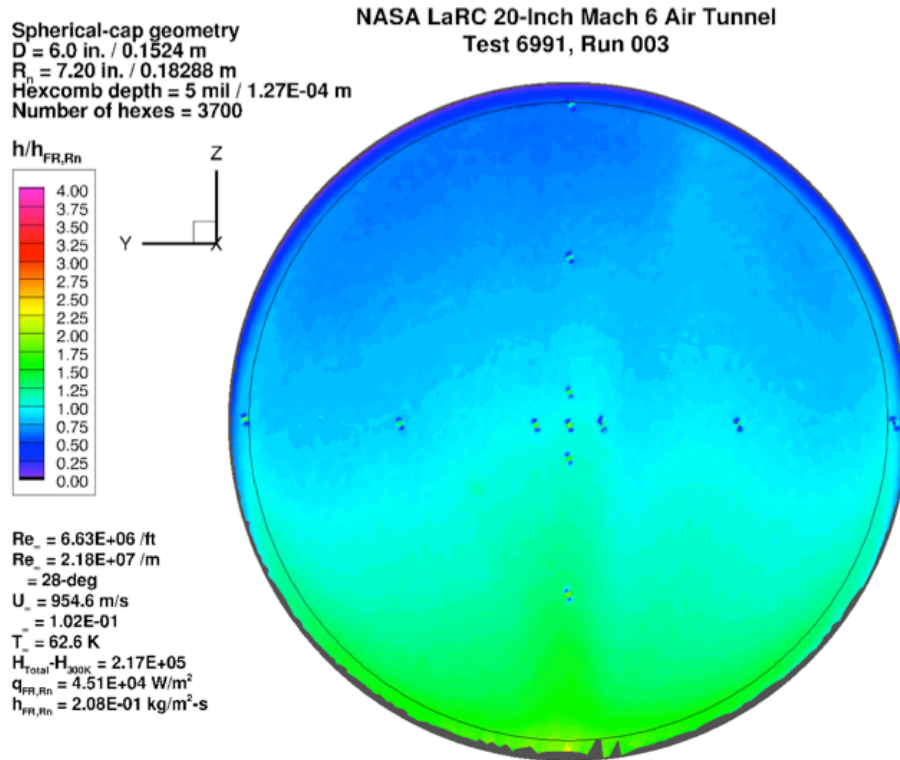


Figure 74. Test 6991, Run 3, $Re_\infty = 6.6 \times 10^6/\text{ft}$, spherical-cap, smooth OML.

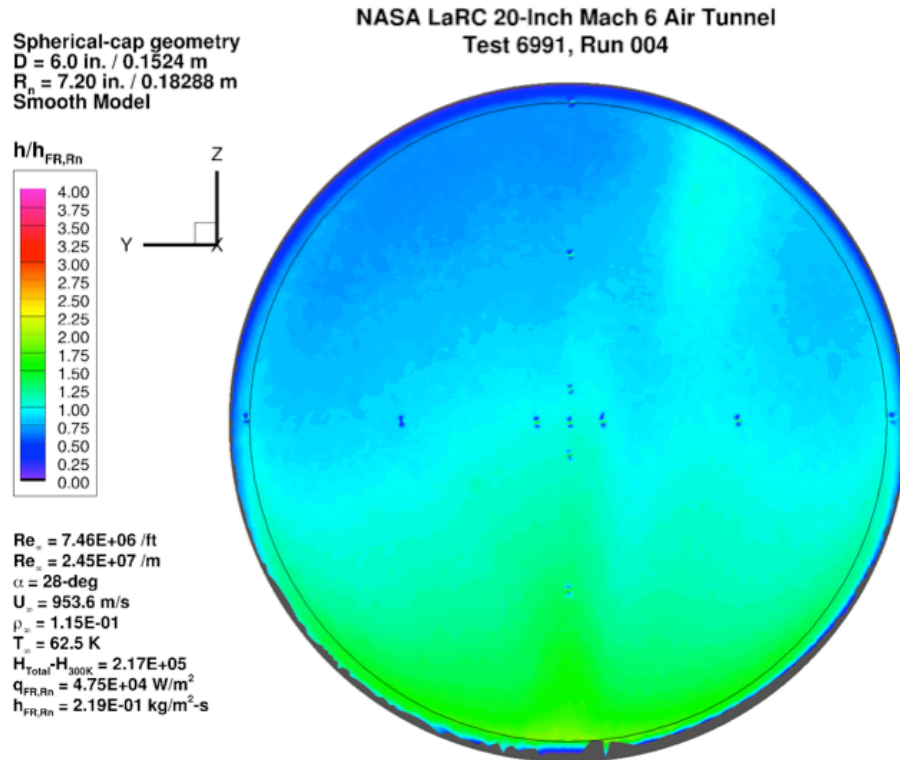


Figure 75. Test 6991, Run 4, $Re_\infty = 7.5 \times 10^6 / \text{ft}$, spherical-cap, smooth OML.

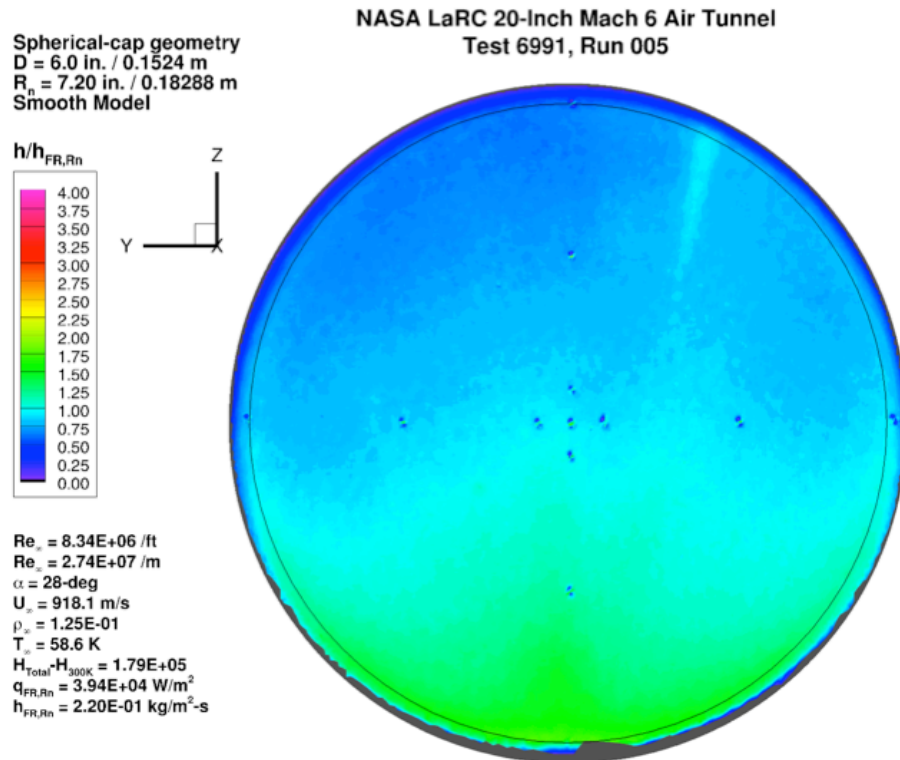


Figure 76. Test 6991, Run 5, $Re_\infty = 8.3 \times 10^6 / \text{ft}$, spherical-cap, smooth OML.

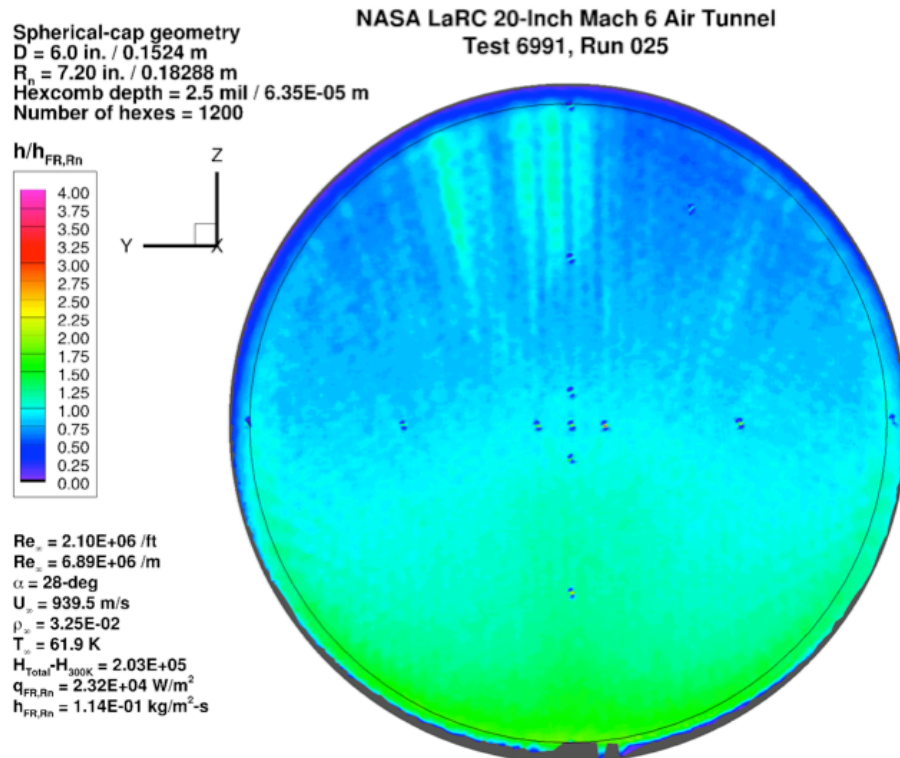


Figure 77. Test 6991, Run 25, $Re_\infty = 2.1 \times 10^6/\text{ft}$, spherical-cap 1200-0025.

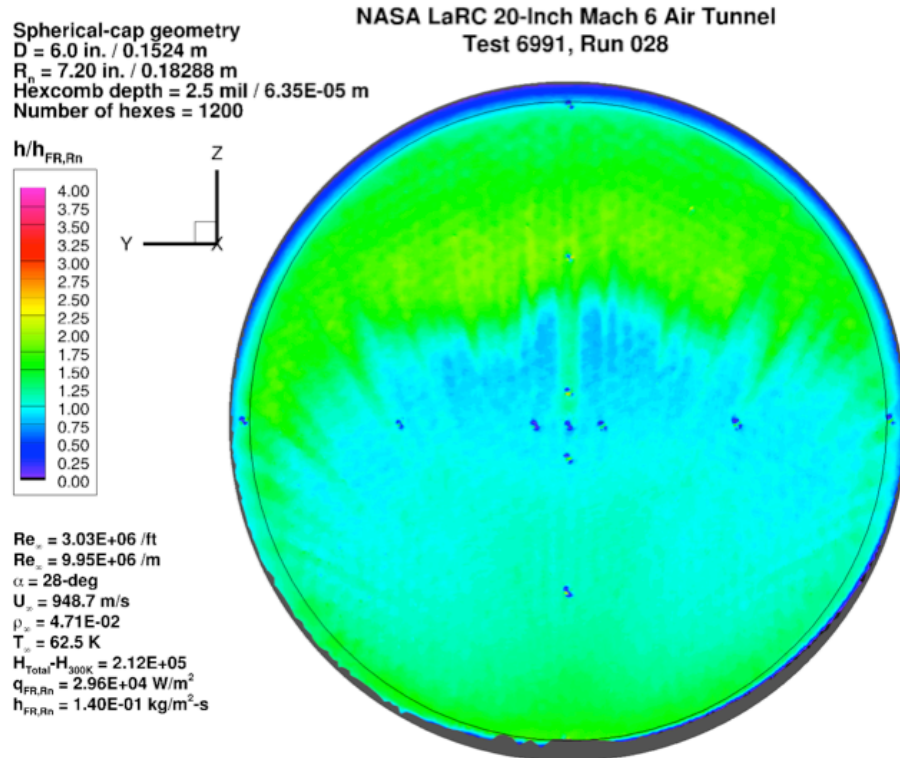


Figure 78. Test 6991, Run 28, $Re_\infty = 3.0 \times 10^6/\text{ft}$, spherical- cap 1200-0025.

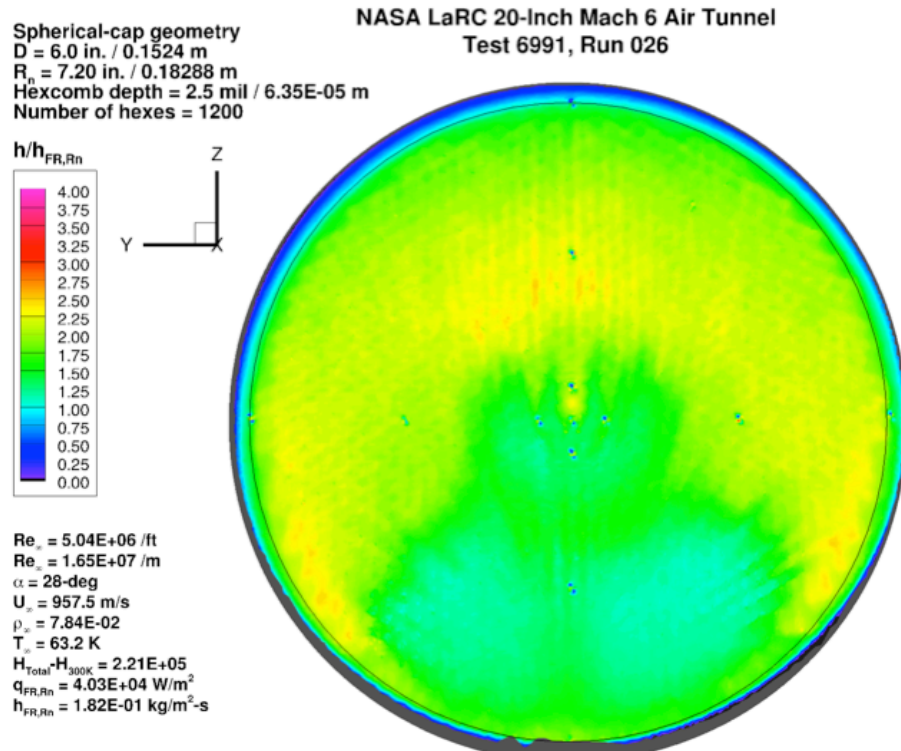


Figure 79. Test 6991, Run 26, $Re_\infty = 5.0 \times 10^6 / \text{ft}$, spherical-cap 1200-0025.

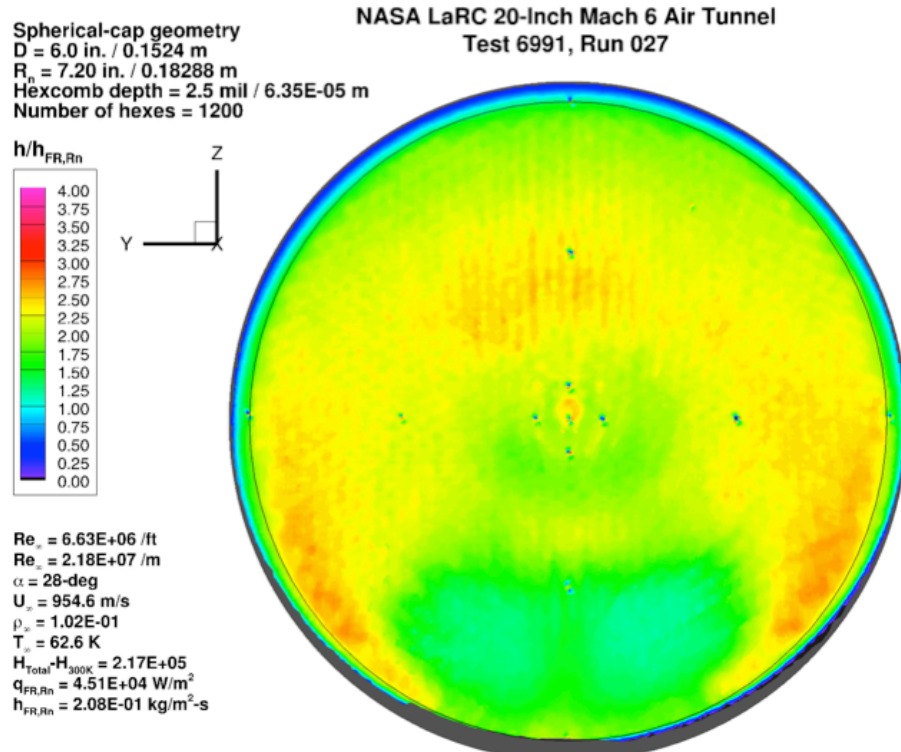


Figure 80. Test 6991, Run 27, $Re_\infty = 6.6 \times 10^6 / \text{ft}$, spherical-cap 1200-0025.

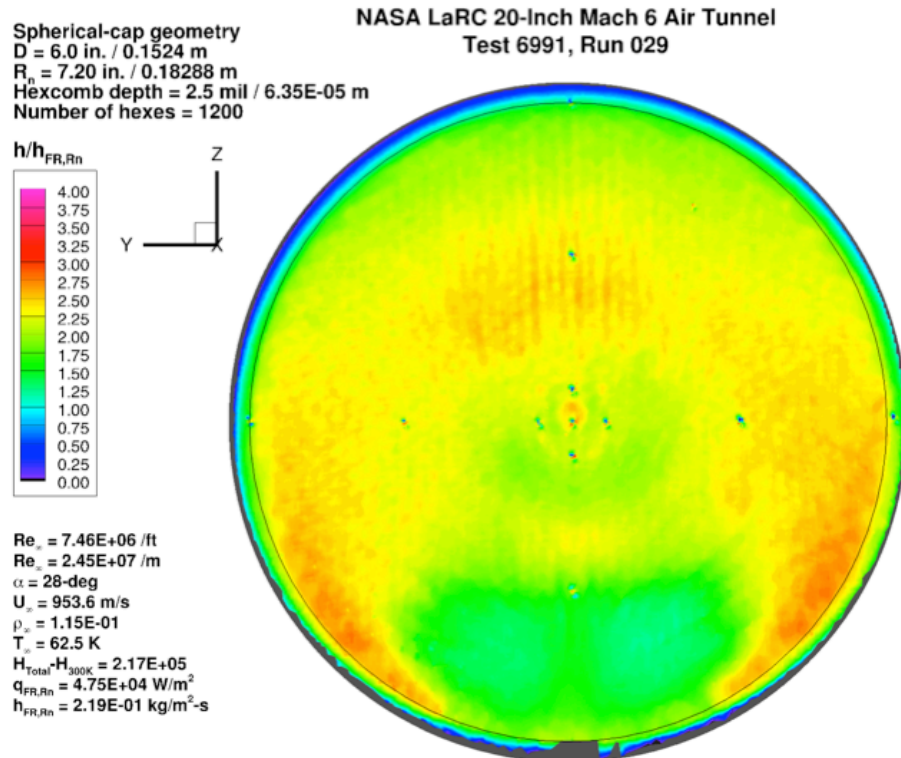


Figure 81. Test 6991, Run 29, $Re_\infty = 7.5 \times 10^6/\text{ft}$, spherical-cap 1200-0025.

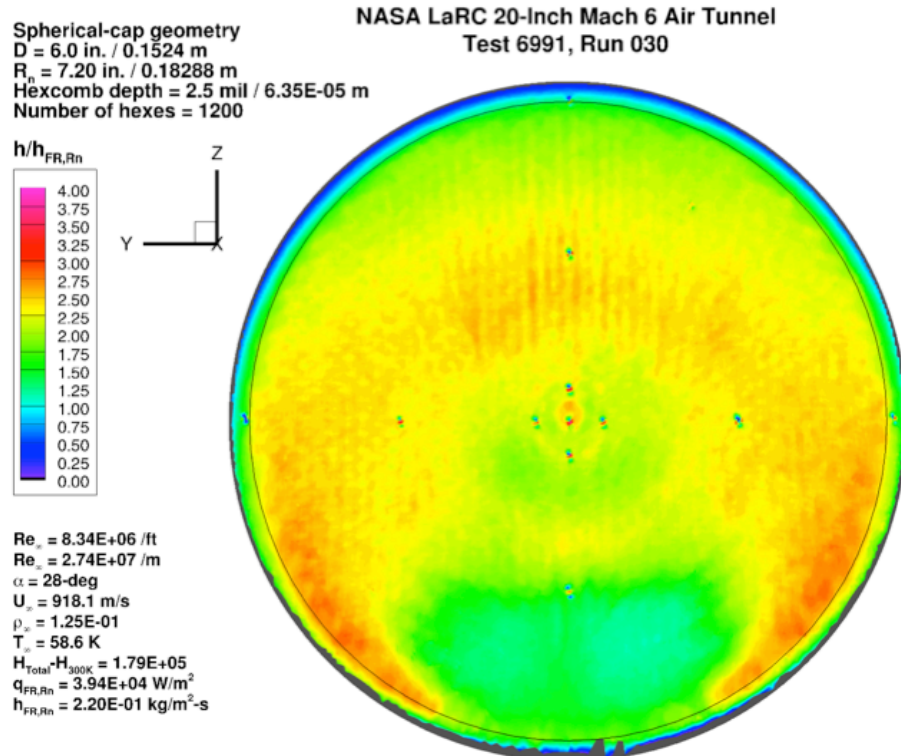


Figure 82. Test 6991, Run 30, $Re_\infty = 8.3 \times 10^6/\text{ft}$, spherical-cap 1200-0025.

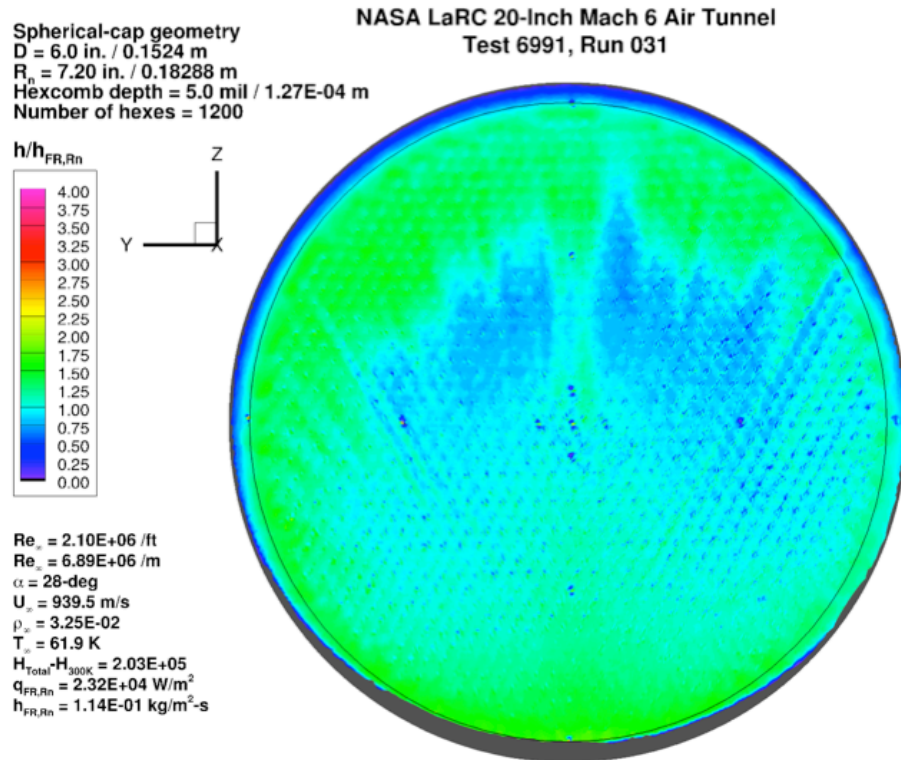


Figure 83. Test 6991, Run 31, $Re_\infty = 2.1 \times 10^6/\text{ft}$, spherical-cap 1200-0050.

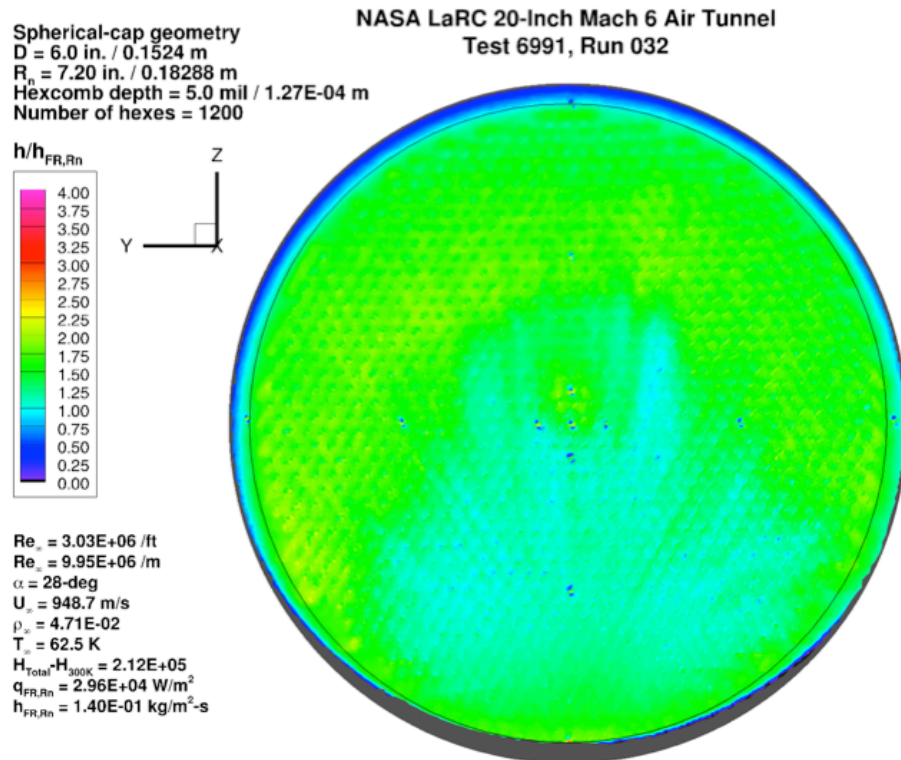


Figure 84. Test 6991, Run 32, $Re_\infty = 3.0 \times 10^6/\text{ft}$, spherical-cap 1200-0050.

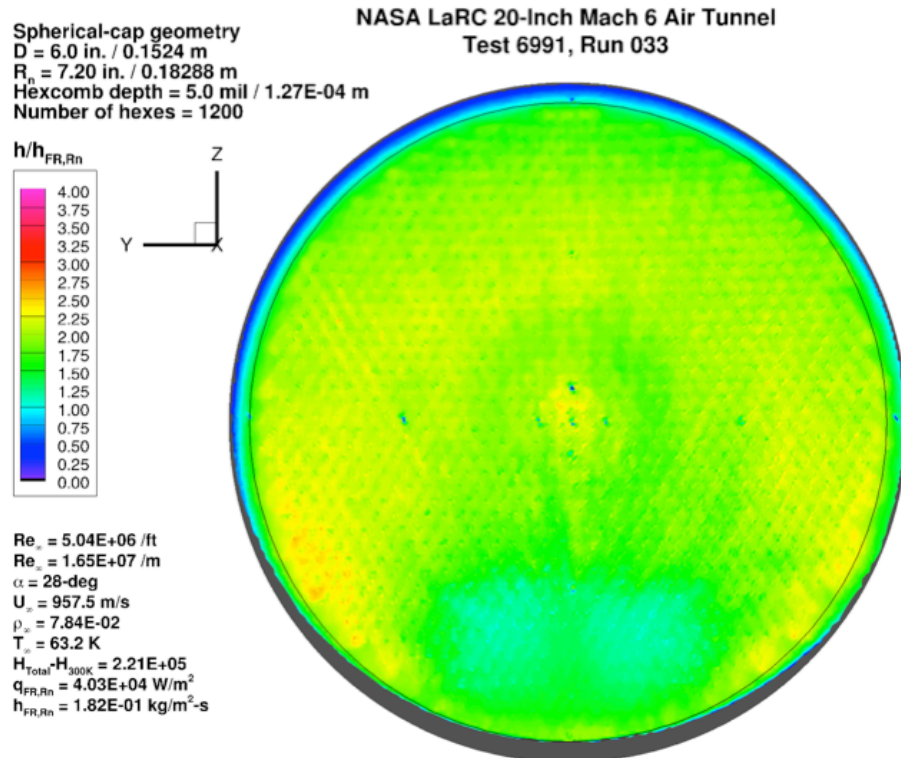


Figure 85. Test 6991, Run 33, $Re_\infty = 5.0 \times 10^6/\text{ft}$, spherical-cap 1200-0050.

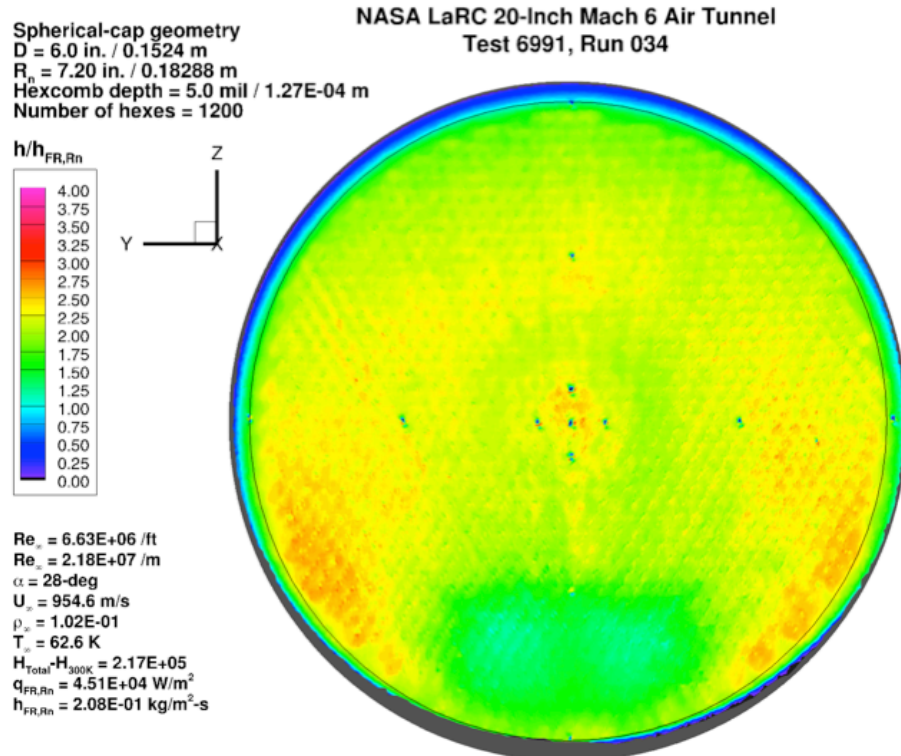


Figure 86. Test 6991, Run 34, $Re_\infty = 6.6 \times 10^6/\text{ft}$, spherical-cap 1200-0050.

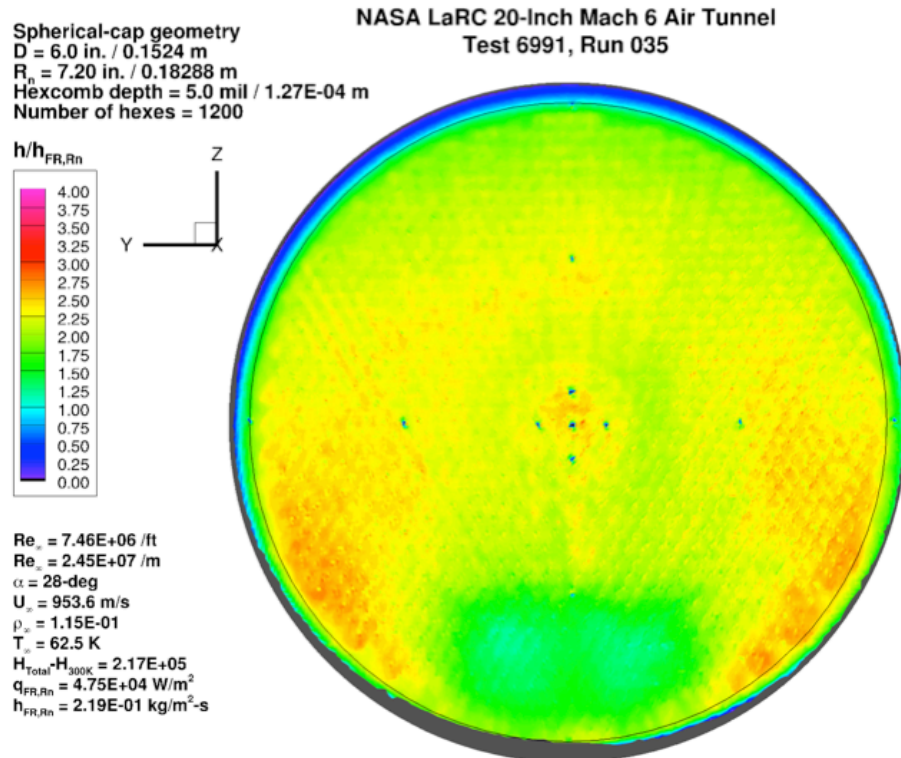


Figure 87. Test 6991, Run 35, $Re_\infty = 7.5 \times 10^6/\text{ft}$, spherical-cap 1200-0050.

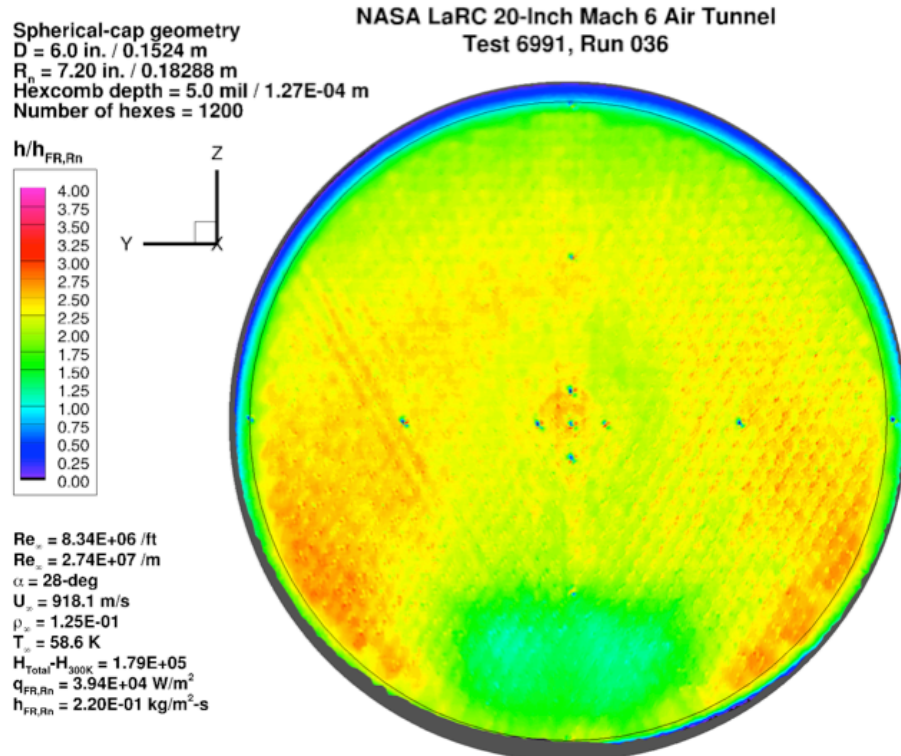


Figure 88. Test 6991, Run 36, $Re_\infty = 8.3 \times 10^6/\text{ft}$, spherical-cap 1200-0050.

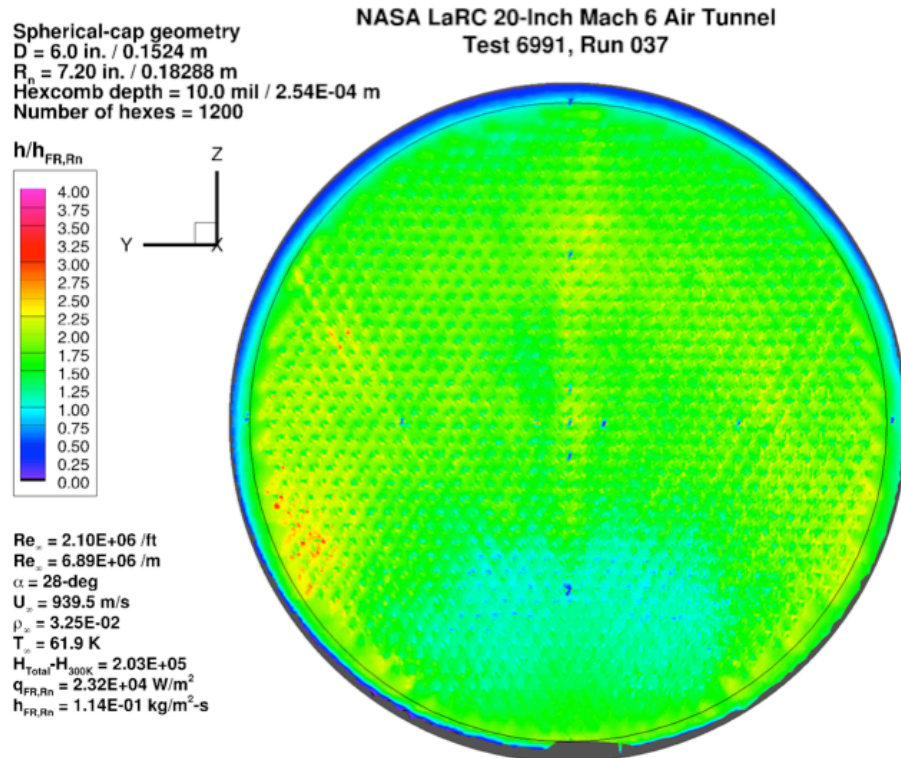


Figure 89. Test 6991, Run 37, $Re_\infty = 2.1 \times 10^6 / \text{ft}$, spherical-cap 1200-0100.

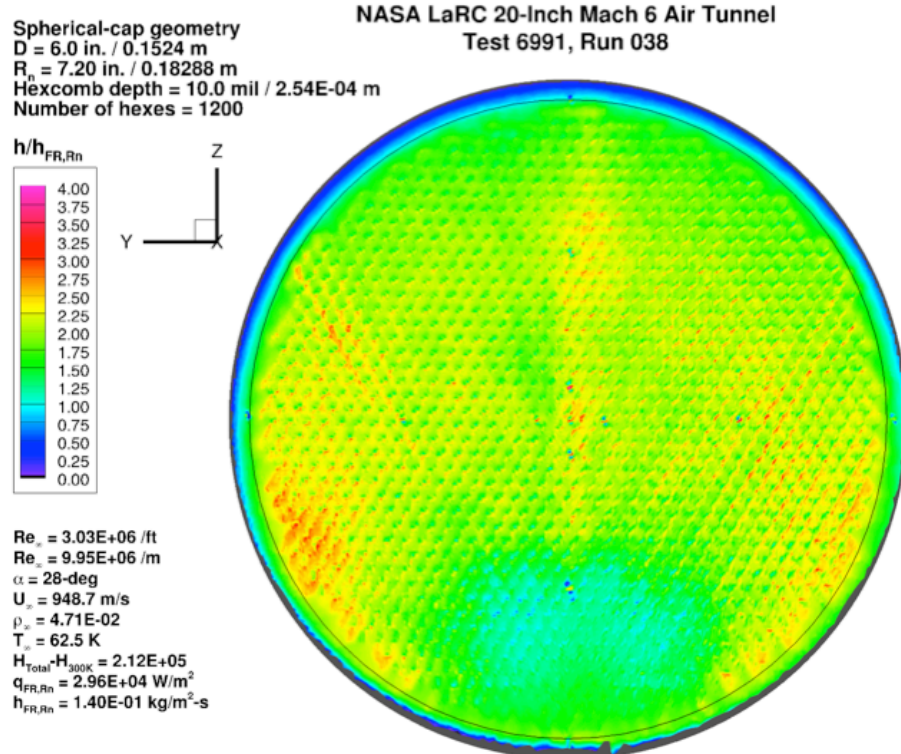


Figure 90. Test 6991, Run 38, $Re_\infty = 3.0 \times 10^6 / \text{ft}$, spherical-cap 1200-0100.

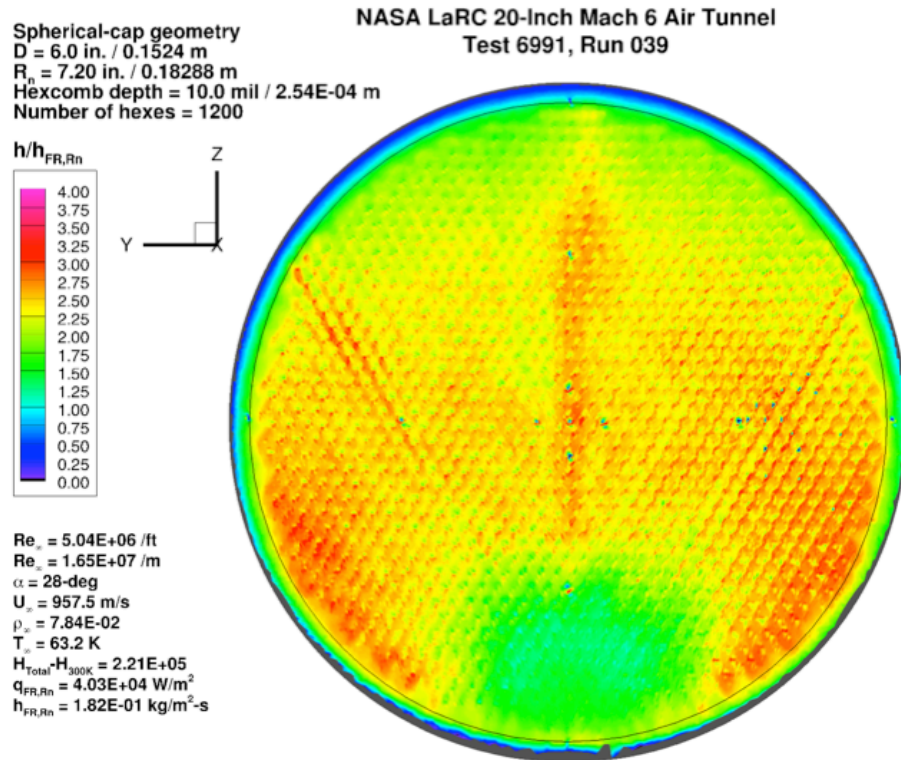


Figure 91. Test 6991, Run 39, $Re_\infty = 5.0 \times 10^6/\text{ft}$, spherical-cap 1200-0100.

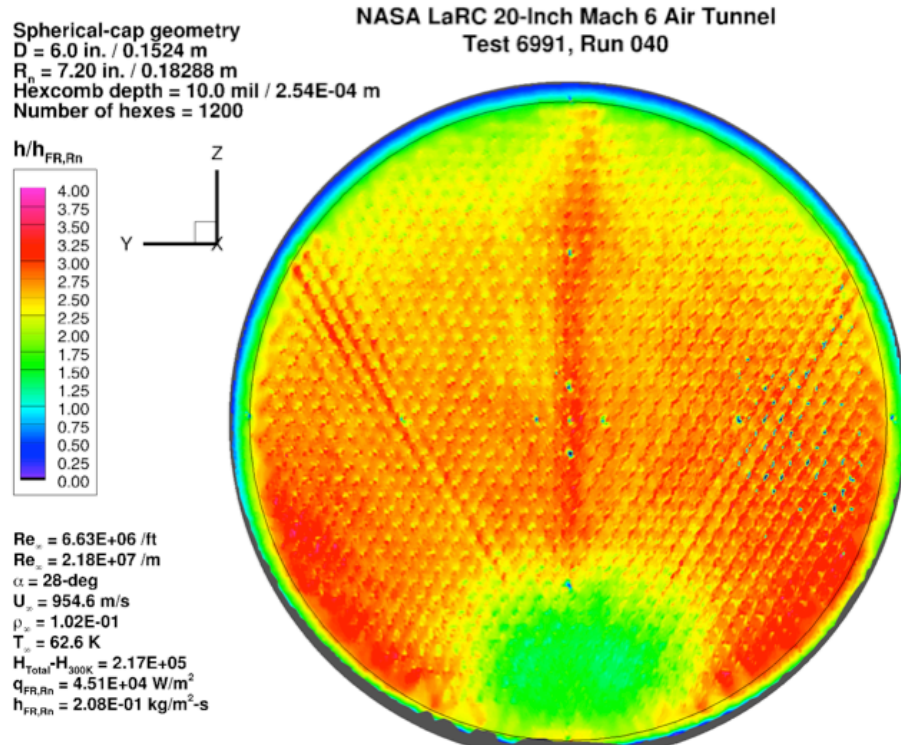


Figure 92. Test 6991, Run 40, $Re_\infty = 6.6 \times 10^6/\text{ft}$, spherical-cap 1200-0100.

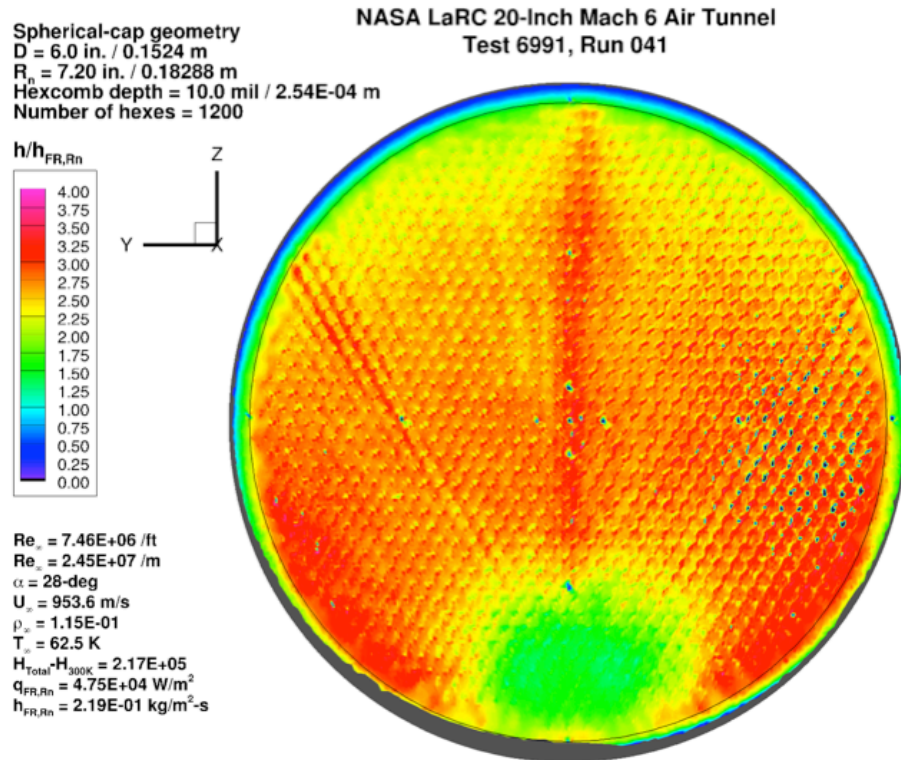


Figure 93. Test 6991, Run 41, $Re_\infty = 7.5 \times 10^6 / \text{ft}$, spherical-cap 1200-0100.

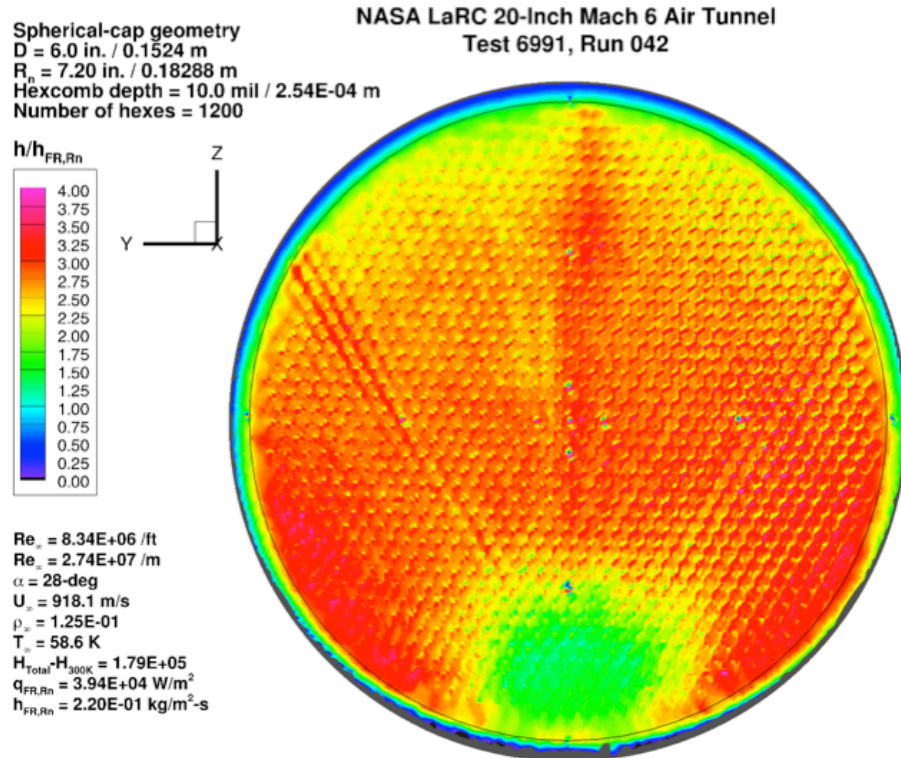


Figure 94. Test 6991, Run 42, $Re_\infty = 8.3 \times 10^6 / \text{ft}$, spherical-cap 1200-0100.

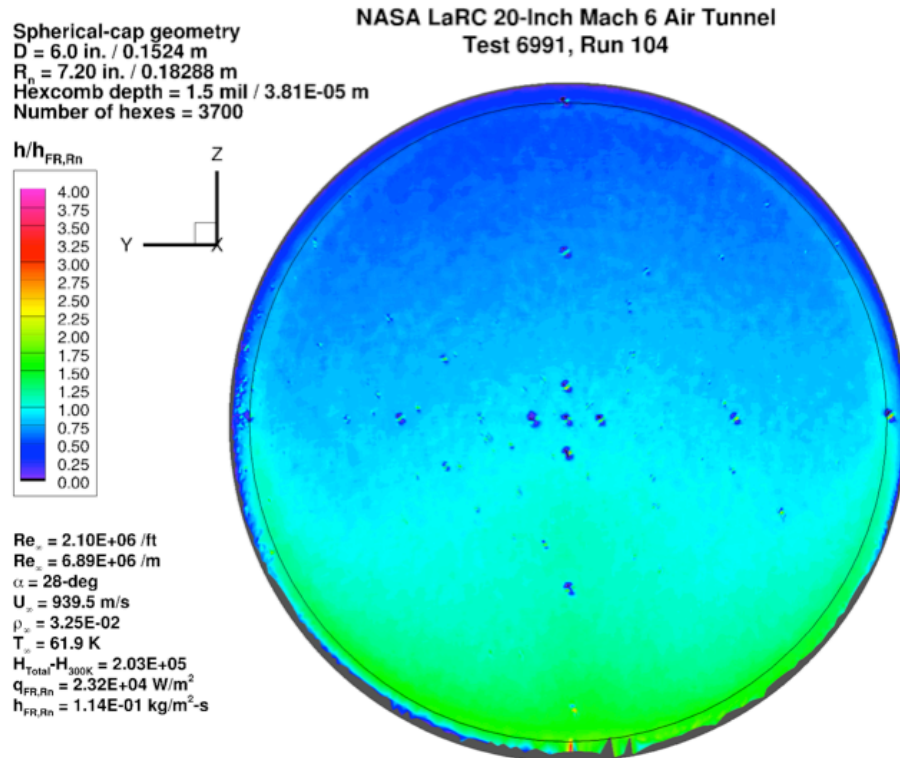


Figure 95. Test 6991, Run 104, $Re_\infty = 2.1 \times 10^6 / \text{ft}$, spherical-cap 3700-0015.

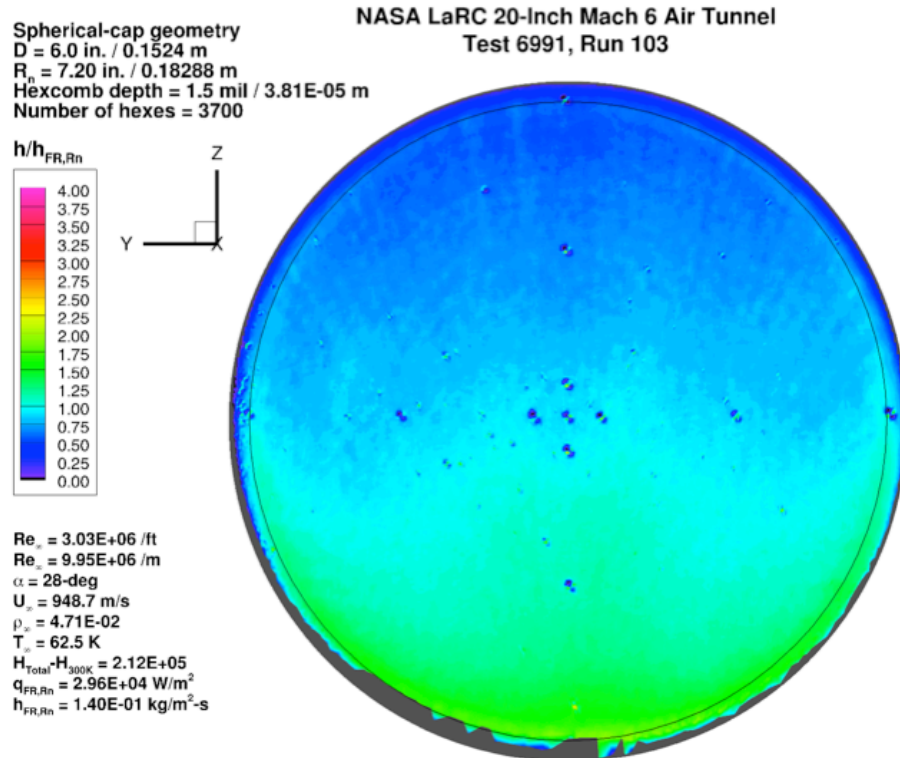


Figure 96. Test 6991, Run 103, $Re_\infty = 3.0 \times 10^6 / \text{ft}$, spherical-cap 3700-0015.

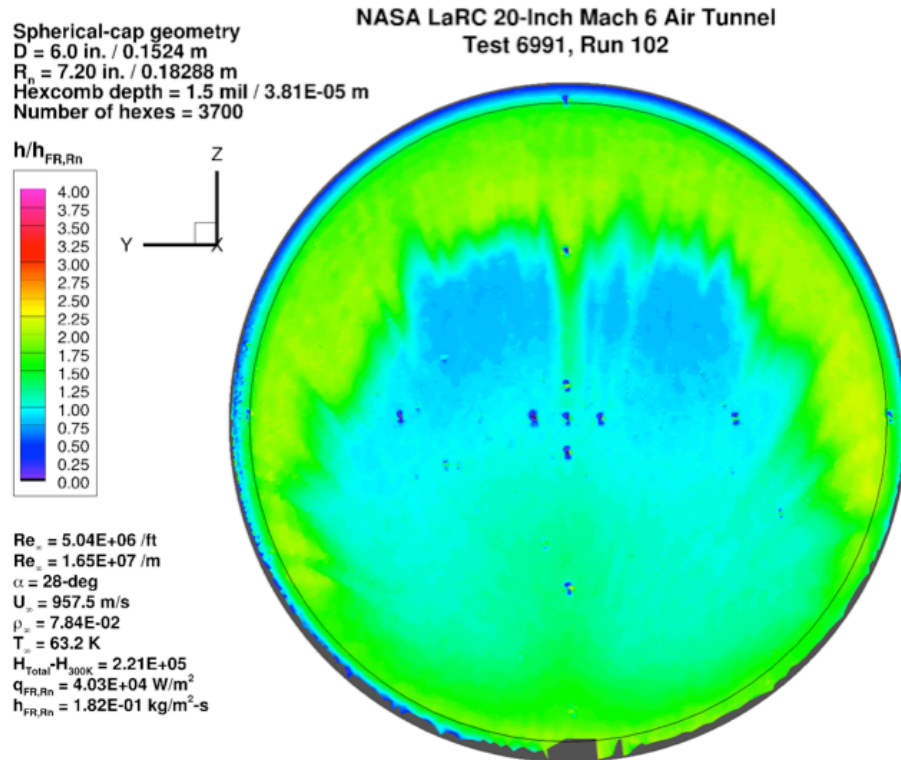


Figure 97. Test 6991, Run 102, $Re_\infty = 5.0 \times 10^6/\text{ft}$, spherical-cap 3700-0015.

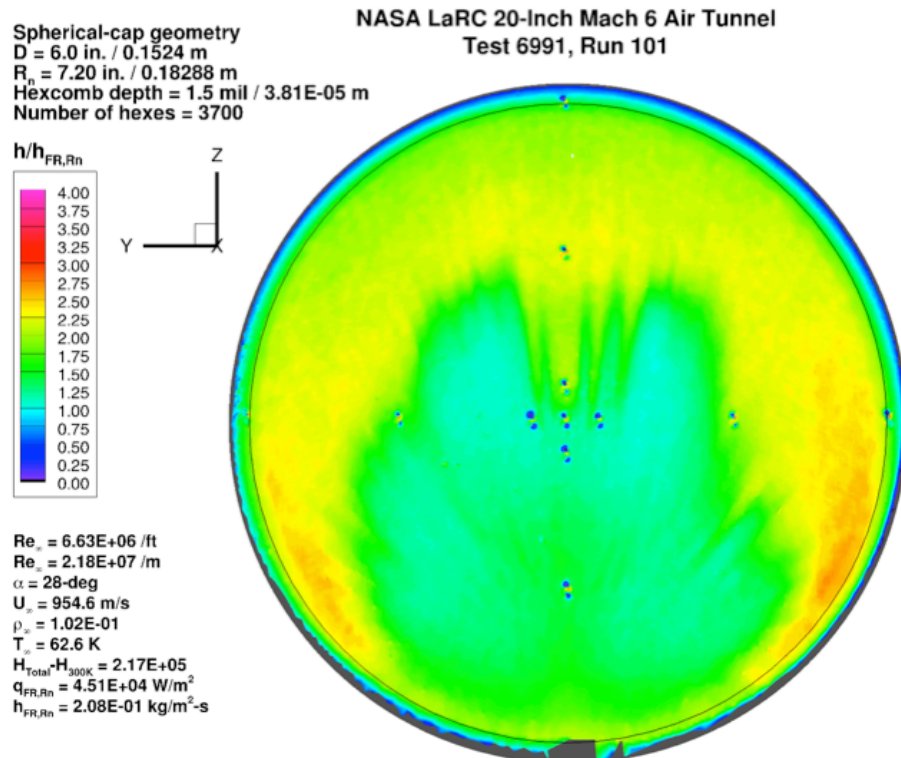


Figure 98. Test 6991, Run 101, $Re_\infty = 6.6 \times 10^6/\text{ft}$, spherical-cap 3700-0015.

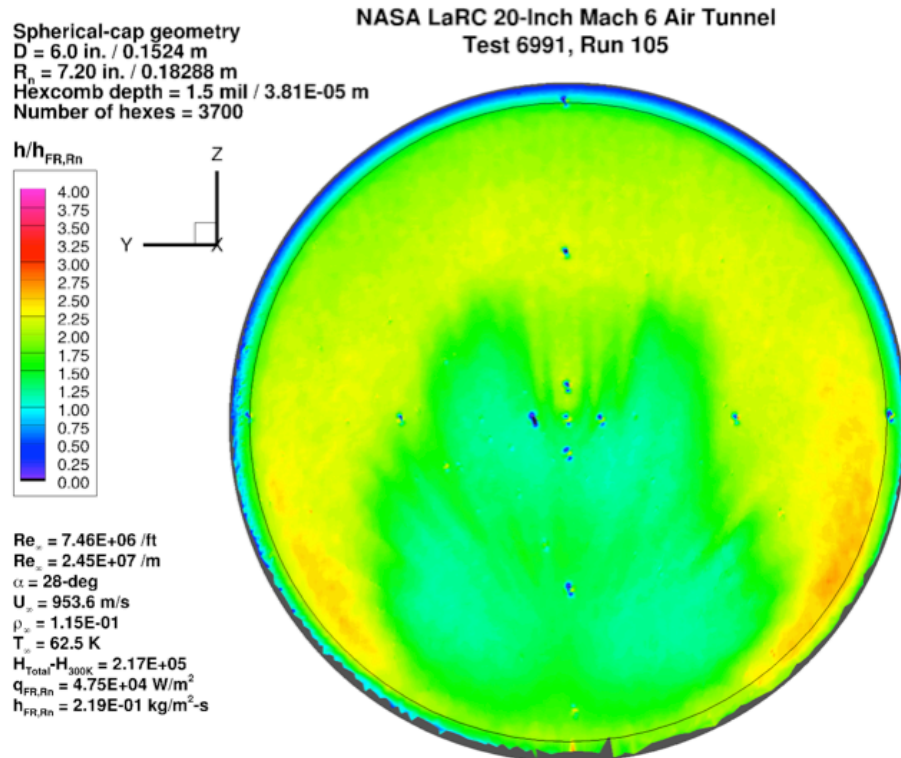


Figure 99. Test 6991, Run 105, $Re_\infty = 7.5 \times 10^6 / \text{ft}$, spherical-cap 3700-0015.

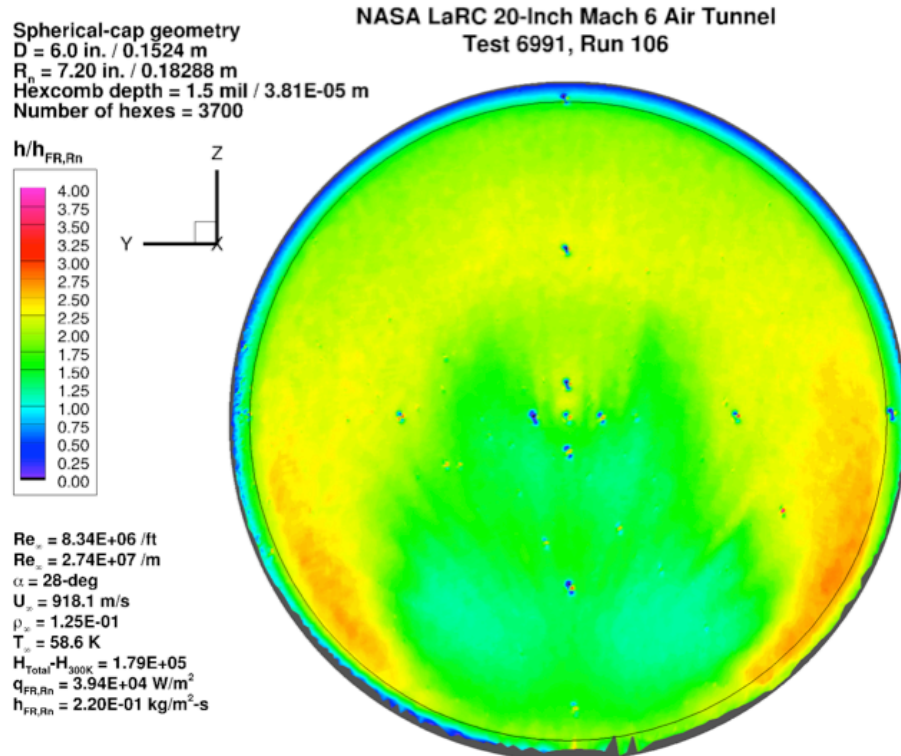


Figure 100. Test 6991, Run 106, $Re_\infty = 8.3 \times 10^6 / \text{ft}$, spherical-cap 3700-0015.

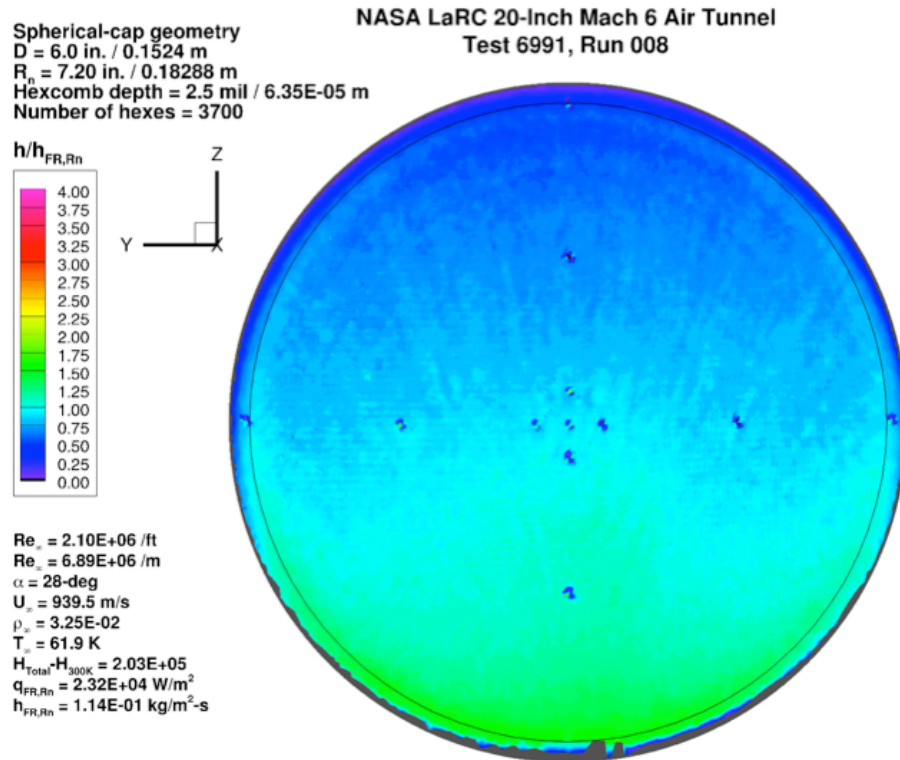


Figure 101. Test 6991, Run 8, $Re_\infty = 2.1 \times 10^6/\text{ft}$, spherical-cap 3700-0025.

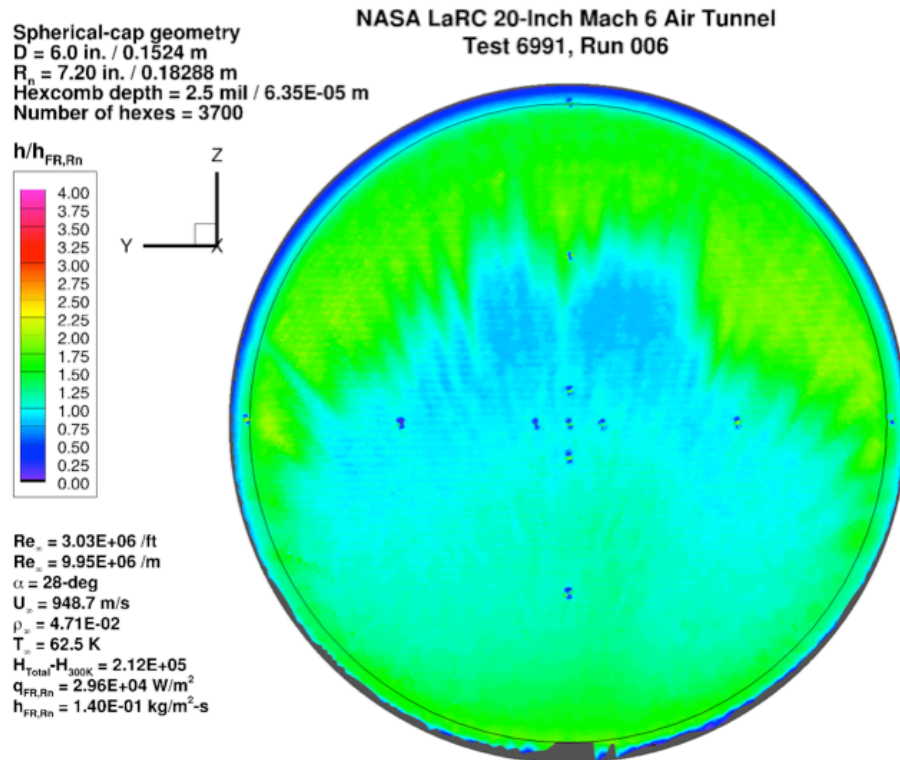


Figure 102. Test 6991, Run 6, $Re_\infty = 3.0 \times 10^6/\text{ft}$, spherical-cap 3700-0025.

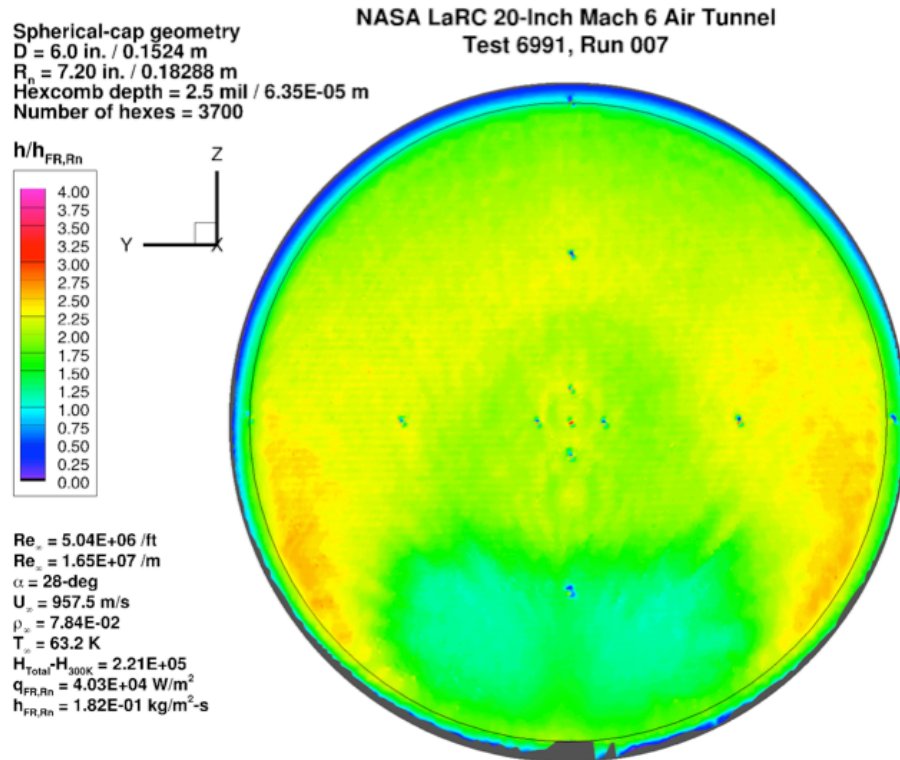


Figure 103. Test 6991, Run 7, $Re_\infty = 5.0 \times 10^6/\text{ft}$, spherical-cap 3700-0025.

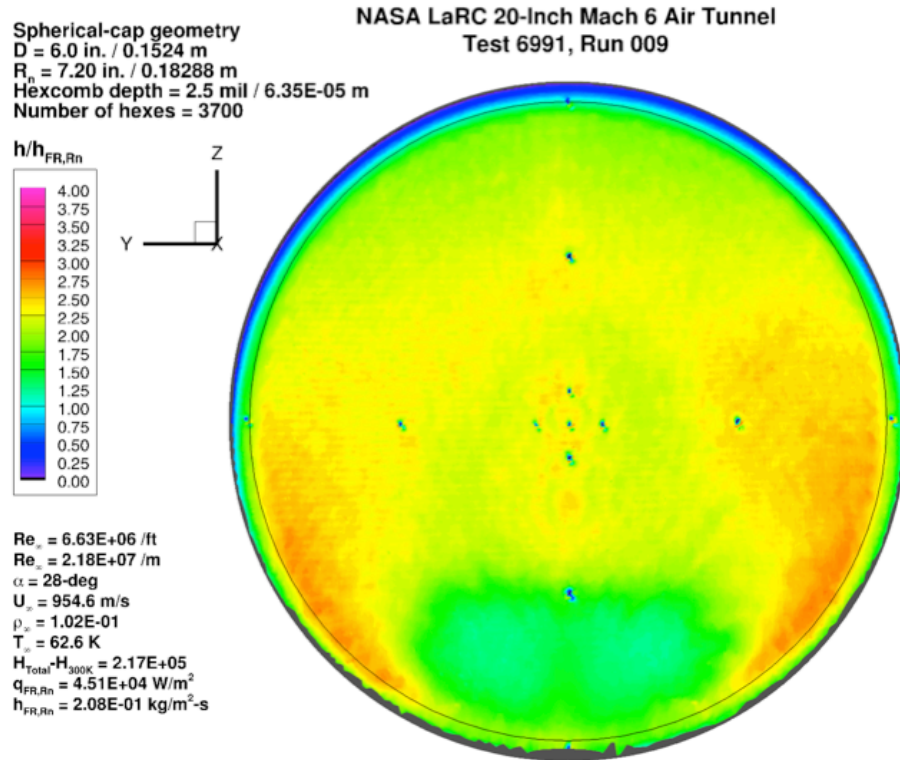


Figure 104. Test 6991, Run 9, $Re_\infty = 6.6 \times 10^6/\text{ft}$, spherical-cap 3700-0025.

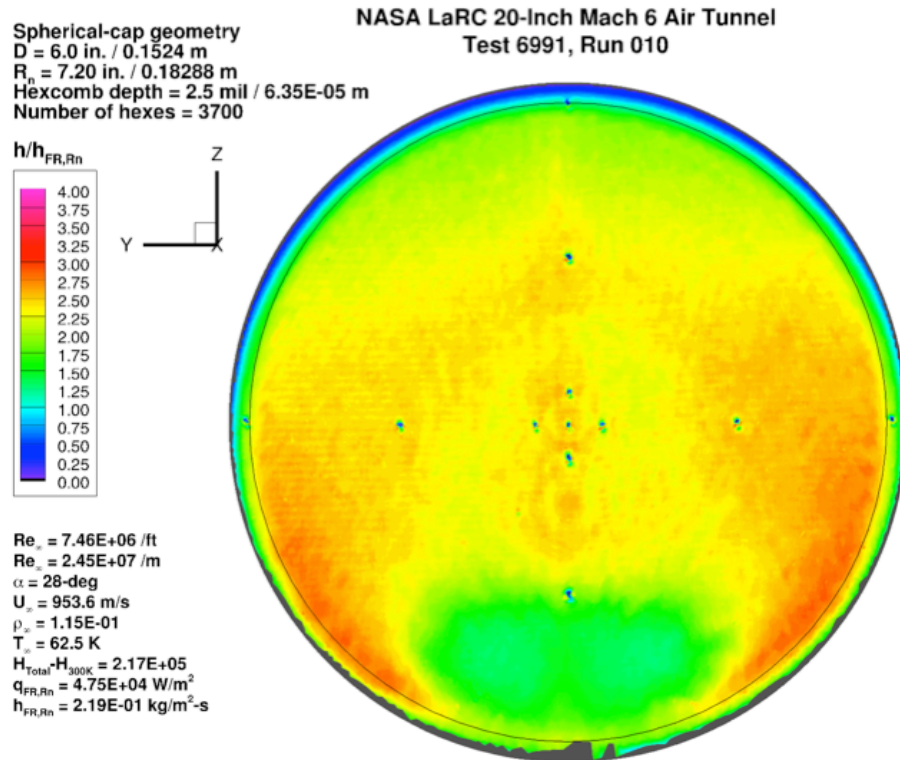


Figure 105. Test 6991, Run 10, $Re_\infty = 7.5 \times 10^6/\text{ft}$, spherical-cap 3700-0025.

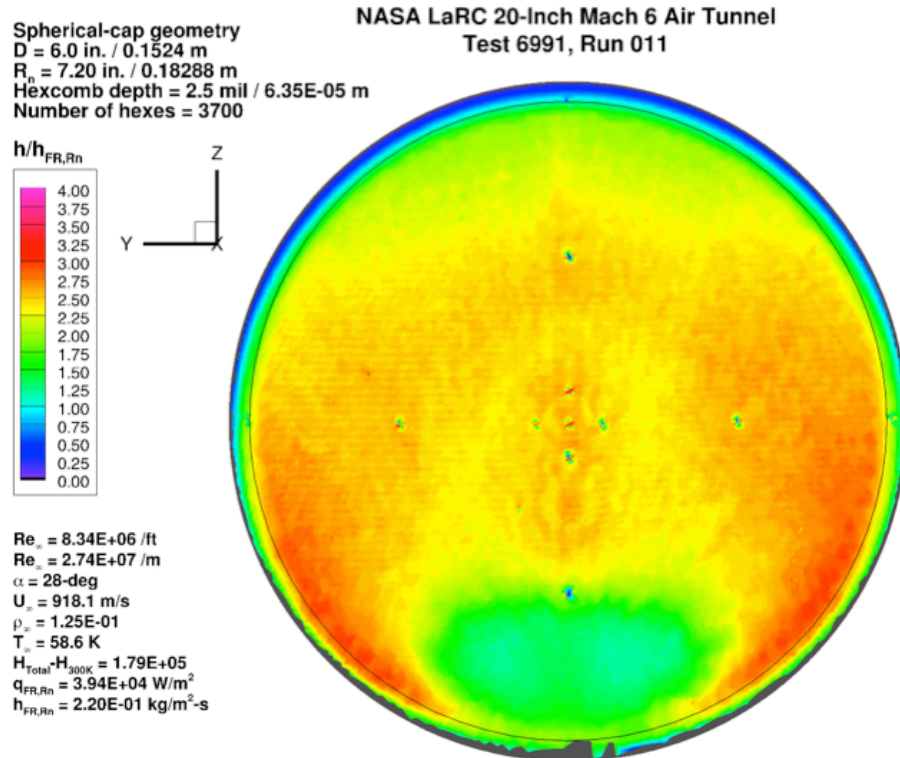


Figure 106. Test 6991, Run 11, $Re_\infty = 8.3 \times 10^6/\text{ft}$, spherical-cap 3700-0025.

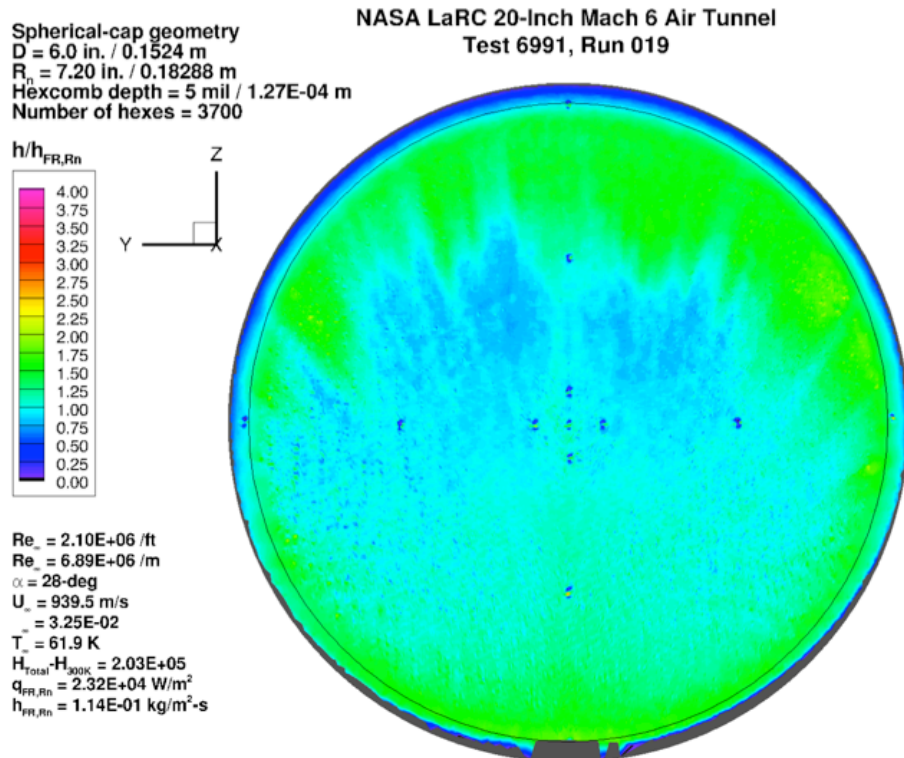


Figure 107. Test 6991, Run 19, $Re_\infty = 2.1 \times 10^6 / \text{ft}$, spherical-cap 3700-0050.

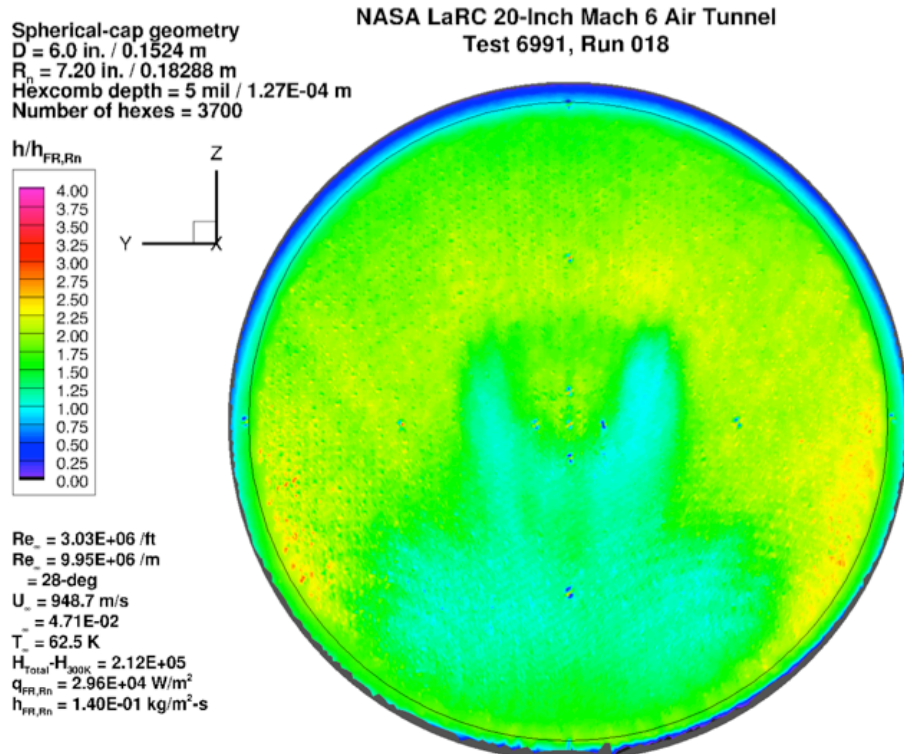


Figure 108. Test 6991, Run 18, $Re_\infty = 3.0 \times 10^6 / \text{ft}$, spherical-cap 3700-0050.

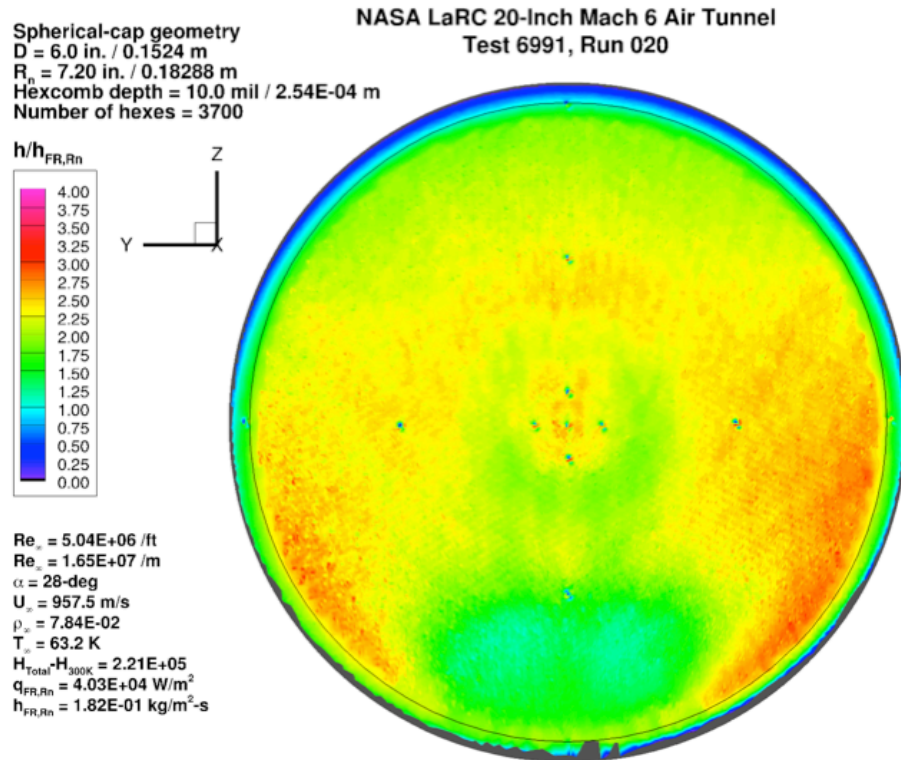


Figure 109. Test 6991, Run 20, $\text{Re}_{\infty} = 5.0 \times 10^6/\text{ft}$, spherical-cap 3700-0050.

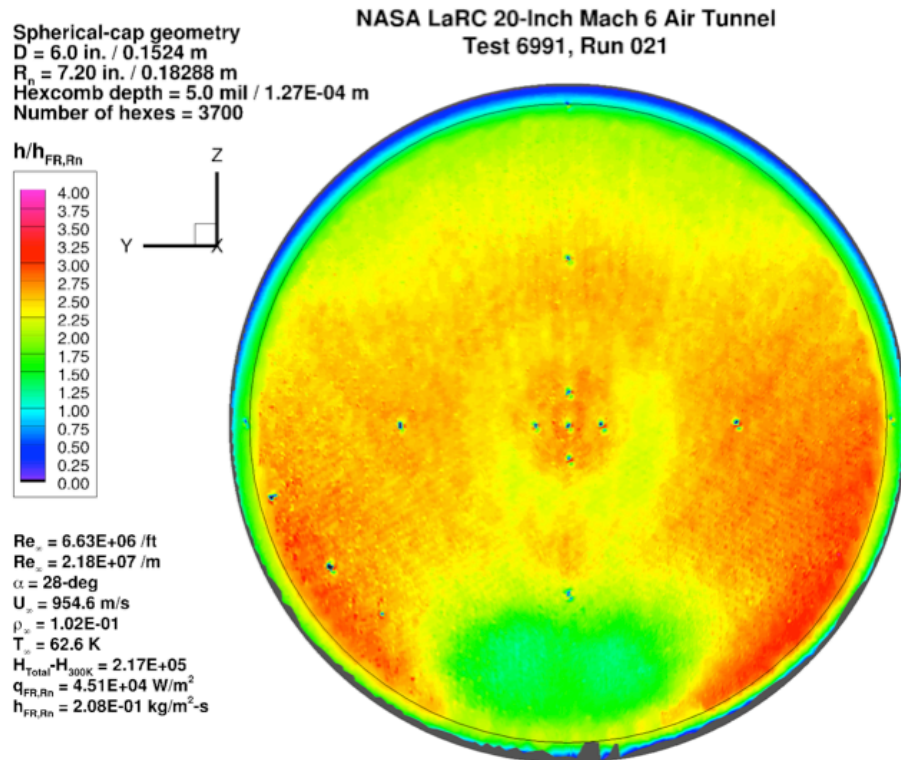


Figure 110. Test 6991, Run 21, $\text{Re}_{\infty} = 6.6 \times 10^6/\text{ft}$, spherical-cap 3700-0050.

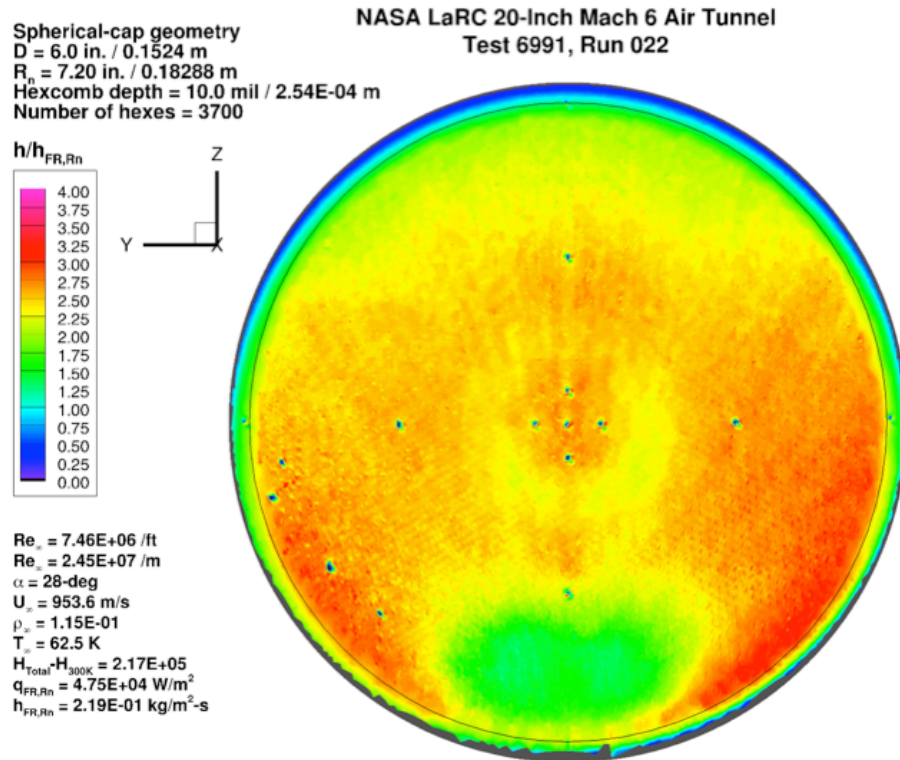


Figure 111. Test 6991, Run 22, $Re_\infty = 7.5 \times 10^6/\text{ft}$, spherical-cap 3700-0050.

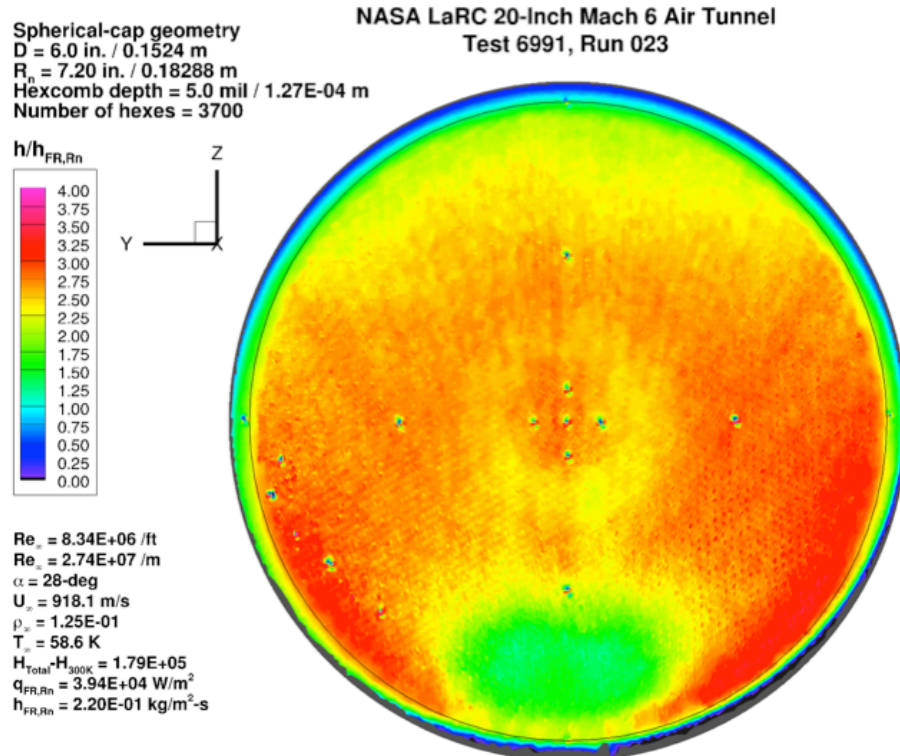


Figure 112. Test 6991, Run 23, $Re_\infty = 8.3 \times 10^6/\text{ft}$, spherical-cap 3700-0050.

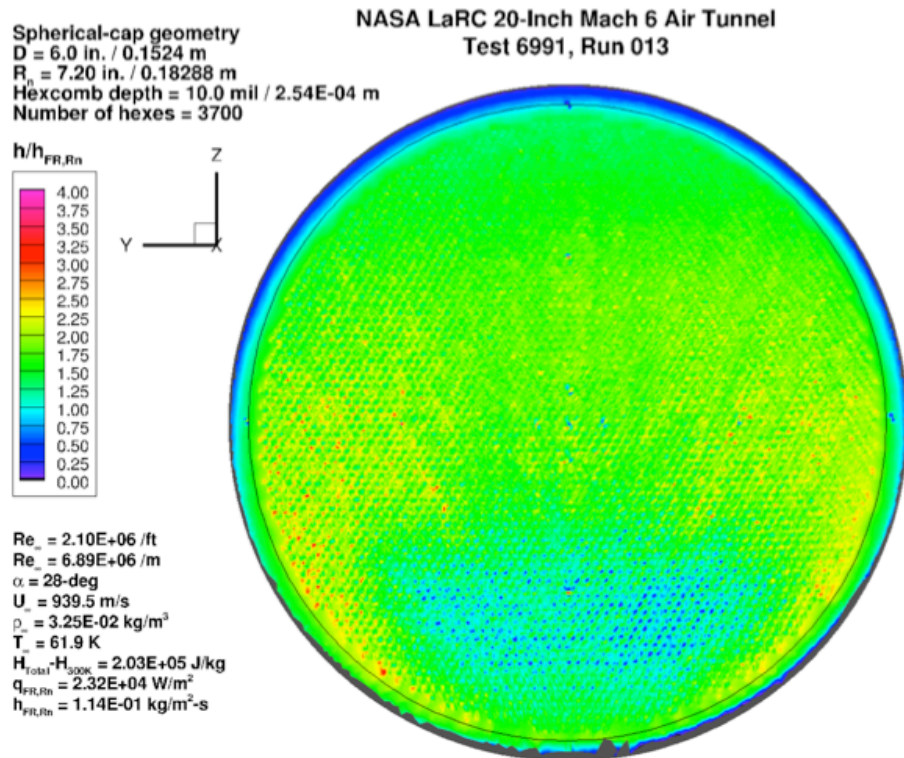


Figure 113. Test 6991, Run 13, $Re_\infty = 2.1 \times 10^6/\text{ft}$, spherical-cap 3700-0100.

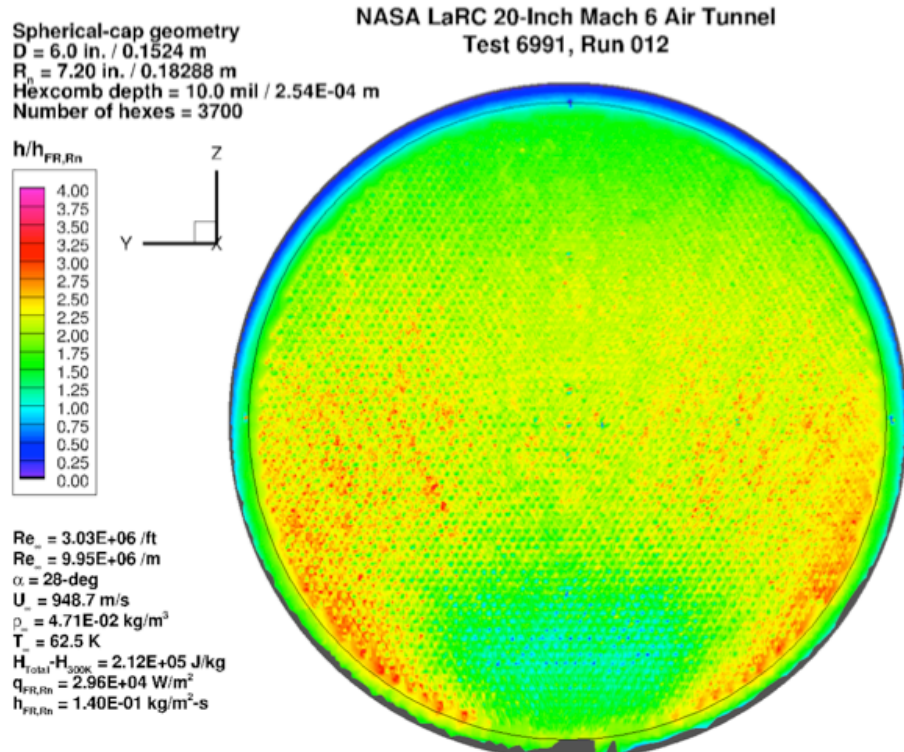


Figure 114. Test 6991, Run 12, $Re_\infty = 3.0 \times 10^6/\text{ft}$, spherical-cap 3700-0100.

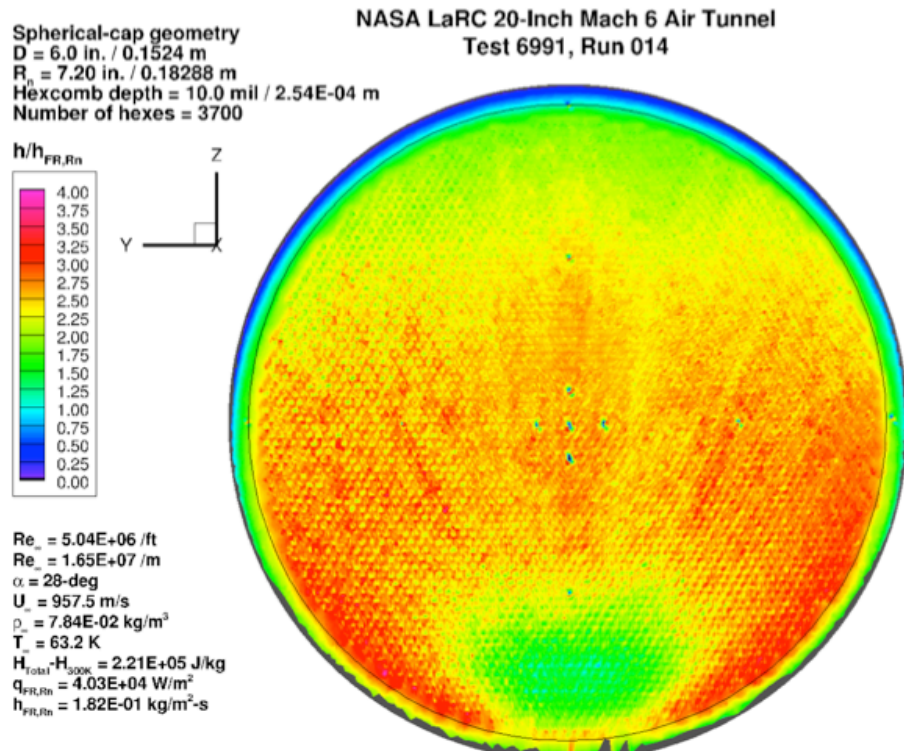


Figure 115. Test 6991, Run 14, $Re_\infty = 5.0 \times 10^6/\text{ft}$, spherical-cap 3700-0100.

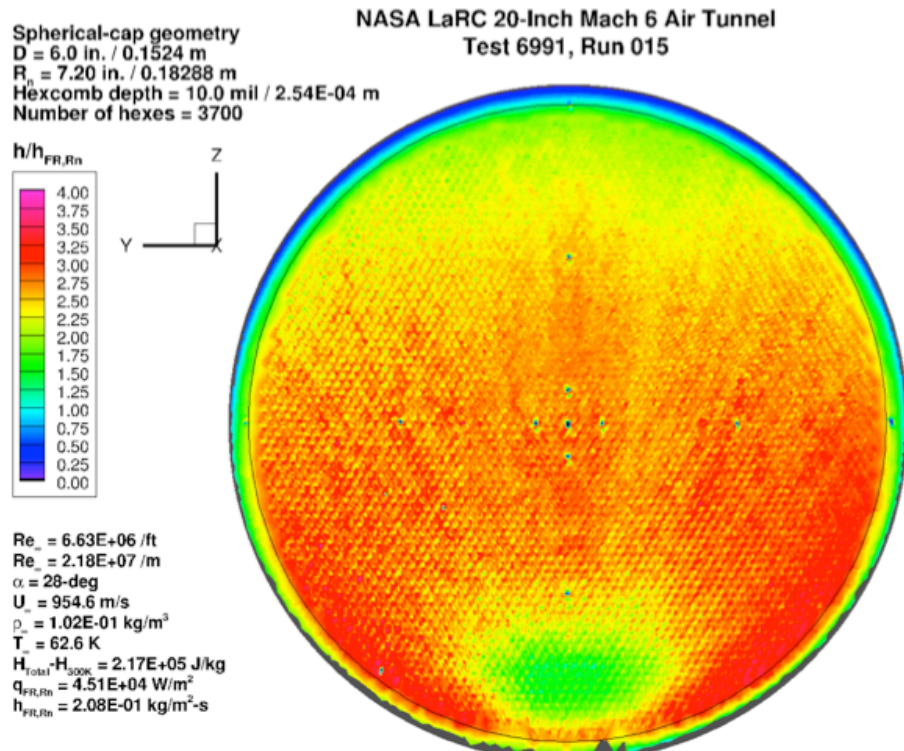


Figure 116. Test 6991, Run 15, $Re_\infty = 6.6 \times 10^6/\text{ft}$, spherical-cap 3700-0100.

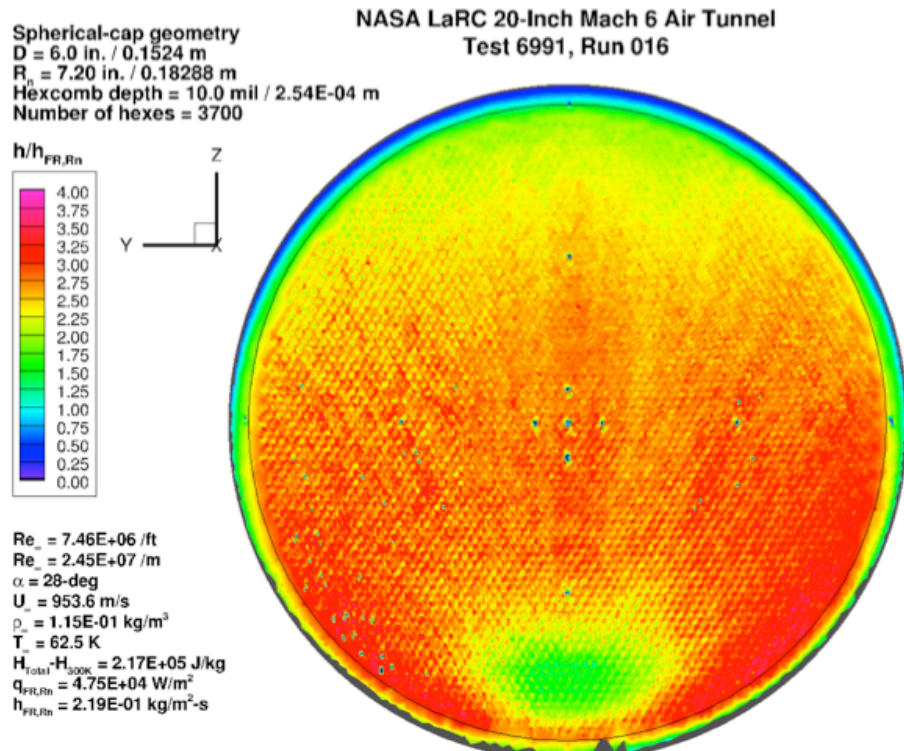


Figure 117. Test 6991, Run 16, $Re_\infty = 7.5 \times 10^6 / \text{ft}$, spherical-cap 3700-0100.

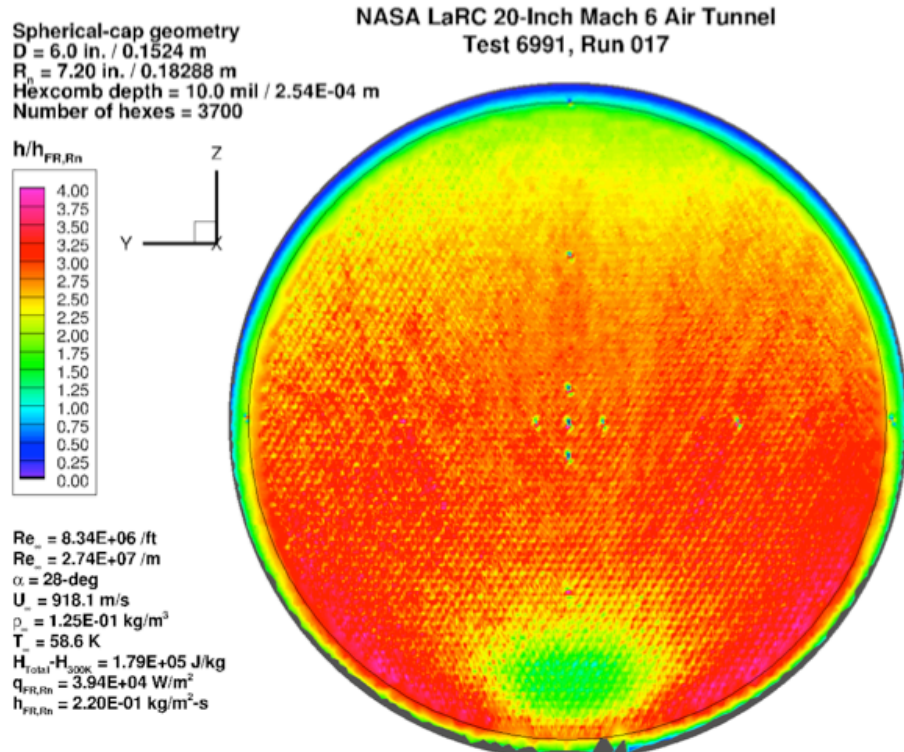


Figure 118. Test 6991, Run 17, $Re_\infty = 8.3 \times 10^6 / \text{ft}$, spherical-cap 3700-0100.

Appendix B. Sphere-Cone Geometry Global Heating Images

Global heating images for the sphere-cone geometry from Test 6991 in the LAL 20-Inch Mach 6 Air Tunnel are presented in this Appendix in Figure 119 - Figure 166.

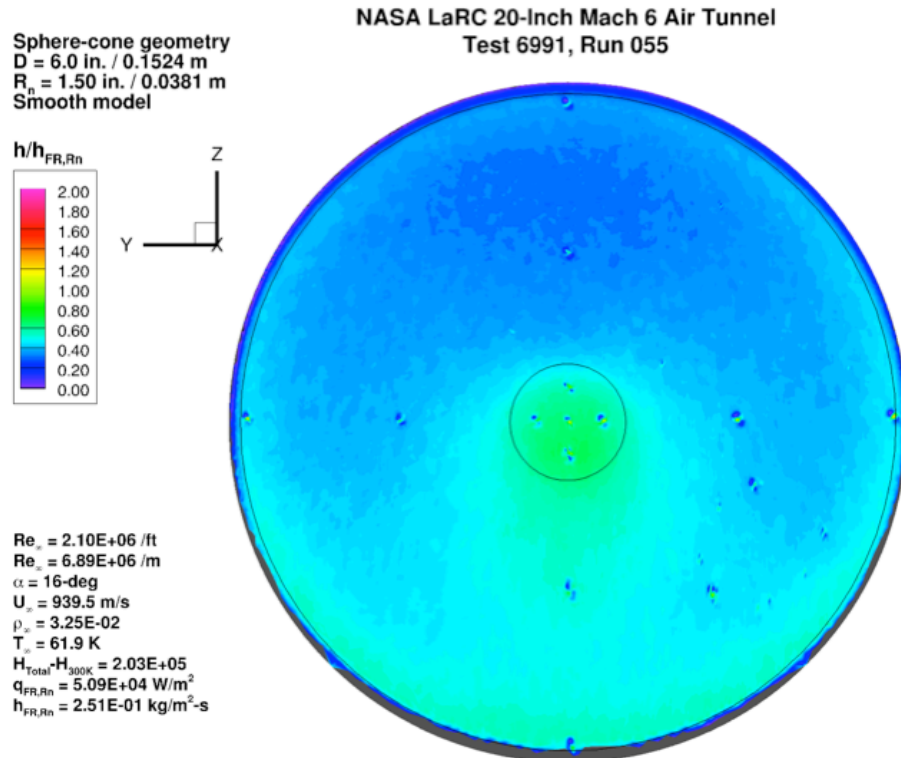


Figure 119. Test 6991, Run 55, $Re_\infty = 2.1 \times 10^6/\text{ft}$, sphere-cone, smooth OML.

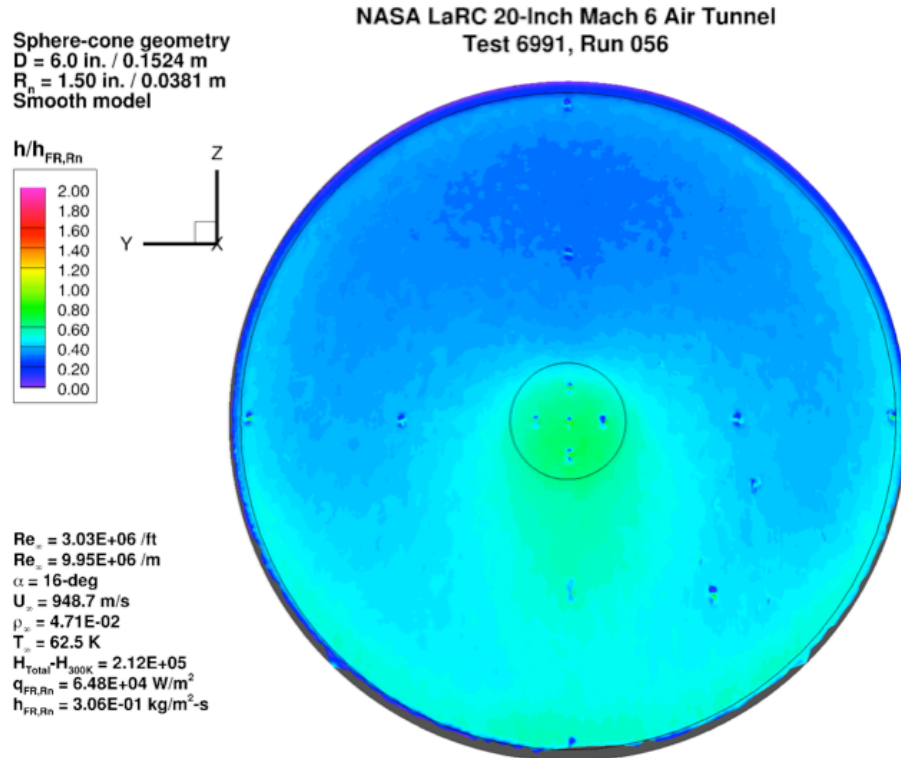


Figure 120. Test 6991, Run 56, $Re_\infty = 3.0 \times 10^6/\text{ft}$, sphere-cone, smooth OML.

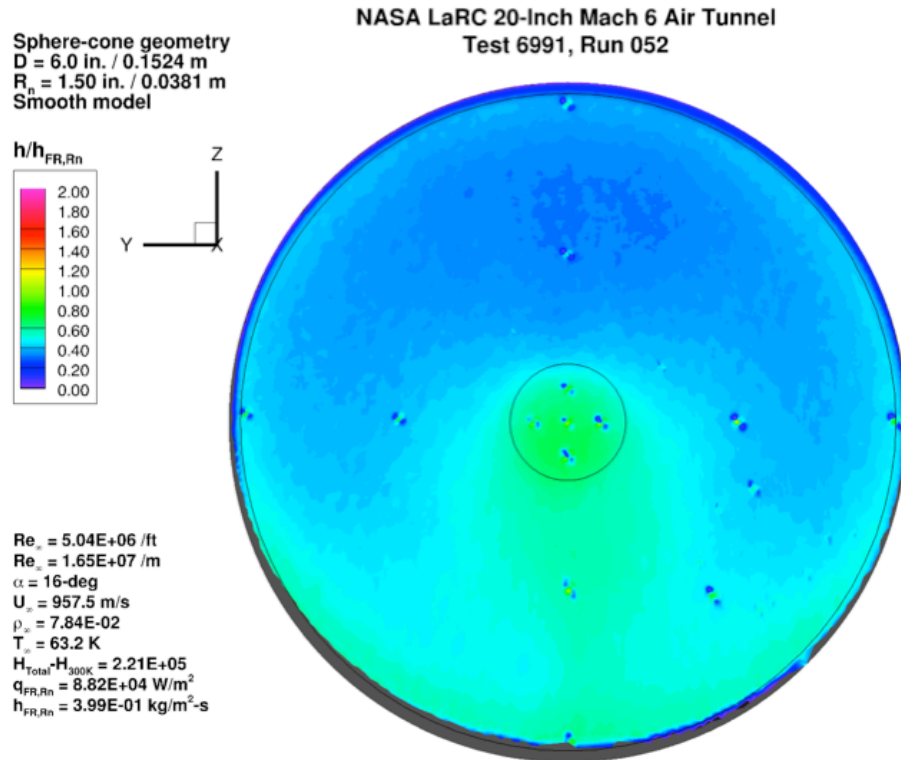


Figure 121. Test 6991, Run 52, $Re_{\infty} = 5.0 \times 10^6/\text{ft}$, sphere-cone, smooth OML.

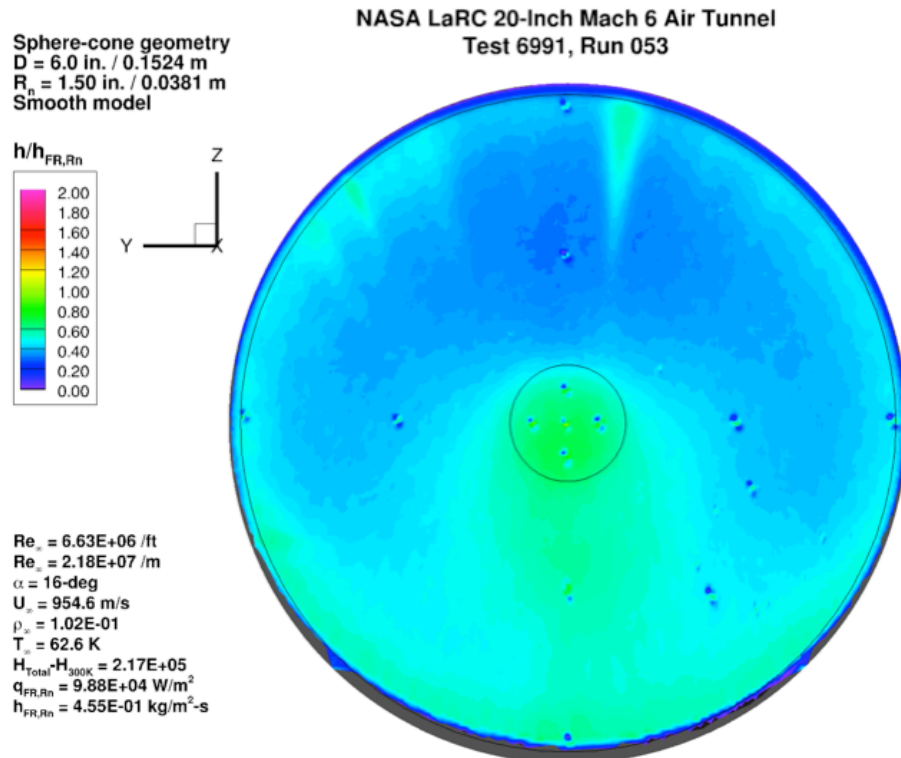


Figure 122. Test 6991, Run 53, $Re_{\infty} = 6.6 \times 10^6/\text{ft}$, sphere-cone, smooth OML.

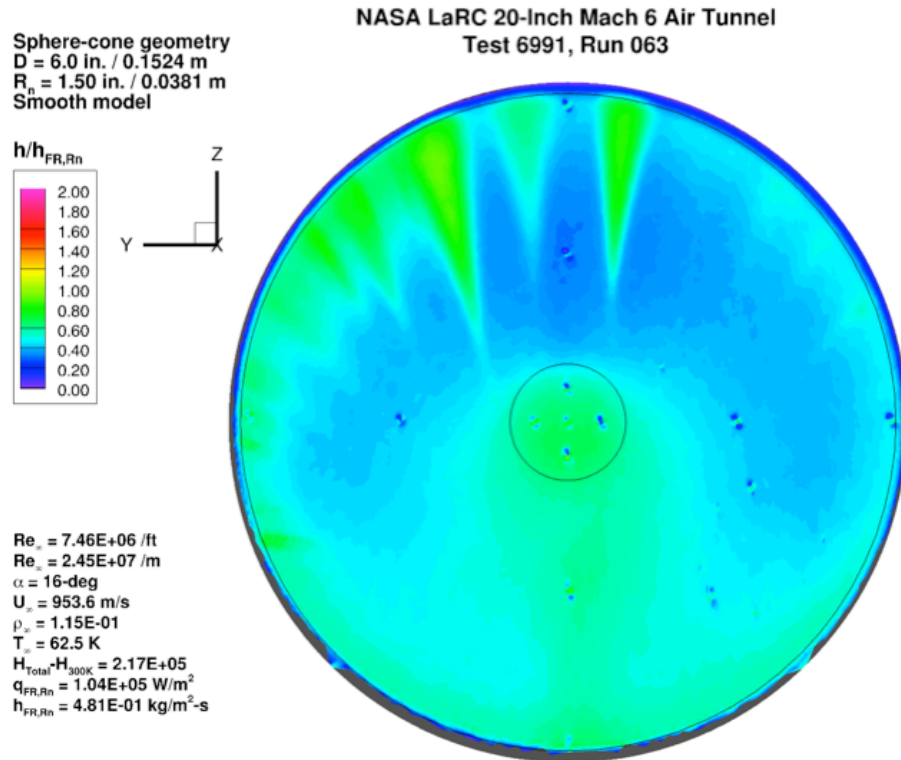


Figure 123. Test 6991, Run 63, $Re_{\infty} = 7.5 \times 10^6 / \text{ft}$, sphere-cone, smooth OML.

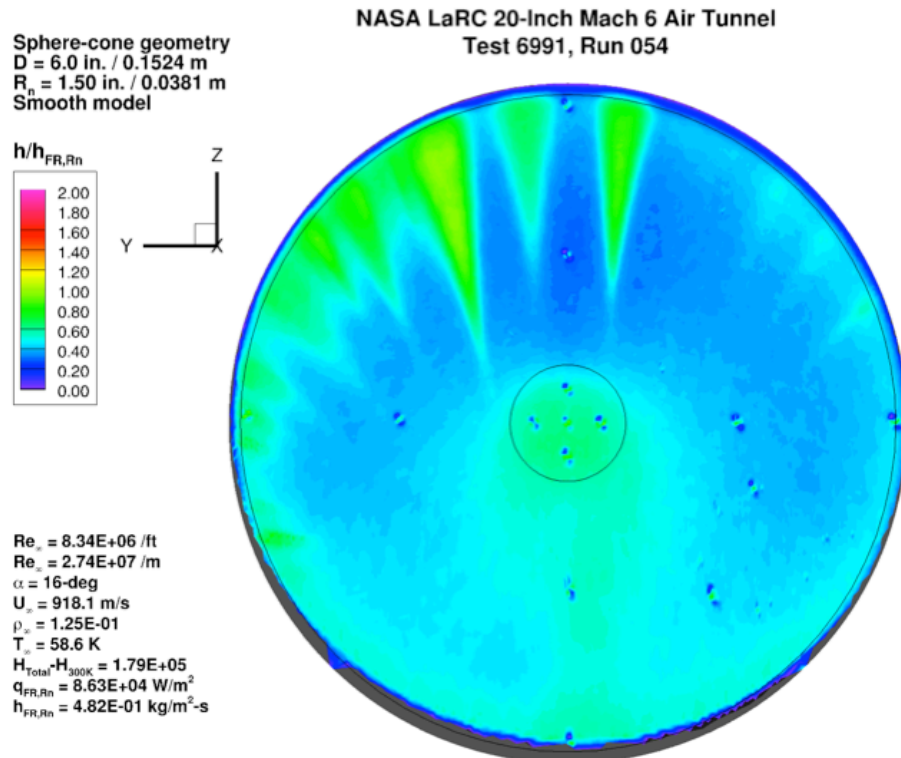


Figure 124. Test 6991, Run 54, $Re_{\infty} = 8.3 \times 10^6 / \text{ft}$, sphere-cone, smooth OML.

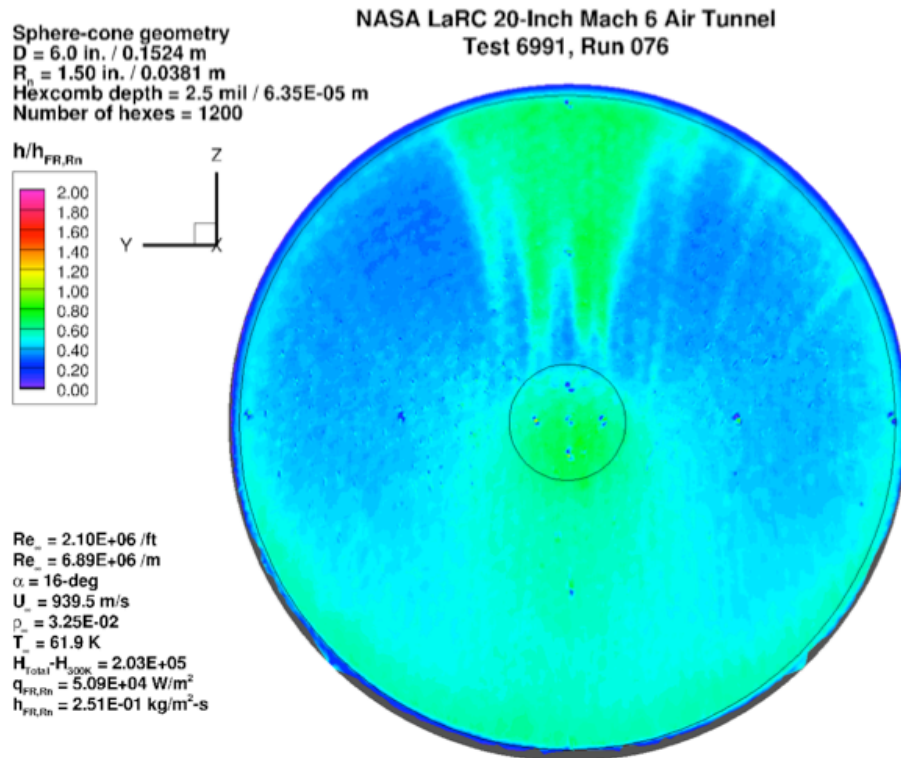


Figure 125. Test 6991, Run 76, $Re_\infty = 2.1 \times 10^6/\text{ft}$, sphere-cone 1200-0025.

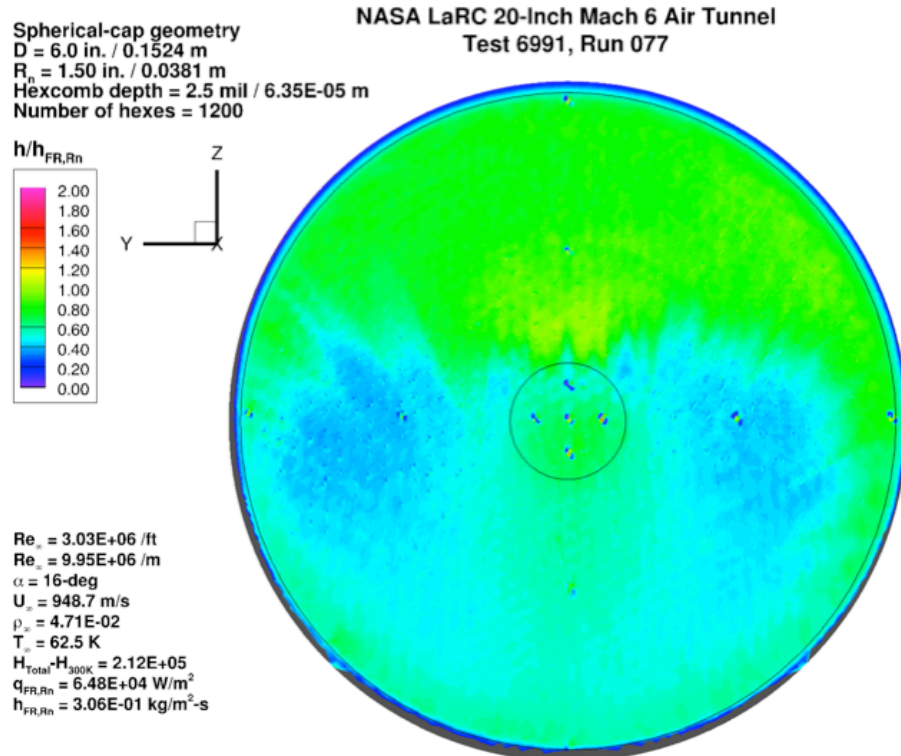


Figure 126. Test 6991, Run 77, $Re_\infty = 3.0 \times 10^6/\text{ft}$, sphere-cone 1200-0025.

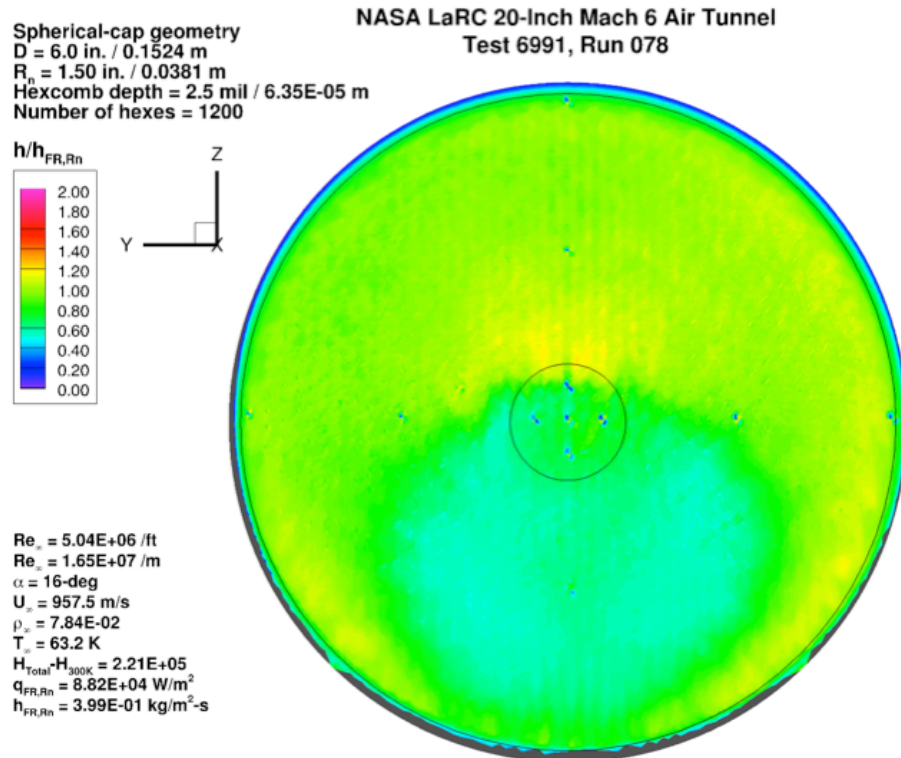


Figure 127. Test 6991, Run 78, $Re_\infty = 5.0 \times 10^6/\text{ft}$, sphere-cone 1200-0025.

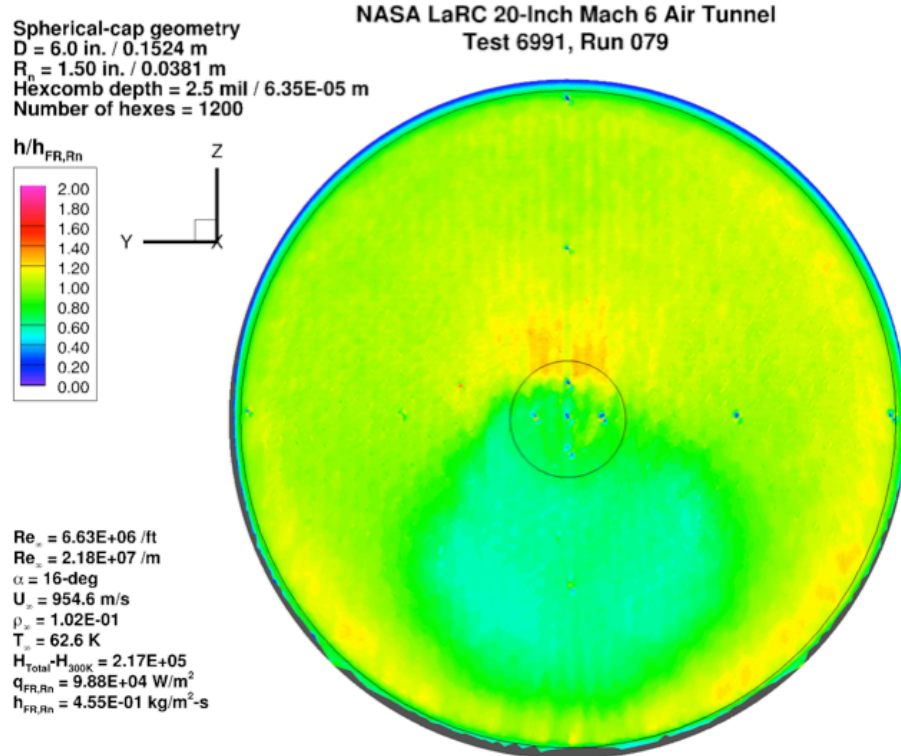


Figure 128. Test 6991, Run 79, $Re_\infty = 6.6 \times 10^6/\text{ft}$, sphere-cone 1200-0025.

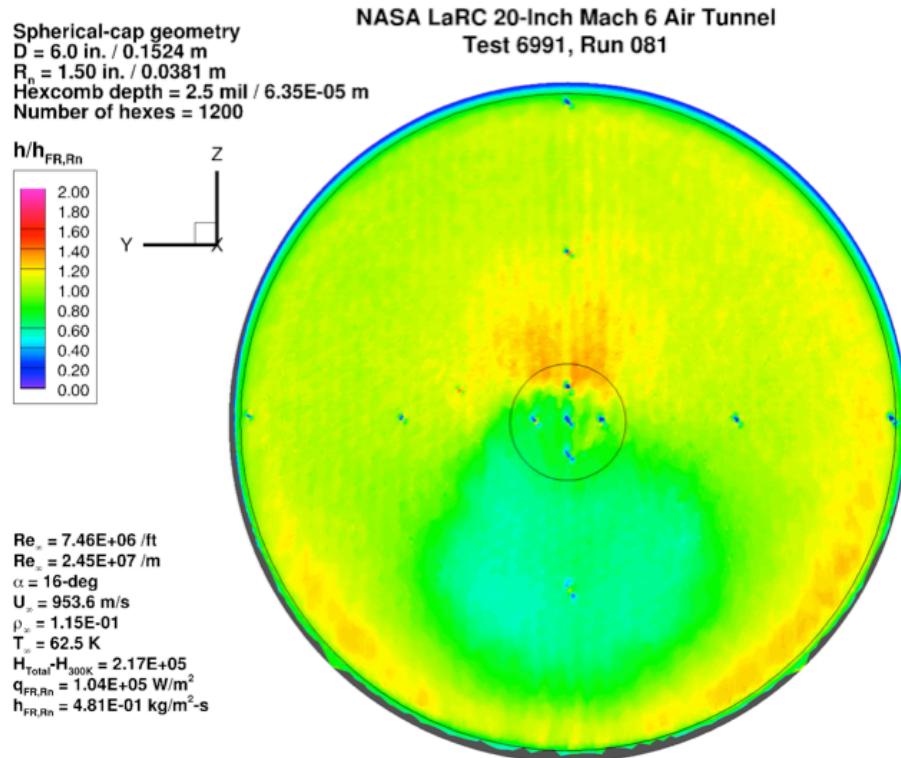


Figure 129. Test 6991, Run 81, $Re_\infty = 7.5 \times 10^6/\text{ft}$, sphere-cone 1200-0025.

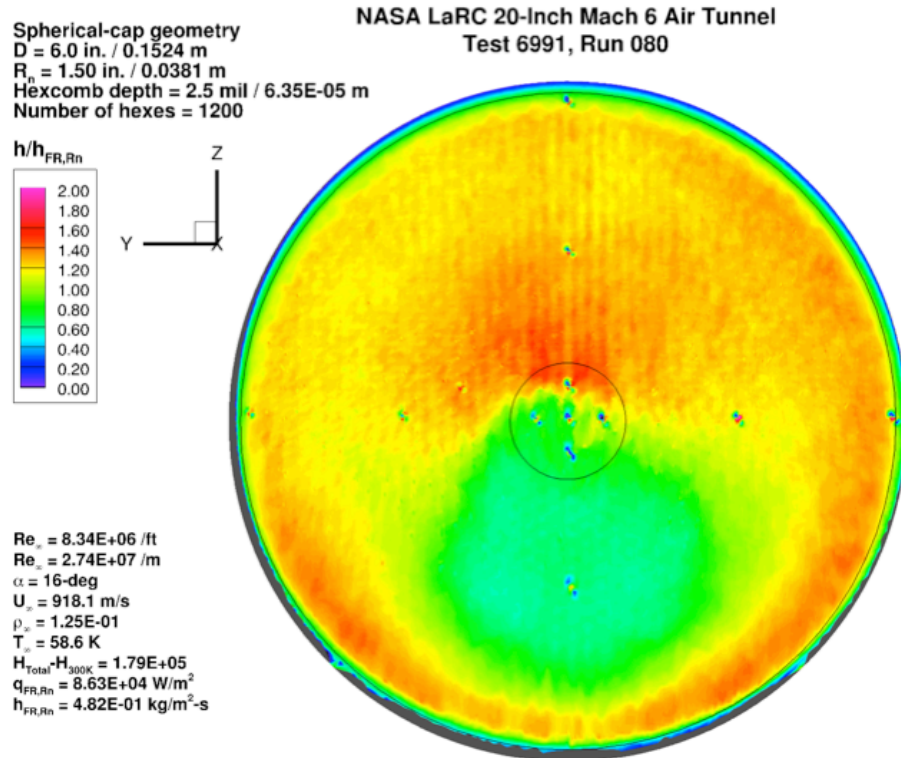


Figure 130. Test 6991, Run 80, $Re_\infty = 8.3 \times 10^6/\text{ft}$, sphere-cone1200-0025.

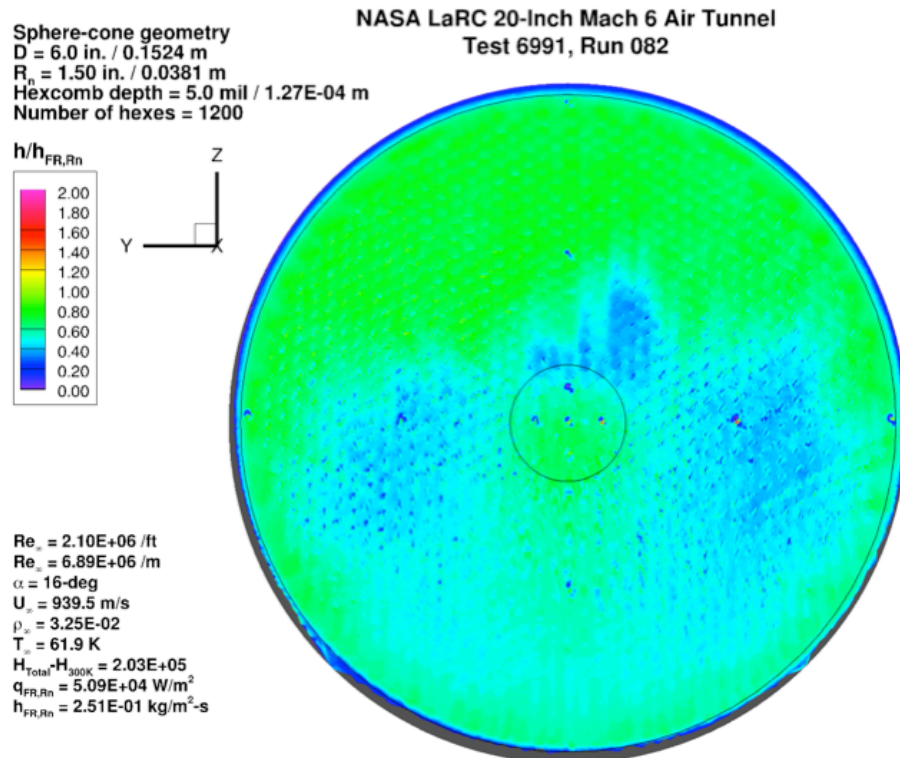


Figure 131. Test 6991, Run 82, $Re_\infty = 2.1 \times 10^6/\text{ft}$, sphere-cone 1200-0050.

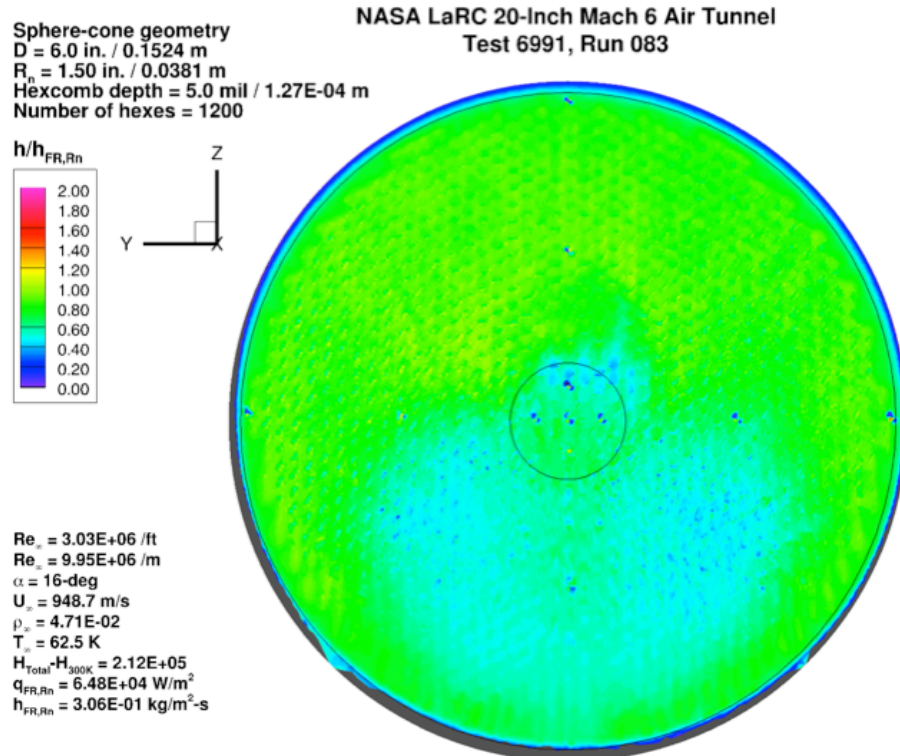


Figure 132. Test 6991, Run 83, $Re_\infty = 3.0 \times 10^6/\text{ft}$, spherical-cap 1200-0050.

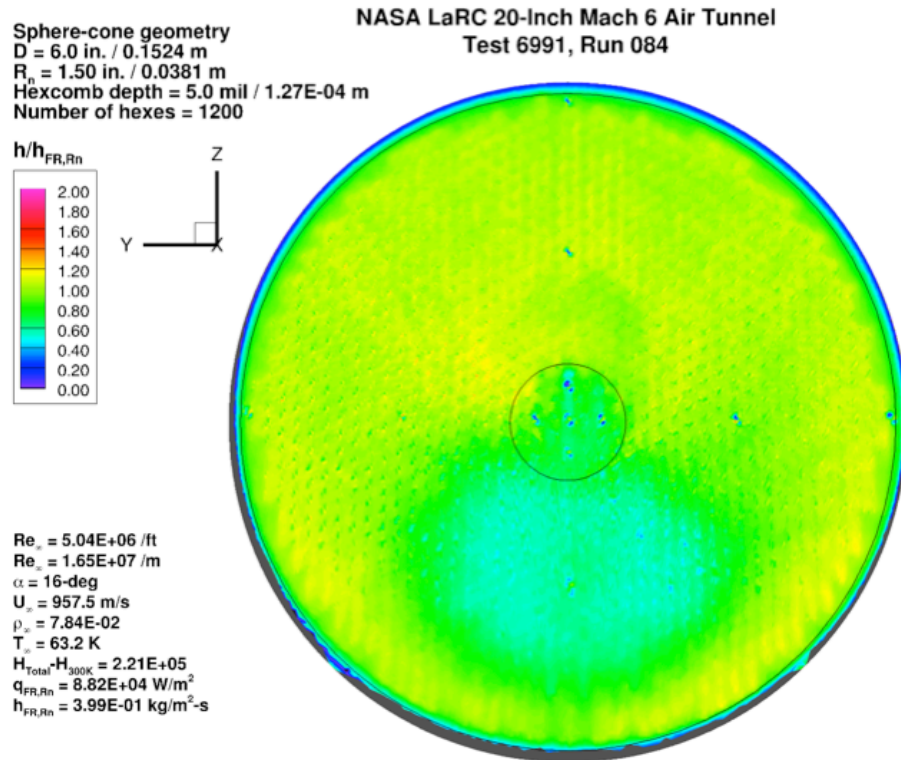


Figure 133. Test 6991, Run 84, $Re_\infty = 5.0 \times 10^6 / \text{ft}$, sphere-cone 1200-0050.

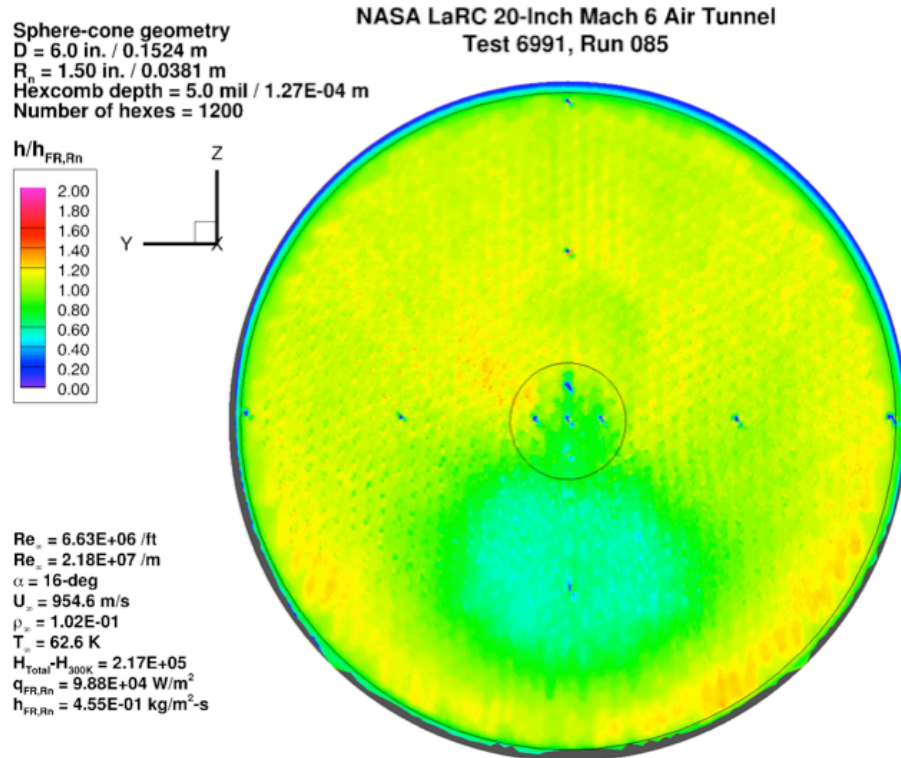


Figure 134. Test 6991, Run 85, $Re_\infty = 6.6 \times 10^6 / \text{ft}$, sphere-cone 1200-0050.

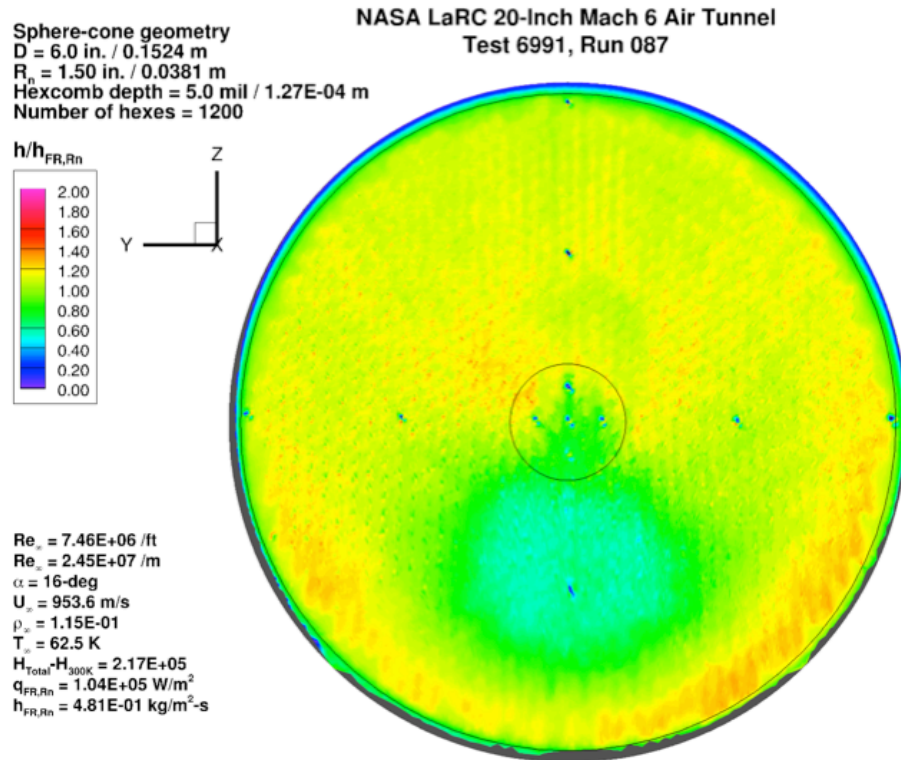


Figure 135. Test 6991, Run 87, $Re_\infty = 7.5 \times 10^6/\text{ft}$, sphere-cone 1200-0050.

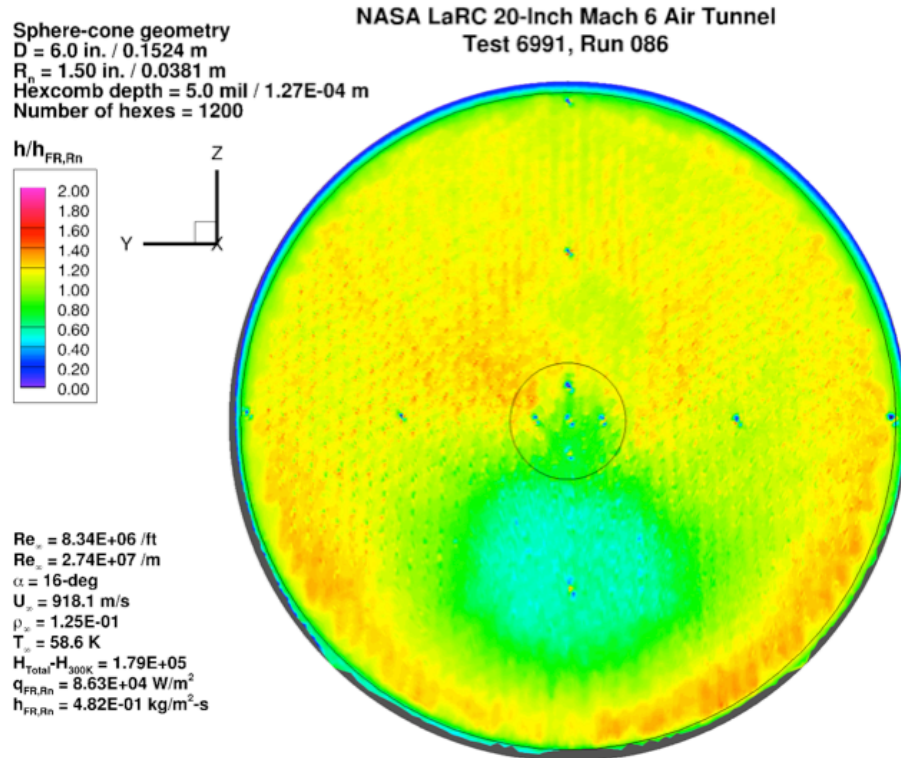


Figure 136. Test 6991, Run 86, $Re_\infty = 8.3 \times 10^6/\text{ft}$, sphere-cone 1200-0050.

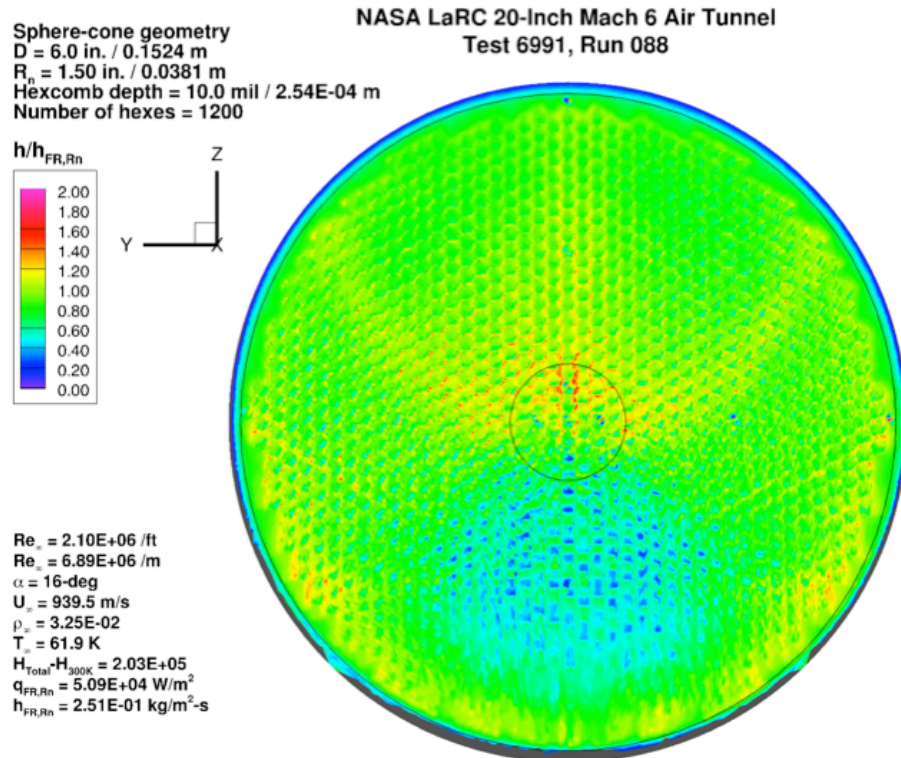


Figure 137. Test 6991, Run 88, $Re_\infty = 2.1 \times 10^6 / \text{ft}$, sphere-cone 1200-0100.

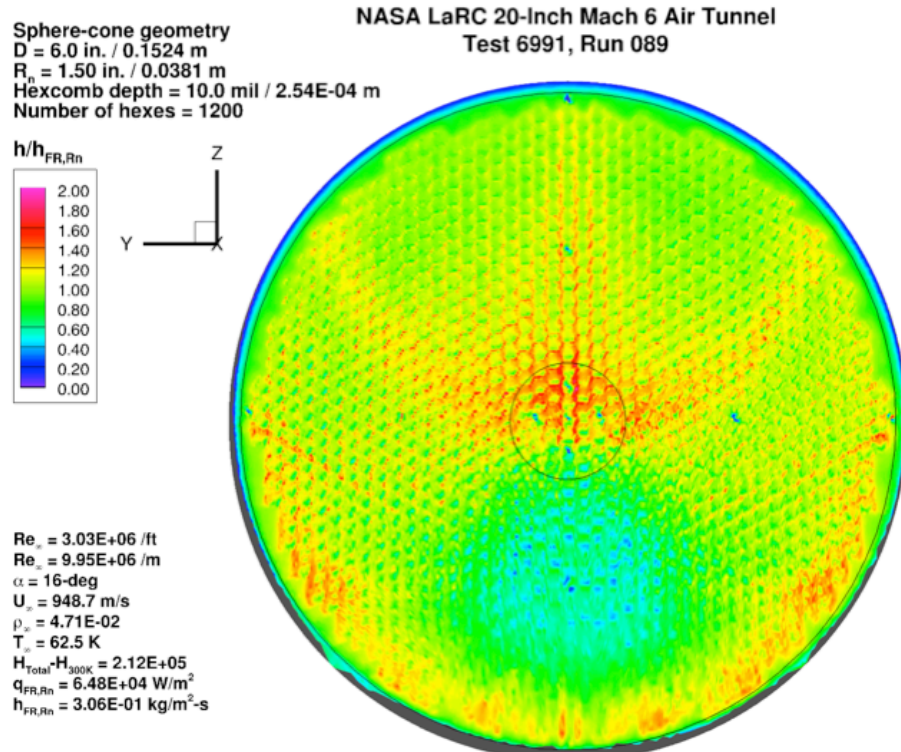


Figure 138. Test 6991, Run 89, $Re_\infty = 3.0 \times 10^6 / \text{ft}$, sphere-cone 1200-0100.

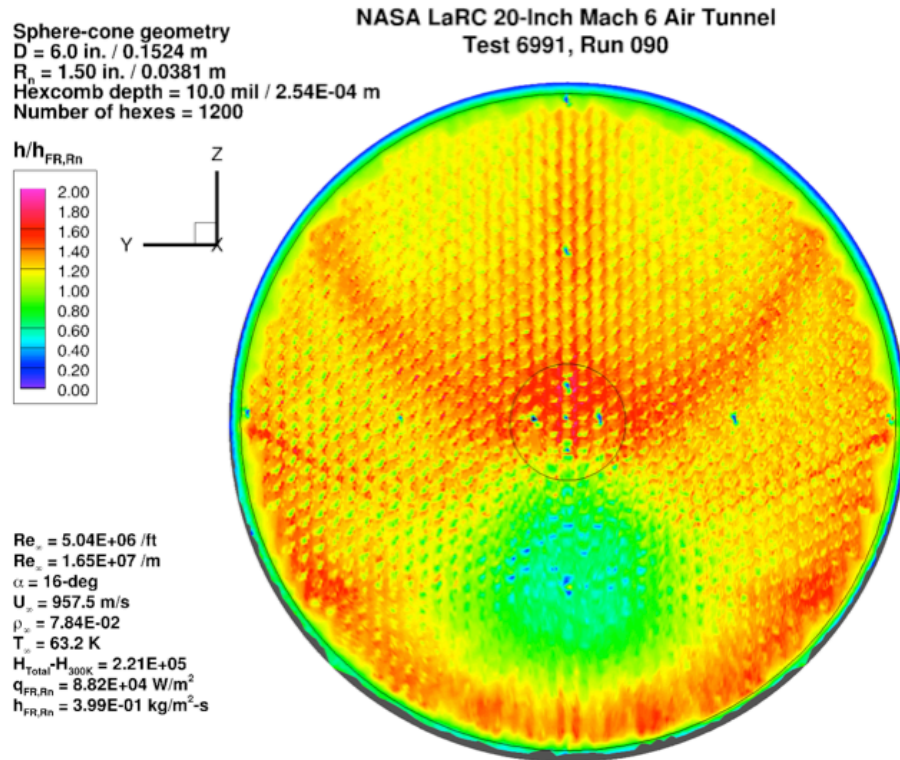


Figure 139. Test 6991, Run 90, $Re_\infty = 5.0 \times 10^6/\text{ft}$, sphere-cone 1200-0100.

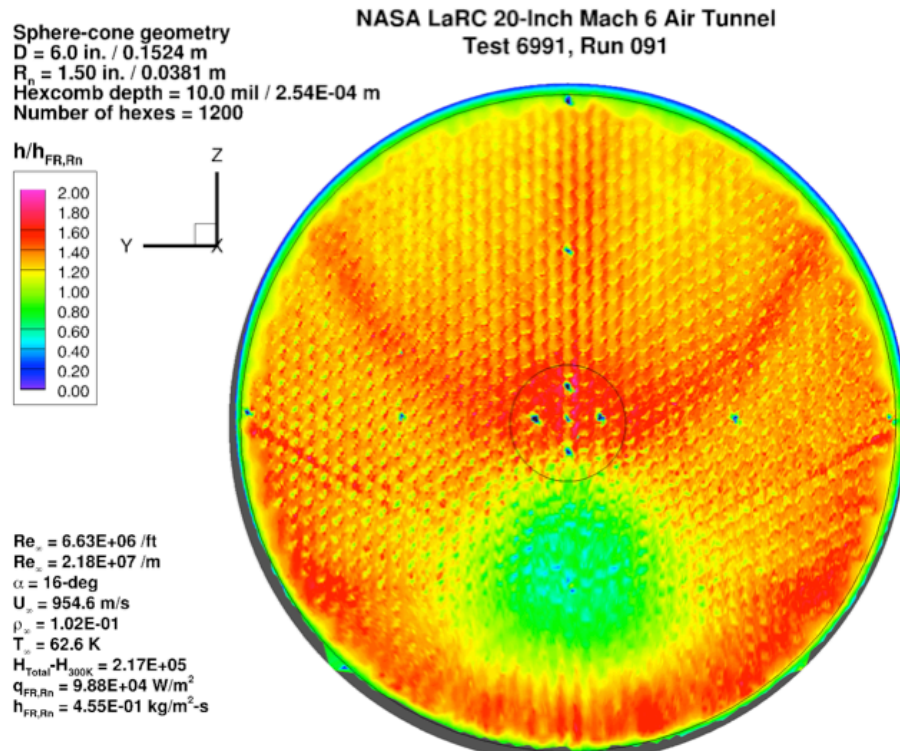


Figure 140. Test 6991, Run 91, $Re_\infty = 6.6 \times 10^6/\text{ft}$, sphere-cone 1200-0100.

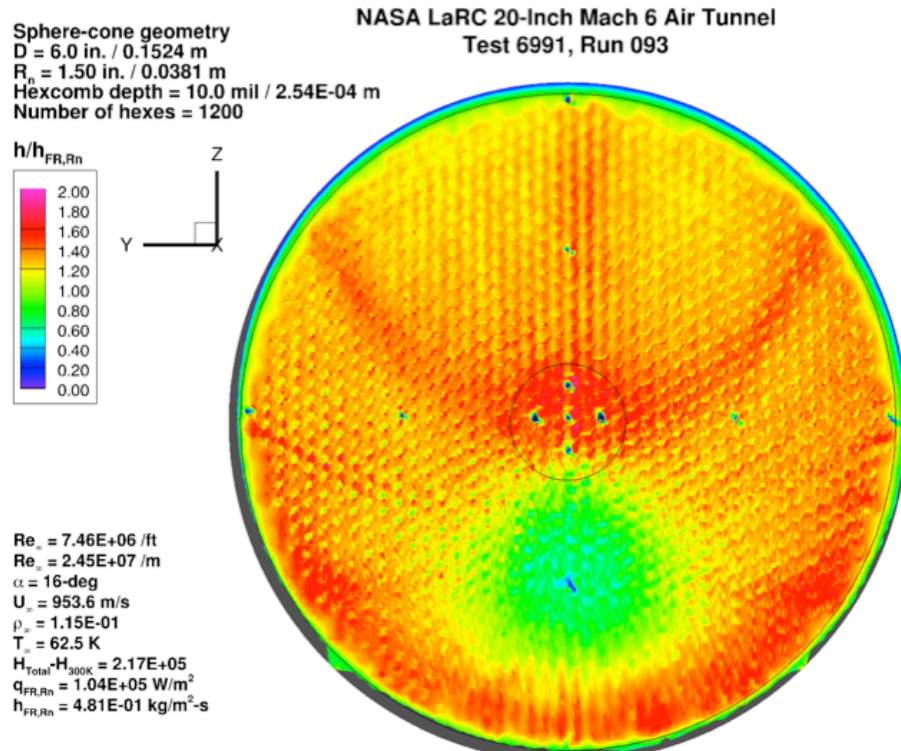


Figure 141. Test 6991, Run 93, $Re_\infty = 7.5 \times 10^6/\text{ft}$, sphere-cone 1200-0100.

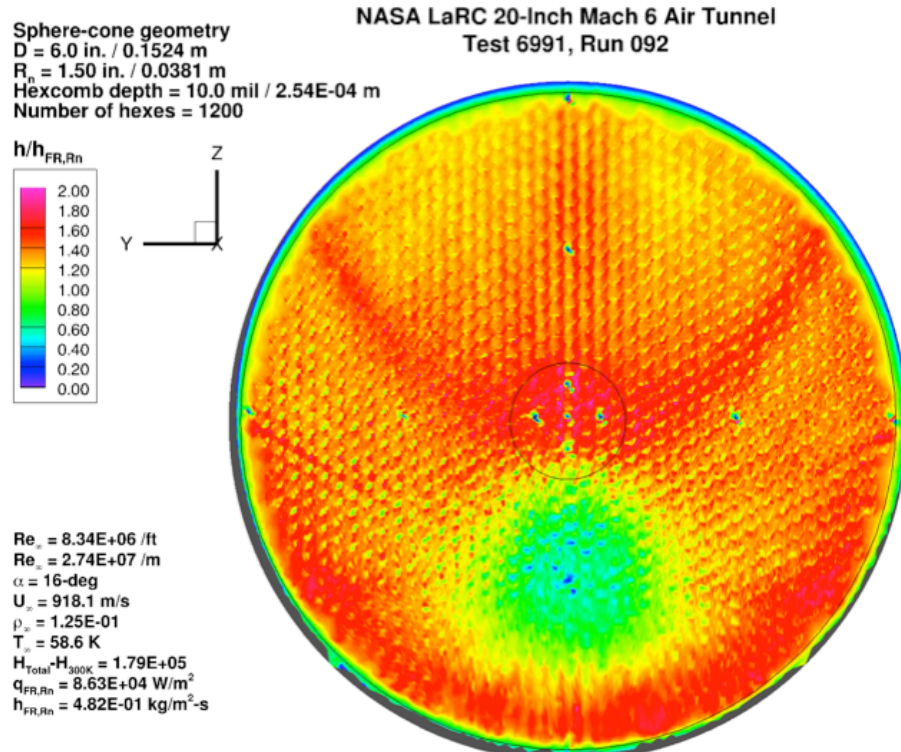


Figure 142. Test 6991, Run 92, $Re_\infty = 8.3 \times 10^6/\text{ft}$, sphere-cone 1200-0100.

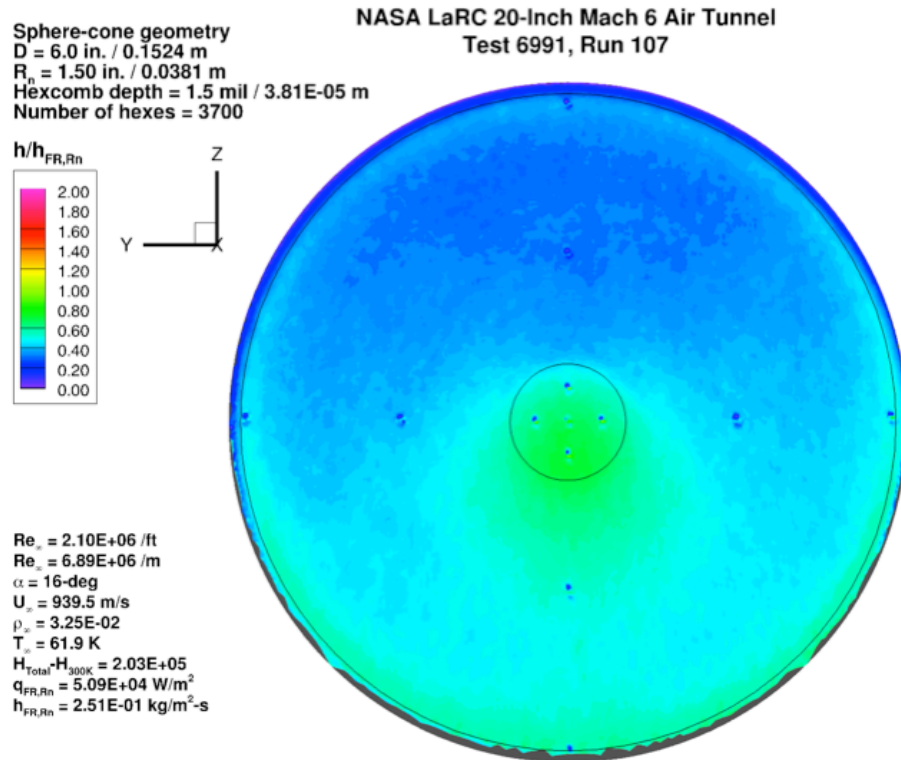


Figure 143. Test 6991, Run 107, $Re_\infty = 2.1 \times 10^6/\text{ft}$, sphere-cone 3700-0015.

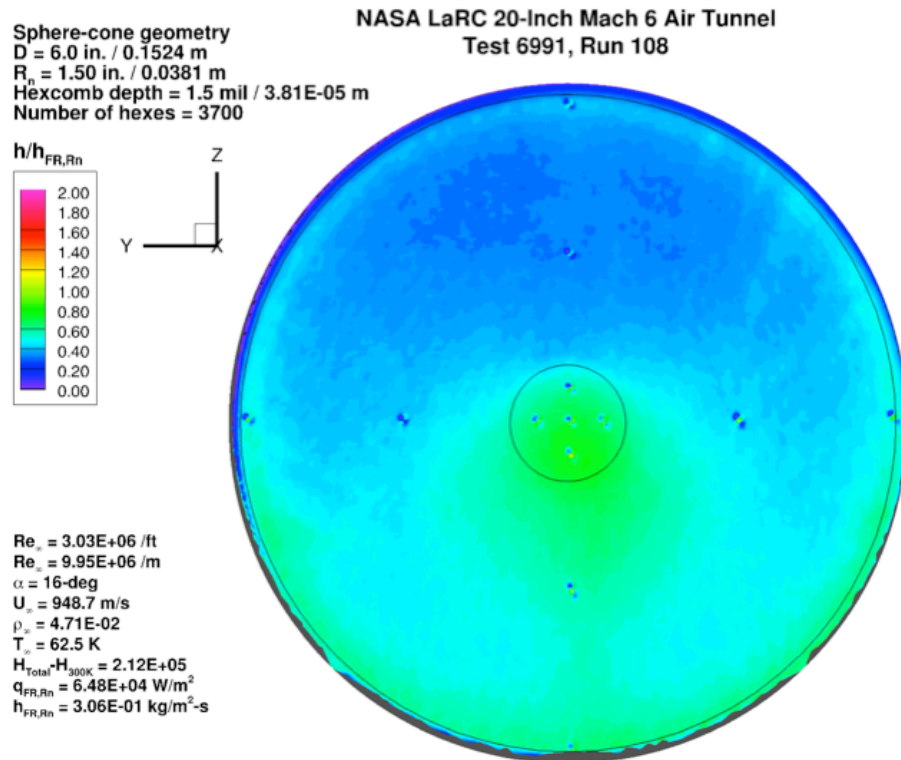


Figure 144. Test 6991, Run 108, $Re_\infty = 3.0 \times 10^6/\text{ft}$, sphere-cone 3700-0015.

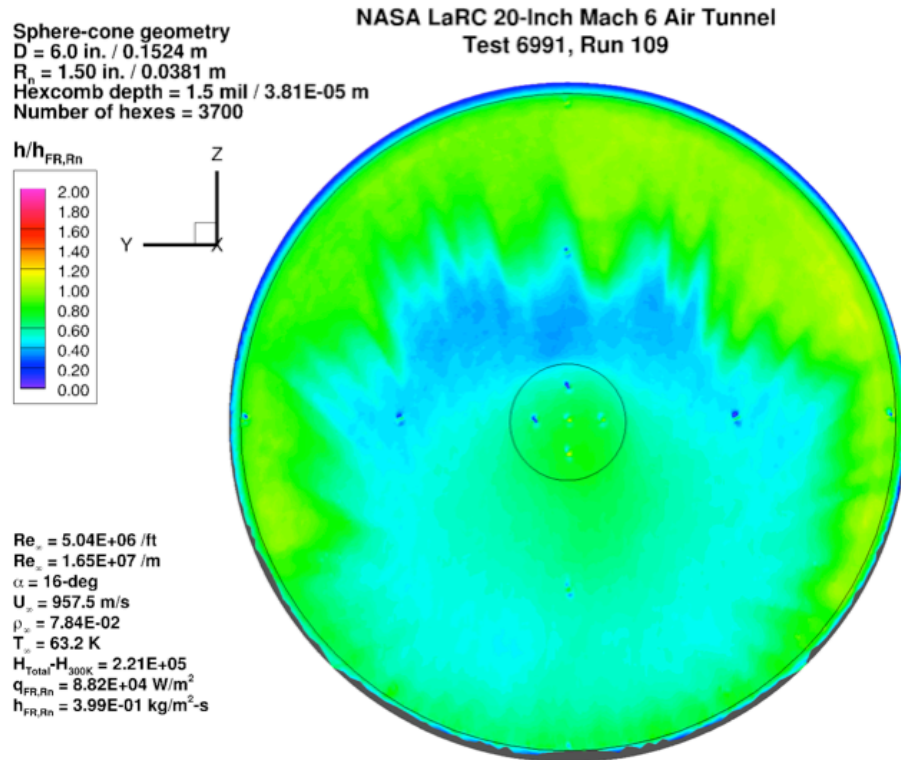


Figure 145. Test 6991, Run 109, $Re_\infty = 5.0 \times 10^6 / \text{ft}$, sphere-cone 3700-0015.

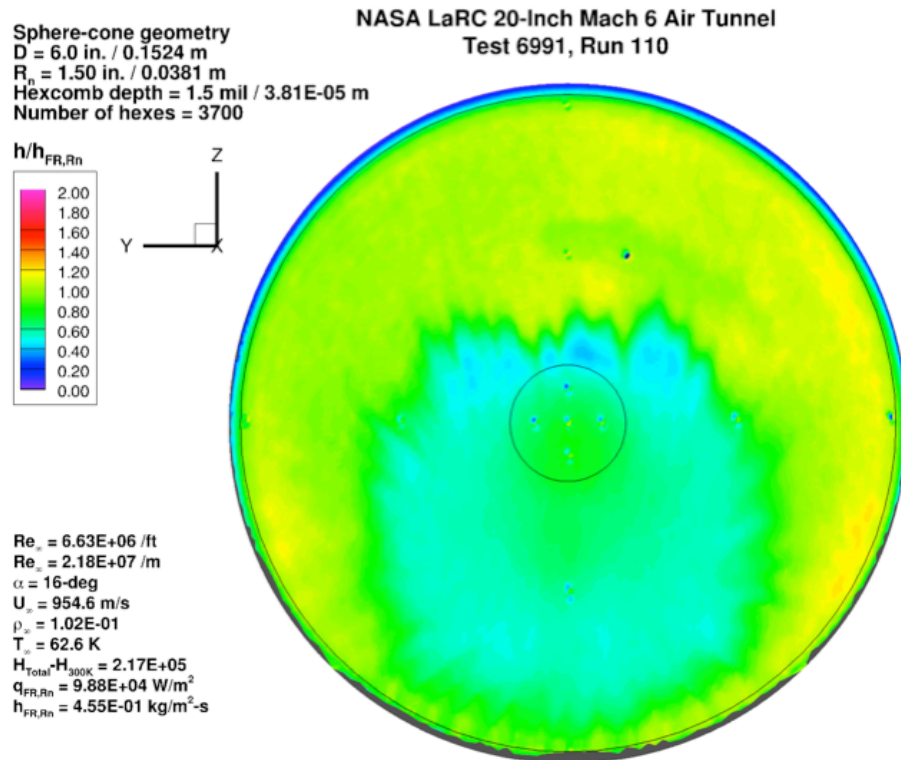


Figure 146. Test 6991, Run 110, $Re_\infty = 6.6 \times 10^6 / \text{ft}$, sphere-cone 3700-0015.

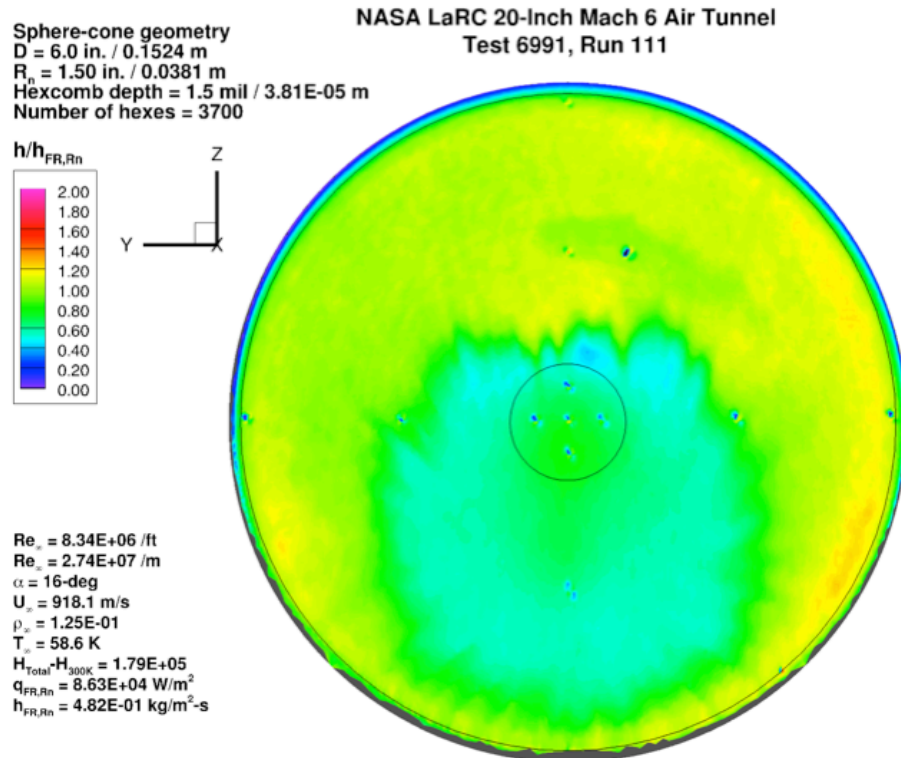


Figure 147. Test 6991, Run 111, $Re_\infty = 7.5 \times 10^6 / \text{ft}$, sphere-cone 3700-0015.

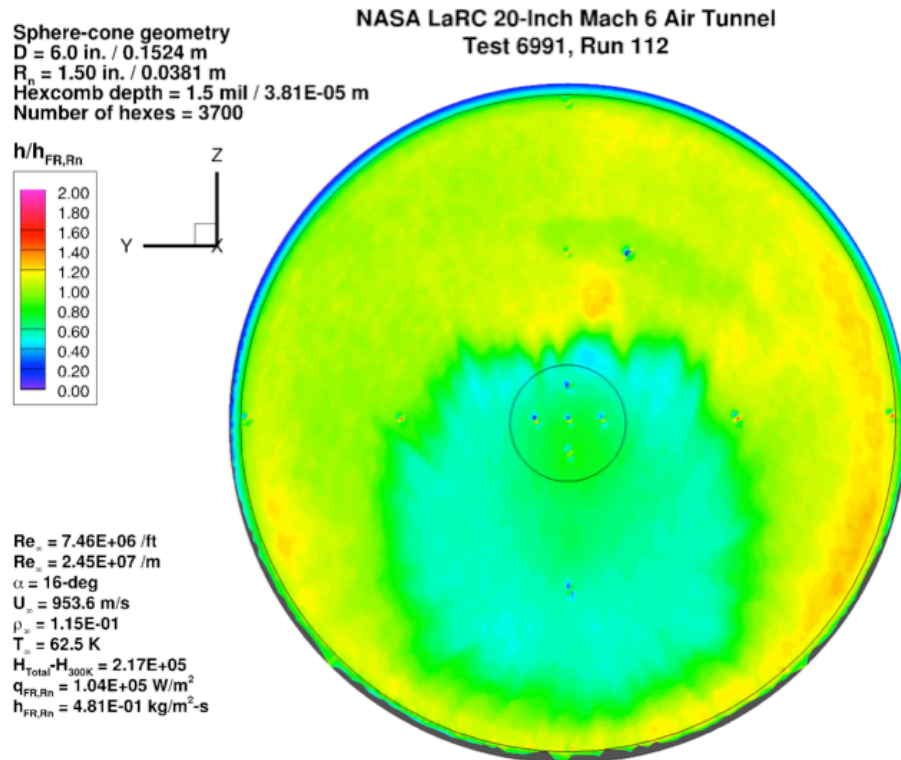


Figure 148. Test 6991, Run 112, $Re_\infty = 8.3 \times 10^6 / \text{ft}$, sphere-cone 3700-0015.

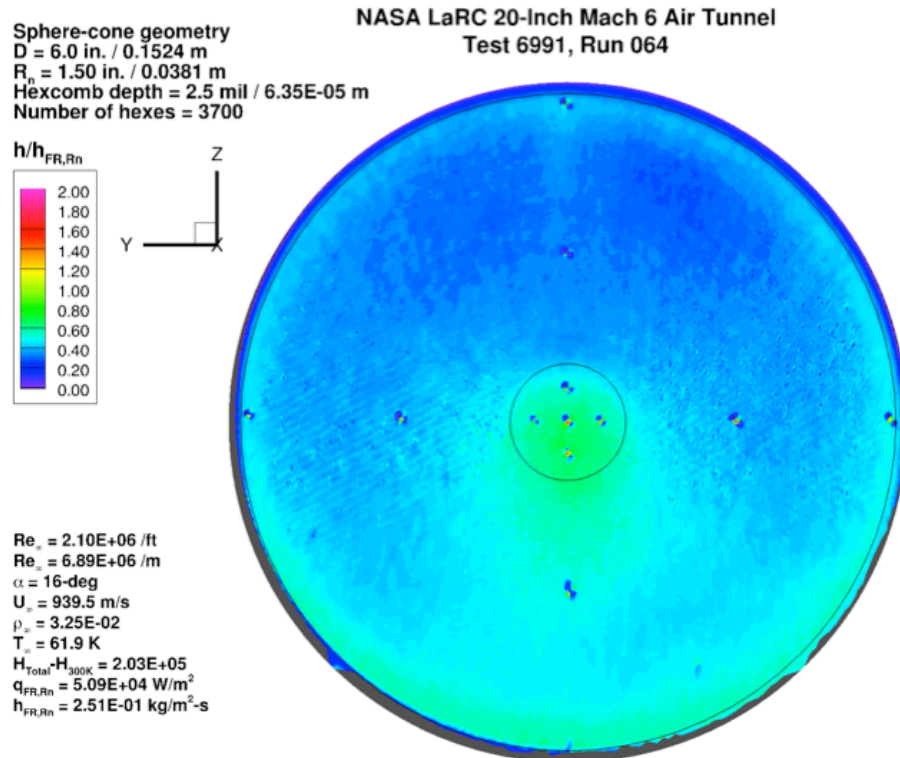


Figure 149. Test 6991, Run 64, $Re_\infty = 2.1 \times 10^6 / \text{ft}$, sphere-cone 3700-0025.

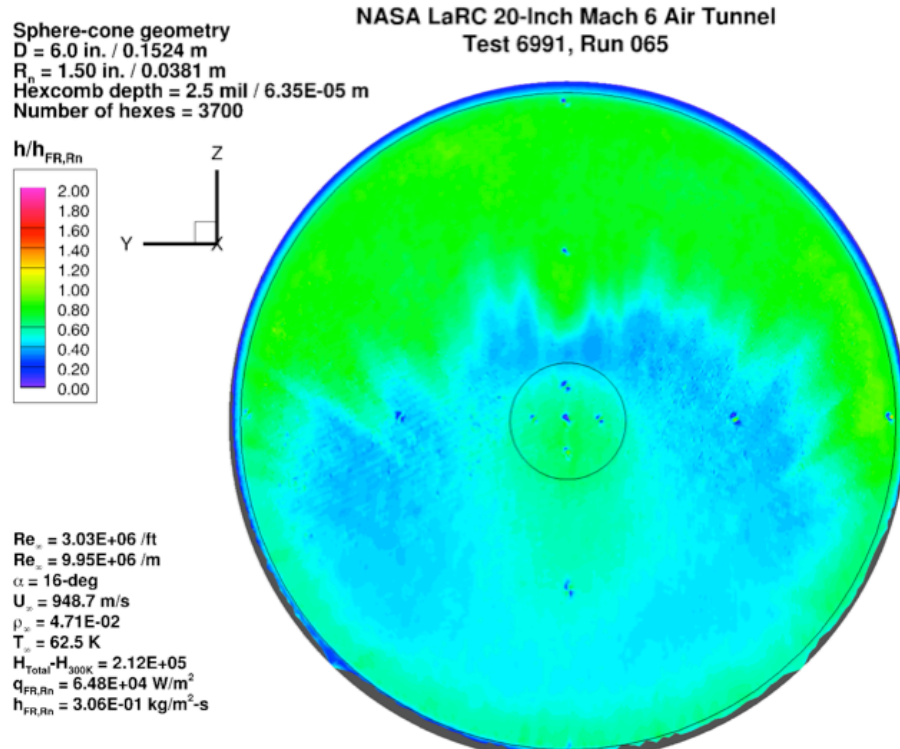


Figure 150. Test 6991, Run 65, $Re_\infty = 3.0 \times 10^6 / \text{ft}$, sphere-cone 3700-0025.

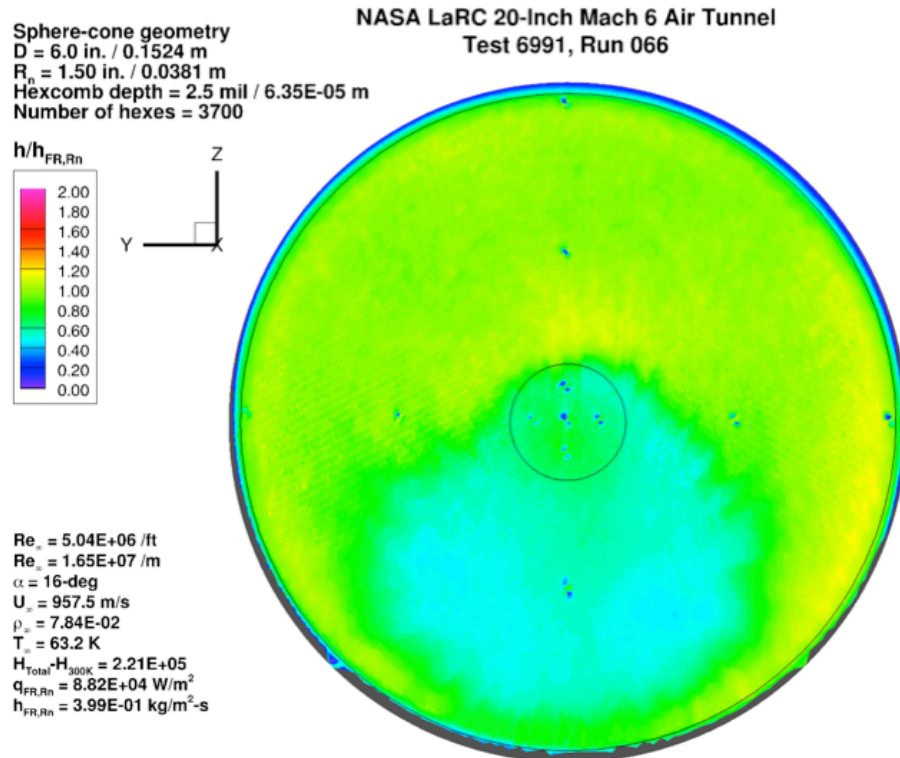


Figure 151. Test 6991, Run 66, $Re_\infty = 5.0 \times 10^6/\text{ft}$, sphere-cone 3700-0025.

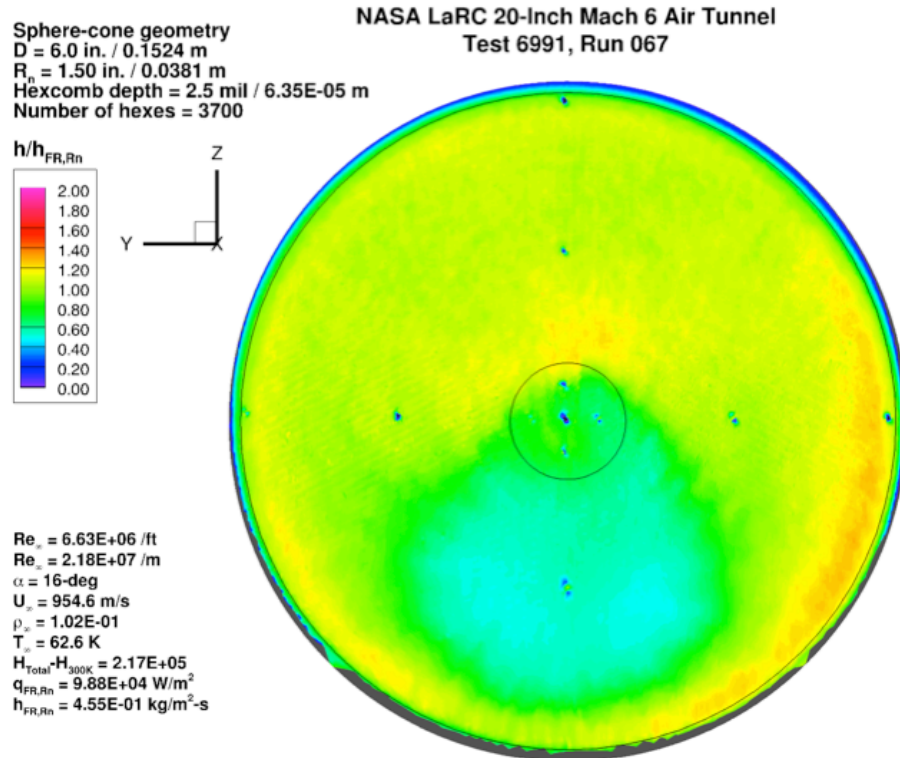


Figure 152. Test 6991, Run 67, $Re_\infty = 6.6 \times 10^6/\text{ft}$, sphere-cone 3700-0025.

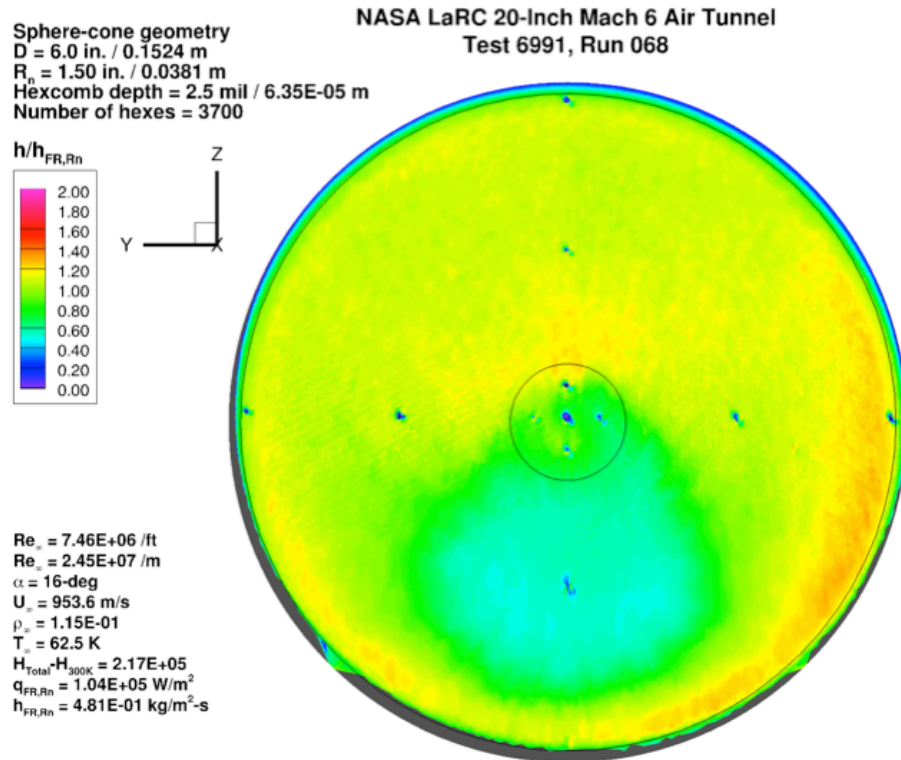


Figure 153. Test 6991, Run 68, $Re_\infty = 7.5 \times 10^6/\text{ft}$, sphere-cone 3700-0025.

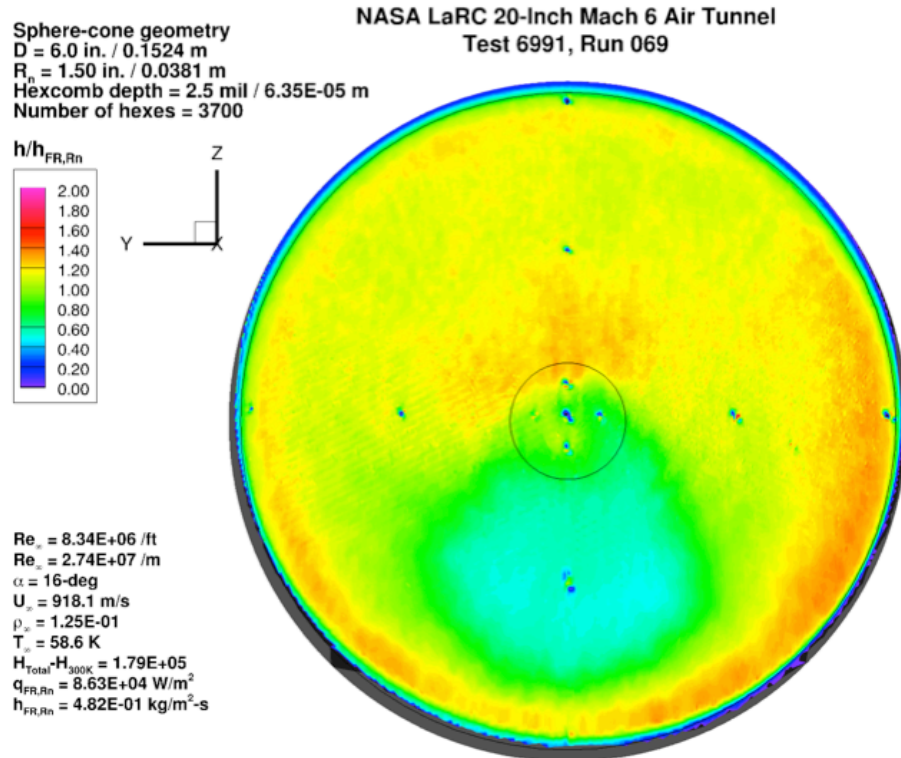


Figure 154. Test 6991, Run 69, $Re_\infty = 8.3 \times 10^6/\text{ft}$, sphere-cone 3700-0025.

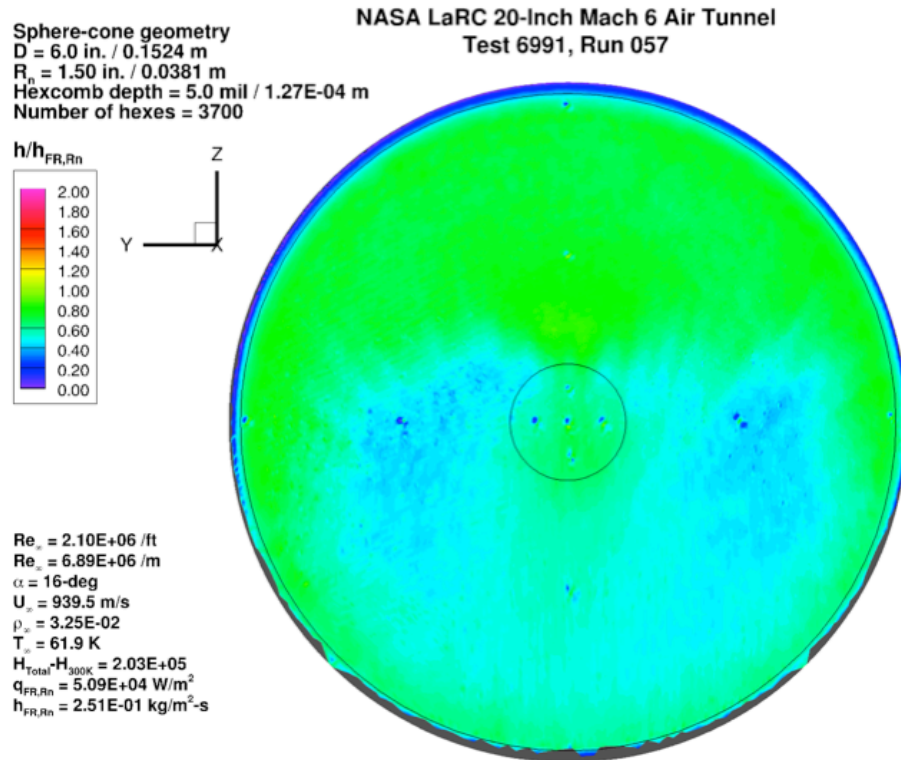


Figure 155. Test 6991, Run 57, $Re_\infty = 2.1 \times 10^6 / \text{ft}$, sphere-cone 3700-0050.

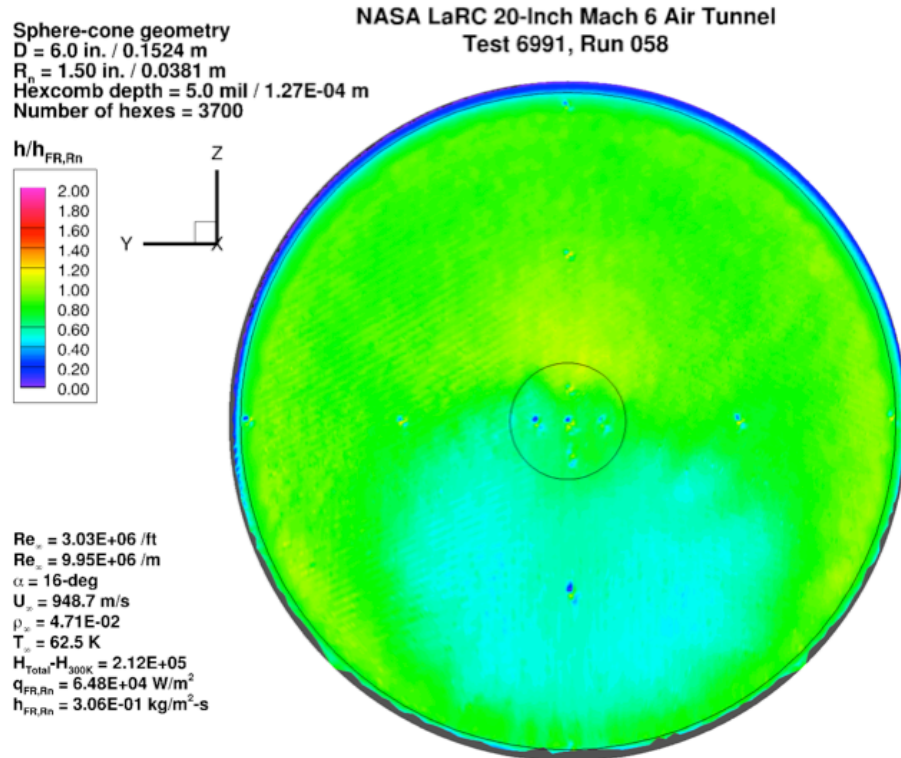


Figure 156. Test 6991, Run 58, $Re_\infty = 3.0 \times 10^6 / \text{ft}$, sphere-cone 3700-0050.

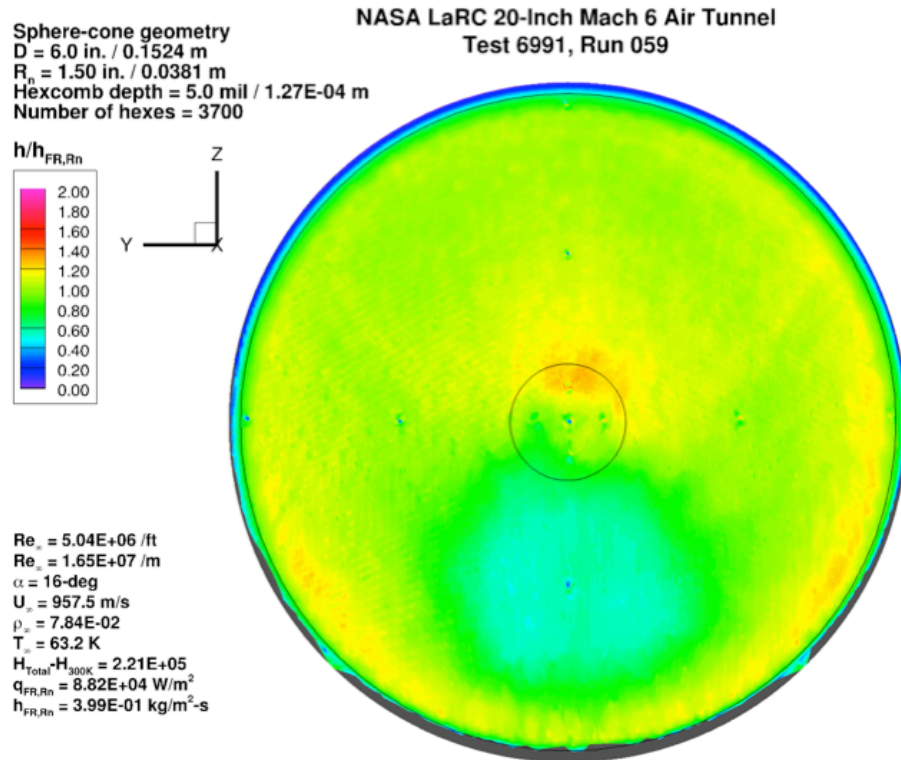


Figure 157. Test 6991, Run 59, $Re_\infty = 5.0 \times 10^6/\text{ft}$, sphere-cone 3700-0050.

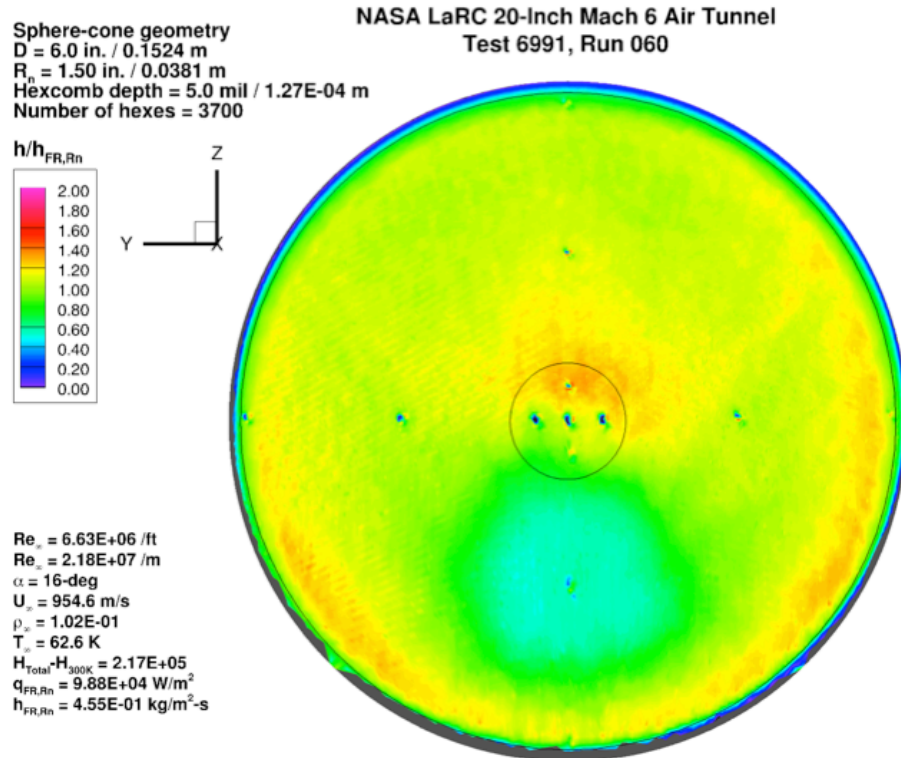


Figure 158. Test 6991, Run 60, $Re_\infty = 6.6 \times 10^6/\text{ft}$, sphere-cone 3700-0050.

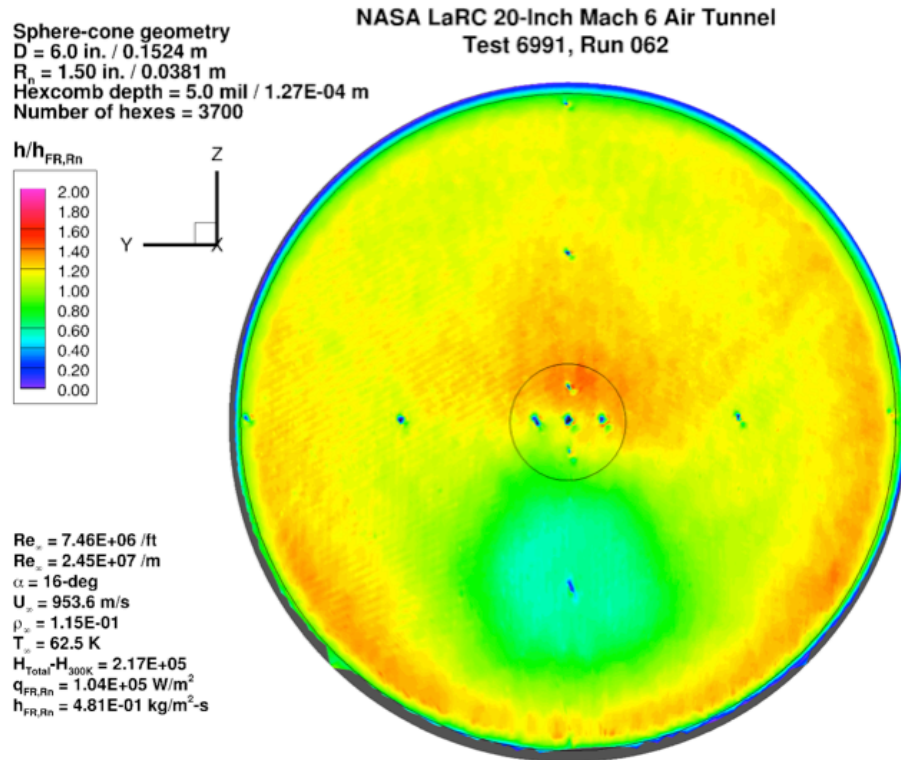


Figure 159. Test 6991, Run 62, $Re_\infty = 7.5 \times 10^6/\text{ft}$, sphere-cone 3700-0050.

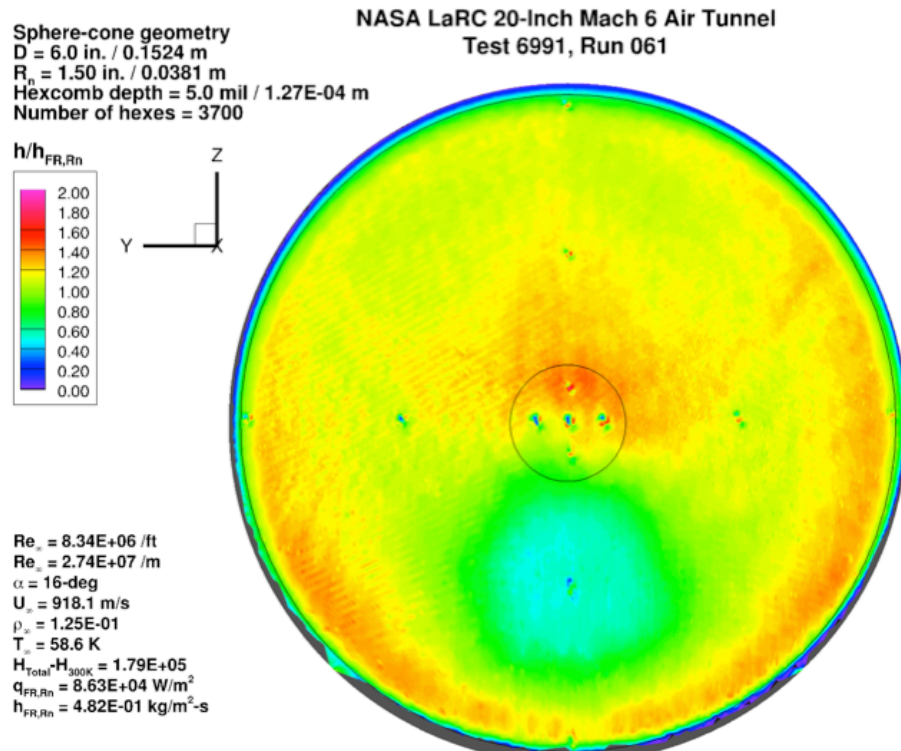


Figure 160. Test 6991, Run 61, $Re_\infty = 8.3 \times 10^6/\text{ft}$, sphere-cone 3700-0050.

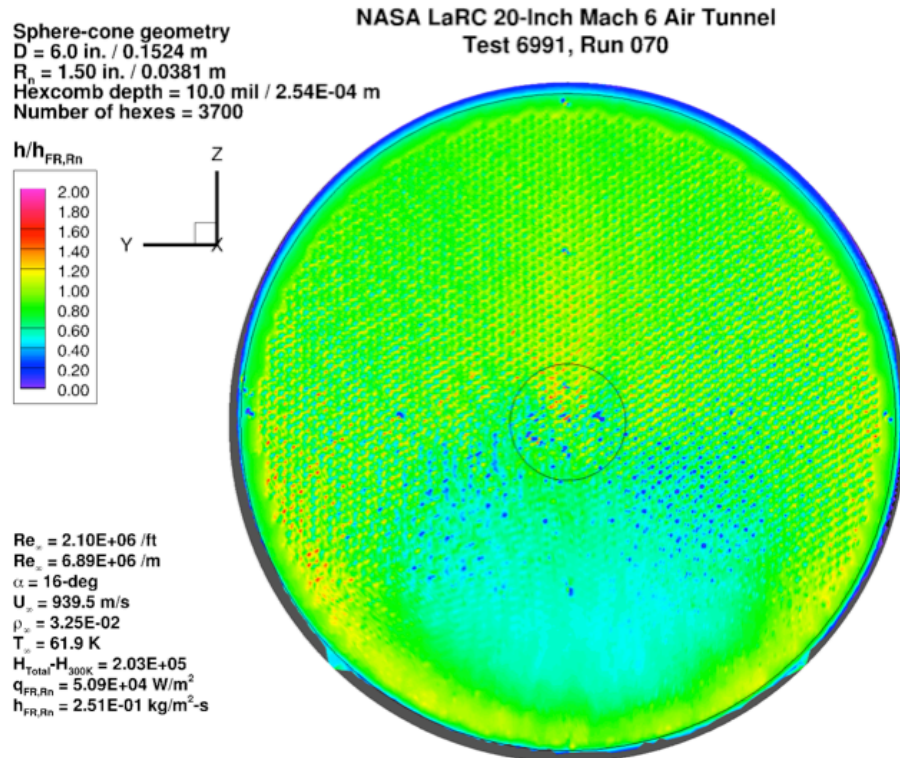


Figure 161. Test 6991, Run 70, $Re_\infty = 2.1 \times 10^6 / \text{ft}$, sphere-cone 3700-0100.

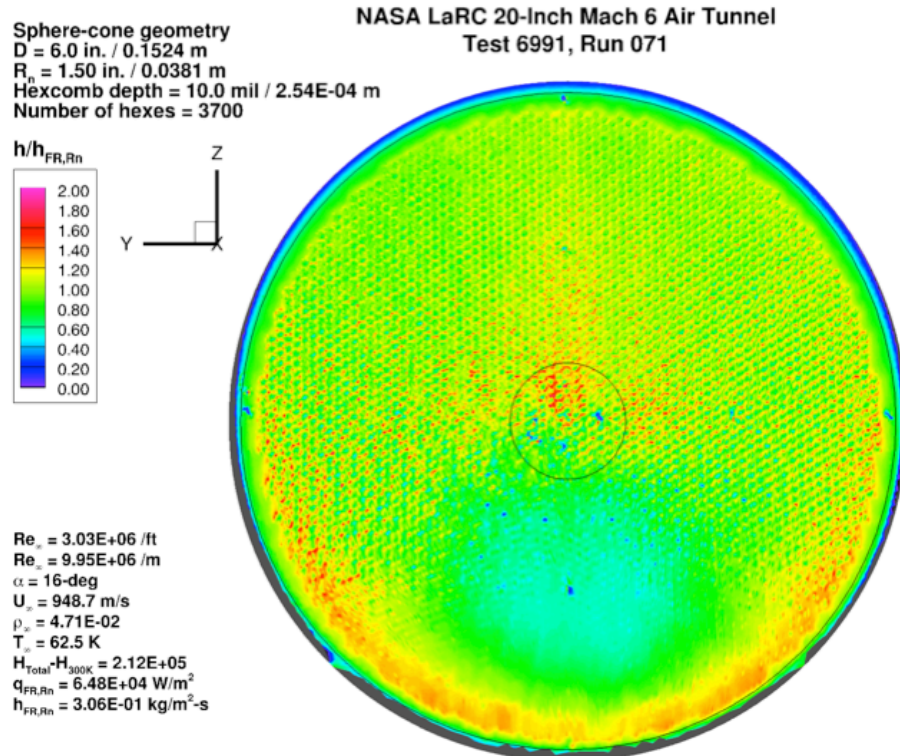


Figure 162. Test 6991, Run 71, $Re_\infty = 3.0 \times 10^6 / \text{ft}$, sphere-cone 3700-0100.

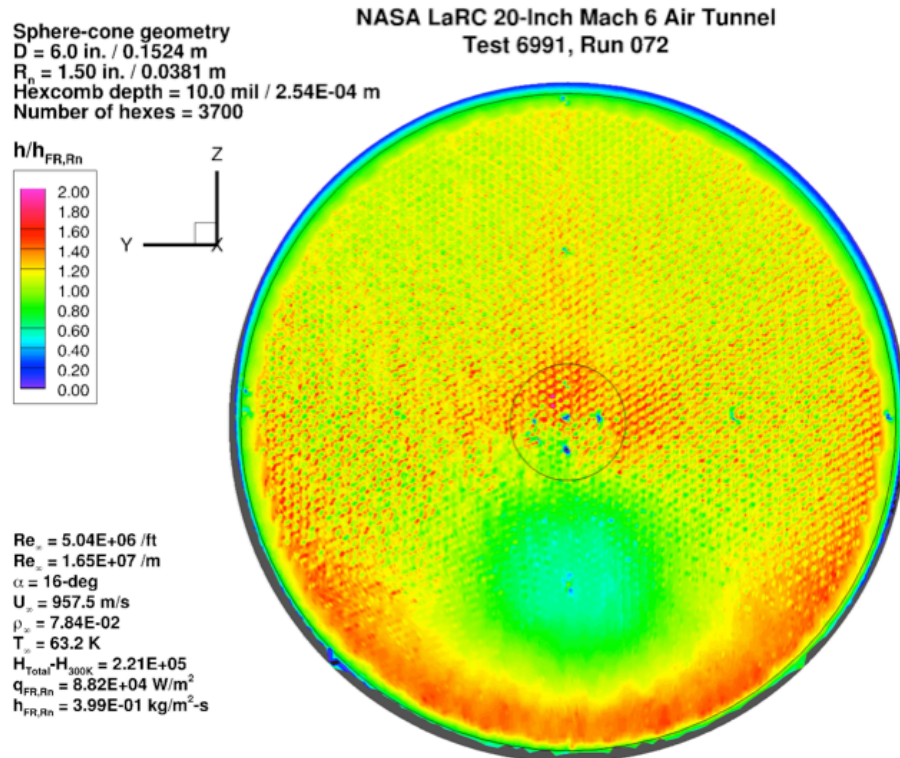


Figure 163. Test 6991, Run 72, $Re_\infty = 5.0 \times 10^6/\text{ft}$, sphere-cone 3700-0100.

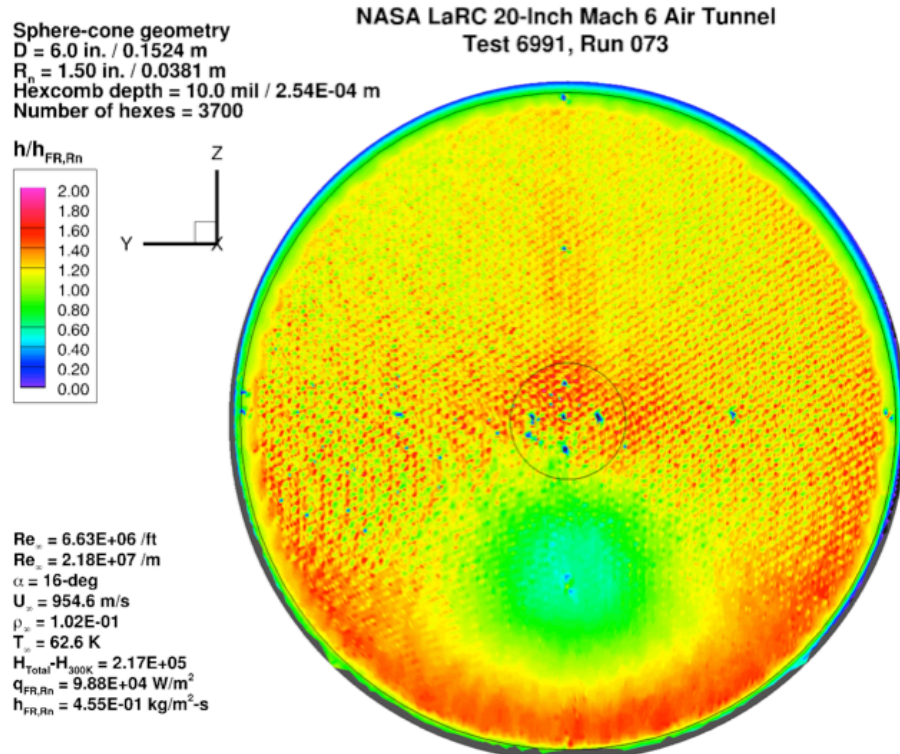


Figure 164. Test 6991, Run 73, $Re_\infty = 6.6 \times 10^6/\text{ft}$, sphere-cone 3700-0100.

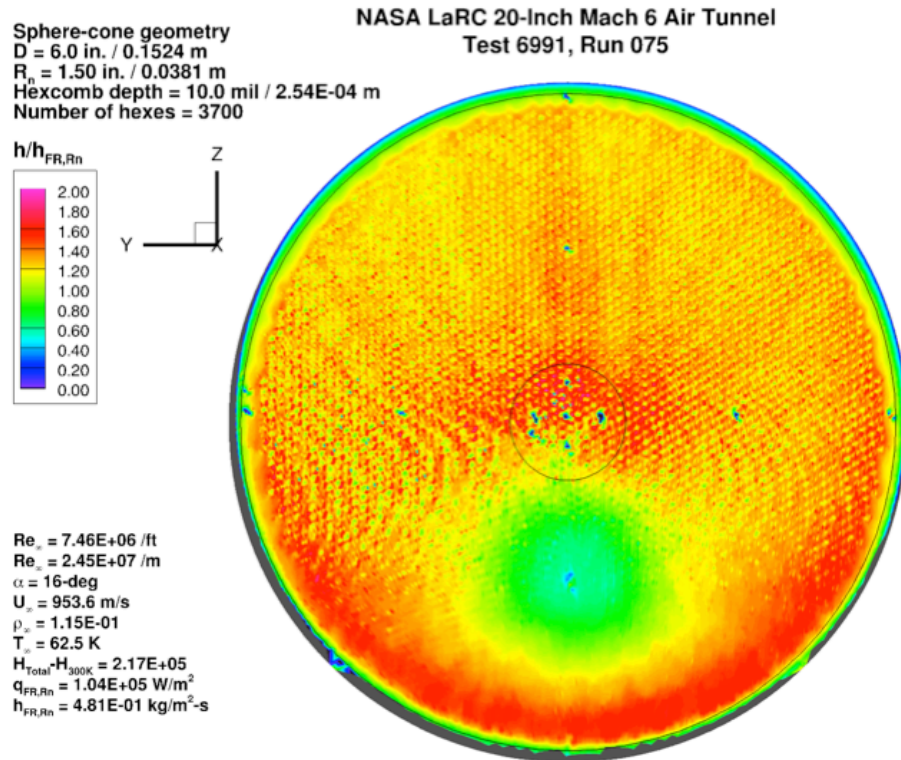


Figure 165. Test 6991, Run 75, $Re_\infty = 7.5 \times 10^6 / \text{ft}$, sphere-cone 3700-0100.

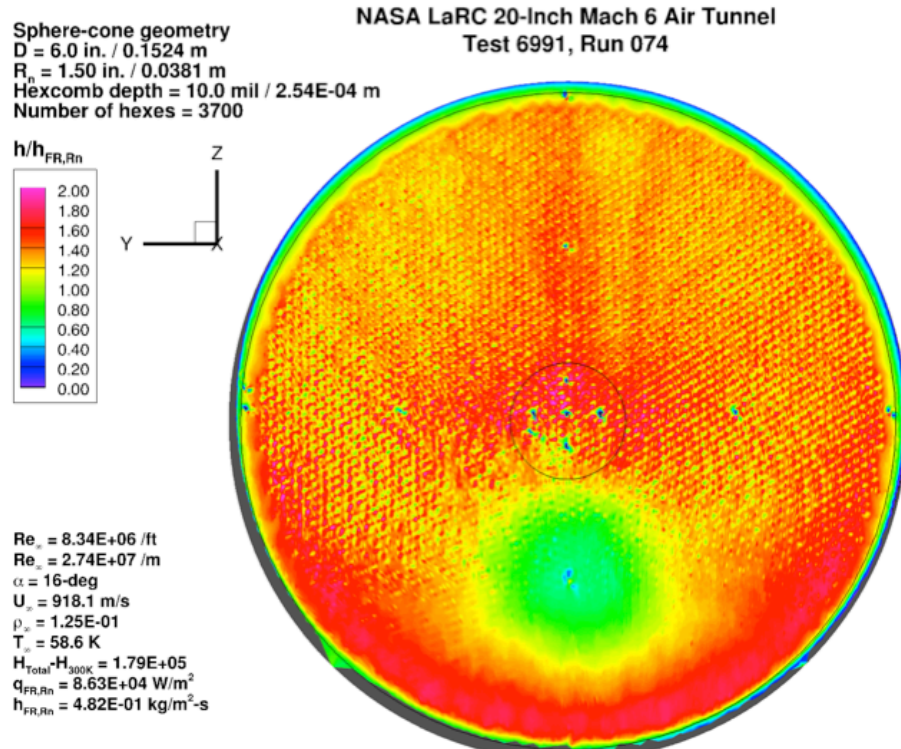


Figure 166. Test 6991, Run 74, $Re_\infty = 8.3 \times 10^6 / \text{ft}$, sphere-cone 3700-0100.

REPORT DOCUMENTATION PAGE

Form Approved
OMB No. 0704-0188

The public reporting burden for this collection of information is estimated to average 1 hour per response, including the time for reviewing instructions, searching existing data sources, gathering and maintaining the data needed, and completing and reviewing the collection of information. Send comments regarding this burden estimate or any other aspect of this collection of information, including suggestions for reducing the burden, to Department of Defense, Washington Headquarters Services, Directorate for Information Operations and Reports (0704-0188), 1215 Jefferson Davis Highway, Suite 1204, Arlington, VA 22202-4302. Respondents should be aware that notwithstanding any other provision of law, no person shall be subject to any penalty for failing to comply with a collection of information if it does not display a currently valid OMB control number.

PLEASE DO NOT RETURN YOUR FORM TO THE ABOVE ADDRESS.

1. REPORT DATE (DD-MM-YYYY)	2. REPORT TYPE		3. DATES COVERED (From - To)		
1-11-2019	Technical Memorandum				
4. TITLE AND SUBTITLE			5a. CONTRACT NUMBER 5b. GRANT NUMBER 5c. PROGRAM ELEMENT NUMBER 5d. PROJECT NUMBER 5e. TASK NUMBER 5f. WORK UNIT NUMBER		
Experimental Investigation of Hexcomb-Pattern Roughness Effects on Transition Onset and Turbulent Heating Augmentation at Mach 6			394364.04.24.23.01		
6. AUTHOR(S)			5d. PROJECT NUMBER 5e. TASK NUMBER 5f. WORK UNIT NUMBER		
Hollis, Brian R.			394364.04.24.23.01		
7. PERFORMING ORGANIZATION NAME(S) AND ADDRESS(ES)			8. PERFORMING ORGANIZATION REPORT NUMBER		
NASA Langley Research Center Hampton, VA 23681-2199			L-21079		
9. SPONSORING/MONITORING AGENCY NAME(S) AND ADDRESS(ES)			10. SPONSOR/MONITOR'S ACRONYM(S)		
National Aeronautics and Space Administration Washington, DC 20546-0001			NASA		
			11. SPONSOR/MONITOR'S REPORT NUMBER(S)		
			NASA-TM-2019-220424		
12. DISTRIBUTION/AVAILABILITY STATEMENT					
Unclassified- Subject Category 34 Availability: NASA STI Program (757) 864-9658					
13. SUPPLEMENTARY NOTES					
14. ABSTRACT					
An experimental investigation of hexcomb-patterned surface roughness effects on boundary-layer transition and turbulent heating has been performed. Two representative entry vehicle geometries, a spherical-cap aeroshell and a sphere-cone aeroshell, were considered. Multiple cast ceramic models of each geometry were fabricated with varying roughness pattern densities and depths that simulated an ablated hexcomb-structure thermal protection system. Wind tunnel testing was performed at Mach 6 over a range of Reynolds numbers sufficient to produce laminar, transitional, and turbulent flow. Aeroheating and boundary-layer transition onset data were obtained using global phosphor thermography. The experimental heating data are presented herein, as are comparisons to laminar and turbulent smooth-wall heat transfer distributions from computational flow field simulations.					
15. SUBJECT TERMS					
heat-transfer; roughness; wind tunnel boundary-layer transition					
16. SECURITY CLASSIFICATION OF:			17. LIMITATION OF ABSTRACT	18. NUMBER OF PAGES	19a. NAME OF RESPONSIBLE PERSON
a. REPORT	b. ABSTRACT	c. THIS PAGE	UU	157	STI Help Desk (email: help@sti.nasa.gov)
U	U	U	UU		19b. TELEPHONE NUMBER (Include area code) (757) 864-9658